

LOOK INTO THE LIGHT: TUNING PLATINUM ACETYLIDE COMPLEXES
FOR ENHANCED PHOTOPHYSICAL PROPERTIES

By

RUSSELL W. WINKEL

A DISSERTATION PRESENTED TO THE GRADUATE SCHOOL
OF THE UNIVERSITY OF FLORIDA IN PARTIAL FULFILLMENT
OF THE REQUIREMENTS FOR THE DEGREE OF
DOCTOR OF PHILOSOPHY

UNIVERSITY OF FLORIDA

2015

© 2015 Russell W. Winkel

To my family and friends

ACKNOWLEDGMENTS

First and foremost I'd like to thank my advisor, Prof. Kirk Schanze, for giving me the freedom to work in an unrestricted setting, having the patience to allow me to pursue side projects, and always being available to provide guidance when it was needed. The projects that I've been allowed to work on have reinforced my understanding of the basics of photophysics, while pushing the limits of advanced materials.

Next I would like to thank my Committee members: Prof. Ken Wagener, Prof. Stephen Miller, Prof. Adam Veige, and Prof. Bruce Carroll, not only for their guidance when needed, but for making the final defense *scheduling* completely painless as well.

The entire Schanze Group has been phenomenal in my time here. The dynamic of the group, and the willingness of its members to work with and help each other, I believe, is unrivaled in our department. Starting with the former members, I'd like to thank Dr. Galyna Dubinina for showing me the finer points of experimental details and crystallization. Dr. Randi Price was instrumental in teaching me how to use all of the laser systems housed in our labs. Dr. Ali Gundogan, who pioneered the methodology of the Stille-type coupling to generate platinum aryl complexes, which was the basis of my last project. For pointing me in the right direction computationally, I would like to thank Dr. M. Erkan Kose. Finally, I am grateful to Dr. Abby Hobbs-Shelton for her work on platinum acetylide chromophores which led directly into my first project.

For current members, I would like to start by thanking Subhadip Goswami for his insights on organometallic synthesis and general conversations. Seda Cekli has also been very helpful in helping me operate the lesser used Old TA laser and general instrumental troubleshooting. Samantha Phan has put in a ton of work fighting with and

optimizing protocol for the Tsunami laser. An exchange student, Louise Fouquat, was also very helpful in working with and testing the limitations of the Tsunami laser. While not a member of the Schanze Group, I also need to thank Zach Morseth of the Papanikolas Group at UNC for running the MD simulations found in Chapter 3. These members and all of the others not mentioned here made my time in the Schanze Group great.

My time spent in grad school has been made relatively painless thanks to the support of all of my family and friends. I need to first thank my parents, Bob and Mary, for always pushing me to be better and never letting me quit on something that I had started. Those two values have helped propel me to where I am today. I also need to thank my brother, Chris, for keeping me grounded and making sure I don't forget the country life. As for my friends, I need to thank my roommates Mike Costanzo and Andrew Mowson for making sure school didn't take over my life. Whether it be video games, sporting events, or just shootin' the breeze, living with them always kept things light and entertaining.

Last but certainly not least, I need to thank my girlfriend Adeline for always being there. Regardless of how things were going, or how much work I needed to do at home, her love and support for me never wavered.

TABLE OF CONTENTS

	<u>page</u>
ACKNOWLEDGMENTS	4
LIST OF TABLES	10
LIST OF FIGURES	11
ABSTRACT	23
CHAPTER	
1 INTRODUCTION	25
Overview	25
Platinum Carbene Complexes	25
In Non-chromophoric Systems	25
As Chromophoric Ligands	26
As Ancillary Ligands to Acetylene Chromophores	34
Excimers and Dimeric Complexes Tethered by Flexible Linking Units	38
Overview	38
Applications	39
Excimeric Complexes Containing Platinum	40
Monosubstituted Platinum-Aryl Compounds as Precursors to Mixed Ligand Platinum Aryl/Acetylene Systems	42
2 PHOTOPHYSICAL PROPERTIES OF <i>TRANS</i> -PLATINUM ACETYLIDE COMPLEXES FEATURING N-HETEROCYCLIC CARBENE LIGANDS	47
Background	47
Synthesis and Structure	48
Photophysical Properties	52
Electronic Structure Calculations	56
Summary and Conclusions	57
Experimental	59
General Remarks	59
Fourier Transform Infrared Spectroscopy (FTIR)	60
X-ray Structure Determinations	60
Absorption and Emission Spectroscopy	61
Nanosecond Transient Absorption (TA) Spectroscopy	62
Open Aperture Z-Scan	63
Computational Details	63
Synthesis of <i>trans</i> -(ICy) ₂ PtCl ₂ (1)	64
General Procedure for the Hagihara Coupling Reaction (2a-c)	65
<i>trans</i> -(ICy) ₂ Pt(PEt ₂) ₂ (2a)	65
<i>trans</i> -(ICy) ₂ Pt(BTF) ₂ (2b)	66

	<i>trans</i> -(ICy) ₂ Pt(DPAF) ₂ (2c)	66
3	PLATINUM DIMERS LINKED BY ONE, TWO, OR THREE FLEXIBLE GROUPS FOR STUDY OF EXCITED STATE DYNAMICS	68
	Background.....	68
	Synthesis	70
	Photophysical Properties	72
	Molecular Dynamics Simulations	80
	Summary and Conclusions	82
	Experimental.....	85
	General Remarks	85
	Absorption and Emission Spectroscopy	86
	Nanosecond Transient Absorption (TA) Spectroscopy.....	86
	Transient Absorption Power Dependence	87
	Computational Details	87
	Structure optimization	87
	Molecular dynamics calculations.....	87
	Synthesis of bis(4-bromobenzyl) ether (COC-Br)	88
	General Procedure for the Sonogashira Coupling Reaction.....	88
	1,2-bis(4-(trimethylsilylethynyl)phenyl)ethane (CC-TMS).....	89
	Bis(4-(trimethylsilylethynyl)benzyl) ether (COC-TMS).....	89
	General Procedure for the TMS Deprotection Reaction	89
	1,2-bis(4-ethynylphenyl)ethane (CC-H)	90
	Bis(4-ethynylbenzyl) ether (COC-H)	90
	Synthesis of monosubstituted platinum precursor <i>trans</i> -(PBU ₃) ₂ Pt(PE2)Cl (PE2-Pt-Cl).....	90
	Synthesis of model complex <i>trans</i> -(PBU ₃) ₂ Pt(PE2)(CC-p-tolyl) (tol-PtPE2).....	90
	General Procedure for the Hagihara Coupling Reaction for Platinum Dimers.....	91
	<i>trans</i> -[(PE2)Pt(PBU ₃) ₂ (CC-p-Ph)] ₂ CH ₂ (C-PtPE2)	92
	<i>trans</i> -[(PE2)Pt(PBU ₃) ₂ (CC-p-Ph)] ₂ -1,2-ethane (CC-PtPE2).....	92
	<i>trans</i> -[(PE2)Pt(PBU ₃) ₂ (CC-p-Benzyl)] ₂ O (COC-PtPE2)	92
4	PHOTOPHYSICAL PROPERTIES OF COMPLEXES FEATURING A MIXED ARYL-PLATINUM-ACETYLIDE CHROMOPHORE MOTIF	94
	Background.....	94
	Synthesis	95
	Photophysical Properties	98
	Absorption	98
	Fluorescence	101
	Phosphorescence.....	103
	Transient Absorption	105
	Electronic Structure Calculations	107
	Summary and Conclusions	114
	Experimental.....	117

General Remarks	117
Absorption and Emission Spectroscopy	118
Nanosecond Transient Absorption (TA) Spectroscopy.....	118
Computational Details	119
General Procedure for the Hagihara Coupling Reaction for Mixed Platinum Aryl Acetylide Compounds.	119
<i>trans</i> -(PBU ₃) ₂ Pt(BTF)(CCBTF) (BTF-Pt-CCBTF)	120
<i>trans</i> -(PBU ₃) ₂ Pt(DPAF)(CCDPAF) (DPAF-Pt-CCDPAF)	120
<i>trans</i> -(PBU ₃) ₂ Pt(BTF)(CCDPAF) (BTF-Pt-CCDPAF).....	121
<i>trans</i> -(PBU ₃) ₂ Pt(DPAF)(CCBTF) (DPAF-Pt-CCBTF).....	121

APPENDIX

A TSUNAMI FEMTOSECOND LASER MANUAL	123
Overview.....	123
Laser Start-up	124
Laser Wavelength Selection, Mode-Locking, and Output Power Optimization	125
Wavelength Selection and Mode-Locking	125
Output Power Optimization.....	127
Two-Photon Excited Fluorescence (2PEF)	127
Two-Photon Cross Section Measurements.....	128
Data Conversion	130
Instrument Shut Down	130
Laser Powers and Bandwidths at Given Wavelengths	130
Data Workup.....	131
Troubleshooting	132
Pump Laser is not Coming Up to the Set Power	132
Laser Can Not Be Tuned Below 780 nm.	133
Advanced Troubleshooting	133
B COMPUTATIONAL METHODS	136
Overview.....	136
Accessing the HPC	137
General Considerations	138
Using Gaussian 09 and GaussView 5 via the HPC	139
Creating Input Files and Submitting Jobs	140
Geometry Optimization/Standard Input Parameters.....	141
Frequency	145
Time Dependent Density Functional Theory (TDDFT)	147
Triplet Computations	148
General considerations	148
Estimation of phosphorescence energy	149
Stability.....	149
Population	149
Volume	151

PBS Script.....	151
Reading and Interpreting Output Files	155
Geometry Optimization.....	156
Frequency	157
TDDFT.....	160
Stability.....	161
Population	161
Volume	165
Visualizing Results.....	166
GaussView	167
Molecular geometry	167
Molecular orbitals.....	167
Chemcraft.....	169
Generating cube files	169
Molecular geometry/molecular orbitals	170
Charge difference density	171
Considerations for Triplet Graphics Generation	174
C SUPPORTING INFORMATION FOR CHAPTER 2	176
X-ray Experimental and Data.....	176
NMR Spectra	181
IR Spectra.....	185
Emission Lifetime Decays.....	187
Transient Absorption Decays.....	189
Triplet-Triplet Absorption Power Dependence	191
Computational Studies.....	192
D SUPPORTING INFORMATION FOR CHAPTER 3	200
NMR Spectra	200
Emission Lifetime Decays.....	211
Transient Absorption Decays.....	213
E SUPPORTING INFORMATION FOR CHAPTER 4	217
NMR Spectra	217
Emission Lifetime Decays.....	226
Transient Absorption Decays.....	228
Computational Results.....	230
Monosubstituted Platinum Model Complexes.....	230
Mixed Ligand Platinum Aryl/Acetylide Complexes.....	232
LIST OF REFERENCES	239
BIOGRAPHICAL SKETCH.....	245

LIST OF TABLES

<u>Table</u>	<u>page</u>
2-1 Key interatomic distances (Å) and angles (deg) for platinum acetylide complexes.	50
2-2 Summary of photophysical data for platinum acetylides 2a-c and 3a-c	53
2-3 Summary of TD-DFT computations for the $S_0 \rightarrow S_1$ transition of 2a'-c'	57
3-1 Summary of photophysical data for R-PtPE2	73
4-1 Summary of photophysical data for mixed aryl/acetylide ligated Pt(II) complexes.	100
4-2 Summary of TD-DFT computations for the $S_0 \rightarrow S_1$ transition of monosubstituted platinum aryl and platinum acetylide compounds.	108
4-3 Summary of TD-DFT computations for transitions of oscillator strength > 0.1 and $\lambda > 345$ nm for the mixed platinum aryl/acetylide complexes.....	111
A-1 Laser powers and bandwidths at given wavelengths.....	130
C-1 Summary of crystallographic data	177
C-2 Summary of TDDFT computations for vertical excitations of oscillator strength greater than 0.1 for compounds 2a'-c'	193

LIST OF FIGURES

<u>Figure</u>	<u>page</u>
1-1 Structure of a generic NHC showing resonance from nitrogen lone pairs.	27
1-2 Core structure of the platinum-NHCs explored by the Strassner Group.	27
1-3 Structures of 1-aryl and 4-aryl 1,2,4-triazole-5-ylidenes studied in Reference 27. Triazole rings are numbered.....	27
1-4 Nitrile containing Pt-NHC, featuring the mesacac ligand, with an 85% phosphorescence quantum yield in a 2 wt% PMMA film.	28
1-5 Dibenzofuran containing Pt-NHC with a 90% quantum yield in a 2 wt% PMMA film.	29
1-6 Representative crystal packing diagrams of Pt-NHCs with A) low steric bulk of the ancillary ligand allowing close packing and dimeric interactions, and B) high steric bulk of the ancillary ligand	31
1-7 Nitro-functionalized Pt-NHCs which are modestly emissive despite bearing a ketoamine ancillary ligand.	32
1-8 Pt-NHCs featuring tetradentate bonding motifs.	33
1-9 Platinum carbene and platinum phosphine complexes with phenylacetylene chromophores. The carbene complex shows room temperature phosphorescence in deaerated solution	34
1-10 Qualitative d-orbital splitting diagram for a square-planar platinum(II) phosphine complex versus a square-planar platinum(II) carbene complex..	35
1-11 A Pt-NHC complex featuring monodentate carbene ligands and <i>trans</i> stereochemistry.	36
1-12 Structure of the Pt-NHC featuring monodentate carbene ligands demonstrating an 80% emission quantum yield in a PMMA film.	37
1-13 Structure of the Pt-NHC featuring monodentate carbene ligands demonstrating an 80% emission quantum yield in a PMMA film.	37
1-14 A Jablonski diagram illustrating the energy levels of monomeric and excimeric excited states.	38
1-15 The structure of 1,3-(di-2-pyrenyl)propane.	39
1-17 The structure of PE2-octyl.	41

1-18	Transient absorption spectrum of 57 mM PE2-octyl in deoxygenated benzene after 476 nm laser excitation. Decay traces start at t=0 and were taken in increments of 150 ns.....	42
1-13	The four mixed ligand platinum aryl/acetylide complexes synthesized by the Low Group.....	45
2-1	One-pot synthesis of <i>trans</i> -(ICy) ₂ PtCl ₂ (1).....	48
2-2	ORTEP diagram of <i>trans</i> -(ICy) ₂ PtCl ₂ (1) with the asymmetric unit labeled. Ellipsoids are at the 50% probability level. Hydrogen atoms are omitted for clarity.	48
2-3	Hagihara reaction to generate the platinum acetylide compounds 2a-c	49
2-4	ORTEP diagrams of the molecular structures of 2a-c , with thermal ellipsoids given at the 50% probability level. The hydrogen atoms are omitted for clarity. C: Black, N: Blue, S: Yellow, Pt: Pink, Chlorine: Green.....	50
2-5	Asymmetric C≡C bond stretch of platinum acetylide compounds 2a-c	51
2-6	The A) ground state absorption, B) normalized fluorescence, and C) normalized phosphorescence spectra of 2a-c in THF. Excitation was at the ground state absorption maxima, and the plots were normalized.....	53
2-7	Principal component transient absorption spectra of 2a-c , with excitation at 355 nm, 10 ns pulse width, 180 μJ/pulse excitation energy. Solutions had an absorptivity value of 0.62 at 355 nm after four freeze-pump-thaw cycles.	55
2-8	Open aperture z-scan transmittance using 606 nm light. Solutions were 1 mM in aerated THF and the laser energy was 600 μJ/pulse. 3c was used as the reference.	56
2-9	DFT optimized structures (top row), and charge difference densities (bottom row) for the calculated transitions corresponding to the experimental ground-state absorption maxima.	57
3-1	Structure of the target platinum acetylide dimers and mono-platinum model.	68
3-2	Synthesis of diarylacetylides tethered by 1-3 flexibilizing units.....	71
3-3	Synthesis of platinum diarylacetylides and a mono-platinum model complex. ...	72
3-4	The A) ground state absorption, B) normalized fluorescence, and C) normalized phosphorescence spectra of R-PtPE2 in THF. Excitation was at the ground state absorption maxima, and all plots were normalized.	73

3-5	Principal component transient absorption spectra of R-PtPE2 , with excitation at 355 nm, 10 ns pulse width, 180 μ J/pulse excitation energy. Solutions had an absorptivity value of 0.58 at 355 nm after five freeze-pump-thaw cycles.....	75
3-6	First five time slices of the transient absorption spectra of COC-PtPE2 with a camera delay interval of 400 ns. Excitation was at 355 nm, with a 10 ns pulse width, and 180 μ J/pulse excitation energy.....	76
3-7	Transient absorption power dependence of A) R-PtPE2 monitored at 550 nm, with B) an expansion of the low fluence region to show initial slopes.....	76
3-8	Transient absorption lifetime decays measured at 550 nm with variable fluence. A) C-PtPE2 . B) CC-PtPE2 . C) COC-PtPE2 . D) tol-PtPE2	78
3-10	Normalized transient absorption lifetime decays measured at 550 nm for R-PtPE2 on a logarithmic scale at A) low fluence (1.7 ± 0.3 mJ/(cm ² pulse)), and B) high fluence (61 ± 7 mJ/(cm ² pulse)).....	79
3-11	Histograms showing the probability of the internuclear Pt-Pt distance for A) C-PtPE2 , B) CC-PtPE2 , and C) COC-PtPE2	81
3-12	DFT optimized gas phase structures of A) C-PtPE2 , B) CC-PtPE2 , and C) COC-PtPE2	81
3-13	Representative drawings of the <i>anti-anti</i> , <i>syn-anti</i> , and <i>anti-anti</i> rotational isomers of COC-PtPE2	82
4-1	The four combinations of platinum aryl/acetylide complexes featuring DPAF and BTF chromophores.	94
4-1	Synthesis of monosubstituted platinum(II) aryl precursors.	97
4-2	Hagihara reaction to generate the four mixed aryl/acetylide Pt(II) complexes....	98
4-4	Ground state absorption spectra of A) the four mixed ligand platinum complexes containing the BTF and DPAF chromophores99	
4-5	Fluorescence spectra of the four mixed ligand platinum complexes containing the BTF and DPAF chromophores.	101
4-6	Fluorescence spectra of DPAF-Pt-CCBTF with excitation at 378 and 330 nm.102	
4-7	Emission spectra after at least five freeze-pump-thaw cycles of A) the four mixed ligand platinum complexes containing the BTF and DPAF chromophores.....	104

4-8	Principal component transient absorption spectra with excitation at 355 nm, 10 ns pulse width, 180 μ J/pulse excitation energy. Solutions had an absorptivity value of 0.58 at 355 nm after five freeze-pump-thaw cycles. 106
4-9	DFT optimized structures of the singlet ground state and charge difference densities for the computed $S_0 \rightarrow S_1$ vertical transition for A) BTFCC-Pt-Cl' , B) DPAFCC-Pt-Cl' , C) BTF-Pt-Cl' , and D) DPAF-Pt-Cl' 110
4-10	DFT optimized structures of the singlet ground state and charge difference densities for the computed $S_0 \rightarrow S_1$ vertical transition for A) BTF-Pt-CCBTF' and B) DPAF-Pt-CCDPAF' 112
4-11	DFT optimized structure of the singlet ground state and charge difference density for the vertical transition predicted at 376 nm of BTF-Pt-CCDPAF' 114
4-12	DFT optimized structure of A) the singlet ground state, and charge difference densities for the vertical transitions predicted at B) 401 nm and C) 350 nm of DPAF-Pt-CCBTF' 115
A-1	Spectra-Physics software showing A) the instrument has warmed-up and is ready for to be used. B) Pump laser is operational, but has not come up to the requested power. C) Pump laser is operational..... 125
A-4	Absorption (solid colored lines) and emission (dotted lines) of two complexes showing excitation and registration wavelength selections (solid black lines), respectively..... 129
A-6	Defeating the safety shutter on the Tsunami Laser. 134
B-1	General workflow of computations..... 137
B-2	A) 2-D Chemdraw model of (ThPt)₂BTd . B) 3-D model of (ThPt)₂BTd built and visualized in GaussView. C: Gray, H: White, N: Blue, P: Orange, S: Yellow, Pt: Cerulean. 139
B-3	GaussView main window showing options of the Calculate tab. 140
B-4	Blank calculation setup window with notable areas labeled. 140
B-5	Major conformations of (ThPt)₂BTd 141
B-6	Appended input file for the geometry optimization/frequency calculation of (ThPt)₂BTd 142
B-7	Example input file for the frequency calculation of (ThPt)₂BTd 146
B-8	Example input file for the TDDFT calculation of (ThPt)₂BTd 147
B-9	Example input file for a stability job on a platinum aryl compound..... 150

B-10	Example input file for generation of Natural Atomic Orbitals.	150
B-11	Example input file for a volume job of a gold acetylide compound.	152
B-12	Example PBS script for submitting jobs to the HPC.	152
B-13	Routine information given in every Gaussian output file.	155
B-14	Successful optimization of (ThPt)₂BTd to a stationary point.	156
B-15	N-pole moments for (ThPt)₂BTd	156
B-16	Final lines of the optimization of (ThPt)₂BTd	157
B-17	Intermediate steps of a frequency job showing the number of vectors yet to converge.	158
B-18	Frequency output of (ThPt)₂BTd with negative frequencies, indicating that the geometry is not at an energy minimum.	159
B-19	Frequency output of (ThPt)₂BTd with no negative frequencies, indicating that the geometry is at an energy minimum.	159
B-20	TDDFT output of (ThPt)₂BTd showing relevant vertical transitions.	160
B-21	Output of a stability job indicating that an instability is present in the wavefunction.	162
B-22	Output of a stability job indicating that the wavefunction is now stable.	162
B-23	Multiwfn startup screen with input file path typed in the last line of text.	163
B-24	Multiwfn orbital composition analysis options.	164
B-25	Percent contributions of a specified fragment to a pair of specified MOs.	165
B-26	Output of a volume job with the suggested radius boxed.	166
B-27	MO Editor window in GaussView displaying (ThPt)₂BTd with the HOMO and LUMO highlighted for MO generation.	169
B-28	MO Editor window in GaussView displaying the HOMO of (ThPt)₂BTd visualized with an isovalue of 0.02.	170
B-29	Chemcraft program displaying the HOMO of (ThPt)₂BTd visualized with an isovalue of 0.02. Useful buttons are labeled.	171
B-30	The 'Cubes layout' window with the operators displayed.	173

B-31	CDD for the lowest energy computed transition of (ThPt)₂BTD . Blue lobes indicate electron density being lost, while red lobes indicate electron density being gained. Image visualized at an isovalue of 0.0004.	173
B-32	MO editor window with the highest numbered alpha orbital of (ThPt)₂BTD pointed out. Singly occupied MOs are also boxed.....	175
B-33	The triplet of (ThPt)₂BTD in Chemcraft with the highest energy MO of both the alpha and beta electrons loaded. Note that the numbering in this program is sequential.....	175
C-1	ORTEP diagram of <i>trans</i> -(ICy) ₂ PtCl ₂ (1) with the asymmetric unit labeled. Ellipsoids are at the 50% probability level. Hydrogen atoms are omitted for clarity.	178
C-2	ORTEP diagram of <i>trans</i> -(ICy) ₂ Pt(PE2) ₂ (2a) with the asymmetric unit labeled. Ellipsoids are at the 50% probability level. Hydrogen atoms are omitted for clarity.	179
C-3	ORTEP diagram of <i>trans</i> -(ICy) ₂ Pt(BTF) ₂ (2b) with the asymmetric unit labeled. Ellipsoids are at the 50% probability level. Hydrogen atoms are omitted for clarity.	179
C-4	ORTEP diagram of <i>trans</i> -(ICy) ₂ Pt(DPAF) ₂ (2c) with the asymmetric unit labeled. Ellipsoids are at the 50% probability level. Hydrogen atoms are omitted for clarity.	180
C-5	¹ H NMR (500 MHz, CDCl ₃) of 1	181
C-6	¹³ C NMR (125.7 MHz, CDCl ₃) of 1	181
C-7	¹ H NMR (500 MHz, CD ₂ Cl ₂) of 2a	182
C-8	¹³ C NMR (125.7 MHz, CD ₂ Cl ₂) of 2a	182
C-9	¹ H NMR (500 MHz, CD ₂ Cl ₂) of 2b	183
C-10	Insets for selected peaks from the ¹ H NMR (500 MHz, CD ₂ Cl ₂) of 2b	183
C-11	¹³ C NMR (125.7 MHz, CD ₂ Cl ₂) of 2b	184
C-12	¹ H NMR (500 MHz, CD ₂ Cl ₂) of 2c . Residual hexanes are present.	184
C-13	¹³ C NMR (125.7 MHz, CD ₂ Cl ₂) of 2c	185
C-14	FTIR spectrum of 1	185
C-15	FTIR spectrum of 2a	186

C-16	FTIR spectrum of 2b	186
C-17	FTIR spectrum of 2c	187
C-18	Fluorescence lifetime decay for 2a (light blue) with instrument response function (dark blue).....	187
C-19	Phosphorescence lifetime decay for 2a	188
C-20	Phosphorescence lifetime decay for 2b	188
C-21	Phosphorescence lifetime decay for 2c	189
C-22	Transient absorption decay for 2a . Initial camera delay: 100ns, camera delay increment: 15 μ s, 100 images averaged per trace, Q-switch delay: 380 μ s, 180 μ J per pulse.....	189
C-23	Transient absorption decay for 2b . Initial camera delay: 100ns, camera delay increment: 20 μ s, 100 images averaged per trace, Q-switch delay: 382 μ s, 180 μ J per pulse.....	190
C-24	Transient absorption decay for 2c . Initial camera delay: 100ns, camera delay increment: 20 μ s, 100 images averaged per trace, Q-switch delay: 379 μ s, 180 μ J per pulse.....	190
C-25	Transient absorption decay profile for 2a . Conditions: 200 μ J per pulse, 380 μ J Q-switch delay, 128 scans averaged, decay measured at 584 nm.....	191
C-26	Transient absorption decay profiles for 2a at varying laser energies. Conditions: 200 μ J – 18 mJ per pulse, 380-200 μ J Q-switch delay, 128 scans averaged per trace, decays measured at 584 nm.	191
C-27	DFT optimized structure of 2a'	192
C-28	373.8 nm CDD of 2a' . Blue coloring indicates electron density being lost, while red coloring indicates electron density being gained in the electronic transition.....	194
C-29	Normalized overlay of the experimental absorption spectrum of 2a with the TDDFT computed line spectra of 2a' . Only vertical excitations with $f > 0.1$ are shown.....	194
C-30	LUMO+1 (orbital 168) of compound 2a'	194
C-31	LUMO (orbital 167) of compound 2a'	195
C-32	HOMO (orbital 166) of compound 2a'	195
C-33	HOMO-1 (orbital 165) of compound 2a'	195

C-34	DFT optimized structure of 2b'	195
C-35	429.3 nm CDD of 2b' . Blue coloring indicates electron density being lost, while red coloring indicates electron density being gained in the electronic transition.....	196
C-36	Normalized overlay of the experimental absorption spectrum of 2a with the TDDFT computed line spectra of 2b' . Only vertical excitations with $f > 0.1$ are shown.....	196
C-37	LUMO+1 (orbital 262) of compound 2b'	196
C-38	LUMO (orbital 261) of compound 2b'	197
C-39	HOMO (orbital 260) of compound 2b'	197
C-40	LUMO+1 (orbital 259) of compound 2b'	197
C-41	DFT optimized structure of 2c'	197
C-42	381.5 nm CDD of 2c' . Blue coloring indicates electron density being lost, while red coloring indicates electron density being gained in the electronic transition.....	198
C-43	Normalized overlay of the experimental absorption spectrum of 2c with the TDDFT computed line spectra of 2c' . Only vertical excitations with $f > 0.1$ are shown.....	198
C-44	LUMO+1 (orbital 282) of compound 2c'	198
C-45	LUMO (orbital 281) of compound 2c'	199
C-46	HOMO (orbital 280) of compound 2c'	199
C-47	HOMO-1 (orbital 279) of compound 2c'	199
D-1	^1H NMR (500 MHz, CDCl_3) of COC-Br	200
D-2	^{13}C NMR (126 MHz, CDCl_3) of COC-Br	200
D-3	^1H NMR (500 MHz, CDCl_3) of CC-TMS	201
D-4	^{13}C NMR (126 MHz, CDCl_3) of CC-TMS	201
D-5	^1H NMR (500 MHz, CD_2Cl_2) of COC-TMS	202
D-6	^{13}C NMR (126 MHz, CD_2Cl_2) of COC-TMS	202
D-7	^1H NMR (500 MHz, CD_2Cl_2) of CC-H	203

D-8	^{13}C NMR (126 MHz, CD_2Cl_2) of CC-H .	203
D-9	^1H NMR (500 MHz, CD_2Cl_2) of COC-H .	204
D-10	^{13}C NMR (126 MHz, CD_2Cl_2) of COC-H .	204
D-11	^1H NMR (500 MHz, CDCl_3) of C-PtPE2 .	205
D-12	^{13}C NMR (126 MHz, CDCl_3) of C-PtPE2 .	205
D-13	^{31}P NMR (121 MHz, CDCl_3) of C-PtPE2 .	206
D-14	^1H NMR (500 MHz, CD_2Cl_2) of CC-PtPE2 .	206
D-15	^{13}C NMR (126 MHz, CD_2Cl_2) of CC-PtPE2 .	207
D-16	^{31}P NMR (121 MHz, CD_2Cl_2) of CC-PtPE2 .	207
D-17	^1H NMR (500 MHz, CD_2Cl_2) of COC-PtPE2 .	208
D-18	^{13}C NMR (126 MHz, CD_2Cl_2) of COC-PtPE2 .	208
D-19	^{31}P NMR (121 MHz, CD_2Cl_2) of COC-PtPE2 .	209
D-20	^1H NMR (500 MHz, CDCl_3) of tol-PtPE2 .	209
D-21	^{13}C NMR (126 MHz, CDCl_3) of tol-PtPE2 .	210
D-22	^{31}P NMR (121 MHz, CDCl_3) of tol-PtPE2 .	210
D-23	Phosphorescence lifetime decay for C-PtPE2 .	211
D-24	Phosphorescence lifetime decay for CC-PtPE2 .	211
D-25	Phosphorescence lifetime decay for COC-PtPE2 .	212
D-26	Phosphorescence lifetime decay for tol-PtPE2 .	212
D-27	Normalized transient absorption for R-PtPE2 . Initial camera delay: 100ns, camera delay increment: 15 μs , 100 images averaged per trace, 180 μJ per pulse.	213
D-28	Transient absorption decay for C-PtPE2 . Initial camera delay: 100ns, camera delay increment: 15 μs , 100 images averaged per trace, 180 μJ per pulse.	213
D-29	Transient absorption decay for CC-PtPE2 . Initial camera delay: 100ns, camera delay increment: 15 μs , 100 images averaged per trace, 180 μJ per pulse.	214

D-30	Transient absorption decay for COC-PtPE2 . Initial camera delay: 100ns, camera delay increment: 15 μ s, 100 images averaged per trace, 180 μ J per pulse.....	214
D-31	Transient absorption decay for tol-PtPE2 . Initial camera delay: 100ns, camera delay increment: 15 μ s, 100 images averaged per trace, 180 μ J per pulse.....	215
D-32	Representative molecular geometry of C-PtPE2 during the molecular dynamics simulation process.....	215
D-33	Representative molecular geometry of CC-PtPE2 during the molecular dynamics simulation process.....	216
D-34	Representative molecular geometry for the primary distribution of COC-PtPE2 during the molecular dynamics simulation process.	216
D-35	Representative molecular geometry for the secondary distribution of COC-PtPE2 during the molecular dynamics simulation process.	216
E-1	^1H NMR (500 MHz, CD_2Cl_2) spectra of BTF-Pt-CCBTF	217
E-2	A) Aromatic region of the ^1H NMR spectra of BTF-Pt-CCBTF . B) Aliphatic region of the ^1H NMR spectra of BTF-Pt-CCBTF	217
E-3	^{13}C NMR (126 MHz, CD_2Cl_2) spectra of BTF-Pt-CCBTF	218
E-4	Aromatic region of the ^{13}C NMR spectra of BTF-Pt-CCBTF	218
E-5	^{31}P NMR (121 MHz, CD_2Cl_2) of BTF-Pt-CCBTF	219
E-6	^1H NMR (500 MHz, CD_2Cl_2) spectra of DPAF-Pt-CCDPAF	219
E-7	^{13}C NMR (126 MHz, CD_2Cl_2) spectra of DPAF-Pt-CCDPAF	220
E-9	^{31}P NMR (121 MHz, CD_2Cl_2) of DPAF-Pt-CCDPAF	221
E-10	^1H NMR (500 MHz, CD_2Cl_2) spectra of BTF-Pt-CCDPAF	221
E-11	Aromatic region of the ^1H NMR spectra of BTF-Pt-CCDPAF	222
E-12	^{13}C NMR (126 MHz, CD_2Cl_2) spectra of BTF-Pt-CCDPAF	222
E-13	Aromatic region of the ^{13}C NMR spectra of BTF-Pt-CCDPAF	223
E-14	^{31}P NMR (121 MHz, CD_2Cl_2) of BTF-Pt-CCDPAF	223
E-15	^1H NMR (500 MHz, CD_2Cl_2) spectra of DPAF-Pt-CCBTF	224

E-16	Aromatic region of the ^1H NMR spectra of DPAF-Pt-CCBTF	224
E-17	^{13}C NMR (126 MHz, CD_2Cl_2) spectra of DPAF-Pt-CCBTF	225
E-18	Aromatic region of the ^{13}C NMR spectra of DPAF-Pt-CCBTF	225
E-19	^{31}P NMR (121 MHz, CD_2Cl_2) of DPAF-Pt-CCBTF	226
E-20	Phosphorescence lifetime decay for BTF-Pt-CCBTF	226
E-21	Phosphorescence lifetime decay for DPAF-Pt-CCDPAF	227
E-22	Phosphorescence lifetime decay for BTF-Pt-CCDPAF	227
E-23	Phosphorescence lifetime decay for DPAF-Pt-CCBTF	228
E-24	Transient absorption decay for BTF-Pt-CCBTF . Initial camera delay: 100ns, camera delay increment: 10 μs , 100 images averaged per trace, 180 μJ per pulse.....	228
E-25	Transient absorption decay for DPAF-Pt-CCDPAF . Initial camera delay: 100ns, camera delay increment: 10 μs , 100 images averaged per trace, 180 μJ per pulse.....	229
E-26	Transient absorption decay for BTF-Pt-CCDPAF . Initial camera delay: 100ns, camera delay increment: 10 μs , 100 images averaged per trace, 180 μJ per pulse.....	229
E-27	Transient absorption decay for DPAF-Pt-CCBTF . Initial camera delay: 100ns, camera delay increment: 10 μs , 100 images averaged per trace, 180 μJ per pulse.....	230
E-28	LUMO of BTFCC-Pt-Cl'	230
E-29	HOMO of BTFCC-Pt-Cl'	230
E-30	LUMO of DPAFCC-Pt-Cl'	231
E-31	HOMO of DPAFCC-Pt-Cl'	231
E-32	LUMO of BTF-Pt-Cl'	231
E-33	HOMO of BTF-Pt-Cl'	231
E-34	LUMO of DPAF-Pt-Cl'	232
E-35	HOMO of DPAF-Pt-Cl'	232
E-36	LUMO+1 of BTF-Pt-CCBTF	232

E-37	LUMO of BTF-Pt-CCBTF .	233
E-38	HOMO of BTF-Pt-CCBTF .	233
E-39	HOMO-1 of BTF-Pt-CCBTF .	233
E-40	CDD of the predicted transition at 360 nm for BTF-Pt-CCBTF .	233
E-41	LUMO+1 of DPAF-Pt-CCDPAF .	234
E-42	LUMO of DPAF-Pt-CCDPAF .	234
E-43	HOMO of DPAF-Pt-CCDPAF .	234
E-44	HOMO-1 of DPAF-Pt-CCDPAF .	234
E-45	CDD of the predicted transition at 350 nm for DPAF-Pt-CCDPAF .	235
E-46	LUMO+1 of BTF-Pt-CCDPAF .	235
E-47	LUMO of BTF-Pt-CCDPAF .	235
E-48	HOMO of BTF-Pt-CCDPAF .	235
E-49	HOMO-1 of BTF-Pt-CCDPAF .	236
E-50	HOMO-2 of BTF-Pt-CCDPAF .	236
E-51	CDD of the predicted CT transition at 438 nm for BTF-Pt-CCDPAF . This transition is not observed in the experimental UV-Vis spectrum.	236
E-52	CDD of the predicted transition at 350 nm for BTF-Pt-CCDPAF .	236
E-53	LUMO+1 of DPAF-Pt-CCBTF .	237
E-54	LUMO of DPAF-Pt-CCBTF .	237
E-55	HOMO of DPAF-Pt-CCBTF .	237
E-56	HOMO of DPAF-Pt-CCBTF .	237
E-57	Normalized UV-Vis absorption spectrum of A) BTF-Pt-CCBTF , B) DPAF-Pt-CCDPAF , C) BTF-Pt-CCDPAF , and D) DPAF-Pt-CCBTF with the TDDFT predicted vertical transitions overlaid.	238

Abstract of Dissertation Presented to the Graduate School
of the University of Florida in Partial Fulfillment of the
Requirements for the Degree of Doctor of Philosophy

LOOK INTO THE LIGHT: TUNING PLATINUM ACETYLIDE COMPLEXES
FOR ENHANCED PHOTOPHYSICAL PROPERTIES

By

Russell W. Winkel

August 2015

Chair: Kirk S. Schanze
Major: Chemistry

My research focuses on enhancing the photophysical properties of *trans*-platinum(II) acetylide compounds by altering the properties of the ligand environment around the metal center. Platinum acetylide compounds have been studied for decades due to their rich photophysical properties and potential material applications.

The synthetic work described herein has three main facets. The first involves replacing the typical tributylphosphine (PBu₃) ancillary ligands on the platinum atom with N-heterocyclic carbenes (NHCs) to reduce the overall spin-orbit coupling of the system and extend the excited state lifetime. Second, a series of platinum acetylide dimers, tethered by one, two, or three flexibilizing units was used to study excited state dynamics. Specific properties include inter- versus intramolecular excimer formation and triplet-triplet annihilation. Finally, a series of complexes featuring one aryl chromophore and one aryl-acetylide chromophore, with the connectivity being *trans*-(Ar-Pt-CCAr), was studied, as a method to monosubstitute an aryl ligand to platinum was recently developed by our Group. These mixed chromophore compounds show dual emission in the singlet manifold and potentially the triplet manifold, giving rise to emission across most of the visible region. Additionally, the ligands may be tuned such that the emission

intensity of the fluorescence and phosphorescence are similar in intensity, so the emitted light appears white.

Lastly, two manuals are presented. One is for use of our Group's femtosecond laser, the other for use of Gaussian on the UF HPC. The laser manual covers basic operation, trouble shooting, two-photon induced fluorescence measurements, and two-photon absorption cross section measurements. The Gaussian/HPC manual lays out instructions for creation, execution, and interpretation of computational results.

CHAPTER 1 INTRODUCTION

Overview

Electronic excitation of a molecule is induced when a photon of sufficient energy is absorbed, causing the molecule to be promoted from the ground state to the excited state. The decay of the molecule back to the ground state can follow a variety of pathways, and tuning these pathways is essential for modern applications. This introduction will assume that the reader knows the fundamentals of photophysics, but will elaborate on the specific properties of the core system that were tuned, as well as how and why they were tuned.

Square planar platinum(II)-arylacetylide complexes have been known and intensely studied for several decades due to their wide range of applications that include non-linear absorption, polymer light emitting diodes, and polymer photovoltaic devices.¹⁻

¹¹ When π -conjugated aryl-acetylide ligands are coupled to a heavy metal with large spin-orbit coupling, intersystem crossing to the triplet excited state can be very efficient.^{1, 6} This allows for strong triplet-triplet absorption which can contribute to non-linear absorption (NLA). Many variations of platinum acetylide complexes have been synthesized and their properties explored.^{6, 12} The following details of this chapter will introduce the concepts and motifs of the chapters to come.

Platinum Carbene Complexes

In Non-chromophoric Systems

A SciFinder search for 'platinum' and 'carbene' using only the 'CAPLUS' database (to remove duplicate citations) returns 571 journal articles. The earliest synthesis of a platinum carbene was in 1969 and was derived from a platinum

isocyanide.¹³ Most of the non-chromophoric complexes are synthesized with the intention of imparting some form of reactivity on an outside system (485 citations), with a fair subset of this being catalysis (160 citations).

As Chromophoric Ligands

When the above search is narrowed by adding the term ‘emission or luminescence’, only 49 articles remain. The earliest report of a luminescent platinum carbene is from 1999,¹⁴ but it wasn’t until 2010 that using carbenes in luminescent platinum complexes really took off (43 of 49 articles published since 2010). A vast majority of these complexes have two things in common. First, is that the form of the carbene is typically (90% of reports) a N-heterocyclic carbene (NHC). This carbene structure is popular because the empty p-orbital on the carbene carbon can be stabilized by resonance with lone pairs from adjacent nitrogen atoms. A generic structure of a NHC, with resonance structures shown, can be found in Figure 1-1. Second, is that the carbene ligand had never been monodentate. It has always been bonded to another chelating moiety and used in bi- or tridentate motifs. The bidentate structure is exemplified in a couple of the earliest reports, where platinum(II) tetracarbene dihalide complexes were synthesized using a bis(dicarbene) motif.^{15, 16} Tridentate ligands featuring NHCs followed not long after.¹⁷

While a few of these compounds have been synthesized for medicinal purposes,^{18, 19} a majority tend to be for used in organic light emitting diodes (OLEDs). While development of red and green OLEDs has advanced quickly, efficient, deep blue OLEDs have lagged considerably behind.²⁰ Platinum-NHCs (Pt-NHCs) have proven their potential in this field through a variety of cyclometallated complexes. Zhang and co-workers used a carbene-phenyl-carbene, or CCC (based on the atoms that bond to

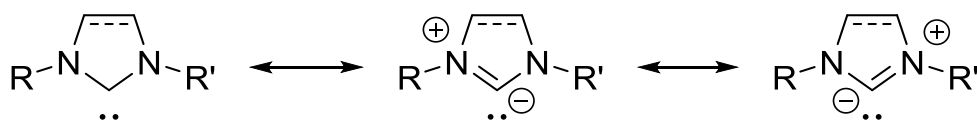


Figure 1-1. Structure of a generic NHC showing resonance from nitrogen lone pairs.

the metal center), tridentate motif which shows excellent air stability under photoexcitation, but low emission quantum yields.²¹ Both of these factors are attributed to excited state distortion around the platinum center in the excited state.

Strassner and co-workers have been the primary contributors to the field of blue phosphorescent platinum carbene compounds. While some of their work was mentioned earlier, the recent focus has been on modifying a core structure consisting of a platinum center cyclometallated by both a phenyl-NHC and an acetylacetonate (acac) ligand. These investigations focus primarily on the solid state properties, both in poly(methyl methacrylate) (PMMA) films and neat films. A core structure for this series of work is shown in Figure 1-2. The first modification made to this core structure was to look at the effect of phenyl connectivity in a 1,2,4-triazole-5-ylidene and substituent

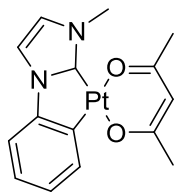


Figure 1-2. Core structure of the platinum-NHCs explored by the Strassner Group.

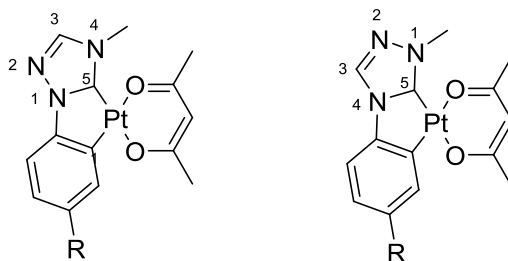


Figure 1-3. Structures of 1-aryl and 4-aryl 1,2,4-triazole-5-ylidenes studied in Reference 27. Triazole rings are numbered.

effect on the aryl group.²² Specifically, the effect of whether the phenyl is bonded to the NHC through the nitrogen at the 1 or 4 position. These structures are shown in Figure 1-3. The authors found that the 1-aryl complexes were up to three times more emissive than the 4-aryl complexes (~40% vs. ~13%), but no explanation was proposed for this phenomenon.

The next report described the photophysics of four 1-(4-cyanoaryl)imidazole-2-ylidenes, with modifications to both the imidazolylidene and acac ligands.²³ The two complexes with a plain acac ligand showed quantum yields around 60%, while those with a dimesitylmethane (mesacac) were in excess of 80%. The crystal packing, given by single crystal X-ray crystallography, lends some insight as the cause of this observation. The packing of Pt-NHCs with the minimal acac ligand show Pt-Pt distances slightly shorter than the sum of the van der Waals radius. Thus, if a small percent of the complexes were to pack this way in the PMMA film, a reduction in quantum yield would be expected. However, when the bulky mesacac ligand is used, no Pt-Pt interaction is observed in the crystal packing. Interestingly, the emission lifetimes of the mesacac complexes are about half that of the acac compounds (~16 μ s vs. ~ 8.5 μ s). The compound with the highest quantum yield from this report (85%) is shown in Figure 1-4.

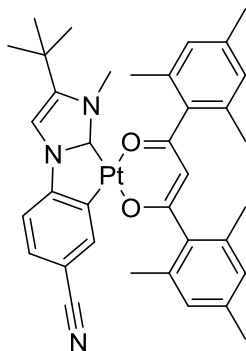


Figure 1-4. Nitrile containing Pt-NHC, featuring the mesacac ligand, with an 85% phosphorescence quantum yield in a 2 wt% PMMA film.

Continuing with the theme of altering the acac ligand, one carbonyl moiety was replaced with an amine to give a β -ketoimine ligand.²⁴ Substituents on the 4-position of the phenyl group were also tested opposite of the β -ketoimine ligand. The use of this NO bidentate ligand results in a mixture of isomers, both of which can be isolated. There is a preference for the imine nitrogen to be opposite of the carbene carbon, as evidenced by higher yields of this conformer and DFT calculations showing it to be of a lower energy. Unfortunately, a majority of these complexes show quantum yields of 15% or less. DFT calculations again explained this phenomenon, as they showed significant distortion of the platinum square plane for these complexes in the triplet state. One ligand, however, stood out from the others, and it is illustrated in Figure 1-5. Modifying the aryl group attached to the NHC from phenyl to 1-dibenzo[b,d]furan-4-ylidene brings the quantum yield back up to 74%. It was also shown that this is purely an effect of the new aryl ligand, as reverting the β -ketoimine back to acac pushes the quantum yield to 90%.

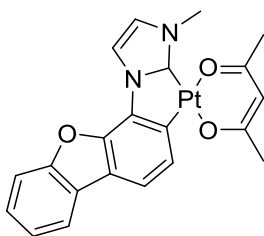


Figure 1-5. Dibenzofuran containing Pt-NHC with a 90% quantum yield in a 2 wt% PMMA film.

The next report strays slightly from the blue emission region by extending the π -conjugation of the phenyl-NHC ligand while holding acac constant.²⁵ The authors find that, as expected, by strategically fusing phenyl groups to the 4,5-bond of either ring of the phenyl-NHC unit, decent quantum yields (> 40%) could be retained while shifting the

emission color to the blue-green and green domain. Addition of phenyl groups to the N-3-position had only a minimal effect.

Returning to the success of the mesacac ligand, the Strassner Group probed the role of methyl groups at various locations of acac and dibenzoylmethane, the latter being the unmethylated parent compound of mesacac.²⁶ The group demonstrates in a step-wise manner, that as steric bulk is increased from acac to dipivaloylmethane to dibenzoylmethane the quantum yield increases (41 to 54 to 78%, respectively). As explained earlier, this is due to inhibited Pt-Pt interaction between complexes. Adding methyl groups to the dibenzoylmethane only increases the quantum yield a few percent, but gives the benefit of added solubility. Using these complexes, devices were fabricated, and peaked at an external quantum efficiency (EQE) of 12.6%.

The most recent report continues to use mesacac, but returns to the triazole NHC.²⁷ Interestingly, most of the complexes reported show broad, structureless emissions that have a maxima shifted to the blue-green region. This shift is attributed to a mesacac centered emission. Further support of this claim stems from a minimal change in emission maxima when substituents are changed on the phenyl-NHC ligand. Although the emitting ligand has changed, emission quantum yields still tended to be greater than 80%.

Taking the recent work of the Strassner Group as a whole, a couple key conclusions can be drawn. The most prominent trend is that of the bulkiness of the ancillary ligand. Evidence for this is provided by the systematic increase in bulk of the base acac system, leading to successively higher quantum yields. Rational of this trend is given by examining the solid state packing. Specifically, if the molecules are allowed

to stack cofacially, interaction of platinum centers leads to non-radiative deactivation of the excited state. This is illustrated in Figure 1-6, where two crystal packing diagrams are shown. The complex showing dimeric interactions has a quantum yield of 35% (2 wt% PMMA film); whereas the complex with the mesacac ligand shows no close packing, and has a quantum yield of 72%.

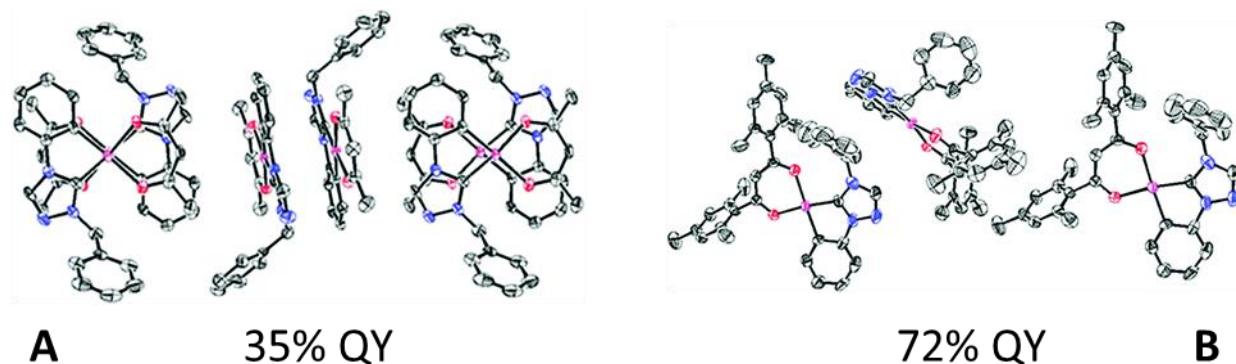


Figure 1-6. Representative crystal packing diagrams of Pt-NHCs with A) low steric bulk of the ancillary ligand allowing close packing and dimeric interactions, and B) high steric bulk of the ancillary ligand preventing any dimeric or Pt-Pt interaction. M. Tenne, S. Metz, G. Wagenblast, I. Munster and T. Strassner, *Dalton Trans.*, 2015, **44**, 8444-8455. – Published by The Royal Society of Chemistry.

The next point regards the ketoamine ancillary ligands used, and the detrimental effects on the quantum yields of the compounds featuring it. Not only did the ketoamine ligands studied lack the steric bulk necessary to inhibit Pt-Pt interactions, they are also capable of forming hydrogen bonds when dimerized. Unfortunately no ketoamine complex with mesityl side groups was modeled to test if the quantum yield returns to previously observed levels. An interesting observation, and insight to the electronic structure, stems from two complexes which show significantly stronger emission than the rest ($\geq 20\%$ QY). Figure 1-7 shows the nitro-functionalized emissive complex, and

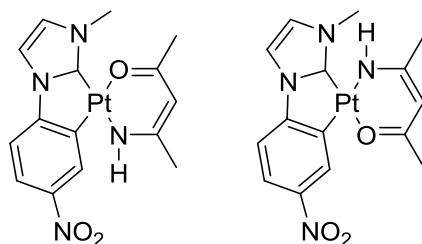


Figure 1-7. Nitro-functionalized Pt-NHCs which are modestly emissive despite bearing a ketoamine ancillary ligand.

the acac congener of the other strongly emissive complex from this report was shown in Figure 1-5.

As mentioned earlier, many of the complexes with the ketoamine ligand show distortion of the square plane around the platinum center in the triplet state. This is caused by the lowest energy state being metal centered, and will be discussed in more detail in the next section. For current purposes, metal centered excited states are readily deactivated via non-radiative decay, thus the excited state of the organic chromophore needs to be of lower energy for the complex to be emissive. Based on the weakly emissive complexes with the ketoamine ligand that were emissive with acac, the lowest metal centered excited state of these ketoamine complexes has been lowered further. While the emissive complexes may not seem to have much in common, the organic moieties have had their excited state energies lowered via two different routes. First, for the complex from Figure 1-5 with the dibenzofuran ligand, this is achieved by extending the π -system. Unfortunately there is no solid state packing information to make assertions about Pt-Pt interactions for this complex, but the assumption based on the reports presented here would be that these interactions do not occur for this complex. The nitro-functionalized Pt-NHC shown in Figure 1-7 has lowered its excited state energy by way of the nitro group being a π -acceptor. Despite this, the crystal

packing shows significant stacking, which may explain why only a modest quantum yield is achieved.

Many of the other complexes studied by the Strassner Group follow a similar trend, in that the complexes give better emission properties when the excited state energy of the organic chromophores have some separation from the metal-centered excited state. The nitrile-functionalized complexes (see Figure 1-4) illustrate this well, as they all have quantum yields above 60%. Polycyclic rings have the same effect on the quantum yield, but push the emission color towards the green region.

Finally, a few tetradentate (but not tetracarbene) platinum complexes using an OCCO²⁸ and CCCN²⁹ bonding motif were synthesized by Li and Fleetham, respectively, and showed double digit EQEs. The structures of the best emitter from each paper referenced above are shown in Figure 1-8. The tetradentate motif allows not only for greater quantum yields, but improved stability as well. This is because if one part of the ligand becomes 'disengaged' from the metal, it cannot leave the system completely without breaking three more bonds. Thus the disengaged ligand can come back and reform a bond with the metal center. Both of the complexes shown in Figure 1-6 have phosphorescence spectra which lack vibronic structure; however, Li's Pt-OCCO complex has a broad emission, while Fleetham's Pt-NCCC complex has a very narrow

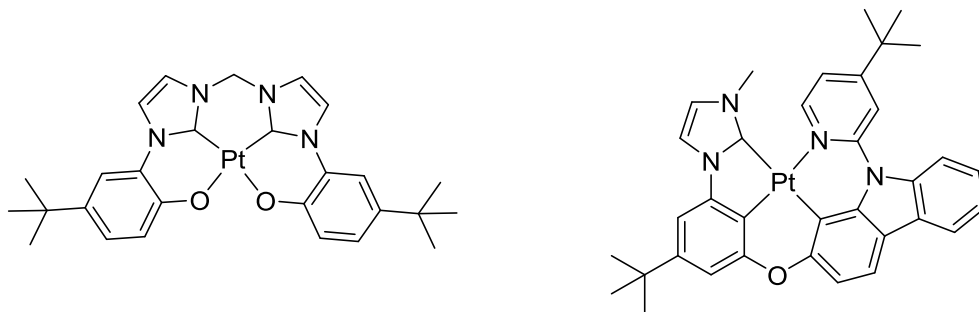


Figure 1-8. Pt-NHCs featuring tetradentate bonding motifs.

emission. This results in Li's complex being 'less blue' than ideal. Regardless, a device was made and shows an ~15% EQE. Fleetham's complex, because its emission band is so narrow, gives a 'pure' blue color. Just as noteworthy is the EQE of an optimized device, which gives a peak efficiency of 24.8%, while holding at 22.7% at 100 cd m^{-2} , which is a practical luminance for display applications. The aforementioned device is, at the time of this writing, the record holder for EQE of a pure blue emitting device.

As Ancillary Ligands to Acetylene Chromophores

Reports of using a carbene as an ancillary ligand to other, lower energy, chromophoric ligands come primarily from the Venkatesan group, and first appeared in 2011.³⁰ The first series of complexes again relied on a bidentate bis(NHC). The neutral NHC systems are good σ -donors, which destabilize the metal centered states, and allow for efficient luminescent decay from the triplet state even when high bandgap acetylide chromophores are ligated. This is in direct contrast to the platinum phosphine (Pt-PR_3) systems, where decay with the same or similar ligands is non-radiative unless frozen in a glass at 77 K.³¹ Figure 1-9 shows the structures of the platinum carbene and platinum phosphine complexes compared in the previous statement. Additionally, Figure 1-10 shows a qualitative orbital energy diagram illustrating the differences between Pt-

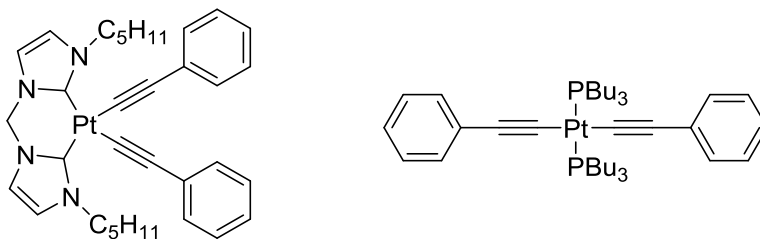


Figure 1-9. Platinum carbene and platinum phosphine complexes with phenylacetylene chromophores. The carbene complex shows room temperature phosphorescence in deaerated solution, while the phosphine complex does not.

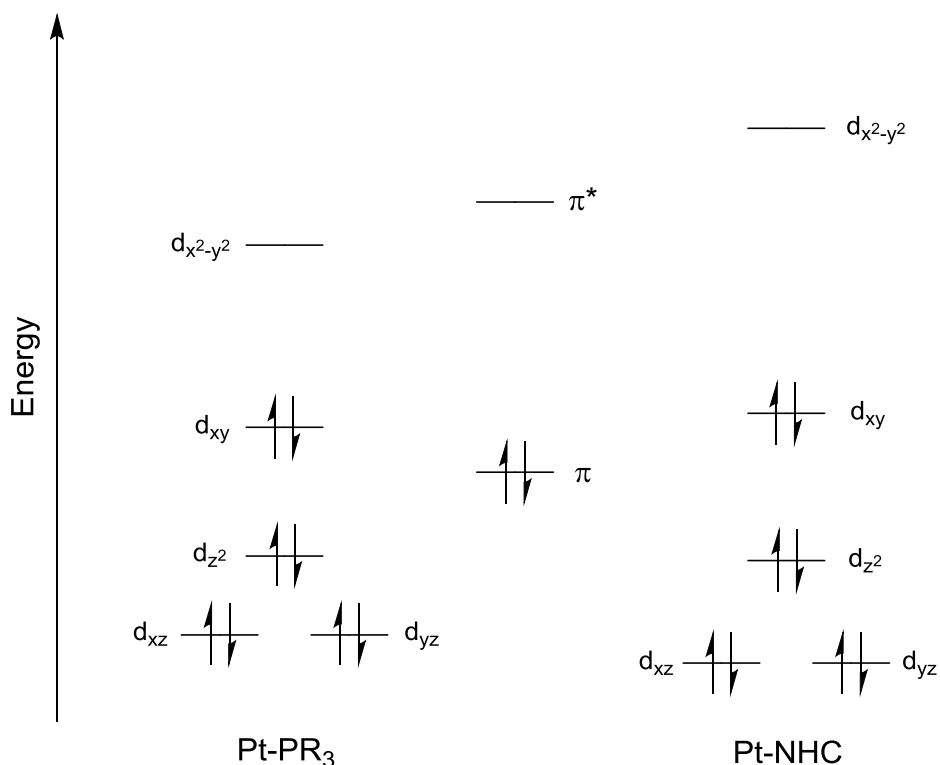


Figure 1-10. Qualitative d-orbital splitting diagram for a square-planar platinum(II) phosphine complex versus a square-planar platinum(II) carbene complex. Shown for comparison are the frontier orbitals of a high energy aryl-acetylide ligand, such as phenylacetylene.

NHCs and Pt-PR₃s that allows high energy emission at room temperature. Venkatesan and co-workers continued to explore these high energy acetylide chromophores, and in 2014 described how altering the bidentate carbene ligand affected the emission energy of the system.³²

The first report of a monodentate NHC, with *trans* stereochemistry, as an ancillary ligand came in 2013, also from the Venkatesan group.³³ This study was published shortly before the work reported here in Chapter 2.³⁴ The authors chose to use a benzimidazole functionalized with dodecyl, or in one case isopropyl, chains to improve solubility. A generic structure is shown in Figure 1-11.

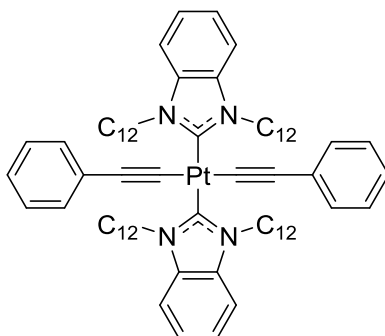


Figure 1-11. A Pt-NHC complex featuring monodentate carbene ligands and *trans* stereochemistry.

The synthesis of these Pt-NHC final products stemmed from a platinum acetylide precursor functionalized with cyclooctadiene (COD) as the ancillary. The COD was replaced by NHC ligands by refluxing the platinum COD, three equivalents of imidazolium salt, and three equivalents of potassium tert-butoxide (KO^tBu) to give the *cis*-Pt-NHC in good yield. The *trans*-Pt-NHC complexes were then made from the *cis* complexes via thermal isomerization at 200°C , as direct synthesis of the *trans*-Pt-NHCs were very poor. The mechanism for this isomerization was studied and found to be catalyzed by a Pt^0 -NHC complex formed by reductive elimination of a diacetylide. The platinum of the Pt^0 -NHC then coordinates to the platinum of a Pt^{II} -NHC, allowing for pseudorotation of the ligands, which is then followed by dissociation of the Pt-Pt interaction to give the *trans*-Pt-NHC in good yield.

Continuing with their pursuit of blue phosphorescent OLEDs, high energy aryl-acetylide chromophores were again used as the emitting species. Phenyl- and 4-fluorophenylacetylide performed the best in PMMA films, with a maximum quantum yield of 65%. Interestingly, when the dodecyl solubilizing groups were replaced with isopropyl groups (structure shown in Figure 1-12), the quantum yield jumped to 80%, suggesting that the long alkyl chains have a deleterious effect on emission efficiency.

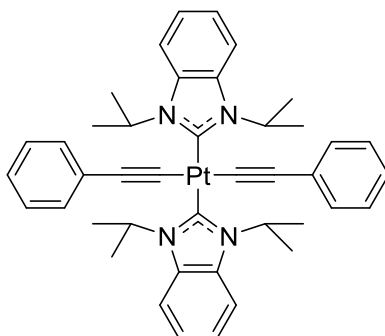


Figure 1-12. Structure of the Pt-NHC featuring monodentate carbene ligands demonstrating an 80% emission quantum yield in a PMMA film.

In a change of pace, a Pt-NHC was synthesized in this report that contained a π -extended chromophore. Coincidentally, it is the same chromophore (1-Ethynyl-4-(phenylethynyl)benzene (PE2)) as one that was used in Chapter 2, and the structure is shown in Figure 1-13. The reported solution photophysics of the Pt-NHC complex featuring PE2 (again, shown in Figure 1-13) are significantly different from that which is studied in this manuscript. Possible explanations for this discrepancy may be the solvent used for photophysics, detrimental effects of benzimidazole versus imidazole, or that the alkyl chains provide minimal protection of the Pt center relative to the bulkier cyclohexyl groups used in Chapter 2.

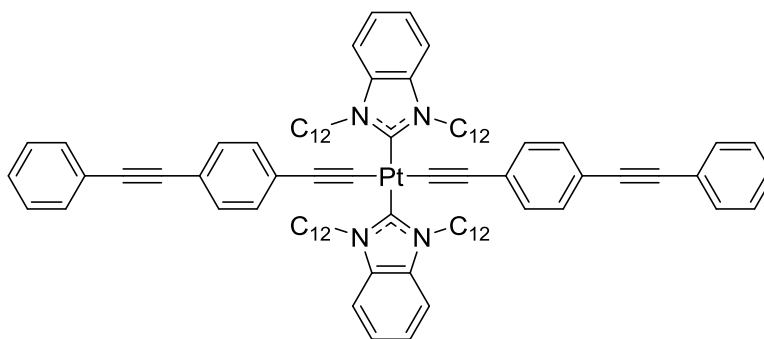


Figure 1-13. Structure of the Pt-NHC featuring monodentate carbene ligands demonstrating an 80% emission quantum yield in a PMMA film.

Excimers and Dimeric Complexes Tethered by Flexible Linking Units

Overview

Excimer formation occurs when a molecule in the excited state interacts with a molecule in the ground state and the two associate to form a complex with a lower energy excited state. A Jablonski diagram illustrating this process is shown in Figure 1-14. One of the most well-known systems that displays this behavior is pyrene. At low concentrations in solution, pyrene exhibits only a single, structured emission. However, as the concentration of pyrene increases, a new, broad, low energy emission band starts to form. This process is concentration dependent because the key rate limiting step is the diffusional encounter of excited pyrene interacting with ground state pyrene. Thus, as the concentration of pyrene increases, the number of excited molecules and interactions increase, leading to the excimer emission band becoming over an order of magnitude stronger than the monomeric emission.³⁵

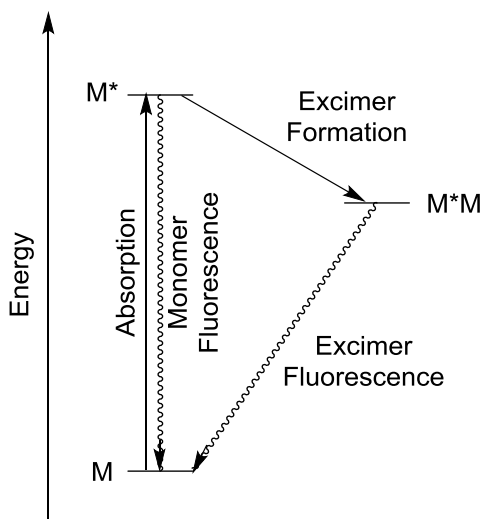


Figure 1-14. A Jablonski diagram illustrating the energy levels of monomeric and excimeric excited states.

If two pyrene molecules are covalently linked (tethered) through a molecule with three flexibilizing units (i.e. 1,3-(dipyrenyl)propane, structure shown in Figure 1-15), the

excimer emission dominates the spectra regardless of concentration.³⁵ Three linking units are necessary for intramolecular excimer formation, because it allows for a cofacial overlap of the chromophores. Any shorter linker will force the chromophores to diverge from each other, and will impede excimer formation.

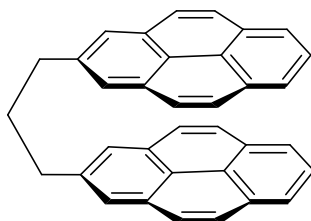


Figure 1-15. The structure of 1,3-(di-2-pyrenyl)propane.

Applications

The utility of excimer formation and detection in organic molecules has led to a variety of applications for determining the kinetics and dynamics of a system. One of the earliest uses was to determine the lateral diffusion rate in the hydrophobic region of lipid bilayers.³⁶ This was accomplished by dispersing pyrene in an aqueous lipid solution, and observing the ratio of monomeric emission to excimeric emission. Because of the low solubility of pyrene in water, all of the excimer emission can be assigned to interactions within the lipid bilayer.

Cyclization dynamics of polymer systems can be explored by using excimeric chromophores as end groups. An early report by Redpath and Winnik described the cyclization rate constants of variable lengths of polystyrene with pyrene end groups.³⁷ Once again, detection of the desired property, in this case cyclization of the polymer, relies on detection of excimer emission. If the chain does not cyclize, then no excimer emission should be detected. Dilute solutions were used to minimize intermolecular excimer interactions.

Excimeric Complexes Containing Platinum

The earliest report of a platinum complex displaying excimeric properties came from Hiraga and co-workers, using crystals of $K_4[Pt_2(P_2O_5H_2)_4] \cdot 2H_2O$ under variable pressure.³⁸ As pressure was increased from 1 atmosphere (atm) to 2.0 gigapascals (GPa), a new emission band formed between the fluorescence and phosphorescence. Observation of an excimeric band in this system is attributed to reduced Pt-Pt distance as pressure increases, as observed by X-ray diffraction and IR spectroscopy. Additionally, only well-grown crystals were suitable for these experiments, as microcrystalline material did not show the same behavior.

Organometallic platinum complexes are also capable of excimer formation in solution. The compound $Pt(5dpb)Cl$, where 5dpb = 1,3-di(5-methyl-2-pyridyl)benzene (shown in Figure 1-16), shows typical excimeric behavior in solution, with a broad band emission at ~670 nm when dissolved at high concentrations.³⁹ Interestingly, this complex shows solid state emission properties in direct contrast to the platinum salt described in the previous report. Crystalline $Pt(5dpb)Cl$ shows yellow luminescence, but when ground into a fine powder the emission became orange in color and had a similar λ_{max} as the excimer in solution. X-ray diffraction (XRD) data shows nearly identical packing in both the crystalline and powder samples, so stronger Pt-Pt interactions were ruled out. However, the surface area had been greatly increased by creating the powder, which generates a high number of labile surface molecules. These surface molecules may move to form a dimer or aggregate, giving rise to low energy emission.

Observation of excimer formation is most commonly observed as fluorescence; however, it can also be observed in the form of phosphorescence⁴⁰ or triplet-triplet absorption.⁴¹⁻⁴³ A report from 2007 suggested the ability of a platinum acetylide to form

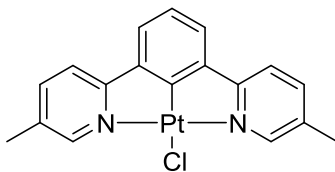


Figure 1-16. The structure of Pt(5dpb)Cl.

an excimer in the triplet state, which was then probed by transient absorption.⁴⁴ The platinum complex used for this study, which the authors call 'PE2-octyl', was designed to be a liquid at room temperature, and is shown in Figure 1-17. A highly soluble oil was needed for this experiment because very high loading levels were necessary. A 57 mM PE2-octyl solution in benzene was required to see this behavior, and the transient absorption spectrum is reproduced in Figure 1-18. Additionally, no emission was observed from this excimer, thus transient absorption was the only method that could be used to study it.

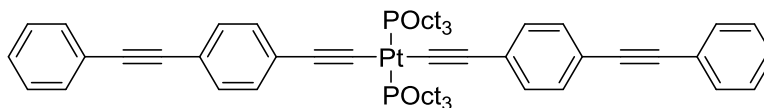


Figure 1-17. The structure of PE2-octyl.

Looking closer at Figure 1-18, one can see the absorption of a new species taking form, which is attributed to the triplet excimer. Interestingly, the absorption of this excimer is relatively narrow and shows a semblance of vibronic structure, suggesting localization of the triplet exciton on a single PE2-octyl unit, which has been previously shown for the PE2 chromophore in a platinum complex.⁴⁵ Thus it is reasonable to assess that excimer formation is primarily of ligand-ligand interaction. Kinetic studies of the PE2-octyl TA using free PE2 ligand as a triplet quencher showed almost an order of magnitude greater quenching than excimer formation. The preference for quenching via PE2 ligand over excimer formation implies that the potential energy barrier to

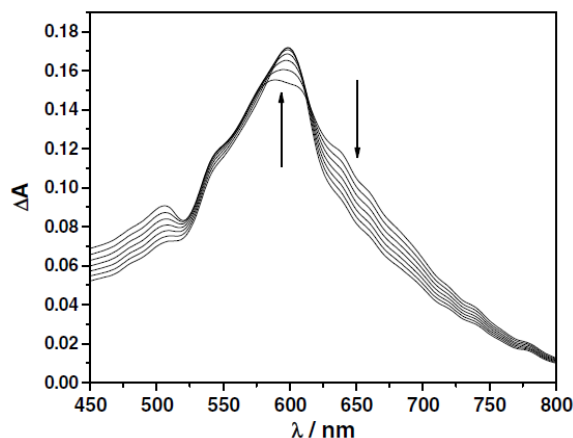


Figure 1-18. Transient absorption spectrum of 57 mM PE2-octyl in deoxygenated benzene after 476 nm laser excitation. Decay traces start at $t=0$ and were taken in increments of 150 ns. Reprinted from Chemical Physics Letters, Vol. 447, Slagle, J. E. et al. Triplet excimer formation in a platinum acetylide, 65-68, Copyright 2007, with permission from Elsevier.

excimer formation is affected by the sterics of the alkyl phosphine ligands around the platinum center.

The concentration of PE2-octyl in solution is noteworthy on its own, because it opens the door to potential use in non-linear optical applications. There are many potential uses for non-linear materials including, but not limited to goggles, windscreens, and optical coatings. Despite this, there are very few reports in which these molecules have been incorporated into a matrix to study the solid state properties for potential commercialization.⁴⁶⁻⁴⁸ Practically speaking, the concentration required to reach a useful saturation level should be as high as possible. Saturation is dependent on the deactivation of the excited state, which is directly proportional to the number of collision events between separate molecules, and thus the concentration.

Monosubstituted Platinum-Aryl Compounds as Precursors to Mixed Ligand Platinum Aryl/Acetylene Systems

As noted earlier, platinum acetylide complexes have been, and continue to be, intensely studied for their photophysical properties. However, the study of platinum

complexes with monodentate aryl ligands leaves a considerable amount to be desired. Platinum aryl (Pt-aryl) complexes of higher denticity are indeed well-known, and were repeatedly mentioned earlier in this manuscript in various cyclometallating ligands. The forced co-planar conformation of ligand and metal presumably has a large effect on the photophysical properties of the system compared to if the aryl ligand were allowed to rotate freely. Platinum systems, with phosphine ancillary ligands, containing monodentate aryl ligands typically are bound through a nitrogen atom.⁴⁹ The result though, is a non-neutral system with labile ligands.

When the literature is searched for platinum aryl systems, with the aryl group bonded through carbon, a vast majority of the aryl groups are monocyclic with only simple functional groups (e.g. phenyl and its derivatives). This lack of variety stems from the harsh conditions that had been required for platinum-carbon (Pt-C) bond formation.^{50, 51} Additionally, these harsh conditions led to primarily disubstitution of the aryl ligand. The monoaryl platinum complex can be obtained from the diaryl complex, but this requires another harsh reaction (HCl in Et₂O).⁵⁰ A second route to forming this platinum-carbon bond lies with oxidative addition. This route too is not without its drawbacks, as it requires the use of zero-valent metal precursors,⁵²⁻⁵⁴ which are air-sensitive.

Recently, a new platinum-carbon bond formation reaction was devised by a member of the Schanze Group.⁵⁵ This new reaction draws on the methodology of the Stille reaction, in that it uses an aryl-stannane in the presence of 10 mol% Cu(I) to form the Pt-C bond under mild conditions. When the aryl-stannane is reacted with *cis*-(PBU₃)₂PtCl₂ at any ratio, the monosubstituted Pt-aryl product is strongly favored. With a

facile synthetic pathway in hand, the route to chromophoric mixed ligand platinum aryl/acetylide (not to be confused with aryl-acetylide) complexes has been paved.

It would be remiss to not point out that many mixed aryl-acetylide platinum complexes (mixed ligand complexes) have already been synthesized. However, a vast majority of these complexes use a phenyl platinum moiety $(\text{Ph})(\text{PBU}_3)_2\text{Pt}(\text{CCR})$ as a non-chromophoric end group.⁵⁶⁻⁵⁸ Another recent report from the Low Group details the synthesis of a set of mixed ligand complexes featuring triaryl amine chromophores, all of which are shown and given reference numbers in Figure 1-13.⁵⁹ This report describes the synthesis, electrochemical, and spectroelectrochemical properties of these compounds. The authors use the synthetic route of oxidative addition, proceeding in high yield, to generate their monosubstituted platinum-aryl complex. They then use Hagihara coupling with a mono, di, or trifunctional acetylide ligand to synthesize a set of mixed aryl/acetylide ligand platinum complexes.

The monofunctional acetylide ligands were chosen with electrochemistry experiments in mind, as one of the ligands should not show an oxidation wave ($-\text{CCPh}-4\text{-OMe}$), while the other ligand should show a strong oxidation ($-\text{CCPhN}(4\text{-(OMe)Ph})_2$). Specifically, the aforementioned ligands will serve two purposes. First, the mixed ligand platinum complex functionalized with the redox inactive acetylide, **1**, will allow for characterization of the oxidation wave of the triphenyl amine moiety that is bonded to the platinum center through an aryl carbon. Second, the mixed complex functionalized with the redox active triarylamine acetylide ligand, **2**, will give insight to how strongly the aryl and acetylide electrophores are coupled through the platinum center. A platinum dimer (**3**) and trimer (**4**) were also synthesized to study the redox properties when

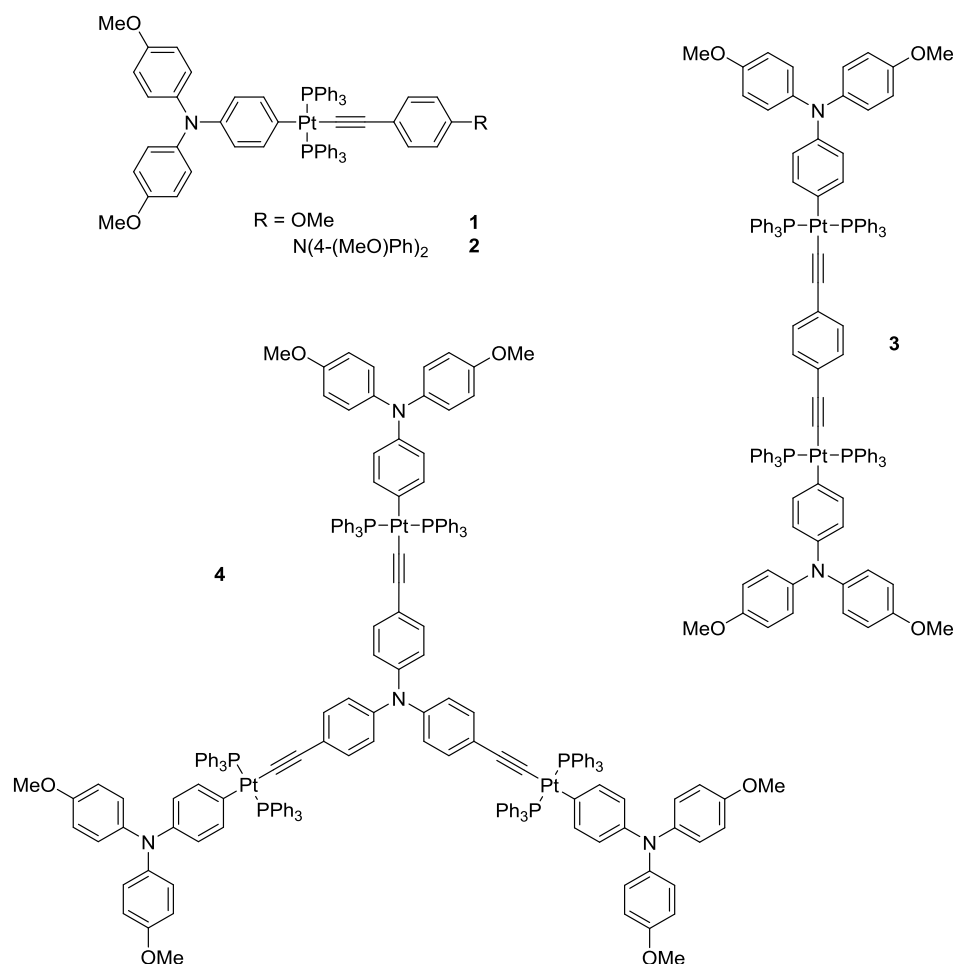


Figure 1-13. The four mixed ligand platinum aryl/acetylide complexes synthesized by the Low Group.

conjugated organic linking units are used. Upon examination of the cyclic voltammograms (CVs) of all four complexes, the authors note that distinct oxidation waves are present for each non-identical triarylamine moiety. Thus, the individual electrophores are acting independently, as they are isolated from each other by the platinum center(s).

Further experimentation using UV-Vis-NIR spectroelectrochemistry shows the formation of weak intervalence charge transfer (IVCT) bands in the 8500 cm⁻¹ region upon oxidation of **2** and **4** (**2**→[**2**]⁺ and **4**→[**4**]³⁺, respectively). Upon further oxidation

($[2]^+ \rightarrow [2]^{2+}$ and $[4]^{3+} \rightarrow [4]^{4+}$), the IVCT band collapses, allowing assignment of the band to a transition of $\{Ar'_2NArCC\} \rightarrow \{PtArN^+Ar'_2\}$. From these data, a coupling of 170 cm^{-1} for the ligands of **2**, and 130 cm^{-1} for the ligands of **4** were calculated. Thus these complexes show very weak interactions between aryl and acetylide chromophores.

CHAPTER 2

PHOTOPHYSICAL PROPERTIES OF *TRANS*-PLATINUM ACETYLIDE COMPLEXES FEATURING N-HETEROCYCLIC CARBENE LIGANDS

Background

Aryl-acetylide ligands have been tuned by altering conjugation length,^{6,12} varying the internal and external functionality,^{6, 12, 60, 61} including donor-acceptor motifs,⁶ and cross conjugation.^{7, 62} A square planar platinum(II) complex featuring two aryl-acetylide ligands can adopt either *cis* and *trans* geometries;¹² however, the *trans* configuration is prevalent in the complexes that have been reported. Unlike most platinum acetylides that contain monodentate ligands, bi and tridentate ligands use a variety of atoms for bonding to the metal center and altered structural motifs to achieve the desired chelating and electronic effects.^{12, 30, 63}

The focus of the work reported here was to directly compare the properties of platinum phosphine complexes studied previously in the Schanze Group⁶⁴ to the newly synthesized Pt-NHCs. The working theory was that replacement of the phosphine moieties with NHCs would reduce the spin-orbit coupling of the system, allowing for longer excited state lifetimes and enhanced triplet properties. In this chapter, we report the synthesis and photophysical properties of a series of *trans*-platinum acetylide complexes that feature monodentate N-heterocyclic carbene ligands in place of phosphine ligands. The aryl-acetylide ligands used in this work were chosen for their substantial two-photon absorption (2PA) cross-sections and proven non-linear optical

R. W. Winkel, G. G. Dubinina, K. A. Abboud and K. S. Schanze, *Dalton. Trans.*, 2014, **43**, 17712-17720.
– Reproduced by permission of The Royal Society of Chemistry. <http://pubs.rsc.org/en/content/articlelanding/2014/dt/c4dt01520g>

properties.^{2, 64} Finally, DFT computations were used to gain insight into the exact nature of the dominant electronic transitions for each complex.

Synthesis and Structure

Platinum NHC complexes are generally prepared by first generating and isolating the silver carbene precursor, then in a separate reaction transmetallating to platinum.⁶⁵ It has been shown that the needed silver carbenes can be generated in high yield *in situ*, but upon isolation material was lost.⁶⁶ To alleviate this problem in the present work, a one-pot method was developed as shown in Figure 2-1, and by using this approach *trans*-(ICy)₂PtCl₂ (**1**) was prepared in a 95% yield.

This one-pot reaction is quite robust, as there is no detectable formation of any byproducts even after extended reaction times, which is consistent with previously

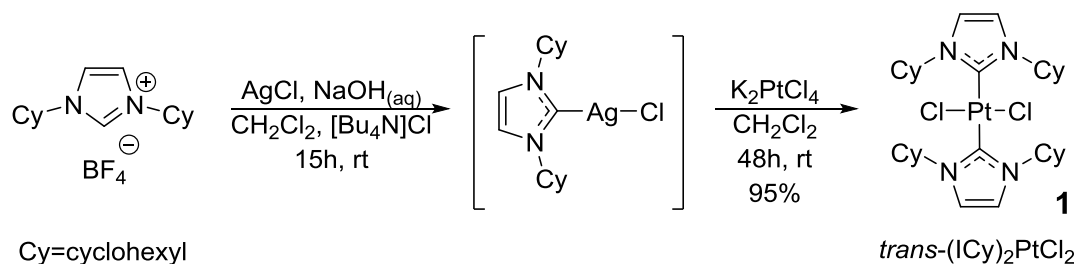


Figure 2-1. One-pot synthesis of *trans*-(ICy)₂PtCl₂ (**1**).

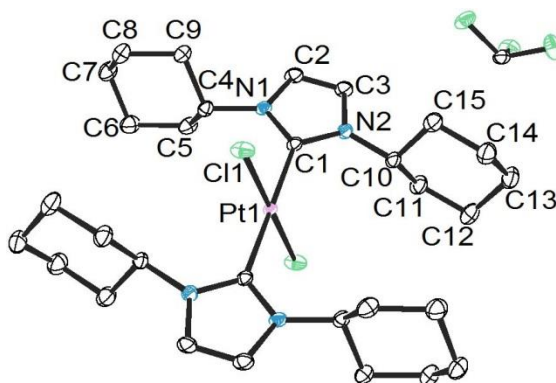


Figure 2-2. ORTEP diagram of *trans*-(ICy)₂PtCl₂ (**1**) with the asymmetric unit labeled. Ellipsoids are at the 50% probability level. Hydrogen atoms are omitted for clarity.

reported reactions.⁶⁵ The ^1H NMR spectrum could not confirm the *trans* nature of the complex, although it did differ as expected from the spectrum of the known *cis*-(ICy) $_2$ PtCl $_2$.⁶⁷ Single-crystal X-ray crystallography was employed to confirm the structure of **1**, and the structure is shown in Figure 2-2. Once the structure of **1** was confirmed, the complex was subjected to Hagihara reaction conditions as depicted in Figure 2-3 to introduce three different aryl-acetylide ligands (1-ethynyl-4-(phenylethynyl)benzene (PE2), 2-(9,9-diethyl-9*H*-fluoren-7-yl)benzo[*d*]thiazole (BTF), and 9,9-diethyl-7-ethynyl-*N,N*-diphenyl-9*H*-fluoren-2-amine (DPAF)). Single-crystal X-ray crystallography was again used in conjunction with ^1H NMR to confirm the structures of *trans*-(ICy) $_2$ Pt(PE2) $_2$ (**2a**), *trans*-(ICy) $_2$ Pt(BTF) $_2$ (**2b**), and *trans*-(ICy) $_2$ Pt(DPAF) $_2$ (**2c**).

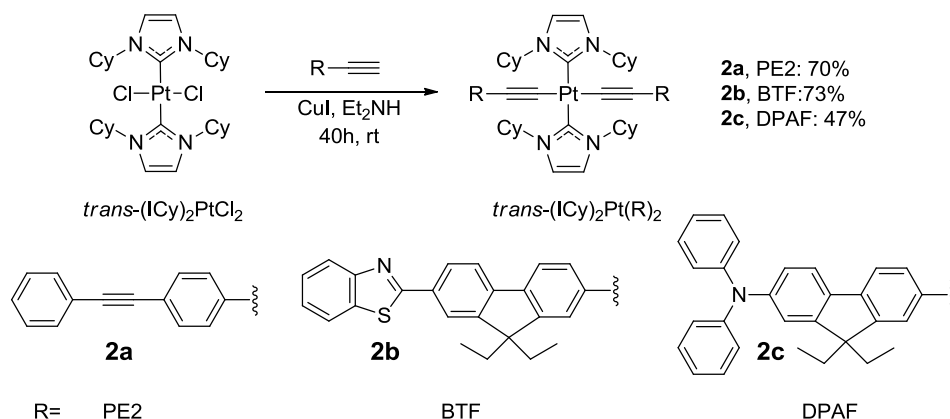


Figure 2-3. Hagihara reaction to generate the platinum acetylide compounds **2a-c**.

ORTEP diagrams of **2a-c** are shown in Figure 2-4. Important bond lengths and angles are presented in Table 2-1 and compared to their respective tributyl phosphine (PBu $_3$) analogues. The *trans* phosphine complexes (PBu $_3$) $_2$ Pt(PE2) $_2$, (PBu $_3$) $_2$ Pt(BTF) $_2$, and (PBu $_3$) $_2$ Pt(DPAF) $_2$ will be referred to as **3a-c** respectively. A full table of crystallographic data, and the structures of **2a-c** with the asymmetric unit fully labeled, can also be found in Appendix C.

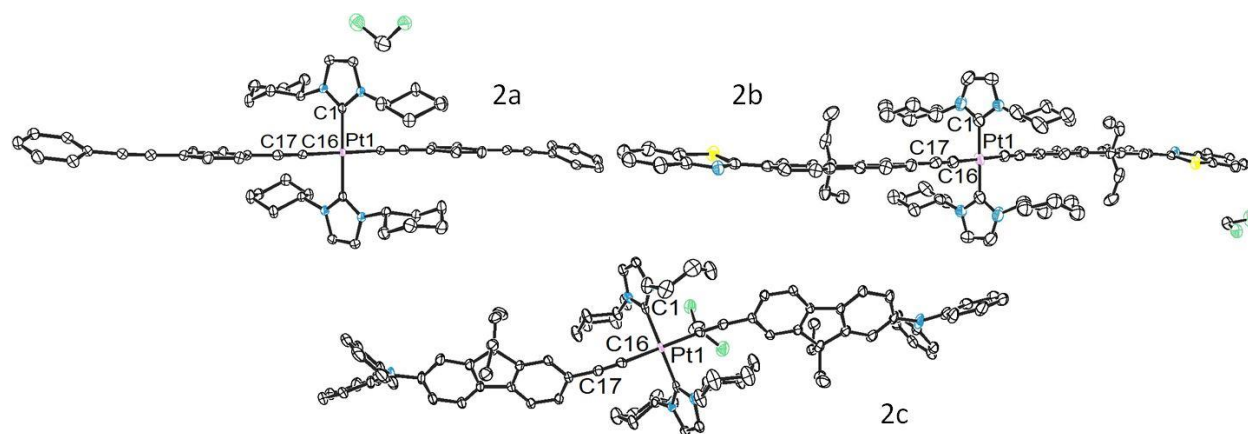


Figure 2-4. ORTEP diagrams of the molecular structures of **2a-c**, with thermal ellipsoids given at the 50% probability level. The hydrogen atoms are omitted for clarity. C: Black, N: Blue, S: Yellow, Pt: Pink, Chlorine: Green

Table 2-1. Key interatomic distances (Å) and angles (deg) for platinum acetylide complexes.

Complex	Pt1-C1	Pt1-C16(1) ^a	C16(1)≡C17(2) ^a	C1-Pt1-C16	N-C1-Pt1-C16 ^b
2a	2.033(3)	2.016(3)	1.198(4)	88.64(10)	63.3
2b	2.012(5)	2.012(5)	1.180(6)	88.88(17)	74.3
2c	2.029(2)	2.032(2)	1.175(3)	89.73(8)	65.9
3a ⁶⁸		1.981(6)	1.229(8)		
3b ²		2.000(3)	1.208(4)		
3c ²		2.023(8)	1.144(12)		

a Numbers in parentheses denote atomic numbering used in the crystal structures of the phosphine complexes. b N-C1-Pt1-C16 dihedral angles were selected to be acute and positive for ease of comparison.

Two major observations can be made from the crystal structures of **2a-c**. The first is a correlation of the N-C1-Pt-C16 dihedral angle (i.e., twisting of the carbene ligand) and the length of the Pt1-C1 bond. In particular, as the dihedral angle becomes smaller, the platinum-carbene bond length increases. Computations have shown that $d\pi \rightarrow \pi^*$ backbonding of metals to NHC ligands contributes to the Pt1-C1 bonding interaction.⁶⁹ As the N-C1-Pt-C16 dihedral angle decreases, the overlap of the Pt- d_{xy} and C1- p_x orbitals responsible for the backbonding also decreases, resulting in a longer bond. Additionally, the Pt1-C16 and C16≡C17 bond lengths lend insight into the strength of the interaction between the metal center and the π system of the aryl-

acetylide ligands ($d\pi \rightarrow \pi^*$ backbonding). The extent of coupling likely influences the degree of interaction (conjugation and spin-orbit coupling) between the platinum center and the aryl-acetylide ligands. Compounds **2a** and **2b** have shorter C16 \equiv C17 bond lengths than **3a** and **3b** and compound **2a** also has a longer Pt1-C16 bond than **3a**, both of which imply slightly less $d\pi \rightarrow \pi^*$ interaction in the carbenes. Unfortunately, conclusions cannot be drawn about the Pt1-C16 distance of **2b** nor either property of **2c**, because the values are within experimental error.

As a further measure of the degree of metal-ligand conjugation and extent of platinum backbonding, IR spectra were recorded for **2a-c**. An expanded view of the C \equiv C bond stretching region of the IR spectra is shown in Figure 2, the full IR spectra can be found in Appendix C. Viewing the platinum center as a π -donor, increasing ligand acceptor strength should weaken the C16 \equiv C17 bond. This holds true in the experimental data, as the BTF ligand in **2b** is a good acceptor, giving the complex the lowest frequency C \equiv C bond stretch at 2075 cm^{-1} . Complexes **2a** and **2c**, which contain neutral and donor ligands, respectively, both show a C \equiv C bond stretch at slightly higher

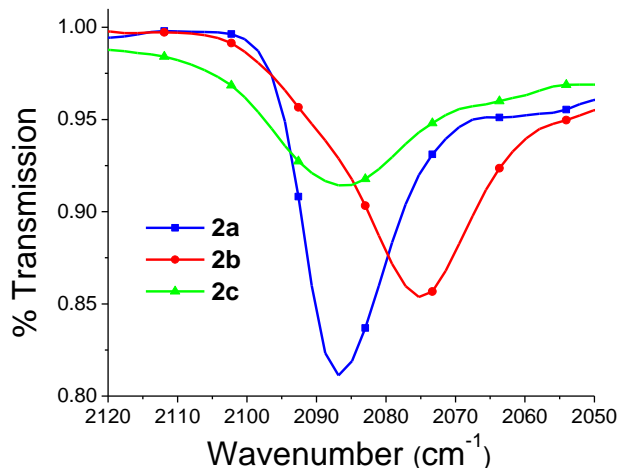


Figure 2-5. Asymmetric C \equiv C bond stretch of platinum acetylide compounds **2a-c**.

frequency $\sim 2087\text{ cm}^{-1}$. The second triple bond of the PE2 ligand in **2a** does not display a strong vibrational mode and cannot be directly assigned to a peak in the recorded spectrum. In summary, the X-ray structural data suggest that there is a slightly greater interaction between the metal center and the alkyne ligand in the phosphine complexes relative to the carbene congeners.

Photophysical Properties

The ground state absorption spectra for the platinum acetylide series in THF solution are shown in Figure 3 along with fluorescence and phosphorescence spectra of the complexes in aerated solution and after at least three freeze-pump-thaw vacuum degassing cycles, respectively. (Phosphorescence spectra were initially attempted by degassing with argon; however, due to their long triplet lifetimes, *vide infra*, compounds **2a-c** are very sensitive to oxygen and significantly reduced phosphorescence was observed for argon deaerated solutions.) Absorption, fluorescence, and phosphorescence maxima, as well as extinction coefficients, emission quantum yields, and emission lifetimes are given in Table 2-2. The absorption maximum of **2b** is red-shifted relative to that of **2a** due to the increased conjugation length offered by the electron-accepting benzothiazole moiety. In **2c**, when benzothiazole is substituted for the electron-donating diphenylamino moiety, the absorption maximum lies between **2a** and **2b**. Absorption maxima of **2a-c** are within 6 nm of **3a-c**, with **2a** and **2b** being red-shifted and **2c** slightly blue-shifted. The extinction coefficients can be used as a qualitative measure of conjugation through the platinum center.⁶⁴ When the extinction coefficients of **2a-c** are compared to **3a-c**, **2a** shows similar ligand interaction with the platinum center, whereas **2b** and **2c** show significantly less interaction. Like the ground-state absorption, the fluorescence is red-shifted for **2a** and **2b** and blue-shifted for **2c**.

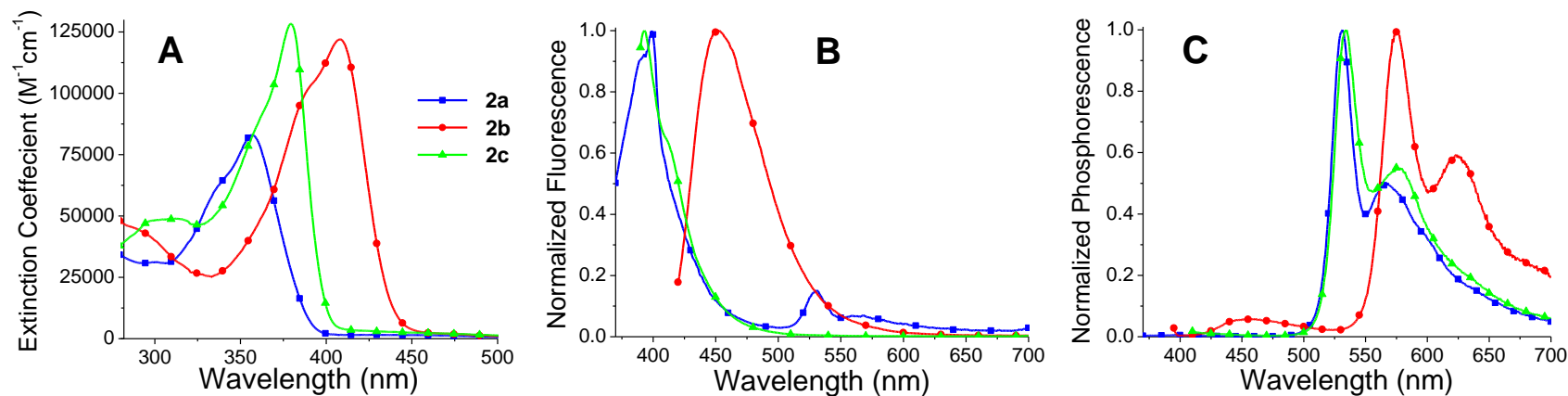


Figure 2-6. The A) ground state absorption, B) normalized fluorescence, and C) normalized phosphorescence spectra of **2a-c** in THF. Excitation was at the ground state absorption maxima, and the plots were normalized.

Table 2-2. Summary of photophysical data for platinum acetylides **2a-c** and **3a-c**.

Complex	Abs _{max} (nm)	ϵ (M ⁻¹ cm ⁻¹)	Fl _{max} (nm)	Φ_{Fl}^a	τ_{Fl}^b (ns)	Ph _{max} (nm)	Φ_{Ph}^e	τ_{Ph}^b (μ s)	TA _{max}	τ_{T1-Tn}^b (μ s)
2a	357	83000	399	0.002	0.710 ^c	531	0.541	575 ^f	584	80.8
2b	408	122000	452	0.043	< 0.100 ^d	576	0.220	355	749	95.9
2c	380	128000	393	0.041	< 0.100 ^d	534	0.450	1080 ^g	606	111
3a^{o4}	353	83000	391	0.0005	< 0.100 ^d	527	0.0108	48.9	577	15.4
3b^{o4}	402	154000	436	0.0092	< 0.100 ^d	567	0.1752	75.6	660	13.3
3c^{o4}	384	160000	401	0.0059	< 0.100 ^d	533	0.3552	61.3	612	8.9

^a Measured at RT using Ru(bpy)₃Cl₂ in aerated water ($\Phi_{fl} = 0.0379$)⁷⁰ and anthracene in THF ($\Phi_{fl} = 0.33$)⁷¹ as standards. ^b All decay profiles can be found in Appendix C. ^c τ_1 (α_1) = 0.309 ns (66.1%), τ_2 (α_2) = 1.37 ns (31.8%), τ_3 (α_3) = 3.33 (2.1%). ^d Lifetime is shorter than the lower threshold of the PicoQuant instrument, 100 ps. ^e Measured at RT using 9,10-diphenylanthracene in aerated cyclohexane ($\Phi_{fl} = 0.75$) as a standard. ^f τ_1 (α_1) = 635 μ s (87.9%), τ_2 (α_2) = 143 μ s (12.1%). ^g τ_1 (α_1) = 1693 μ s (48.9%), τ_2 (α_2) = 495 μ s (51.1%).

relative to the respective PBu_3 analogues. The phosphorescence of **2a-c** all show less than a 10 nm red-shift relative to **3a-c**, with **2b** again showing the greatest difference. Consistent with reduced metal-ligand interaction, the fluorescence quantum yields of **2a-c** are 4-7 times greater than **3a-c**, but nonetheless are comparatively low on an absolute scale (<4.5%). Only the fluorescence lifetime of **2a** was long enough to be measurable with our apparatus, with the primary component being ~310 ps and two longer lived components greater than 1 ns with comparatively low amplitude. Interestingly, the phosphorescence lifetimes are enhanced ~5 times for **2b** and greater than an order of magnitude for **2a** and **2c** in the carbene complexes compared to the PBu_3 congeners. The phosphorescence quantum yields are similarly enhanced in the carbene complexes relative to the phosphines.

Nanosecond transient absorption (TA) data were collected on **2a-c** to gain insight into the triplet excited states, and the absorption-difference spectra, assigned to triplet-triplet absorption, are shown in Figure 2-7. All of the spectra show bleaching in the region of the ground-state absorption, with a strong, broad, and long-lived absorption in the visible region. The triplet-triplet spectra are qualitatively similar to those for the phosphine analogues, consistent with the notion that the triplet is localized on the arylacetylide ligands.⁶⁴ The TA absorption maximum of **2b** (749 nm) was significantly red-shifted relative to **3b** (660 nm), while **2a** (584 nm) and **2c** (606 nm) remained almost unchanged as in **3a** (577 nm) and **3c** (612 nm). By analogy to the phosphorescence decay lifetimes, the lifetimes of the triplet-triplet absorption of **2a-c** are significantly enhanced relative to **3a-c**. However, the transient absorption decay lifetimes were shorter than expected on the basis of the phosphorescence lifetimes (Table 2-2), and it

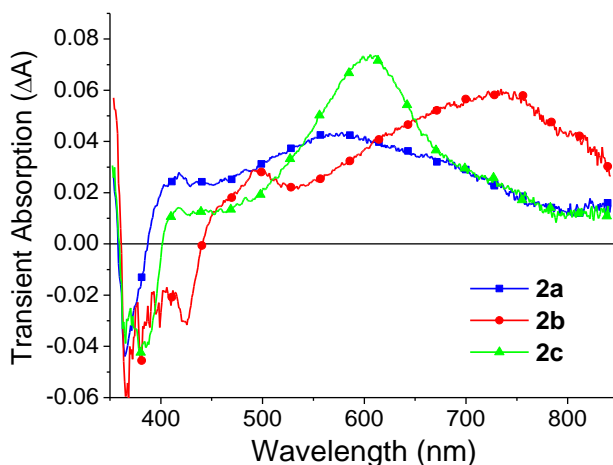


Figure 2-7. Principal component transient absorption spectra of **2a-c**, with excitation at 355 nm, 10 ns pulse width, 180 $\mu\text{J/pulse}$ excitation energy. Solutions had an absorptivity value of 0.62 at 355 nm after four freeze-pump-thaw cycles.

was suspected that they were attenuated by triplet-triplet annihilation, which would be power dependent. A power dependence study of the transient absorption decay kinetics was carried out on **2a** and the results showed that the kinetics are power dependent (see Appendix C).

Nanosecond open aperture z-scan studies were carried out on aerated solutions of **2a-c** to determine their relative non-linear absorption response with respect to **3c**. Complex **3c** was used as a reference because of its well established non-linear response under similar laser excitation conditions.^{2, 64} When this experiment is done using near-infrared nanosecond laser pulses, the combined effects of 2-photon absorption and triplet-triplet excited state absorption combine to give rise to the overall optical attenuation. An excitation wavelength of 606 nm was chosen due to the lack of any ground state absorption at this wavelength. Figure 5 shows the relative z-scan response of each complex; the order of response of this series of complexes is **2a** < **2b** < **2c** \approx **3c**. Complexes **3a-c** follow the same trend.⁶⁴

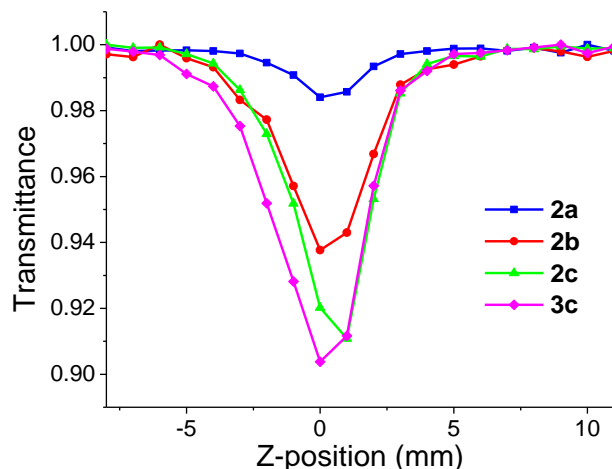


Figure 2-8. Open aperture z-scan transmittance using 606 nm light. Solutions were 1 mM in aerated THF and the laser energy was 600 μ J/pulse. **3c** was used as the reference.

Electronic Structure Calculations

To further probe the nature of the metal-chromophore interaction, DFT and TD-DFT calculations were performed in the Gaussian 09, revision C.01,⁷³ suite of programs at the B3LYP level with the 6-31G(d) basis set for nonmetals and the SDD basis set for Pt. Carbene cyclohexane groups were replaced by methyl groups to improve computational efficiency, and these truncated complexes are denoted as **2a'-c'**.

The property of interest is the nature of the electronic excitation corresponding to the ground state absorption maximum of each complex. TD-DFT confirms that these transitions are predominantly HOMO \rightarrow LUMO with minor contributions from the HOMO-1 \rightarrow LUMO+1 transition, as shown in Table 2-3. As expected, all HOMOs are composed of ligand π -orbitals with the occupied Pt- d_{xy} giving rise to interaction between the two ligands. In turn, the LUMOs are all acetylide ligand centered π^* , with no contribution from the platinum. The predicted energies of these theoretical electronic transitions all match well with the experimental data. Computed vertical excitation energies for compounds **2a'-c'** are red-shifted by 17, 21, and 2 nm, respectively,

relative to the experimental data. Charge difference densities for the dominant singlet-singlet transitions of **2a'-c'** are shown in Figure 2-9. CDDs show how the charge moves in an electronic transition, and illustrates the charge delocalization across the ligands in **2a'** and **b'** and charge buildup on the fluorene moiety of **2c'**. Relevant molecular orbitals, enlarged CDDs, and a table of all significant vertical excitations for each compound can be found in Appendix C.

Table 2-3. Summary of TD-DFT computations for the $S_0 \rightarrow S_1$ transition of **2a'-c'**.

Complex	Wavelength (nm)	Orbital Transitions (% contribution)	Oscillator Strength, <i>f</i>
2a'	373.8	165→168 HOMO-1 → LUMO+1 (2.4%) 166→167 HOMO → LUMO (97.6%)	2.3830
2b'	429.3	259→262 HOMO-1 → LUMO+1 (5.3%) 260→261 HOMO → LUMO (94.7%)	2.2796
2c'	381.5	279→282 HOMO-1 → LUMO+1 (18.3%) 280→281 HOMO → LUMO (81.7%)	2.6813

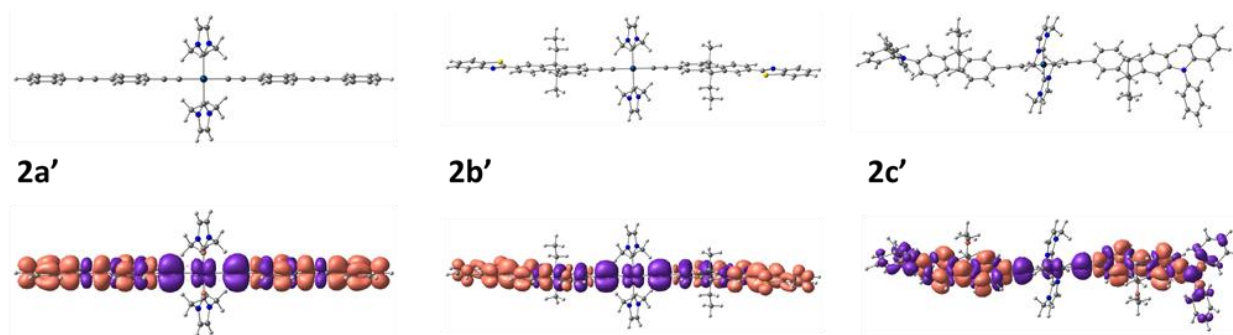


Figure 2-9. DFT optimized structures (top row), and charge difference densities (bottom row) for the calculated transitions corresponding to the experimental ground-state absorption maxima. Blue coloring indicates electron density being lost, while red coloring indicates electron density being gained in an electronic transition. CDDs were imaged at an isovalue of 0.0004.

Summary and Conclusions

In summary, three platinum acetylide complexes (**2a-c**) featuring N-heterocyclic carbenes with the PE2, BTF, and DPAF chromophores, respectively, were synthesized from the platinum carbene precursor (**1**), via a Hagihara reaction to generate the desired products. These complexes were characterized by NMR spectroscopy and

single-crystal X-ray crystallography to confirm that the ligands were in a *trans* geometry with respect to the platinum center.

In order to compare the effect of substituting carbene ligands for the tributyl phosphine ligands which have been used in previous related platinum acetylide complexes, photophysical studies were performed and X-ray data were analyzed. Optical transitions of the carbene complexes are very similar to those of the corresponding phosphines, as these properties are largely determined by the π -conjugated ligand chromophores. However, there is evidence for slightly less metal-ligand interaction (and consequent reduced spin-orbit coupling) in the carbene complexes. Lower extinction coefficients imply weaker conjugation between the two chromophores relative to their phosphine congeners. Fluorescence quantum yields are increased for all carbene complexes, and unlike any of the phosphine complexes, the fluorescence lifetime of **2a** was long enough to be measurable. The phosphorescence lifetimes are also significantly enhanced, as reduced spin-orbit coupling decreases the probability of the spin-forbidden transition back to the singlet ground state. The longer phosphorescence lifetimes result in enhanced phosphorescence quantum yields for all carbene complexes, as there is more time for radiative decay to occur. The triplet-triplet absorptions also followed the same trend, exhibiting significant increases in the triplet lifetimes.

In the solid state, single crystal X-ray crystallography generally showed that the carbene complexes have longer Pt1-C16 and shorter C16 \equiv C17 bond lengths; however, clear trends cannot be established since in some cases the bond lengths for the carbene and phosphine complexes are within experimental error. Decreased

Pt $d\pi \rightarrow$ ligand π^* backbonding is expected to give rise to longer Pt1-C16 bonds due to reduced metal-ligand π -bonding, and shorter C16 \equiv C17 bonds due to reduced electron density in the C16 \equiv C17 π^* levels, which is generally consistent with the experimentally observed trends. FTIR was also used to probe the degree of backbonding in the carbene complexes. These data show a lower frequency stretch for the C16 \equiv C17 bond in **2b**, which contains the electron-accepting BTF ligand. The neutral PE2 ligand and electron donating DPAF ligand show approximately equivalent stretching frequencies.

A non-linear absorption by open aperture, nanosecond z-scan revealed that the carbene complexes display strong non-linear absorption, with a similar response compared to their phosphine analogs. The non-linear absorption response is dependent on the acetylide chromophore, following the trend (**2a** (PE2) < **2b** (BTF) < **2c** (DPAF) ~ **3c** (DPAF)). This is likely due to the response being triggered by two-photon absorption, which has the same trend of increasing response as the z-scan experiment.²

This work shows that platinum acetylide complexes featuring carbene co-ligands show promising photophysical and non-linear optical properties. The properties of the complexes suggest that they may find use in material applications such as optical power limiting or photosensitization of singlet oxygen with near-infrared, two-photon excitation. Given the wide range of carbene ligands that are available,⁷⁴ their use can allow tuning of the electronic and steric properties of the Pt-acetylide complexes, affording systems with tunable properties that can be optimized for specific applications.

Experimental

General Remarks

All reactions were carried out under argon atmosphere. All starting chemicals used for the synthesis of the *trans* platinum acetylide complexes were purchased from

commercial suppliers, reagent grade, and used without additional purification. K_2PtCl_4 was purchased from Strem Chemicals. Solvents were of reagent grade unless otherwise noted. PE2, BTF, and DPAF ethynyl-ligands were synthesized according to literature procedures.^{2, 64} *trans*-(ICy)₂PtCl₂ was synthesized by a one-pot synthesis via modified transmetallation procedures.^{65, 75} Silica gel (230-400 mesh, 60 Å, Silicycle Inc.) was used for column and flash chromatography. ¹H (500 MHz) and ¹³C (125.7 MHz) NMR spectra were recorded on a Varian Inova spectrometer. The chemical shifts were reported in ppm relative to tetramethylsilane (TMS) or residual protonated solvent peaks in ¹H NMR spectra. Mass spectrometry and elemental analysis were performed by Mass Spectrometry Services and CHN Elemental Analysis Services respectively, both of which are located in house at the University of Florida.

Fourier Transform Infrared Spectroscopy (FTIR)

FTIR spectra were taken on a Bruker Vertex 80V FTIR using a Pike Technologies GladiATR ATR accessory and the OPUS 6.5 software package. The spectra were taken neat with the apparatus open to the atmosphere. Data was acquired in the range of 4500-400 cm⁻¹ with a precision of ± 4 cm⁻¹.

X-ray Structure Determinations

A CHCl₃ solution of **1** and a CH₂Cl₂ solution of **2b** were layered with hexanes and refrigerated. After two days, colorless prisms of **1** and yellow prisms of **2b** were isolated. CH₂Cl₂ solutions of **2a** and **2c** were placed in a vial, which was then placed in a beaker of hexanes and covered for vapor diffusion. After two days colorless needles of **2a** and colorless prisms of **2c** were isolated.

X-ray intensity data were collected at 100 K on either a Bruker **SMART** diffractometer using MoK α radiation ($\lambda = 0.71073$ Å) for (**1** and **2c**) and on a Bruker

DUO diffractometer using MoK α or CuK α radiation ($\lambda = 1.54178 \text{ \AA}$) (**2b** and **2a**, respectively), from an ImuS power source and both using an APEXII CCD area detector. Raw data frames were read by program SAINT⁷⁶ and integrated using 3D profiling algorithms. The resulting data were reduced to produce hkl reflections and their intensities and estimated standard deviations. The data were corrected for Lorentz and polarization effects and numerical absorption corrections were applied based on indexed and measured faces. The structure was solved and refined in SHELXTL6.1, using full-matrix least-squares refinement. The non-H atoms were refined with anisotropic thermal parameters and all of the H atoms were calculated in idealized positions and refined riding on their parent atoms. Further details about the asymmetric units of all reported complexes are given in Appendix C

Absorption and Emission Spectroscopy

Steady-state absorption spectra were recorded on a Varian Cary 50 or a Cary 100 dual-beam spectrophotometer. Corrected steady-state emission measurements were performed on a Photon Technology International spectrophotometer (QuantaMaster). Absorption and fluorescence samples were run in aerated solution, while phosphorescence samples were deaerated with at least four freeze-pump-thaw cycles. Optically dilute samples with O.D. < 0.1 at the excitation wavelength were used. Fluorescence quantum yields were determined by relative actinometry, with Ru(bpy)₃Cl₂ as an actinometer ($\Phi_{\text{FI}} = 0.0379$ in air saturated water)⁷⁰ for (ICy)₂Pt(BTF)₂, and anthracene ($\Phi_{\text{FI}} = 0.33$ in THF)⁷¹ for (ICy)₂Pt(PE2)₂ and (ICy)₂Pt(DPAF)₂. Phosphorescence quantum yields were determined in the same manner using 9,10-diphenylanthracene ($\Phi_{\text{FI}} = 0.75$ in cyclohexane)⁷² as an actinometer.

Fluorescence lifetimes were obtained with a PicoQuant FluoTime 100 Compact Fluorescence counting technique (TCSPC) with a PicoQuant FluoTime 100 Compact Fluorescence Lifetime Spectrophotometer. A UV-pulsed diode laser provided the excitation at 375 nm (power < 10 mW). The laser was pulsed using an external BK Precision 4011A 5MHz function generator. The decay of **2a** was obtained using tri-exponential fitting parameters (FluoFit software). The decays of **2b** and **2c** were faster than the instrument response time (<100 ps).

Phosphorescence lifetimes were obtained with a multichannel scaler/photon counter system with a NanoQuant FluoTime 100 Compact Phosphorescence Lifetime Spectrophotometer. A UV-pulsed diode laser provided the excitation at 375 nm (power < 10 mW). The laser was pulsed by a PDL800-B, which is a pulsed diode laser driver. Optically dilute solutions were freeze-pump-thawed a minimum of four times. The decay of **2b** was obtained using single exponential fitting parameters, and the decays of **2a** and **2c** were obtained using biexponential fitting parameters (FluoFit software).

Nanosecond Transient Absorption (TA) Spectroscopy

Measurements were performed on an in-house apparatus that is described in detail elsewhere.⁷⁷ The third harmonic of a Continuum Surelite series Nd:YAG laser ($\lambda = 355$ nm, 10 ns fwhm, 180 $\mu\text{J-pulse}^{-1}$) was used as the excitation source. Probe light was produced by a xenon flash lamp and the transient absorption signal was detected with a gated-intensified CCD mounted on a 0.18 M spectrograph (Princeton PiMax/Acton Pro 180). Solutions had a matching optical density of 0.62 after a minimum of four freeze-pump-thaw cycles. An initial CCD image capture delay of 100 ns following the laser pulse was used to ensure full conversion to the triplet state before observation.

An average of 100 images were acquired and the laser energy was 180 $\mu\text{J}/\text{pulse}$, which was established as being sufficiently low to minimize triplet-triplet power dependence.

Open Aperture Z-Scan

Nonlinear transmission measurements were performed via an open aperture z-scan apparatus.⁷⁸ The excitation wavelength (606 nm) was generated by a Continuum Surelite OPO Plus pumped with the third harmonic (355 nm) of a Continuum Surelite II-10 Nd:YAG laser. The laser beam was split with a 50:50 beam splitter to two OPH PE10-SH V2 pyroelectric detectors, which measured the transmitted pulse energy as a function of the input pulse energy using an Ophir Laserstar dual-channel optical laser energy meter. The beam was focused with a 25.4 mm diameter, 50.8 mm focal length concave lens. A ThorLabs motorized translation stage (Z825B and TDC001) allowed mm movement along the z-axis.

Computational Details

DFT and TD-DFT calculations were performed in the Gaussian 09, revision C.01,⁷³ suite of programs at the B3LYP level with the 6-31G(d) basis set for nonmetals and the SDD basis set for Pt. Carbene cyclohexane groups were replaced by methyl groups to improve computational efficiency. The ground state structures were optimized in the gas phase from idealized starting configurations without symmetry constraints. The optimized structures were confirmed to be minima by the lack of imaginary frequencies. Structures and orbitals were visualized using Chemcraft Version 1.7,⁷⁹ which was also used to generate charge difference density (CDD) plots. CDDs were imaged at an isovalue of 0.0004.

Synthesis of *trans*-(ICy)₂PtCl₂ (1)

To a flask charged with 60 mL of argon degassed dichloromethane, 1,3-bis(cyclohexyl)imidazolium tetrafluoroborate (1.0 g, 3.1 mmol, 1 eq.) and AgCl (0.492 g (3.4 mmol, 1.1 eq.) were added, and the solution was bubbled with argon for an additional 15 minutes. On the side, 0.125g of NaOH (3.1 mmol, 1 eq.) and ~1 eq of [Bu₄N]Cl were added to 10 mL of argon degassed deionized water. The aqueous solution was then added to the reaction mixture via cannula. The mixture was bubbled with argon for an additional 15 minutes before being allowed to react for 15 hours at room temperature with vigorous stirring in the dark. The reaction mixture was then filtered and washed with deionized water (3 x 5 mL). The organic layer containing 1,3-bis(cyclohexyl)imidazole-2-yl silver chloride was then separated and used for the next step without identification or further purification.

K₂PtCl₄ (0.615 g, 1.48 mmol, 0.475 eq.) was added to the resulting dichloromethane solution of 1,3-bis(cyclohexyl)imidazole-2-yl silver chloride and the mixture was stirred vigorously for 48 hours at room temperature under argon in the dark. The reaction mixture was then filtered to remove the precipitate and the filtrate was reduced in vacuum. This was then purified by column chromatography (CH₂Cl₂) resulting in product **1** as a white powder. Yield, 1.08 g, 95% Mp: 275 °C (dec). Anal. Calc. for C₃₀H₄₈N₄PtCl₂: C, 49.31; H, 6.62; N, 7.67. Found: C, 49.20; H, 6.73; N, 7.44. ¹H NMR (500 MHz, CDCl₃): δ 6.87 (s, 4H, -CH=CH-), 5.53 (tt, *J* = 11.6 Hz, 4.0 Hz, 4H, CH), 2.39 (d_{br}, *J* = 10.9 Hz, 8H, CH₂), 1.94 (d_{br}, *J* = 12.5 Hz, 8H, CH₂), 1.79 (d_{br}, *J* = 13.2 Hz, 4H, CH₂), 1.64-1.45 (m, 16H, CH₂), 1.25 (qt, *J* = 12.8 Hz, 6.3 Hz, 4H, CH₂). ¹³C {¹H} NMR (126 MHz, CDCl₃): δ 166.9, 116.6, 59.0, 34.1, 26.3, 25.8. Mass Spec. ESI-

TOF-MS (found) m/z. 753.2809 [M+Na]⁺, 1483.5698 [2M+Na]⁺. (calcd) 753.2787 [M+Na]⁺, 1483.5683 [2M+Na]⁺.

General Procedure for the Hagihara Coupling Reaction (**2a-c**)

To a flask charged with 10 mL of Et₂NH and 20 mL of dichloromethane, 0.146 of **1** (0.146 g, 0.2 mmol, 1 eq.) and 0.4 mmol (2 eq.) of the corresponding deprotected aryl-acetylide (PE2, BTF, DPAF) were added. The solution was then bubbled with argon for 15 minutes before addition of 5 mol% CuI (1.9 mg, 0.01 mmol, 0.025 eq). The reaction mixture was then stirred for 40 hours at room temperature, under argon, in the dark. The final mixture was diluted with 40 mL of dichloromethane, washed with deionized water (3 x 20 mL), dried over sodium sulfate and filtered. The filtrate was reduced in vacuum until a significant amount of precipitate formed. The precipitate was filtered, washed with cold methanol and hexanes and dried under vacuum. The obtained products **2a-c** showed a single spot in TLC and were pure by NMR. Additional fractions were obtained from the filtrate and purified by flash chromatography (eluent: 90:10 ethyl acetate/hexanes gradient shifted to 10:90 ethyl acetate/hexanes). Complexes **2a** and **2c** were obtained as off-white solids, while **2b** was obtained as a light yellow solid.

Note: Any chromatography that did not pass the product through in a short amount of time significantly decreased the yield of the products. The same trend was observed for TLC: additional side-product spots appeared if the product was allowed to sit for a few minutes on the TLC plate before chromatography.

trans-(ICy)₂Pt(PE2)₂ (**2a**)

Yield, 0.149 g, 70%. Mp: 272 °C (dec). Anal. Calcd for C₆₂H₆₆N₄Pt: C, 70.10; H, 6.26; N, 5.27. Found: C, 69.78; H, 6.50; N, 5.20. ¹H NMR (500 MHz, CD₂Cl₂): δ 7.48 (m, 4H, Ph-H terminal), 7.36-7.30 (m, 6H, Ph-H terminal), 7.25 (d, J = 8.5 Hz, 4H, Ph-H

internal), 7.03 (d, $J = 8.5$ Hz, 4H, Ph-H internal), 7.00 (s, 4H, -CH=CH-), 5.39 (tt, $J = 11.5$ Hz, 3.7 Hz, 4H, CH), 2.38 (m, 8H, CH₂), 1.93 (m, 8H, CH₂), 1.78 (m, 4H, CH₂), 1.63-1.51 (m, 16H, CH₂), 1.28 (qt, $J = 12.6$ Hz, 3.5 Hz, 4H, CH₂). ¹³C NMR (126 MHz, CD₂Cl₂): δ 168.7, 131.9, 131.5, 131.2 130.5, 128.9, 128.6, 124.1, 118.7, 117.0, 113.1, 106.3, 90.6, 89.9, 60.1, 34.3, 26.7, 26.1. APCI-TOF-MS (found) m/z . 1062.4967 [M]⁺ (calcd) 1062.4950 [M]⁺.

***trans*-(ICy)₂Pt(BTF)₂ (2b)**

Yield, 0.207 g, 73%. Anal. Calcd for C₈₂H₈₈N₆PtS₂: C, 69.51; H, 6.26; N, 5.93. Found: C, 69.59; H, 6.72; N, 5.83. Mp: 294°C (dec). ¹H NMR (500 MHz, CD₂Cl₂): δ 8.06 (dd, $J = 1.6$ Hz, 0.4 Hz 2H, Ar-H fluorene), 8.03-7.99 (m, 4H, Ar-H fluorene, Ar-H benzothiazole), 7.94 (ddd, $J = 8.0$ Hz, 1.2 Hz, 0.6 Hz, 2H, Ar-H benzothiazole), 7.70 (dd, $J = 7.9$ Hz, 0.4 Hz, 2H, Ar-H fluorene), 7.53 (dd, $J = 7.8$ Hz, 0.4 Hz, 2H, Ar-H fluorine), 7.49 (ddd, $J = 8.3$ Hz, 7.2 Hz, 1.2 Hz, 2H, Ar-H benzothiazole), 7.39 (ddd, $J = 8.3$ Hz, 7.2 Hz, 1.2 Hz, 2H, Ar-H benzothiazole), 7.12 (m, 2H, Ar-H fluorene), 7.10 (dd, $J = 7.8$ Hz, 1.4 Hz, 2H, Ar-H fluorine), 7.03 (s, 4H, -CH=CH-), 5.51 (m, 4H, CH), 2.45 (m, 8H, CH₂), 2.11 (dq, $J = 14.6$ Hz, 7.4 Hz, 4H, CH₂-ethyl), 2.04-1.92 (m, 12H, CH₂-ethyl, CH₂-cyclohexyl), 1.81 (d_{br}, $J = 13.5$ Hz, 4H, CH₂), 1.69-1.55 (m, 16H, CH₂), 1.36-1.27 (m, 4H, CH₂), 0.30 (t, $J = 7.3$ Hz, 12H, CH₃). ¹³C NMR (126 MHz, CD₂Cl₂): δ 169.2, 168.9, 154.9, 151.2, 150.8, 145.6, 137.2, 135.6, 132.1, 130.3, 130.1, 127.6, 126.8, 125.9, 125.5, 123.3, 122.2, 122.0, 120.2, 120.0, 117.1, 110.8, 107.1, 60.1, 56.7, 34.3, 33.3, 26.7, 26.2, 8.8. APCI-TOF-MS (found) m/z . 1417.6271 [M+H]⁺ (calcd) 1417.6253.

***trans*-(ICy)₂Pt(DPAF)₂ (2c)**

Yield, 0.139 g, 47% Mp: 222°C (dec). Anal. Calcd for C₉₂H₁₀₀N₆Pt: C, 74.41; H, 6.79; N, 5.66. Found: C, 74.37; H, 7.34; N, 5.58. ¹H NMR (500 MHz, CD₂Cl₂): δ 7.48 (d,

$J = 8.2$ Hz, 2H, Ar-H fluorene), 7.37 (dd, $J = 8.6$ Hz, 1.3 Hz, 2H, Ar-H fluorene), 7.23 (m, 8H, Ph-H), 7.09-6.94 (m, 24H, Ph-H, Ar-H fluorine, -CH=CH- imidazole), 5.51 (m, 4H, CH), 2.44 (m, 8H, CH₂), 1.94 (m, 8H, CH₂), 1.88-1.75 (m, 12H, CH₂-ethyl, CH₂-cyclohexyl), 1.59 (m, 16H, CH₂), 1.28 (m, 4H, CH₂), 0.29 (t, $J = 7.3$ Hz, 12H, CH₃), residual hexanes are present in the spectrum. ¹³C NMR (126 MHz, CD₂Cl₂): δ 169.2, 151.7, 149.9, 148.7, 147.0, 138.0, 137.9, 130.0, 129.6, 128.4, 125.7, 124.4, 124.1, 122.8, 120.3, 119.0, 117.0, 109.0, 106.8, 60.0, 56.3, 34.3, 33.2, 26.7, 26.2, 8.8. MALDI-TOF-MS (found) m/z . 1484.7692 [M]⁺ (calcd) 1484.7677.

CHAPTER 3

PLATINUM DIMERS LINKED BY ONE, TWO, OR THREE FLEXIBLE GROUPS FOR STUDY OF EXCITED STATE DYNAMICS

Background

For most platinum acetylide materials, it is not possible to achieve the high loading levels necessary to reach an energy saturation level suitable for commercial non-linear optical applications. Despite this, very few studies have looked at intramolecular deactivation, i.e. self-quenching via triplet-triplet annihilation (TTA), as a method of achieving saturation.⁸⁰ Thus a series of platinum(II) aryl-acetylide dimers containing one, two, or three sp^3 hybridized linking units were synthesized. The saturation levels of these dimers should ideally be half that of a system containing only a monomeric platinum acetylide chromophore, and so a model complex containing only a single platinum center was synthesized for comparison purposes. The structures of the four target complexes are shown in Figure 3-1.

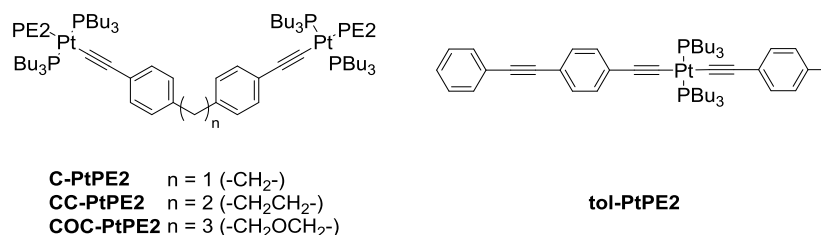


Figure 3-1. Structure of the target platinum acetylide dimers and mono-platinum model.

By using a series of dimers with varying tether length, inter- versus intra-molecular processes can be compared. The rationale being that intermolecular events are diffusion mediated, with no dependence on the tether. Conversely, intramolecular events will require that the chromophoric platinum acetylide ‘arms’ have some interaction with each other, whether this be through bond, through space, or co-facial overlap of the aromatic π -systems. Because the dimers are tethered via sp^3 hybridized

atoms, through bond interactions can presumably be ruled out. Furthermore, the dimers tethered with only one or two linking units are forced to have the chromophoric arms diverge from each other due to geometry restrictions, eliminating the possibility of a co-facial overlap and leaving through-space interactions as the only possibility for these two compounds. Transient absorption spectroscopy will be the primary probe for observing these deactivation processes.

As explained earlier, chromophores tethered by three linking units are capable of adopting a co-facial overlap. So in addition to studying TTA behavior, the platinum dimer that is tethered with three linking units may be able to adopt this conformation which would allow for the routine formation and study of a triplet excimeric state. Excimeric behavior has been observed in both solution³⁹ and solid state⁸¹ photophysics of platinum(II) complexes, and the nature of the excimer is not confined to solely ligand-ligand or metal-metal interactions.^{44, 81}

Contrary to most of the previous reports of excimeric Pt(II) species, the complexes studied in this report contain bulky tributylphosphine ancillary ligands. While the report of a Pt(II) aryl-acetylide complex which used trioctylphosphine ancillary ligands⁴⁴ may allow one to believe that the steric effects of these phosphines are negligible, the nature of the reported excimer is thought to be highly ligand localized with only some hindrance by phosphine ligands, rather than a system featuring interaction of the Pt d-orbitals. Additional evidence for the bulk of phosphine ligands inhibiting Pt-Pt interactions is shown by the Che Group, where a tridentate cyclometallated Pt(II) complex with triphenylphosphine (PPh₃) as the final ligand shows a Pt-Pt distance of > 4Å in the solid state, as the PPh₃ groups do not allow the platinum

atoms to approach each other.⁸¹ Interestingly, excimeric behavior is seen from the aforementioned system in the solid state because of weak interactions between the cyclometallating ligands. Again, this may lead one to believe that the system reported herein has a chance of intramolecular excimer formation through interactions of the aryl-acetylide ligands. However, the bulk of the phosphine ligands would prevent chromophore interaction as readily as it would prevent Pt-Pt interactions. Thus an excimer from the systems reported here are unlikely, but would represent a notable result.

Synthesis

Synthesis of the platinum dimers was started by making a series of three diarylacetylides of the form (4-(HCC)Ph)₂R, where R is -CH₂-, -CH₂CH₂-, or -CH₂OCH₂-. The synthetic scheme for these three targets is shown in Figure 3-2. The full synthesis of bis(4-ethynylphenyl)methane (**C-H**),⁸² and the individual compounds 1,2-bis(4-bromophenyl)ethane (**CC-Br**),⁸³ 1,2-bis(4-ethynylphenyl)ethane (**CC-H**),⁸⁴ and bis(4-bromobenzyl)ether (**COC-Br**)⁸⁵ have been previously reported. However, **COC-Br** was made by modification of a different method,⁸⁶ and reports and characterization data of **CC-H** in the journal literature are scarce, so both will be reported here.

In general, the diaryl halide is formed, followed by Sonogashira coupling with TMS-acetylene, and finally removal of the silyl protecting group to give the diarylacetylide. This was accomplished in various ways depending on the linking unit required. Bis(4-iodophenyl)methane (**C-I**) was made from bis(4-aminophenyl)methane via a Sandmeyer reaction. **CC-Br** was synthesized from 4-bromobenzyl bromide by inducing homocoupling of the methylene using 0.5 equivalents of iron powder and catalytic CuCl in hot water. Finally, **COC-Br** was formed by the S_N2 reaction of 4-

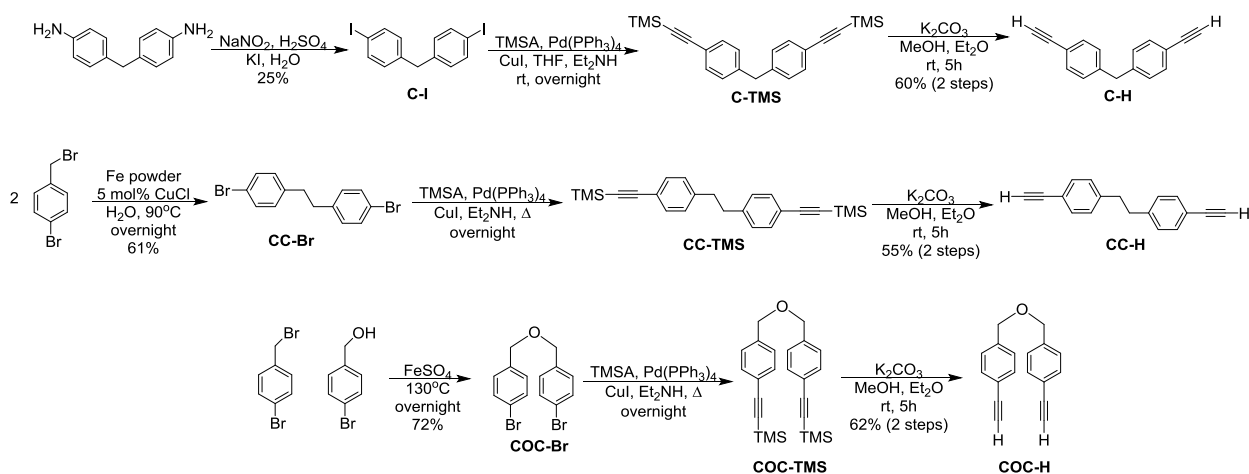


Figure 3-2. Synthesis of diarylacetylenes tethered by 1-3 flexibilizing units.

bromobenzyl bromide with 4-bromobenzyl alcohol. This reaction was done in the melt, using 5 equivalents of 4-bromobenzyl alcohol, relative to 4-bromobenzyl bromide, as the solvent and with 1 equivalent of FeSO_4 as a Lewis acid mediator. The yield of this reaction is reported as 72%; however, this is with respect to all organic compounds added to the reaction. This is because once all 4-bromobenzyl bromide has been consumed, excess 4-bromobenzyl alcohol proceeds to condense with itself to form additional ether product. Additionally, a monoarylacetylide, p-tolylacetylene, was synthesized in order to make a mono-platinum complex to be used as a model. Once the linking units were in hand, **PE2-Pt-Cl** was synthesized by a modified literature procedure.⁸⁷ The copper-free Hagihara reaction gives predominately monosubstituted platinum acetylide complexes. Thus, 1 equivalent of *cis*-(PBU_3)₂PtCl₂, and 0.95 equivalents of **PE2** were stirred overnight in diethylamine. The reaction does give a mixture of mono- and disubstituted products, which are difficult to separate for this system. The impure solid can be washed with methanol, as this will dissolve primarily the desired monosubstituted product, while leaving most of the disubstituted product behind. The filtrate can then be fully purified by chromatography with hexanes/ CH_2Cl_2 ,

making sure to exclude the initial fractions which will be contaminated with the disubstituted impurity. A final Hagihara coupling was then done to form the dimers and model complex in good yield. The Hagihara syntheses and model complex formation are shown in Figure 3-3. Novel platinum complexes were characterized by elemental analysis or mass spectrometry, as well as ^1H , ^{13}C , and ^{31}P NMR. Novel aryl-acetylide ligands were characterized by high resolution mass spectrometry (HRMS) rather than CHN analysis. The dimeric complexes are named by their linking unit, thus **C-PtPE2**, **CC-PtPE2**, and **COC-PtPE2** correspond to dimers with one, two, and three units, respectively. The model is named **tol-PtPE2**, and the entire series is **R-PtPE2**.

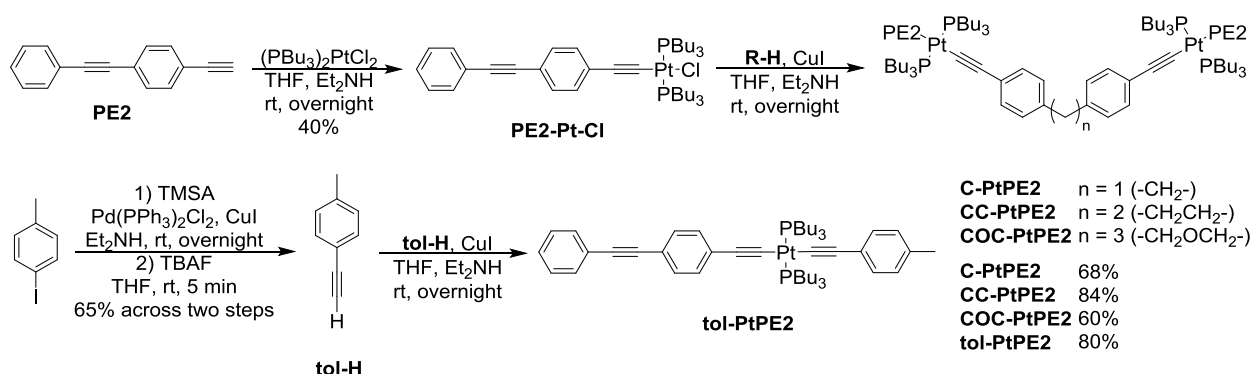


Figure 3-3. Synthesis of platinum diarylacetylides and a mono-platinum model complex.

Photophysical Properties

The normalized absorption, fluorescence, and phosphorescence spectra of **R-PtPE2** are shown in Figure 3-4. As expected, the normalized absorption spectra are virtually superimposable with maxima at 348 nm, and the extinction coefficients of the dimers are all within experimental error of each other. The extinction coefficients of the dimers are approximately double the extinction coefficient of **tol-PtPE2**, signifying that there is no electronic communication through the linking unit. The fluorescence spectra all show a peak around 379 nm. However, **C-PtPE2** shows an additional structured

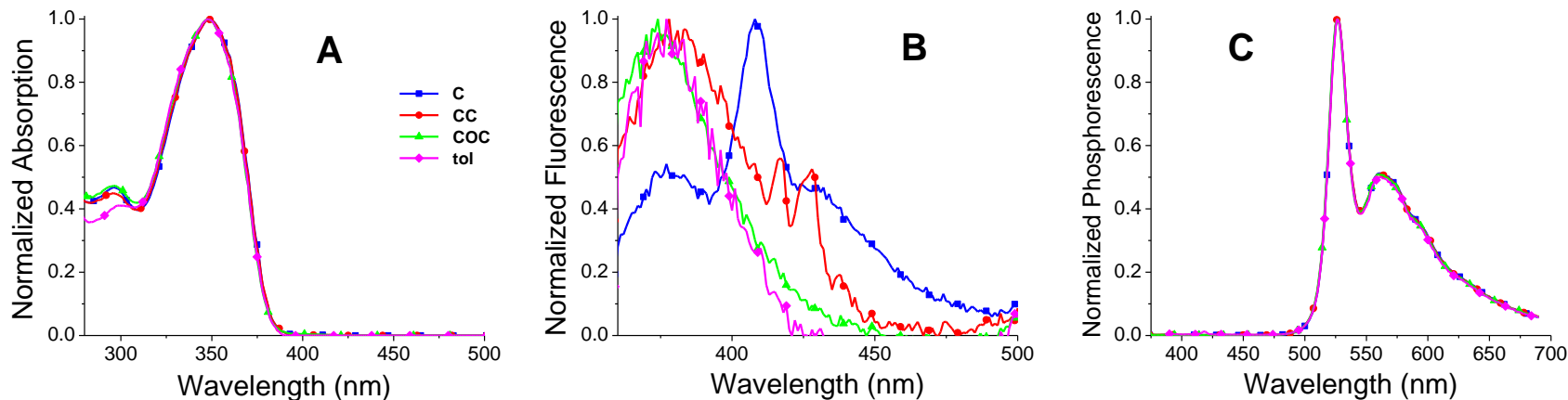


Figure 3-4. The A) ground state absorption, B) normalized fluorescence, and C) normalized phosphorescence spectra of **R-PtPE2** in THF. Excitation was at the ground state absorption maxima, and all plots were normalized.

Table 3-1. Summary of photophysical data for **R-PtPE2**.

Complex	Abs _{max} (nm)	ϵ (M ⁻¹ cm ⁻¹)	Fl _{max} (nm)	Φ_{Fl}^a	τ_{Fl} (ns)	Ph _{max} ^{a,b} (nm)	$\Phi_{Ph}^{a,b}$	τ_{Ph}^b (μ s)	TA _{max} ^b	$\tau_{T1-Tn}^{b,c}$ (μ s)
c	348	116000	409	0.0009	< 0.10 ^d	527	0.30	174	596	69.1
CC	348	107000	379	0.0005	< 0.10 ^d	527	0.26	168	598	65.5
COC	348	109000	379	0.0004	< 0.10 ^d	527	0.29	185	598	62.4
tol	348	57000	379	0.0003	< 0.10 ^d	526	0.34	169	595	61.7

^a Measured at RT using Ru(bpy)₃Cl₂ in aerated water ($\Phi_{fl} = 0.0379$) as a standard. ^b Samples degassed by five freeze-pump-thaw cycles on a high vacuum line. ^c All decay profiles can be found in Appendix D. ^d Lifetime is shorter than the lower threshold of the PicoQuant instrument, 100 ps.

peak at longer wavelengths. These spectra are all very noisy, as the fluorescence quantum yields of these complexes are less than 0.1%, and the fluorescence lifetimes are all less than 100 ps.

Conversion to the triplet state is very efficient in these complexes, and the intersystem crossing yield is nearly unity as shown by the minimal fluorescence quantum yields.^{1, 6} The normalized phosphorescence spectra of **R-PtPE2** are also nearly superimposable in both peak maximum and vibronic structure. The maxima for the dimers appear at 527 nm, while the maximum for the model at is at 526 nm. No observation of a broad emission to the red of the phosphorescence, which would indicate an excimeric state, is observed. Phosphorescence quantum yields are just under 30% for the dimers, and just over 30% for the model. Finally, the phosphorescence lifetimes are all single exponential and fall within the range of 175±10 μ s. All photophysical data for **R-PtPE2** can be found in Table 3-1.

A variety of transient absorption (TA) studies were done on solutions of **R-PtPE2**, with matched absorbances of 0.58 at 355 nm, in order to study the higher triplet excited states, determine energy saturation levels, and further probe potential excimer behavior. Figure 3-5 shows the principal components of the transient absorption for **R-PtPE2**. Like most platinum acetylide compounds, the TA shows a strong, broad feature across most of the visible region, and like the other **R-PtPE2** spectra, the line shape is virtually superimposable for all of the compounds. A normalized plot of the transient absorption is shown in Appendix D to illustrate this more clearly. Interestingly, the model complex shows approximately 35% less TA response at 180 μ J/pulse input energy, even though the chromophore concentration is identical to that of the dimers. The lifetimes recorded

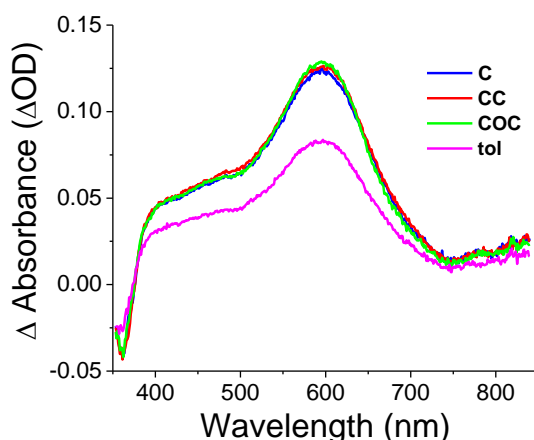


Figure 3-5. Principal component transient absorption spectra of **R-PtPE2**, with excitation at 355 nm, 10 ns pulse width, 180 $\mu\text{J}/\text{pulse}$ excitation energy. Solutions had an absorptivity value of 0.58 at 355 nm after five freeze-pump-thaw cycles.

at this pulse energy for all complexes fall in the 60 to 70 μs regime, and the full spectra with time slices recorded in 15 μs intervals can be found in Appendix D. However, with time slices of 15 μs , any potential excimer formation may not be detected as the lifetime of the PE2-octyl excimer was 1.4 μs .⁴⁴ The spectra for **COC-PtPE2** was recorded on a new solution, with 400 ns time slices, in an attempt to see any excimer formation, an expansion of the maxima is shown in Figure 3-6. While this spectrum appears to decay normally, the experimental noise actually moves the 3rd and 4th time slices above the initial measurement. This is also shown by the lack of an isobestic point, indicating that there is only one species present. Additionally, the experiment was rerun with even shorter time slices. Spectra recorded with 200 and 100 ns time slices confirmed that this observation was purely noise of the detector.

The next transient absorption experiment was a power dependence study to determine saturation levels, and is shown in Figure 3-7. Looking at the full graph, it is apparent that the mono-platinum model complex has a significantly higher saturation

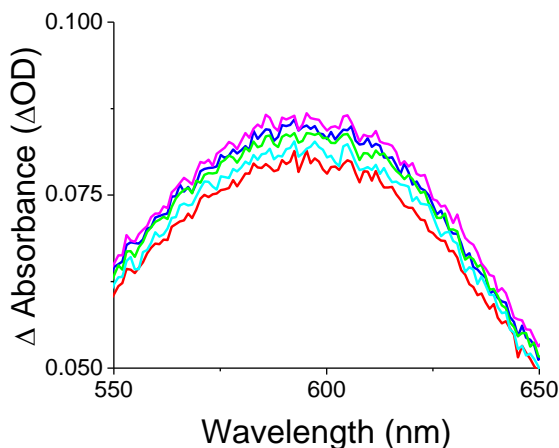


Figure 3-6. First five time slices of the transient absorption spectra of **COC-PtPE2** with a camera delay interval of 400 ns. Excitation was at 355 nm, with a 10 ns pulse width, and 180 $\mu\text{J}/\text{pulse}$ excitation energy. The solution had an absorptivity value of 0.56 at 355 nm after five freeze-pump-thaw cycles.

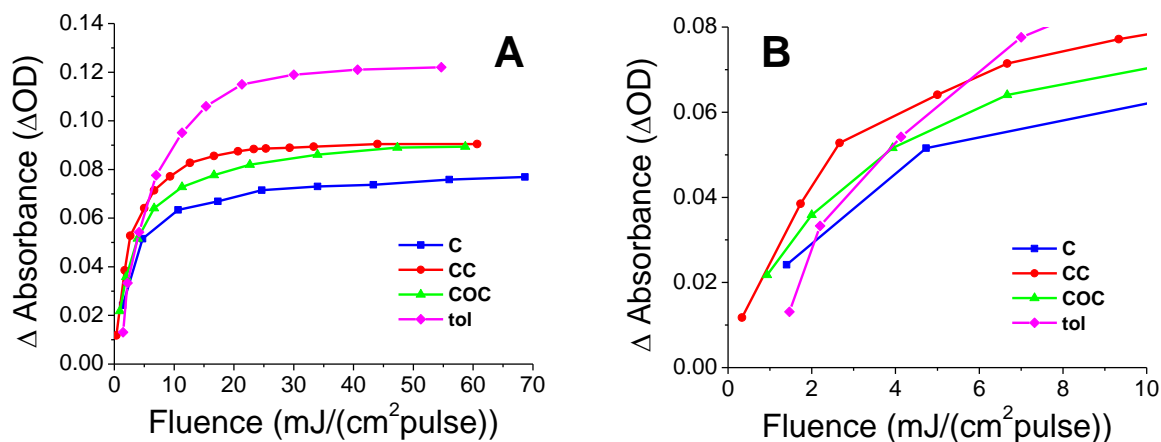


Figure 3-7. Transient absorption power dependence of A) **R-PtPE2** monitored at 550 nm, with B) an expansion of the low fluence region to show initial slopes. Solutions had a concentration of 5.5×10^{-6} M for the dimers, and 1.1×10^{-5} M for the model complex, resulting in an absorptivity value of 0.58 at 355 nm after five freeze-pump-thaw cycles.

level than the dimers. It is expected that a mono-platinum complex will have a higher saturation level than a dimeric complex because dimeric complexes may have both chromophores excited, which will then undergo decay via intramolecular triplet-triplet annihilation before triplet-triplet absorption can take place. What is unexpected, is that

C-PtPE2 has an approximately 15% lower saturation level than **CC-PtPE2** and **COC-PtPE2**. Also shown in Figure 3-7 is an expansion of the lowest fluence region of the power dependence study. The low energy region supports the previous data, shown in Figure 3-5, in that **tol-PtPE2** initially has a weaker TA response than the dimers.

Finally, the lifetime decay as a function of time and fluence for each complex was plotted to visually assess if there are any differences between the complexes. These data are shown in Figure 3-8, and upon initial inspection show similar decays to one another. The trend in lifetime decays was deconvoluted by normalizing the decay of each compound at the strongest fluence prior to decomposition ($61 \pm 7 \text{ mJ}/(\text{cm}^2\text{pulse})$) and plotting them on the same graph. The normalized data are shown in Figure 3-9, along with an expansion of the fast timescale data. The plots show **CC-PtPE2** and **COC-PtPE2** to have a nearly identical TA decay. This can be rationalized by the lack of any notable intramolecular interaction by the two chromophoric moieties in these two dimers. The fastest to decay is **tol-PtPE2**, and it has the same exponential decay properties as the aforementioned dimers with no sign of any perturbation. Contrary to the other compounds, the decay of **C-PtPE2** shows a faster decay component in the first 10 μs , before the primary, long, decay seen in the other complexes.

Further comparison is achieved by plotting the decays of **R-PtPE2** at both low and high fluence (1.7 ± 0.3 and $61 \pm 7 \text{ mJ}/(\text{cm}^2\text{pulse})$, respectively) on a logarithmic scale. These decays are shown in Figure 3-10. The logarithmic scale will help determine if any secondary processes are occurring in the system, as the traces will deviate from linearity if it is not a single exponential decay. At low fluence, the decays are nearly purely single exponential, meaning that the only process occurring is the

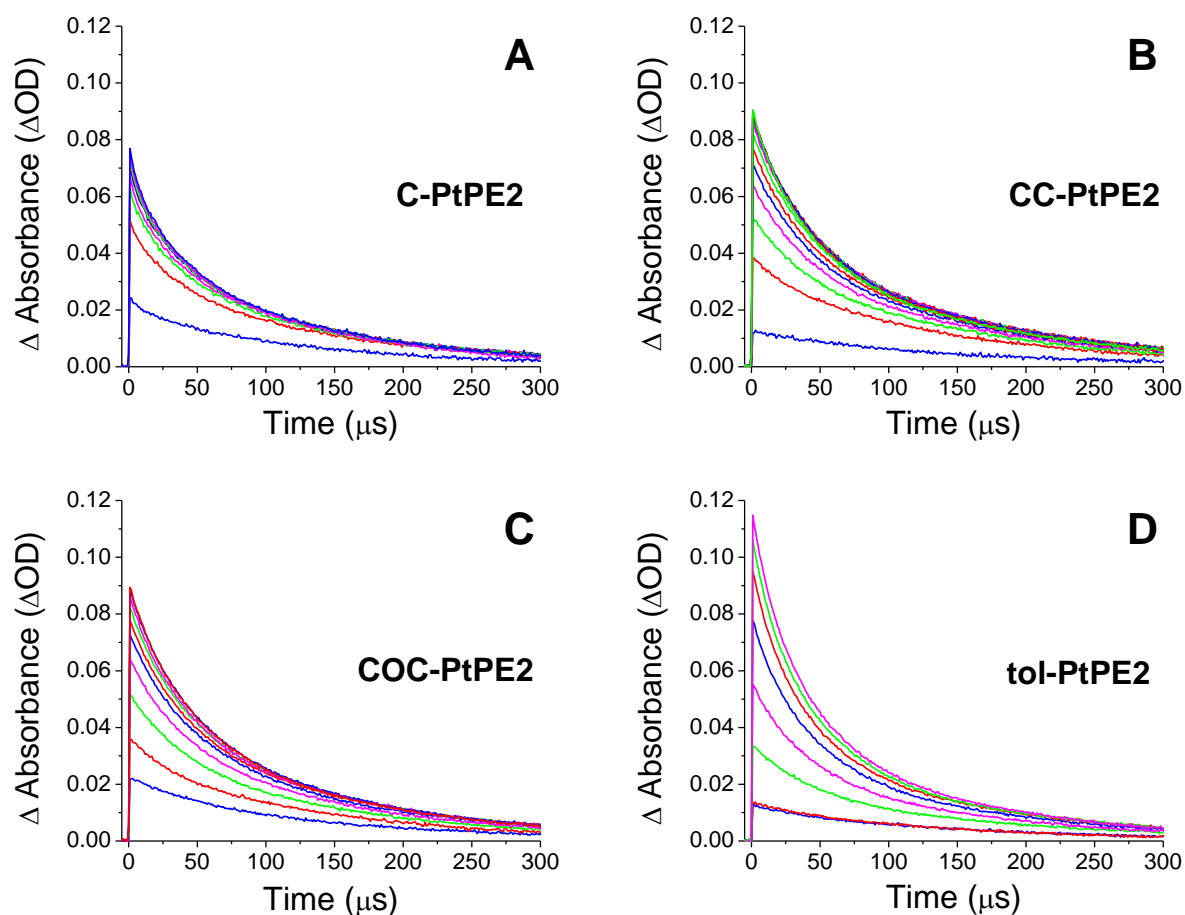


Figure 3-8. Transient absorption lifetime decays measured at 550 nm with variable fluence. A) **C-PtPE2**. B) **CC-PtPE2**. C) **COC-PtPE2**. D) **tol-PtPE2**.

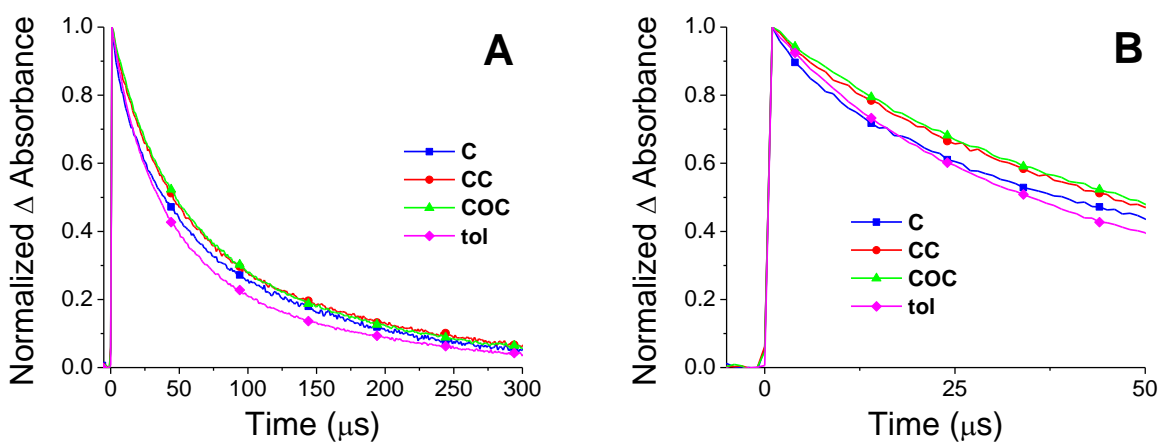


Figure 3-9. A) Normalized transient absorption lifetime decays measured at 550 nm of the strongest fluence measured for **R-PtPE2** (61 ± 7 mJ/(cm²pulse)), with B) an expansion of the early timescale region to show initial slopes.

unimolecular decay of the excited triplet state. At high fluence, the plotted decays deviate from linearity, indicating contributions from bimolecular processes. Because all of the complexes in the **R-PtPE2** series display this behavior, it is believed to be diffusion mediated intermolecular triplet-triplet annihilation. Due to the smaller size of **tol-PtPE2**, it should have a greater diffusion rate, which leads to its diffusion rate being the fastest of the series. Having assigned the intermolecular TTA process to a slow, diffusion mediated process, one may then want to assign the tertiary decay component of **C-PtPE2** (observed in the first 10 μs) to intramolecular TTA. A structurally similar system was previously synthesized by the Schanze Group featuring a tetrakis(Pt(II)-arylacetylde)methane motif,⁸⁸ which showed strong TTA via intramolecular(through-space) pathways, and saturation levels of just over 25% of a mono-platinum model complex. However, this process was shown to take place on the timescale of 10's of nanoseconds, rather than microseconds.

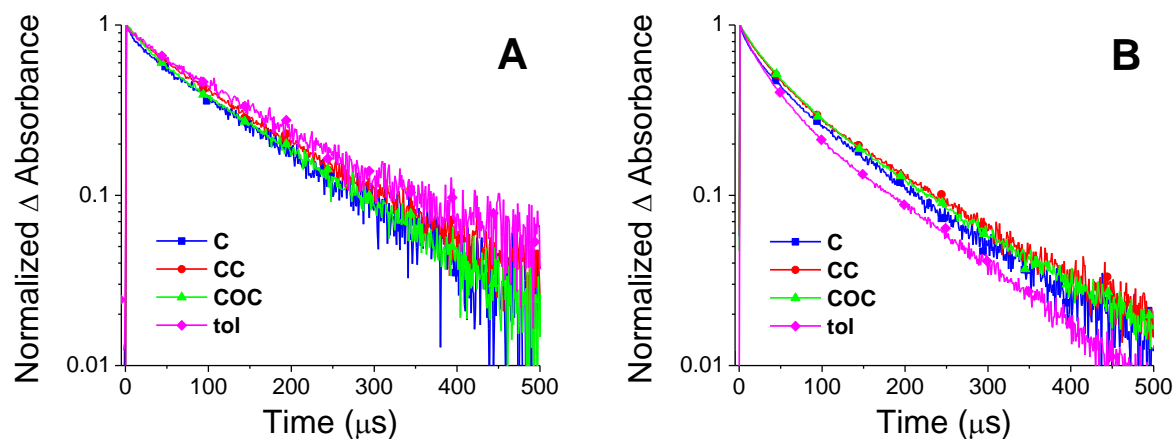


Figure 3-10. Normalized transient absorption lifetime decays measured at 550 nm for **R-PtPE2** on a logarithmic scale at A) low fluence ($1.7 \pm 0.3 \text{ mJ}/(\text{cm}^2 \text{ pulse})$), and B) high fluence ($61 \pm 7 \text{ mJ}/(\text{cm}^2 \text{ pulse})$).

Molecular Dynamics Simulations

To provide further evidence for the hypothesis that **COC-PtPE2** does not show excimeric behavior due to steric factors, molecular dynamics (MD) simulations were invoked. The MD simulation places the optimized molecule in a solvent box at a fixed temperature (298 K for these simulations) and allows the molecule to move freely for a user defined amount of time. Exact details of the geometry optimization and MD procedure are given in the experimental section. A histogram can then be made by recording the distance between platinum centers at each step, thus giving a probability function. Histograms for each dimer are given in Figure 3-11, the DFT optimized structures are shown in Figure 3-12, and representative structures from the MD simulations are shown in Appendix D. The gas phase DFT optimized structures match the predictions of the histograms well for **C-PtPE2** and **CC-PtPE2**, but the structure of **COC-PtPE2** gives a Pt-Pt bond distance 1 Å shorter than what MD simulations would suggest. The deviation between DFT optimized gas phase structure and the MD probability is likely due to stabilization of the anomeric effect in THF solution.

Upon closer inspection of each histogram, it appears that **C-PtPE2** and **CC-PtPE2** maintain the divergent nature of their chromophoric arms, as they were expected to, while **COC-PtPE2** seems incapable of overcoming the rotational energy barrier to adopt a co-facial orientation. **C-PtPE2** shows a broad distribution of distances, from 13 to 16 Angstroms, which can be assigned to rotations of the chromophore arms and distortion of the angle between the chromophores, centered on the linking methylene. **CC-PtPE2** gives a much narrower distribution, centered at 18.5 Angstroms. This is due to the chromophores adopting an *anti*-conformation about the ethylene linking unit and

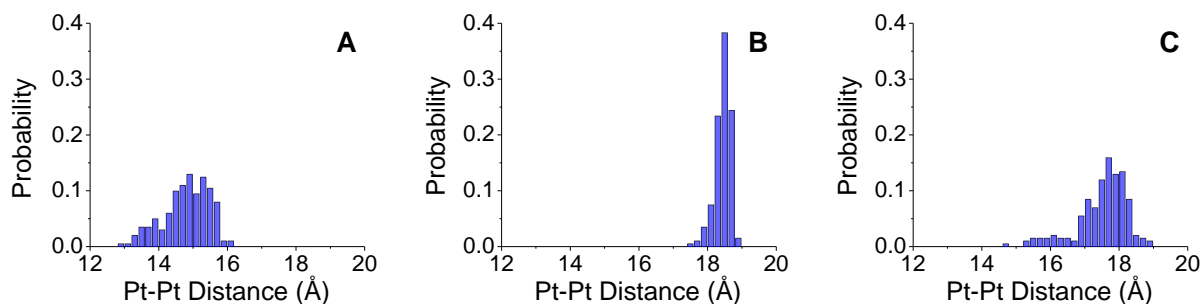


Figure 3-11. Histograms showing the probability of the internuclear Pt-Pt distance for A) **C-PtPE2**, B) **CC-PtPE2**, and C) **COC-PtPE2**.

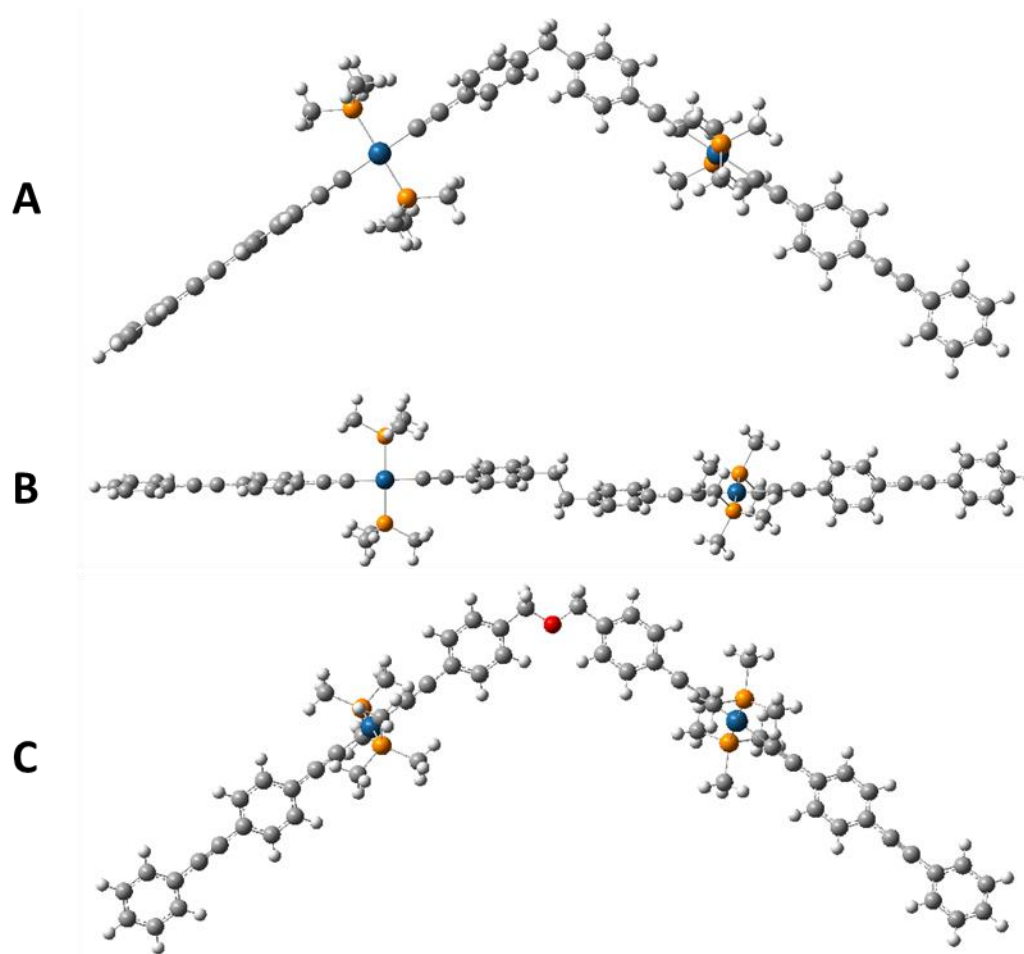


Figure 3-12. DFT optimized gas phase structures of A) **C-PtPE2**, B) **CC-PtPE2**, and C) **COC-PtPE2**.

deviating only slightly from it. Finally, **COC-PtPE2** shows a bimodal distribution, as the dimethylene ether tether allows for greater rotational freedom. The major distribution,

centered just under a Pt-Pt distance of 18 Angstroms, represents an *anti*-configuration about both carbon oxygen bonds. A very minor distribution is also present, and in the vicinity of 16 Angstroms. This set of conformations is the result of one of the chromophores rotating so that the bonds of the linking unit have now adopted a *syn-anti* motif. A simplified drawing of the three possible rotational isomers for the –COC– linking unit are shown in Figure 3-13. It should be noted here that the –COC– linking unit may be affected by the anomeric effect, but the overall contribution is minimal at most based on the photophysical results and dihedral angles centered on the C-O bonds. Despite being able to adopt conformations where one chromophore has rotated to the *syn* position, the MD simulation does not generate any structure where the Pt-Pt distance is less than 14 Angstroms. Thus, even an approach to the *syn-syn* conformer is not found to be populated in the ground state, which implies that co-facial overlap would be difficult to achieve in the excited state as well.

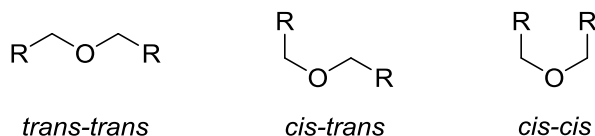


Figure 3-13. Representative drawings of the *anti-anti*, *syn-anti*, and *anti-anti* rotational isomers of **COC-PtPE2**.

Summary and Conclusions

In summary, a series of three platinum(II) aryl-acetylide dimers with one, two, or three linking units were synthesized and their photophysics were fully characterized. Additionally, a mononuclear platinum complex was synthesized and characterized to serve as a model complex. The absorption spectra of all four complexes were qualitatively identical, which shows that there is no electronic communication through

the sp^3 hybridized linking unit(s). This is further supported by the extinction coefficient of the dimers being double that of the model complex (within experimental error).

Looking at the emission spectra, all four complexes show very weak fluorescence ($\Phi < 0.1\%$), which is attributed to highly efficient intersystem crossing. The structure of this emission is broad and featureless for **CC-PtPE2**, **COC-PtPE2**, and **tol-PtPE2**, which is common for the PE2 chromophore. However, **C-PtPE2** shows an emission with pronounced vibronic structure. A possible explanation for this phenomenon is that the chromophoric arms of **C-PtPE2** are not able to rotate nearly as easily as the other dimers, leading to a more well-defined emission. Moving to the phosphorescence, the spectra of all four complexes are once again virtually superimposable and show strong vibronic structure. This is due to the localization of the triplet on a single PE2 chromophore. Phosphorescence quantum yields of the dimers are 30% or slightly less, while the model complex shows a slightly stronger emission (34%). The lifetimes of the four complexes all fall within experimental error of each other ($175 \pm 10 \mu s$); which provides further support for the localization of the triplet. No extra emission bands that could be assigned to a possible excimeric state were observed in aerated, nor freeze-pump-thaw degassed solution. This is not a surprise, as the PE2-octyl excimer did not show any radiative decay.⁴⁴

Following the one-photon photophysics, transient absorption was then studied to observe triplet-triplet and possible excimer absorption. Initially studied was the broad spectrum TA, measured at multiple time slices. Again, the band shape of all four complexes was indistinguishable from one another, but the intensity of the model complex was drastically weaker at the studied energy. Initially, the camera delay

increment was set to 15 μ s so lifetime data could be obtained, and the triplet-triplet lifetimes all fall within the 60-70 μ s regime. The camera delay increment was then set to take spectra every 400 ns, to search for any fast components that would be indicative of excimer formation, but no sign of any secondary species was observed. The steric environment generated by the alkyl phosphines is presumed to prevent any close Pt-Pt interactions or co-facial overlap that would allow an excimeric state to form in this complex. The previously studied PE2-octyl complex is capable of forming an excimer despite its bulky phosphine ligands because the PE2 ligands are still allowed to overlap significantly, and even interact with the platinum center.

Regardless of the previous result, TA power dependence was studied, as these compounds should show good saturation behavior due to their dimeric structure. This behavior is indeed seen, as the dimers saturate at a Δ OD of ~75% that of the model complex when pumped at a fluence of 61 ± 7 mJ/(cm²pulse). Further study of the power dependence relied on observing variances of the decay of each complex as fluence was increased. At low fluence, the decay is nearly single exponential, corresponding to the unperturbed spontaneous decay. As the fluence was increased, triplet-triplet annihilation became more pronounced in all complexes. The rate of this deactivation process is nearly identical for all complexes, leading it to be assigned to diffusion mediated intermolecular TTA. However, **C-PtPE2** also displays a fast decay component which also becomes more prominent as fluence increases, which is not found in any of the other complexes. This fast decay is still too slow to be intramolecular TTA, on the basis of previous studies within the Schanze Group showing the aforementioned process is completed within tens of nanoseconds.

Molecular dynamics simulations were used to study the molecular geometry in solution conditions. Histograms of the internuclear Pt-Pt distance for **C-PtPE2** and **CC-PtPE2** show a single distribution and minimal deviation from the optimized gas-phase geometries. Simulations on **COC-PtPE2** give a bimodal distribution. The major distribution is centered slightly under the maximum achievable Pt-Pt distance, representing a conformation where the two chromophoric arms are slightly deviated from the *anti-anti* conformer. The minor distribution only brings the platinum centers a couple Angstroms closer and is assigned a half-folded *syn-anti* rotational isomer. No evidence of the *syn-syn* isomer, and therefore co-facial overlap, was observed at any time during the simulation. Although no excimeric species was observed, this work demonstrates the ability of platinum dimers to serve as potential agents for power limiting applications.

Experimental

General Remarks

All reactions were carried out under argon atmosphere. All starting chemicals used for the synthesis of the *trans* platinum acetylide complexes were purchased from commercial suppliers, reagent grade, and used without additional purification. K_2PtCl_4 was purchased from Strem Chemicals. Solvents were of reagent grade unless otherwise noted. **PE2-Pt-Cl** was synthesized by a modified literature method.⁸⁷ Chromatography was done on a CombiFlash Rf 150 Medium Pressure Liquid Chromatography (MPLC) system. 1H (500 MHz) and ^{13}C (125.7 MHz) NMR spectra were recorded on a Varian Inova spectrometer. ^{31}P (121 MHz) NMR spectra were recorded on a Varian Mercury spectrometer. The chemical shifts were reported in ppm relative to tetramethylsilane (TMS) or residual solvent peaks. Elemental analysis was

performed by Complete Analysis Laboratories, Inc. Mass spectrometry was performed in house by Mass Spectrometry Services at the University of Florida.

Absorption and Emission Spectroscopy

Steady-state absorption spectra were recorded on a Varian Cary 50 spectrophotometer. Corrected steady-state emission measurements were performed on a Photon Technology International spectrophotometer (QuantaMaster). Absorption and fluorescence samples were carried out in aerated solution, while phosphorescence samples were deaerated with five freeze-pump-thaw cycles. Optically dilute samples with O.D. < 0.1 at the excitation wavelength were used. Fluorescence and phosphorescence quantum yields were determined by relative actinometry, with Ru(bpy)₃Cl₂ as an actinometer ($\Phi_{\text{FI}} = 0.0379$ in air saturated water).⁷⁰

Phosphorescence lifetimes were obtained with a multichannel scaler/photon counter system with a NanoQuant FluoTime 100 Compact Phosphorescence Lifetime Spectrophotometer. A UV-pulsed diode laser provided the excitation at 375 nm (power < 10 mW). The laser was pulsed by a PDL800-B, which is a pulsed diode laser driver. Optically dilute solutions were freeze-pump-thawed five times. All decays were obtained using single exponential fitting parameters (FluoFit software).

Nanosecond Transient Absorption (TA) Spectroscopy

Measurements were performed on an in-house apparatus that is described in detail elsewhere.⁷⁷ The third harmonic of a Continuum Surelite series Nd:YAG laser ($\lambda = 355$ nm, 10 ns fwhm, 180 $\mu\text{J-pulse}^{-1}$) was used as the excitation source. Probe light was produced by a xenon flash lamp and the transient absorption signal was detected with a gated-intensified CCD mounted on a 0.18 M spectrograph (Princeton PiMax/Acton Pro 180). Solutions had a matching optical density of 0.58 after five freeze-

pump-thaw cycles. An initial CCD image capture delay of 100 ns following the laser pulse was used to ensure full conversion to the triplet state before observation. An average of 100 images were acquired and the laser energy was 180 $\mu\text{J}/\text{pulse}$, which was established as being sufficiently low to minimize triplet-triplet power dependence.

Transient Absorption Power Dependence

The third harmonic of a Surelite I-10 Nd:YAG laser ($\lambda = 355 \text{ nm}$, 10 ns fwhm) was used as the excitation source. Probe light was produced by a Xenon arc lamp and the transient absorption signal was detected at a single wavelength (550 nm) using a Triax 180 monochromator and a Si-amplified photodetector from Thorlabs (PDA8A).

Computational Details

Structure optimization

DFT calculations were performed in the Gaussian 09, revision C.01,⁷³ suite of programs at the B3LYP level with the 3-21G basis set for C, H, O, the 6-31G(d) basis set for P, and the SDD basis set for Pt. Phosphine butyl groups were replaced by methyl groups to improve computational efficiency. The ground state structures were optimized in the gas phase from idealized starting configurations without symmetry constraints. The optimized structures were confirmed to be minima by the lack of imaginary frequencies.

Molecular dynamics calculations

Fully-atomistic molecular dynamics simulations were performed using the Forcite module in the Materials Studio 6.0 software package. The dimers were packed inside of a cell that was approximately 10 Å larger than each dimension of the gas-phase dimer, while the remaining volume was packed with 200 tetrahydrofuran (THF) solvent molecules to give a total density of 0.889 g/cm^3 . Atomic charges (Natural Population

Analysis) for each dimer and THF molecule were obtained from the Gaussian DFT calculations. The packed cell was annealed for 5 temperature cycles ranging from 300 to 700 K for a total time of 250 ps using the Universal Force Field (UFF). The annealed simulation cells were used for molecular dynamics calculations with the canonical ensemble, NVT, at a temperature of 298 K controlled by the Nose thermostat with a Q-ratio of 0.01. Dynamics were calculated for a total of 1 ns for each dimer and snapshots were collected every 5 ps.

Synthesis of bis(4-bromobenzyl) ether (COC-Br)

4-Bromobenzyl alcohol (4.7 g, 25 mmol, 13.5 eq.), 4-bromobenzylbromide (0.46 g, 1.8 mmol, 1 eq.), and $\text{FeSO}_4 \cdot 7\text{H}_2\text{O}$ (0.52 g, 1.8 mmol, 1 eq.) were added to a 50 mL round bottom flask. The flask was equipped with a Vigreux column, and the mixture was heated to 130°C. The melt was allowed to react overnight before being cooled to room temperature. The resulting off-white solid was dissolved in CH_2Cl_2 , insolubles were removed by filtration, and the solvent was evaporated. The solid was suspended in a minimum of methanol, and the slurry was filtered to afford pure **COC-Br**. Yield 72%. Mp: 81°C. ^1H NMR (500 MHz, CD_2Cl_2): δ 7.47 (d, J = 8.0 Hz, 4H), 7.21 (d, J = 8.0 Hz, 4H), 4.48 (s, 4H). ^{13}C NMR (126 MHz, CD_2Cl_2): δ 137.2, 131.8, 129.6, 121.8, 71.7.

General Procedure for the Sonogashira Coupling Reaction

The dibromo linking unit (**R-Br**, 0.15 g, 1 eq.) was added to 15 mL of Et_2NH in a 25 mL seal tube. The solution was degassed with argon for 15 minutes before $\text{Pd}(\text{PPh}_3)_4$ (20 mol%, 0.10 eq) and CuI (20 mol%, 0.10 eq.) was added. The solution was bubbled for an additional 10 minutes before trimethylsilylacetylene (0.5 mL, 3.5 mmol, 5 eq) was added, and the tube was sealed. The solution was heated to reflux and allowed to react overnight. The solution was poured into water and extracted with

CH₂Cl₂. The organic layer was separated, filtered through Na₂SO₄, the filtrate was reduced to a minimum, and it was loaded onto silica gel. Purification of both **CC-TMS** and **COC-TMS**, via MPLC using hexanes and hexanes/ethyl acetate, respectively, gave pure product. Additional product with ~10% impurity was also isolated via MPLC, and can be included in further reactions.

1,2-bis(4-(trimethylsilylethynyl)phenyl)ethane (CC-TMS)

Mp: 141°C. ¹H NMR (500 MHz, CDCl₃): δ 7.35 (d, *J* = 8.0 Hz, 4H), 7.02 (d, *J* = 8.0 Hz, 4H), 2.87 (s, 4H), 0.24 (s, 18H). ¹³C NMR (126 MHz, CDCl₃): δ 142.1, 132.2, 128.7, 120.9, 105.4, 93.8, 37.7. Mass Spec. DART-MS (found) *m/z* 392.2225 [M+NH₄]⁺. (calcd) 392.2224 [M+NH₄]⁺.

Bis(4-(trimethylsilylethynyl)benzyl) ether (COC-TMS)

Mp: 120°C. ¹H NMR (500 MHz, CD₂Cl₂): δ 7.43 (d, *J* = 8.5 Hz, 4H), 7.02 (d, *J* = 8.5 Hz, 4H), 4.54 (s, 4H), 0.24 (s, 18H). ¹³C NMR (126 MHz, CD₂Cl₂): δ 139.6, 132.4, 128.1, 122.9, 105.3, 94.7, 72.4. Mass Spec. DART-MS (found) *m/z* 408.2178 [M+NH₄]⁺. (calcd) 408.2173 [M+NH₄]⁺.

General Procedure for the TMS Deprotection Reaction

The TMS protected diarylacetylides (**R-TMS**) were dissolved in 50 mL of 1:1 methanol:diethyl ether, and the solution was degassed with argon for 25 minutes. K₂CO₃ (1 g) was then added, and the mixture was stirred at in the dark and at room temperature for 5 hours. After this time, the mixture was poured into water and extracted with CH₂Cl₂. The organic layer was separated, filtered over Na₂SO₄, the filtrate was reduced to a minimum, and it was loaded onto silica gel. Purification of both **CC-H** and **COC-H**, via MPLC using hexanes and hexanes/ethyl acetate, respectively, afforded the pure products as white solids.

1,2-bis(4-ethynylphenyl)ethane (CC-H)

Yield across two steps: 55%. ^1H NMR (500 MHz, CD_2Cl_2): δ 7.38 (d, J = 8.0 Hz, 4H), 7.11 (d, J = 8.0 Hz, 4H), 3.09 (s, 2H), 2.92 (s, 4H). ^{13}C NMR (126 MHz, CD_2Cl_2): δ 143.1, 132.6, 129.1, 120.2, 84.1, 77.1, 37.9.

Bis(4-ethynylbenzyl) ether (COC-H)

Yield across two steps: 62%. Mp: 68°C. ^1H NMR (500 MHz, CD_2Cl_2): δ 7.48 (d, J = 8.0 Hz, 4H), 7.33 (d, J = 8.0 Hz, 4H), 4.56 (s, 4H), 3.13 (s, 2H). ^{13}C NMR (126 MHz, CD_2Cl_2): δ 139.9, 132.6, 128.1, 121.8, 83.9, 77.6, 72.4. Mass Spec. DART-MS (found) m/z 264.1390 $[\text{M}+\text{NH}_4]^+$. (calcd) 264.1383 $[\text{M}+\text{NH}_4]^+$.

Synthesis of monosubstituted platinum precursor *trans*-(PBu_3)₂Pt(PE2)Cl (PE2-Pt-Cl)

To a flask charged with 30 mL of Et_2NH , *cis*-(PBu_3)₂PtCl₂ (0.35 g, 0.52 mmol, 1 eq.) was added, and the solution was bubbled with argon for 25 minutes. **PE2** (0.10 g, 0.49 mmol, 0.95 eq.) was added, and reaction mixture was then stirred overnight, at room temperature, in the dark. The final mixture was poured into water and extracted with dichloromethane. The organic layer was separated, filtered over Na_2SO_4 , and the solvent was evaporated. The resulting solid was washed with copious MeOH, the filtrate was collected, reduced to a minimum, and loaded onto silica gel. Purification via MPLC using hexanes/dichloromethane afforded pure **PE2-Pt-Cl** as a clear oil. Yield 38% ^1H NMR matched that of the literature.⁸⁹

Synthesis of model complex *trans*-(PBu_3)₂Pt(PE2)(CC-p-tolyl) (tol-PtPE2)

To a flask charged with 30 mL of Et_2NH , **PE2-Pt-Cl** (0.135 g, 0.16 mmol, 1 eq.) was added. The solution was then bubbled with argon for 15 minutes before addition CuI (0.005 g) and 0.026 g 4-(tolyl)acetylene (0.026 g, 0.22 mmol, 1.35 eq.) was added.

The reaction mixture was then stirred overnight at room temperature, in the dark. The final mixture was poured into water and extracted with dichloromethane. The organic layer was separated, filtered over Na₂SO₄, the filtrate was reduced to a minimum, and it was loaded on to silica gel. Purification via MPLC using hexanes/ethyl acetate afforded pure **tol-PtPE2** as an off-white solid. Yield 80% Mp: 100°C. ¹H NMR (500 MHz, CDCl₃): δ 7.54 (d, *J* = 7.5 Hz, 2H, Ph-H, PE2 terminal), 7.42-7.31 (m, 5H, Ph-H, PE2 terminal & tolyl), 7.25 (d, *J* = 8.0 Hz, 2H, Ph-H, tolyl), 7.19 (d, *J* = 8.0 Hz, 2H, Ph-H, PE2 internal), 7.04 (d, *J* = 8.0 Hz, 2H, Ph-H, PE2 internal), 2.29 (s, 3H, tolyl), 2.13 (m, 12H, CH₂), 1.60 (m, 12H, CH₂), 1.44 (sextet, *J* = 7.5 Hz, 12H, CH₂), 0.92 (t, *J* = 7.5 Hz, 18H, CH₃). ¹³C NMR (126 MHz, CDCl₃): δ 134.7, 131.7, 131.4, 130.89, 130.83, 129.5, 128.8, 128.5, 128.2, 126.2, 123.8, 119.3, 109.3, 109.1, 90.3, 89.9, 26.6, 24.6 (t, *J*^{Pt-C} = 6.8 Hz), 24.1 (t, *J*^{Pt-C} = 17.1 Hz), 21.5, 14.1. ³¹P NMR (121 MHz, CDCl₃) 3.07 (*J*^{Pt-P} = 2350 Hz). ESI-TOF-MS (found) *m/z* 916.4654 [M+H]⁺. (calcd) 916.4683 [M+H]⁺.

General Procedure for the Hagihara Coupling Reaction for Platinum Dimers.

PE2-Pt-Cl (0.100 g, 0.11 mmol, 1 eq.) was dissolved in 20 mL of Et₂NH, and the solution was degassed with argon for 15 minutes. CuI (0.005 g) and 0.95 equivalents of the deprotected diarylacetylene were added. The solution was allowed to react overnight at room temperature, in the dark. The resulting mixture was poured into water and extracted with CH₂Cl₂. The organic layer was separated, filtered over Na₂SO₄, the filtrate was reduced to a minimum, and it was loaded on to silica gel. Purification of **R-PtPE2** via MPLC using hexanes/ethyl acetate afforded the pure products as a semi-transparent oil. Microcrystalline product can be obtained by dissolving the compound in acetone and adding to methanol to give an off-white precipitate.

***trans*-[(PE2)Pt(PBu₃)₂(CC-*p*-Ph)]₂CH₂ (C-PtPE2)**

Yield 68% Mp: 89°C. Anal. Calcd for C₉₇H₁₃₆P₄Pt₂: C, 64.15; H, 7.55. Found: C, 64.01; H, 7.32. ¹H NMR (500 MHz, CDCl₃): δ 7.51 (d, *J* = 8.0 Hz, 4H, Ph-H, PE2 terminal), 7.38-7.28 (m, 10H, Ph-H, PE2 terminal & tether), 7.22 (d, *J* = 8.5 Hz, 4H, Ph-H tether), 7.18 (d, *J* = 8.0 Hz, 4H, Ph-H, PE2 internal), 7.00 (d, *J* = 8.0 Hz, 4H, Ph-H, PE2 internal), 3.86 (s, 2H, CH₂, tether), 2.12 (m, 24H, CH₂), 1.60 (m, 24H, CH₂), 1.44 (sextet, *J* = 7.5 Hz, 24H, CH₂), 0.92 (t, *J* = 7.5 Hz, 36H, CH₃). ¹³C NMR (126 MHz, CDCl₃): δ 138.0, 131.7, 131.4, 131.0, 130.9, 129.5, 128.7, 128.5, 128.2, 126.9, 123.8, 119.3, 109.3, 109.1, 90.3, 89.9, 41.8, 26.6, 24.6 (t, *J*^{Pt-C} = 6.8 Hz), 24.1 (t, *J*^{Pt-C} = 17.2 Hz), 14.1. ³¹P NMR (121 MHz, CDCl₃) 3.05 (*J*^{Pt-P} = 2350 Hz).

***trans*-[(PE2)Pt(PBu₃)₂(CC-*p*-Ph)]₂-1,2-ethane (CC-PtPE2)**

Yield 84% Mp: 148°C. ¹H NMR (500 MHz, CDCl₃): δ 7.52 (d, *J* = 8.0 Hz, 4H, Ph-H, PE2 terminal), 7.38-7.34 (m, 10H, Ph-H, PE2 terminal & tether), 7.22 (d, *J* = 8.5 Hz, 4H, Ph-H tether), 7.16 (d, *J* = 8.0 Hz, 4H, Ph-H, PE2 internal), 7.02 (d, *J* = 8.0 Hz, 4H, Ph-H, PE2 internal), 2.84 (s, 4H, CH₂, tether), 2.13 (m, 24H, CH₂), 1.62 (m, 24H, CH₂), 1.46 (sextet, *J* = 7.5 Hz, 24H, CH₂), 0.94 (t, *J* = 7.5 Hz, 36H, CH₃). ¹³C NMR (126 MHz, CDCl₃): δ 139.2, 131.9, 131.7, 131.2, 131.1, 130.1, 129.0, 128.7, 128.6, 127.2, 124.1, 119.6, 109.34, 109.28, 90.4, 90.2, 38.2, 26.9, 25.0 (t, *J*^{Pt-C} = 6.8 Hz), 24.5 (t, *J*^{Pt-C} = 17.3 Hz), 14.2. ³¹P NMR (121 MHz, CDCl₃) 3.27 (*J*^{Pt-P} = 2340 Hz).

***trans*-[(PE2)Pt(PBu₃)₂(CC-*p*-Benzyl)]₂O (COC-PtPE2)**

Yield 60% Mp: 83°C. C₉₈H₁₃₈OP₄Pt₂: C, 63.76; H, 7.53. Found: C, 63.66; H, 7.21. ¹H NMR (500 MHz, CDCl₃): δ 7.52 (m, 4H, Ph-H), 7.39-7.32 (m, 10H), 7.26-7.18 (m, 12H), 4.47 (s, 4H, CH₂, tether), 2.13 (m, 24H, CH₂), 1.62 (m, 24H, CH₂), 1.46 (sextet, *J* = 7.5 Hz, 24H, CH₂), 0.93 (t, *J* = 7.5 Hz, 36H, CH₃). ¹³C NMR (126 MHz, CDCl₃): δ

135.7, 131.9, 131.7, 131.2, 131.1, 130.0, 129.0, 128.7, 128.1, 124.1, 119.6, 113.3
109.4, 109.3, 90.4, 90.2, 72.5, 26.9, 25.0 (t, $J^{\text{Pt-C}} = 6.8$ Hz), 24.5 (t, $J^{\text{Pt-C}} = 17.3$ Hz),
14.2. ^{31}P NMR (121 MHz, CDCl_3) 3.32 ($J^{\text{Pt-P}} = 2340$ Hz).

CHAPTER 4

PHOTOPHYSICAL PROPERTIES OF COMPLEXES FEATURING A MIXED ARYL-PLATINUM-ACETYLIDE CHROMOPHORE MOTIF

Background

As the class of disubstituted platinum(II) chromophores featuring one aryl ligand (R₂Ar-[Pt]) and one acetylide ligand (ArCC-[Pt]) is highly unknown, the goal of the work presented in this chapter is to synthesize and fully characterize the photophysical properties of a series of four mixed complexes using the aryl ligands 2-(9,9-Diethyl-9H-fluorene)benzo[d]thiazole (BTF) and 9,9-Diethyl-N,N-diphenyl-9H-fluoren-2-amine (DPAF) as well as the acetylide congeners of the aryl ligands: 2-(9,9-Diethyl-9H-fluoren-7-yl)benzo[d]thiazole (CCBTF) and 9,9-Diethyl-7-ethynyl-N,N-diphenyl-9H-fluoren-2-amine (CCDPAF). Structures of the four target complexes are shown in Figure 4-1.

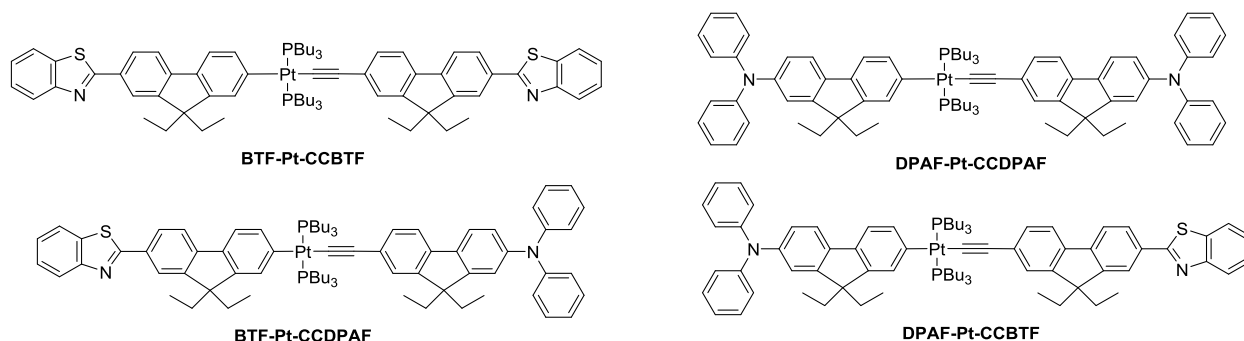


Figure 4-1. The four combinations of platinum aryl/acetylide complexes featuring DPAF and BTF chromophores.

These chromophores were chosen as they have been well studied in platinum acetylide complexes,² and because they show competing excited state properties, as the BTF chromophore is a π -acceptor, and the DPAF chromophore is a π -donor. Based on the nature of the π -system of each chromophore, the order of LUMO energies for these ligands, working from highest to lowest, is DPAF > CCDPAF > BTF > CCBTF.

Overall, these complexes are not expected to be drastically different from those of the purely acetylide congeners, as they are structurally very similar.

Previous studies on platinum acetylide complexes have shown that the triplet exciton is localized to the lowest energy chromophore.⁴⁵ However, due to the weak coupling of the ligands through the platinum center, interesting properties such as dual emission may arise when complexes containing both the BTF and DPAF chromophores are synthesized. Furthermore, emission spectra were seen in purely platinum-aryl systems in which the quantum yields of the fluorescence and phosphorescence were nearly equivalent.⁵⁵ This would lead to a white light emitting species and a new class of white light emitters.

Synthesis

Synthesis of monosubstituted platinum(II) aryl (Pt-aryl) complexes via a Cu(I) assisted Stille-type reaction was recently developed by a previous member of the Schanze group.⁵⁵ These products were isolated, and addition of the acetylide chromophore was achieved via the classic Cu(I) assisted Hagihara reaction to give the mixed aryl/acetylide ligated platinum(II) complex. A discussion of nomenclature is warranted before further discussion of the synthetic details.

Nomenclature of these compounds will be by chromophore and connectivity. The only nomenclature feature that can be held constant for these complexes is the position of the acetylide feature, and the acetylide chromophore will be distinguished from the aryl chromophore by the prefix 'CC'. Thus the complexes will always be named in the form: *aryl-Pt-acetylide*. For example, the complex using the aryl ligand 2-(9,9-diethyl-9*H*-fluorene)benzo[d]thiazole (BTF) and the acetylide 9,9-Diethyl-7-ethynyl-N,N-diphenyl-9*H*fluoren-2-amine (CCDPAF) would be named **BTF-Pt-CCDPAF**. The other

two ligands used are the acetylide congener of BTF: 2-(9,9-diethyl-9H-fluore-2-yl)benzo[d]thiazole (CCBTF), and the aryl congener of CCDPAF: 9,9-Diethyl-N,N-diphenyl-9Hfluoren-2-amine (DPAF). It should be noted that the aryl groups are bonded to the metal in the 7-postion of the fluorene moiety. Additionally, the synthesized monosubstituted platinum-aryl and DFT modeled platinum-acetylide complexes will always be named with the chromophore first, i.e: **BTF-Pt-Cl**. Finally, when referring to the presence of a chromophoric moiety that is not dependent on how it is bonded to the platinum center, it will be referred to as chromophore (i.e. if a complex contains either BTF or CCBTF, it can be referred to as 'containing the BTF chromophore').

As stated earlier, a novel preparation of monosubstituted platinum(II) aryl complexes has been developed, and this methodology will serve as the first step in the synthesis presented here, and is shown in Figure 4-1. The precursor organic ligands **BTF-Br**, **CCBTF**, **DPAF-Br**, and **CCDPAF** were prepared according to literature procedures.² Starting with the aryl bromide (**BTF-Br** or **DPAF-Br**) in argon purged THF solution at -78°C, n-butyl lithium was added dropwise to generate the lithium salt of the organic anion. After an hour, tributyltin chloride was added to quench the anion and form an aryl stannane. The solution was stirred at -78°C for two hours before being allowed to warm to room temperature. The solution was then washed with water, extracted with dichloromethane, and had the solvent removed *in vacuo* to give a crude oil. Beause aryl stannanes are not especially amenable to chromatography, the crude was used as is. NMR was employed to help approximate the conversion to the aryl stannane, typically 50%, as it would be a waste of platinum to assume quantitative yield. The crude oil was redissolved in 15 mL of dimethylformamide and degassed with argon

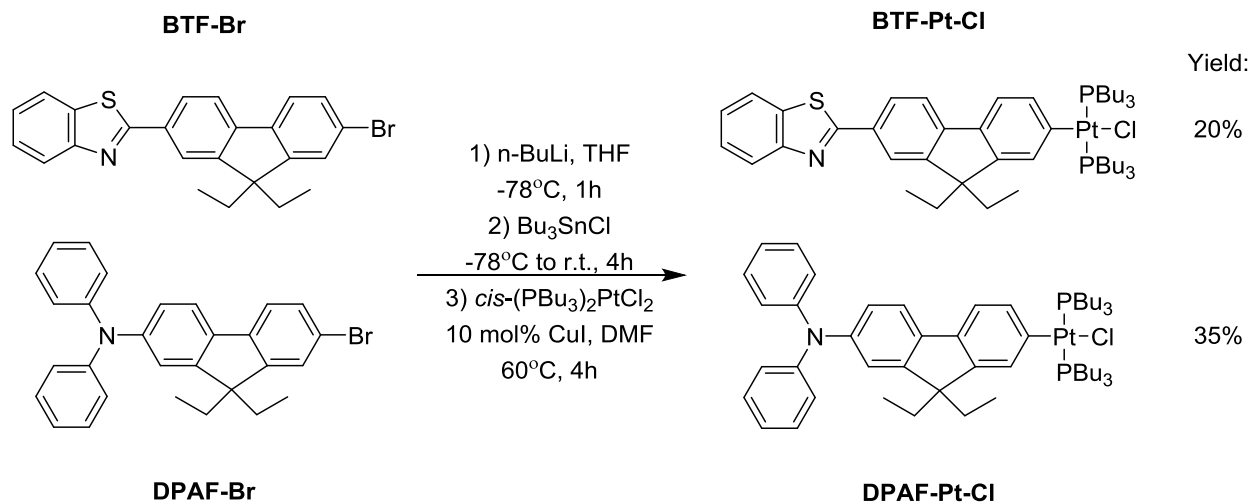


Figure 4-1. Synthesis of monosubstituted platinum(II) aryl precursors.

for 15 minutes before 10 mol% of CuI and 1 equivalent of *cis*-(PBu₃)₂PtCl₂ (assuming 50% conversion to the aryl stannane) were added, and the solution was allowed to react overnight at 60°C. The resulting solution was washed with water, extracted with dichloromethane, separated and filtered through Na₂SO₄, before being purified by medium pressure liquid chromatography (MPLC). While the previously reported **DPAF-Pt-Cl** purified nicely, and was isolated in 35% yield, the isolation of **BTF-Pt-Cl** proved to be problematic. This compound requires nearly pure dichloromethane to elute, and even after multiple columns retains an impurity of ~5%. Furthermore, Pt-aryl complexes of this nature tend to be either oils or waxy solids, so recrystallization cannot be employed. Although not suitable for photophysics, the **BTF-Pt-Cl** was pure enough to be used in further reactions.

The two Pt-aryl complexes were then subject to standard Hagihara reaction conditions with either **CCBTF** or **CCDPAF** to generate four platinum complexes with a mixed aryl/acetylide chromophore motif. The synthesis and yields of these reactions are shown in Figure 4-2, with the structures previously shown in Figure 4-1.

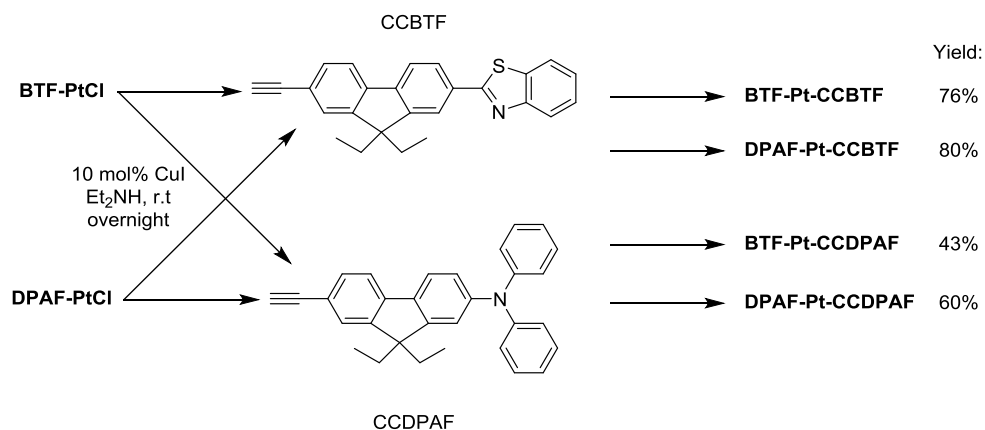


Figure 4-2. Hagihara reaction to generate the four mixed aryl/acetylide Pt(II) complexes.

Isolation of all four mixed complexes proceeded smoothly by washing with water, extracting with dichloromethane, separation and filtering through Na₂SO₄, followed by purification via MPLC using a hexanes:CH₂Cl₂ gradient to elute a mostly pure (>98%) product. The solution can then have the solvent removed *in vacuo* to give an oil, which is easily recrystallized by dissolution in a minimum of warm acetone and precipitating with methanol. Isolated yields are around 75%; similar to that of the typical Hagihara reaction to form platinum(II) acetylide complexes. The exception to this is **BTF-Pt-CCDPAF**, which does not recrystallize as readily and is isolated in lower yield.

Photophysical Properties

Absorption

The UV-Vis spectra of all four mixed ligand complexes show a strong UV absorption which, for the three complexes containing the BTF chromophore, trails into the visible region. The absorption spectra of the mixed complexes are shown in Figure 4-4. The individual chromophores seem to be acting nearly completely independent of each other, suggesting minimal to no coupling through the platinum center. The primary evidence for this stems from the absorption onset of **BTF-Pt-CCBTF** and **DPAF-Pt-**

CCBTF. As the CCBTF ligand has the lowest energy excited state of all four ligands, it is responsible for the onset wavelength in these two complexes. Regardless of if CCBTF has BTF or DPAF bonded across the platinum atom from it, no change is seen in the absorption onset. Absorption, as well as all other tabular photophysical characterization data is given in Table 4-1. Time dependent density functional theory computations were used to clarify the absorption features, and the results will be discussed in detail in a later section.

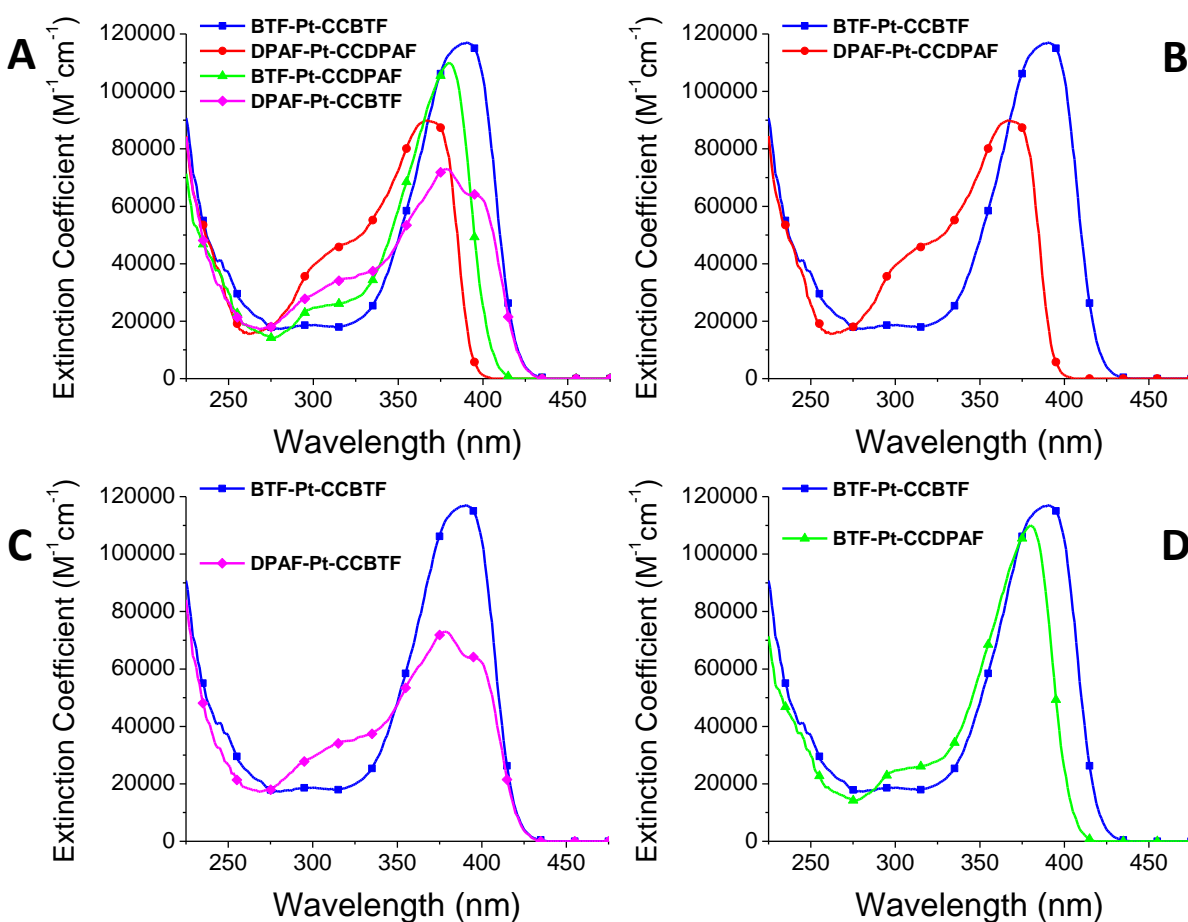


Figure 4-4. Ground state absorption spectra of A) the four mixed ligand platinum complexes containing the BTF and DPAF chromophores, with spectra shown in pairs for B) **BTF-Pt-CCBTF** and **DPAF-Pt-CCDPAF**, C) **BTF-Pt-CCBTF** and **DPAF-Pt-CCBTF**, and D) **BTF-Pt-CCBTF** and **BTF-Pt-CCDPAF** to emphasize trends.

Table 4-1. Summary of photophysical data for mixed aryl/acetylide ligated Pt(II) complexes.

Complex	Abs _{max} (nm)	ϵ (M ⁻¹ cm ⁻¹)	Fl _{max} (nm)	Φ_{Fl} ^a	τ_{Fl} (ns)	Ph _{max} ^{a,b} (nm)	Φ_{Ph} ^{a,b}	τ_{Ph} ^{a,b} (μ s)	TA _{max} ^{a,b}	τ_{T1-Tn} ^{b,c} (μ s)
BTF-Pt-CCBTF	391	117000	438	0.031	< 0.10 ns ^d	569	0.16	900	658	50.5
DPAF-Pt-CCDPAF	368	90000	392	0.022	< 0.10 ns ^d	531	0.10	170	600	53.6
BTF-Pt-CCDPAF	380	110000	432	0.013	< 0.10 ns ^d	536	0.099	370	586	48.9
DPAF-Pt-CCBTF	378	73000	439	0.011	< 0.10 ns ^d	568	0.14	650	660	61.2

^a Measured at RT using Ru(bpy)₃Cl₂ in aerated water (Φ_{fl} = 0.0379) as a standard. ^b Samples degassed by five freeze-pump-thaw cycles on a high vacuum line. ^c All decay profiles can be found in Appendix D. ^d Lifetime is shorter than the lower threshold of the PicoQuant instrument, 100 ps.

Fluorescence

All of the mixed ligand complexes are weakly fluorescent, with quantum yields between 1 and 3%. Thus the intersystem crossing yield is still very high in these mixed complexes, as it is for both pure platinum(II) aryl complexes and platinum(II) acetylide complexes. A high intersystem crossing yield also implies efficient intersystem crossing, for which evidence is provided in that the fluorescence lifetimes are all <100 ps. The fluorescence spectra of all four mixed ligand complexes, when excited at their respective absorption maxima, are shown in Figure 4-5. As **DPAF-Pt-CCDPAF** contains two π -donating ligands, its effective conjugation length is shorter, and its fluorescence is blue-shifted relative to the rest of the complexes. Additionally, this is the only structure to show vibronic structure. This is most likely due to the BTF chromophore having free rotation of the C-C bond connecting the benzothiazole moiety to the fluorene. Conversely, **BTF-Pt-CCBTF** and **DPAF-Pt-CCBTF**, both of which utilize the lowest

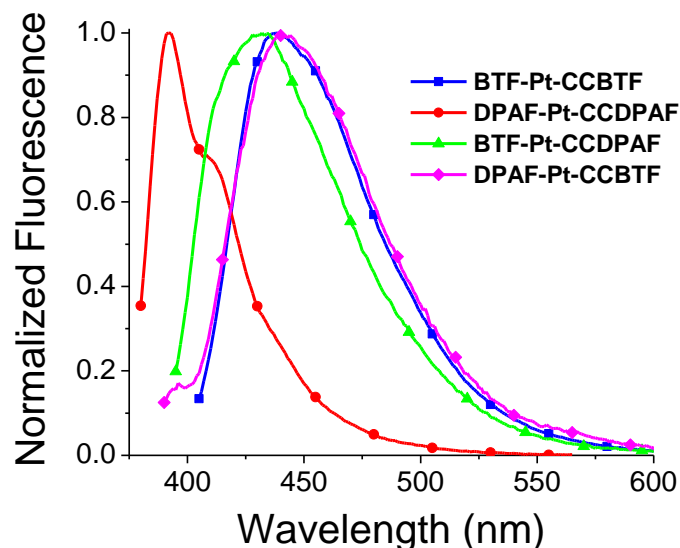


Figure 4-5. Fluorescence spectra of the four mixed ligand platinum complexes containing the BTF and DPAF chromophores.

energy ligand in the series (CCBTF), show nearly identical emission and display the most red-shifted fluorescence in the series. Finally, **BTF-Pt-CCDPAF** shows an emission that is slightly blue-shifted relative to the lowest energy fluorescence, as these two ligands are both of intermediate energy relative to the other two.

After a cursory look at the fluorescence, these complexes seem to be behaving as pure platinum-aryl or platinum-acetylide complexes would. However, excitation at higher energies than that of the absorption maxima reveals a new feature in the emission of **DPAF-Pt-CCBTF**. The fluorescence spectra using an excitation wavelength of 330 nm is shown in a normalized plot alongside the fluorescence from excitation at the ground state absorption maximum of 378 nm in Figure 4-6. The spectrum obtained from 330 nm excitation shows new vibronic bands and shifts the emission maximum from 432 nm to 394 nm. This appears to be a direct result of exciting at the absorption maximum of the DPAF-platinum chromophore.⁵⁵ The observation of emission from both

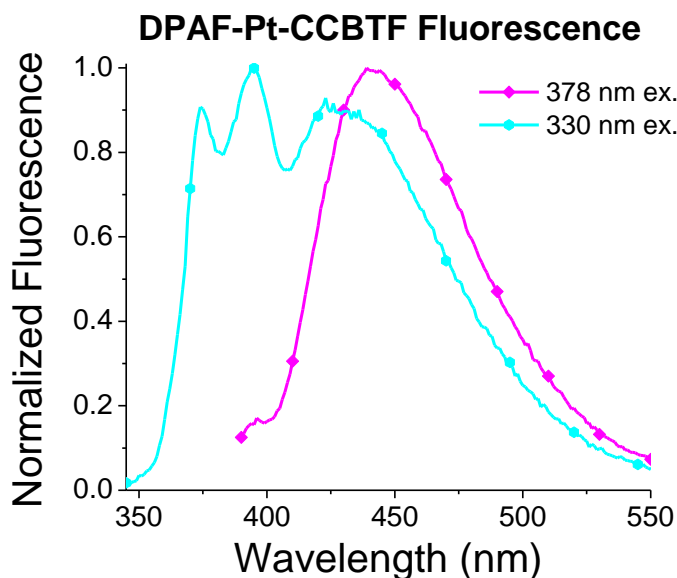


Figure 4-6. Fluorescence spectra of **DPAF-Pt-CCBTF** with excitation at 378 and 330 nm.

ligands implies minimal coupling of the ligands through the platinum center and inefficient internal conversion. Interestingly, none of the other complexes display this behavior. While more data is certainly needed to draw any solid conclusions about this effect, the data presented here leads one to believe that a large gap in the energy of the π^* orbital of each chromophore is required to see dual emission from the singlet manifold.

Phosphorescence

Moving on to the triplet manifold, solutions of the mixed ligand complexes were subject to at least five freeze-pump-thaw cycles on a vacuum line to observe the phosphorescence properties. All complexes show pronounced vibronic structure and fair quantum yields ranging from 10 to 16%. Figure 4-7 shows the normalized phosphorescence spectra of the mixed ligand complexes. Starting with an analogous observation to the fluorescence spectrum, the complexes **BTF-Pt-CCBTF** and **DPAF-Pt-CCBTF** have nearly identical phosphorescence spectrum. This is again due to the CCBTF ligand having the lowest π^* energy, and the triplet emission being confined to the lowest energy ligand.⁴⁵ **DPAF-Pt-CCDPAF** also follows this trend, as its phosphorescence maximum is almost 40 nm blue-shifted from that of the CCBTF containing complexes (531 nm vs 569 nm, respectively). The last complex, **BTF-Pt-CCDPAF**, shares its phosphorescence onset and vibronic energy levels with that of the aforementioned complex, but the individual peaks are significantly broadened. This complex is unique in that the π^* of the aryl ligand (BTF) is expected to be of lower energy than that of the acetylide ligand (CCDPAF). Given that the onset wavelength and vibronic peaks are at the same energies as that of **DPAF-Pt-CCDPAF**, it is fair to tentatively assign the major features of this emission as being primarily localized on the

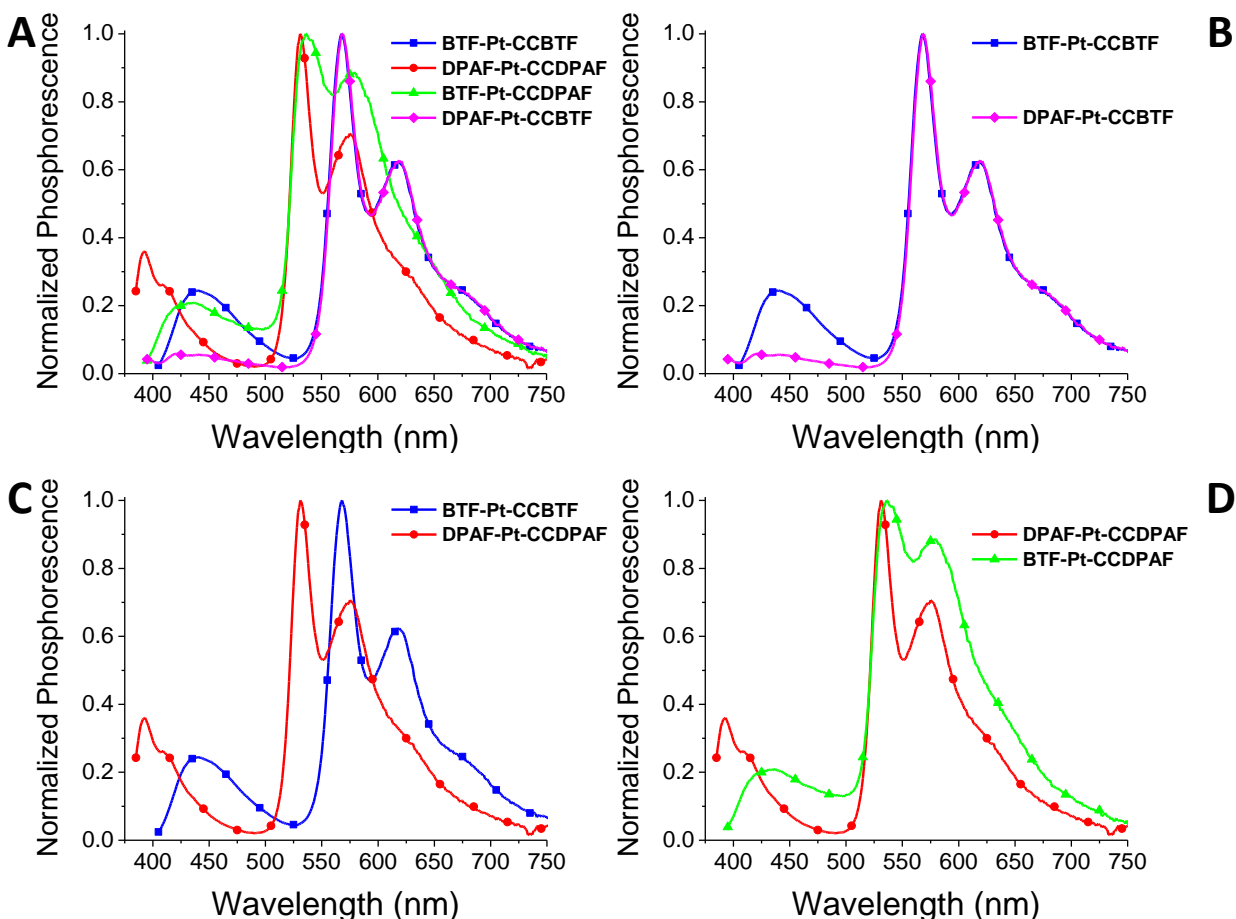


Figure 4-7. Emission spectra after at least five freeze-pump-thaw cycles of A) the four mixed ligand platinum complexes containing the BTF and DPAF chromophores, with spectra shown in pairs for B) **BTF-Pt-CCBTF** and **DPAF-Pt-CCBTF**, C) **BTF-Pt-CCBTF** and **DPAF-Pt-CCDPAF**, and D) **DPAF-Pt-CCDPAF** and **BTF-Pt-CCDPAF** to emphasize trends.

CCDPAF ligand. Broadness would then be caused by minor contributions from the BTF ligand. However, further resolution is required to make definitive assignments to the nature of this emission.

A closer examination of the phosphorescence quantum yields and lifetimes reveals a couple of patterns. First, with respect to the quantum yield, the two mixed ligand complexes containing the CCDPAF ligand have lower radiative emission (10%) than the either **DPAF-Pt-CCBTF** (14%) or **BTF-Pt-CCBTF** (16%). An explanation for

this trend may lie with the known monosubstituted platinum complexes containing the DPAF and CCDPAF ligands.^{3, 55} Both of these compounds show phosphorescence quantum yields on the order of 1%. However, if trying to draw comparisons to the known platinum acetylide complexes which utilize the CCDPAF and CCBTF chromophores (using the nomenclature of this chapter, DPAFCC-Pt-CCDPAF and BTFCC-Pt-CCBTF, respectively), this trend is reversed, as the DPAFCC-Pt-CCDPAF has a higher phosphorescence quantum yield than BTFCC-Pt-CCBTF.⁶⁴

The second observed trend in the triplet state involves the phosphorescence lifetime correlating inversely to the number of DPAF chromophores in the complex and whether the DPAF is bonded as an aryl or acetylide unit. Thus the lifetimes increase for each complex in the order of **DPAF-Pt-CCDPAF** (170 μ s) < **BTF-Pt-CCDPAF** (370 μ s) < **DPAF-Pt-CCBTF** (650 μ s) < **BTF-Pt-CCBTF** (900 μ s). The lifetimes of the known **DPAF-Pt-Cl** and DPAFCC-Pt-Cl were also measured to help deconvolute this series, as they were not measured in previous reports. All lifetime decays can be found in Appendix E. Both **DPAF-Pt-Cl** and DPAFCC-Pt-Cl showed biexponential decay kinetics, with a ‘fast’ component of 8 μ s and a slow component of 68 and 61 μ s, respectively. Additionally, the contribution of the ‘fast’ component makes up only 4% of the decay of **DPAF-Pt-Cl** (average lifetime: 66 μ s), but is 75% of the decay of DPAFCC-Pt-Cl (average lifetime: 21 μ s). These data strongly suggest that the DPAF chromophore largely contributes to the deactivation of the mixed ligand triplet state.

Transient Absorption

To further probe the nature of the triplet manifold, transient absorption was run on solutions with a matched O.D. of 0.58. As seen in previous chapters, all complexes show ground state bleaching in the region of their respective absorptions, and a strong,

broad triplet-triplet absorption (TTA) across most of the visible region. These spectra are plotted in Figure 4-8. Staying true to the notion that the triplet exciton is localized on the lowest energy ligand, the spectra of **DPAF-Pt-CCDPAF**, **DPAF-Pt-CCBTF**, and **BTF-Pt-CCBTF** show absorption features that are qualitatively identical to those found in the purely platinum acetylide compounds DPAFCC-Pt-CCDPAF and BTFCC-Pt-CCBTF.⁶⁴ The TTA of **DPAF-Pt-CCDPAF** shows a single feature with a

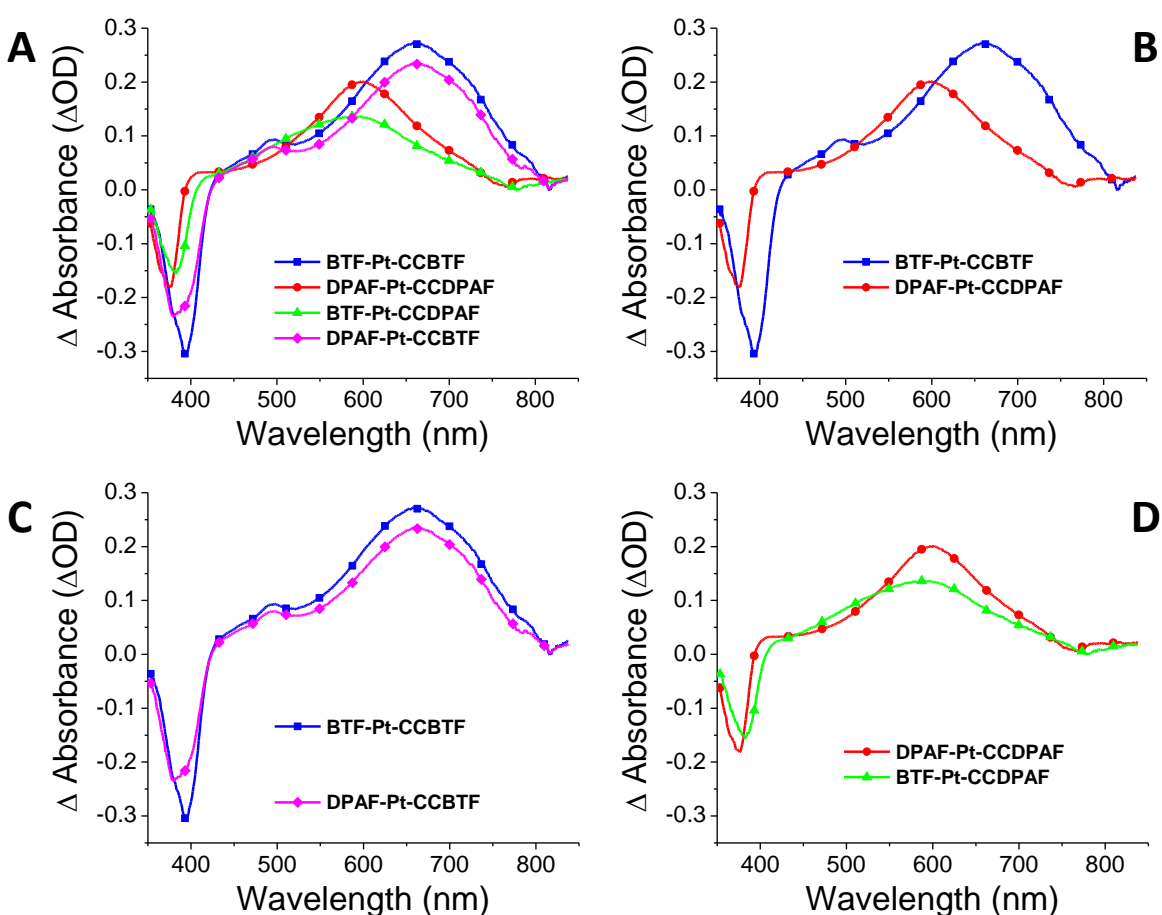


Figure 4-8. Principal component transient absorption spectra with excitation at 355 nm, 10 ns pulse width, 180 $\mu\text{J}/\text{pulse}$ excitation energy. Solutions had an absorptivity value of 0.58 at 355 nm after five freeze-pump-thaw cycles. A) All four mixed ligand platinum complexes containing the BTF and DPAF chromophores, with spectra shown in pairs for B) **BTF-Pt-CCBTF** and **DPAF-Pt-CCDPAF**, C) **BTF-Pt-CCBTF** and **DPAF-Pt-CCBTF**, and D) **DPAF-Pt-CCDPAF** and **BTF-Pt-CCDPAF** to emphasize trends.

maximum at 600 nm. **DPAF-Pt-CCBTF** and **BTF-Pt-CCBTF** complexes show two features, as is typical for the CCBTF ligand. The TTA maximum is found at ~660 nm, and a minor feature is seen at just under 500 nm.

Once again, **BTF-Pt-CCDPAF** shows triplet state behavior that breaks with the trends that have been previously seen in purely platinum acetylide systems. A close examination of the TTA of **BTF-Pt-CCDPAF** relative to the other three mixed ligand complexes first shows that the absorption maximum is blue shifted from **DPAF-Pt-CCDPAF**. Additionally, the absorption of **BTF-Pt-CCDPAF** follows the minor feature of the complexes with the CCBTF ligand in the 425-500 nm region. These two observations from the TA spectra, along with the phosphorescence data the data again point a mixing of the triplet states in **BTF-Pt-CCDPAF**.

Electronic Structure Calculations

To further probe the nature of the electronic structure, and to help deconvolute the absorption spectra of these mixed ligand complexes, DFT and TD-DFT calculations were performed in the Gaussian 09, revision C.01,⁷³ suite of programs at the B3LYP level. The 6-31G(d) basis set was used for C, H, N, the 6-31+G(d) basis set was used for P, S, and the SDD basis set was used for Pt. Phosphine butyl groups and fluorene ethyl groups were truncated to methyl groups to improve computational efficiency. These truncated complexes are denoted by the addition of a prime (') to the end of their name. Thus, the synthesized complex **BTF-Pt-CCBTF** would have its computed congener named **BTF-Pt-CCBTF'**. In addition to studying the mixed complexes, the monosubstituted Pt-aryl and Pt-acetylide complexes were studied to provide further deconvolution.

It is beneficial to start with examination of the TD-DFT results and electronic structure of the monosubstituted complexes, as they contain each ligand individually, allowing for unambiguous assignment of vertical excitations and orbitals unperturbed by a second organic ligand. A table providing data for the lowest energy electronic transition ($S_0 \rightarrow S_1$) is given in Table 4-2. Summarized here is the predicted wavelength of the vertical excitation, the orbital transitions presented as both orbital number and frontier orbital nomenclature, the percent contribution of each individual transition, and finally the oscillator strength of the overall transition. The computed transitions for the model complexes are quite straightforward, as they consist purely of the HOMO-LUMO transition. A qualitative look at the predicted wavelengths for each monosubstituted platinum complex shows the expected energy trend of **DPAF-Pt-Cl'** > **DPAFCC-Pt-Cl'** \approx **BTF-Pt-Cl'** > **BTFCC-Pt-Cl'**, based on the π^* energy of the organic ligand. However, it is dangerous to examine the data quantitatively, as DFT methods are well known to over-delocalize electron density.

Regarding the composition of the orbitals, the HOMO for each monosubstituted platinum complex is delocalized fully across the organic chromophore and is perturbed by the d_{xy} of platinum. In complexes containing the BTF chromophore, the p_y orbital of chlorine also makes a minor contribution. The LUMOs on the other hand show

Table 4-2. Summary of TD-DFT computations for the $S_0 \rightarrow S_1$ transition of monosubstituted platinum aryl and platinum acetylide compounds.

Complex	Wavelength nm	Orbital Transitions (% contribution)		Oscillator Strength f
BTFCC-Pt-Cl'	395.1	151→152 HOMO → LUMO	(100%)	1.4296
DPAFCC-Pt-Cl'	369.8	161→162 HOMO → LUMO	(100%)	1.1782
BTF-Pt-Cl'	367.2	145→146 HOMO → LUMO	(100%)	1.3153
DPAF-Pt-Cl'	349.7	155→156 HOMO → LUMO	(100%)	0.8276

localization of electron density. For platinum complexes containing the BTF chromophore, the system as a whole is an acceptor- π -donor system, and localization is strongest in the vicinity of the C-C bond connecting benzothiazole to fluorene. Platinum complexes functionalized with the DPAF chromophore however, represents a donor- π -donor system, forcing the electron density to build up around the central C-C bond of the fluorene moiety. Minimal perturbations are seen from platinum, and none from chloride. Figures of relevant orbitals are given in Appendix E.

To determine the overall difference in electron density between ground and excited state, charge difference density (CDD) plots were utilized, and are shown in Figure 4-9 alongside the computed singlet ground state structure. In the CDD, blue coloring represents electron density being lost, or where the electron density originated (ground state). Red coloring in the CDD represents electron density being gained, or where the electron density finishes (excited state). For the systems containing the BTF chromophore, the charge originates primarily on the platinum and the phenyl ring of fluorene that is closest to platinum. Charge then moves towards the benzothiazole moiety, which is responsible for the π -acceptor character of BTF. Complexes containing the DPAF chromophore show nearly the opposite effect, as the diphenylamine group is a strong π -donor. Platinum also donates charge to the system, which causes significant localization of charge on the π^* of the central fluorene.

Now that the electronic properties of the monosubstituted complexes have been established, they can be used to deconvolute effects observed in the mixed ligand platinum compounds. TD-DFT data for the mixed compounds are given in Table 4-3, which is formatted in the same manner as Table 4-2. Focusing first on **BTF-Pt-CCBTF'**

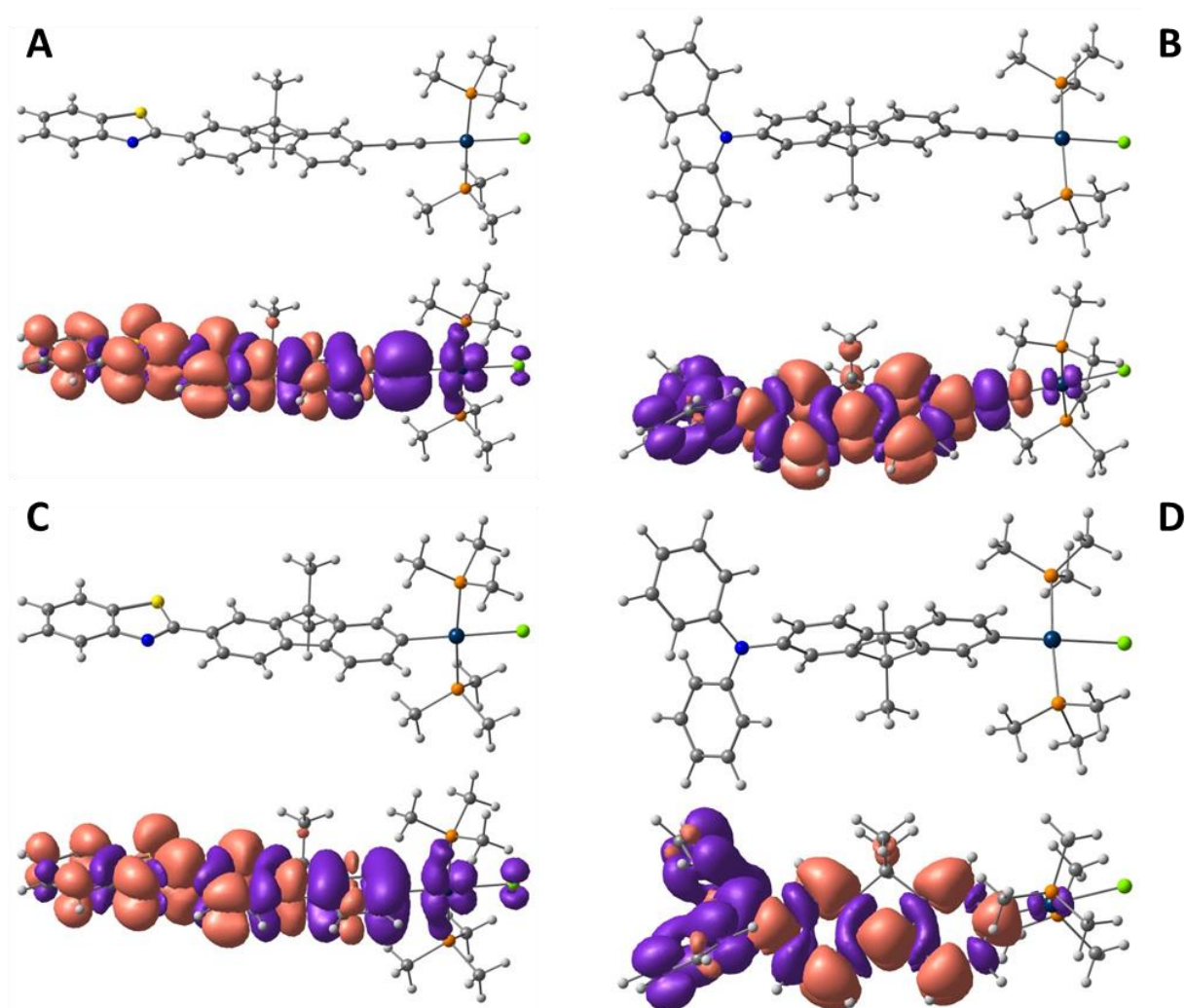


Figure 4-9. DFT optimized structures of the singlet ground state and charge difference densities for the computed $S_0 \rightarrow S_1$ vertical transition for A) **BTFCC-Pt-Cl'**, B) **DPAFCC-Pt-Cl'**, C) **BTF-Pt-Cl'**, and D) **DPAF-Pt-Cl'**. Blue coloring indicates electron density being lost, while red coloring indicates electron density being gained in an electronic transition. CDDs were imaged at an isovalue of 0.0004.

and **DPAF-Pt-CCDPAF'**, the red-most vertical transition is dominated (>90% contribution) by the HOMO \rightarrow LUMO transition. The HOMO \rightarrow LUMO transition for **DPAF-Pt-CCDPAF'** is localized almost exclusively on the CCDPAF ligand, with minor perturbation from the platinum center and DPAF ligand. Interestingly, **BTF-Pt-CCBTF** shows nearly the exact opposite behavior. The HOMO is localized primarily on the

Table 4-3. Summary of TD-DFT computations for transitions of oscillator strength > 0.1 and $\lambda > 345$ nm for the mixed platinum aryl/acetylide complexes.

Complex	Wavelength nm	Orbital Transitions (% contribution)		Oscillator Strength f
BTF-Pt-CCBTf'	408.4	227→230 HOMO-1 → LUMO+1	(2.5%)	2.0824
		228→229 HOMO → LUMO	(94.0%)	
		228→230 HOMO → LUMO+1	(3.5%)	
	359.8	227→229 HOMO-1 → LUMO	(43.7%)	0.8753
		227→230 HOMO-1 → LUMO+1	(53.7%)	
		228→229 HOMO → LUMO	(2.6%)	
DPAF-Pt-CCDPAF'	372.4	247→250 HOMO-1 → LUMO+1	(6.1%)	2.0126
		248→249 HOMO → LUMO	(93.9%)	
	349.5	247→249 HOMO-1 → LUMO	(26.0%)	0.3309
		247→250 HOMO-1 → LUMO+1	(50.5%)	
BTF-Pt-CCDPAF'	438.5 ^a	238→239 HOMO → LUMO	(100%)	0.1089
	375.6	236→239 HOMO-2 → LUMO	(12.0%)	2.5273
		237→239 HOMO-1 → LUMO	(43.0%)	
		238→240 HOMO → LUMO+1	(45.0%)	
	350.3	236→239 HOMO-2 → LUMO	(86.3%)	0.2525
		237→239 HOMO-1 → LUMO	(11.6%)	
		238→240 HOMO → LUMO+1	(2.1%)	
DPAF-Pt-CCBTf'	421.9 ^a	237→239 HOMO-1 → LUMO	(7.9%)	0.5378
		238→239 HOMO → LUMO	(92.1%)	
	401.4	237→239 HOMO-1 → LUMO	(91.6%)	1.2439
		238→239 HOMO → LUMO	(8.4%)	
	350.0	238→240 HOMO → LUMO+1	(100%)	0.7622

^a These predicted vertical transitions are charge transfer bands which are not observed in the experimental absorption spectrum at concentrations ranging from 0.4 mM to 0.4 μ M.

Pt-CCBTf unit, but the LUMO is completely delocalized across both BTF chromophores with no contribution from the platinum core. These two processes are illustrated in the CDDs presented in Figure 4-10. The higher energy predicted transition for both of these complexes are mostly similar in that they show primarily a $\pi \rightarrow \pi^*$ transition on the aryl ligand, with slight ligand \rightarrow ligand charge transfer (LLCT) from the aryl to the acetylide

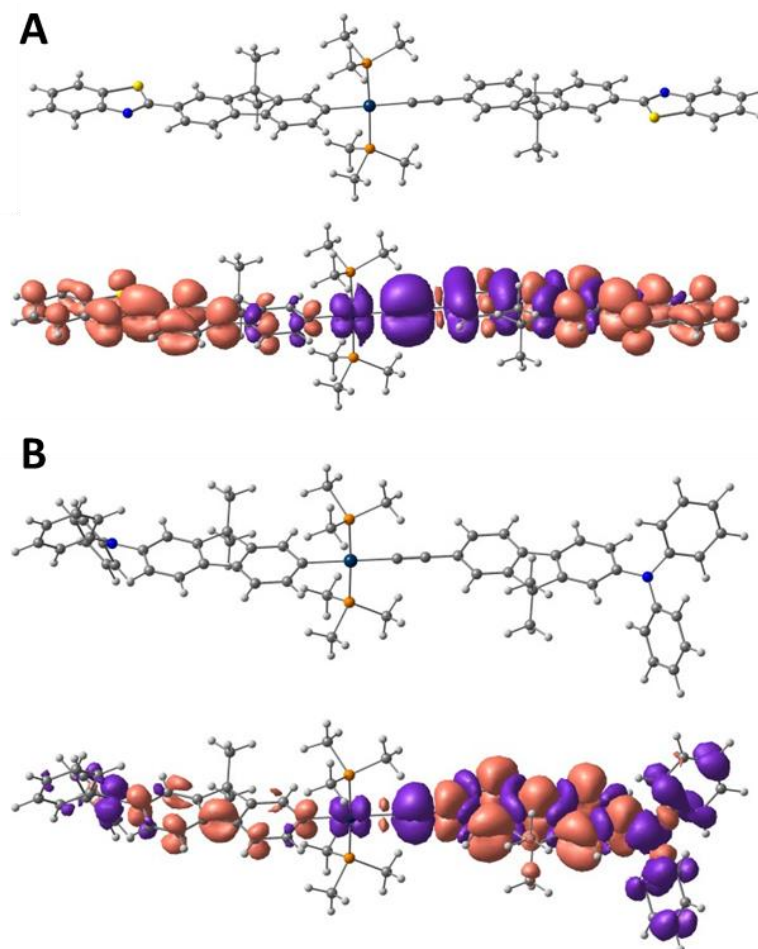


Figure 4-10. DFT optimized structures of the singlet ground state and charge difference densities for the computed $S_0 \rightarrow S_1$ vertical transition for A) **BTF-Pt-CCBTF'** and B) **DPAF-Pt-CCDPAF'**. Blue coloring indicates electron density being lost, while red coloring indicates electron density being gained in an electronic transition. CDDs were imaged at an isovalue of 0.0004.

ligand. Molecular orbitals for these compounds and CDDs for the high energy predicted vertical transition are given in Appendix E.

Moving on to the mixed ligand complexes utilizing both chromophores, **BTF-Pt-CCDPAF'** and **DPAF-Pt-CCDPAF'** are predicted to have three transitions relevant to this study. However, the lowest energy predicted transition for both of these compounds shows purely charge transfer character from either CCDPAF to BTF or DPAF to CCBTF, respectively. These charge transfer bands are not observed in the

experimental UV-Vis at concentrations between 0.4 mM and 0.4 μ M. Aside from overdelocalization and through-space interactions, charge transfer processes are the other well-known deficiency of the DFT methodology. With these two erroneous bands dismissed, each mixed ligand complex now has two predicted vertical transitions that are of interest.

As stated earlier, the individual ligands in **BTF-Pt-CCDPAF'** are expected to be quite close in energy. This is exemplified by a single strong absorption in the experimental UV-Vis spectrum, and the claim is strengthened by the TDDFT computation predicting a high degree of mixing of orbital contribution to a transition with very high oscillator strength. The CDD for this transition reveals π -donor character across the complete π -system of the CCDPAF ligand as well as from the platinum center and even moderately from the fluorene of the BTF ligand. Furthermore, π -acceptor character is seen on both ligands, but with preference for BTF. The CDD for **BTF-Pt-CCDPAF'** is shown in Figure 4-11.

The final compound to be discussed is **DPAF-Pt-CCBTF**, and it has the largest energy gap between its two ligands. In looking at the experimental UV-Vis spectra, this becomes apparent as vibronic structure of the [Pt]-CCBTF absorption can be plainly seen. The other three compounds do not show vibronic structure due to increased overlap of the absorption bands of the two ligands. Looking at the vertical transition with the lowest energy (that is not the erroneous CT band), the transition is dominated by the HOMO-1 \rightarrow LUMO transition, which is almost purely $\{PtCCBTF\}\pi \rightarrow \{CCBTF\}\pi^*$. In an analogous manner, the high energy TDDFT predicted transition of 100% HOMO \rightarrow LUMO+1. This corresponds to a $\{DPAFPtCC\}\pi \rightarrow \{DPAF\}\pi^*$ transition, with trace

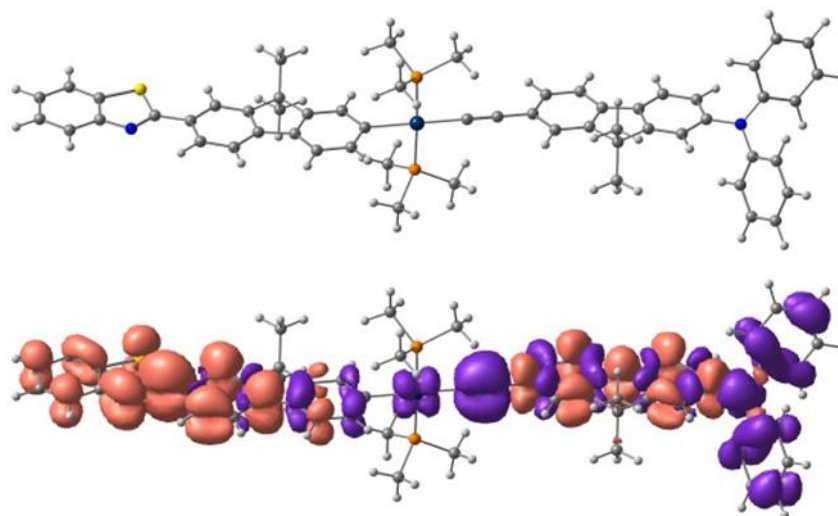


Figure 4-11. DFT optimized structure of the singlet ground state and charge difference density for the vertical transition predicted at 376 nm of **BTF-Pt-CCDPAF'**. Blue coloring indicates electron density being lost, while red coloring indicates electron density being gained in an electronic transition. CDDs were imaged at an isovalue of 0.0004.

contribution from platinum. This finding gives a great amount of insight as to the phenomenon of dual fluorescence in **DPAF-Pt-CCBTF**. The ligands of this compound have such a large difference in π^* energy that they are effectively insulated from each other, and are allowed to decay independently of one another. The CDDs for both predicted transitions are shown in Figure 4-12.

Summary and Conclusions

In summary, four platinum(II) complexes featuring one aryl and one acetylide ligand were synthesized and photophysically characterized. Synthesis was achieved by first using a recently developed Stille-type coupling reaction of an aryl stannane with catalytic CuI to generate a pair of monosubstituted platinum(II) aryl precursors. These two compounds were each reacted with two acetylide ligands, containing the same two chromophores, via standard Hagihara reaction conditions to afford the mixed ligand platinum complexes in good yield.

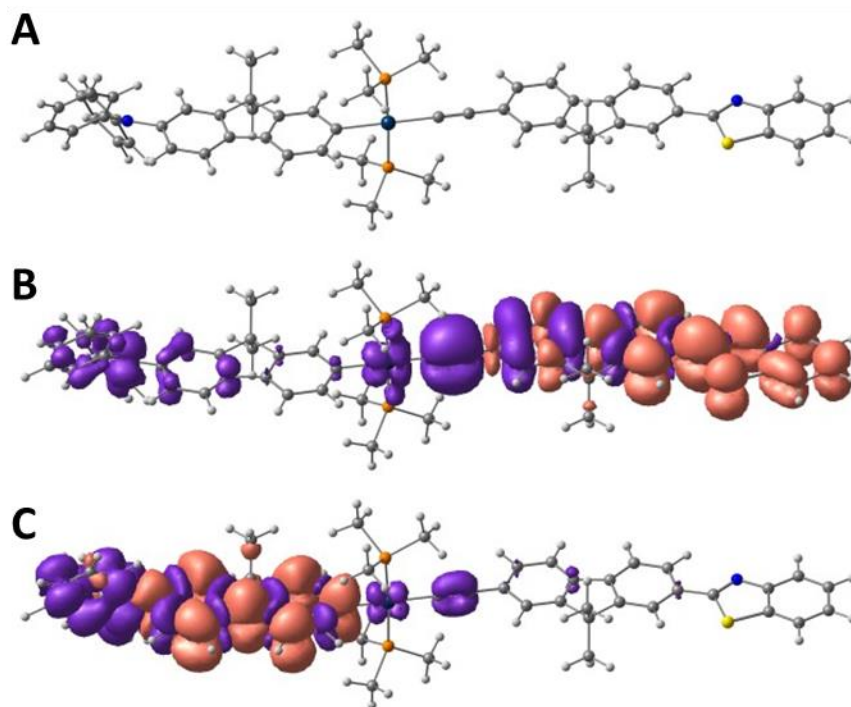


Figure 4-12. DFT optimized structure of A) the singlet ground state, and charge difference densities for the vertical transitions predicted at B) 401 nm and C) 350 nm of **DPAF-Pt-CCBTF'**. Blue coloring indicates electron density being lost, while red coloring indicates electron density being gained in an electronic transition. CDDs were imaged at an isovalue of 0.0004.

The absorption spectra show minimal coupling of the ligands through the platinum center. This is evidenced by the absorption onset of the two compounds containing the lowest energy CCBTF ligand being identical. Additional evidence is given by TDDFT computations. Specifically, the absorption of the mixed ligand complexes can be reasonably well modeled by the sum of the absorptions of the respective monosubstituted platinum aryl and platinum acetylide constituents.

When the mixed ligand platinum complexes are excited at their absorption maxima, weak fluorescence is observed for all species, with no unusual features. However, **DPAF-Pt-CCBTF** gives a very pronounced dual emission upon excitation with 330 nm light. The TDDFT calculations inadvertently shine light onto the potential nature

of this process, as they show the two main absorption processes are localized mostly on a single ligand (one absorption per ligand). Thus it seems the two excited state potential wells do not intersect at a point where efficient internal conversion can occur, and radiative decay is seen from both states.

All complexes show efficient intersystem crossing, as evidenced by low fluorescence quantum yields ($\leq 3\%$) and fluorescence lifetimes of less than 100 ps. Additionally, all complexes show phosphorescence at room temperature with fair quantum yields between 10 and 16%. While **DPAF-Pt-CCBTf** does not show any unique emission in the triplet state, its structural isomer **BTF-Pt-CCDPAF** does appear to show more than one radiative process. The resolution at room temperature does not allow for any definitive assignment, but the broadness of the structured emission as well as the significant increase in the ratio of the $0 \rightarrow 1$ vibronic band relative to the $0 \rightarrow 0$ band suggests that a second emission is present.

Transient absorption spectroscopy provides further evidence for a mixing of the triplet states in **BTF-Pt-CCDPAF**. The three other mixed ligand compounds in the series behave nearly identically to their platinum acetylide congeners in the TA spectrum, in that the characteristics are based solely on the lowest energy chromophore. However, **BTF-Pt-CCDPAF** shows characteristics of both the BTF and CCDPAF ligands in the TA experiment.

As the energy of the excited state for the BTF and CCDPAF ligands are the closest in this series, a couple of pathways for population of non- T_1 states is possible. The most straightforward would be the thermal population of T_2 if it is close enough in energy. The other option would invoke a similar explanation to the rationale for dual

fluorescence in **DPAF-Pt-CCBTF**. Excitation at the main absorption band of **BTF-Pt-CCDPAF** creates an excited state where charge is delocalized across a majority of the molecule, according to TDDFT computations. This potential well most likely has overlap with the triplet state potential wells of both the BTF and CCDPAF ligands. Intersystem crossing would then occur before internal conversion in the singlet state could finish, allowing the exciton to decay to either ligand. The individual triplet potential wells of BTF and CCDPAF would have poor overlap at reasonable energies, allowing radiative decay from either triplet state.

The class of mixed ligand platinum(II) aryl/acetylide complexes marks a very interesting development in platinum chromophores. While more experiments are certainly necessary to pin down the exact nature of the dual emission phenomena, this class of compounds shows promise that these observations were more than just good luck in choice of chromophore. With further study, it may become routine to generate fully conjugated platinum chromophores that display predictable dual emission.

Experimental

General Remarks

All reactions were carried out under argon atmosphere. All starting chemicals used for the synthesis of the *trans* platinum acetylide complexes were purchased from commercial suppliers, reagent grade, and used without additional purification. K_2PtCl_4 was purchased from Strem Chemicals. Solvents were of reagent grade unless otherwise noted. **BTF-Br**, **BTFCC-H**, **DPAF-Br**, and **DPAFCC-H** were synthesized according to literature procedures.² **DPAF-Pt-Cl** was synthesized by a literature technique,⁵⁵ and **BTF-Pt-Cl** was synthesized by modification of this technique, but could not be purified past 95%, and was carried on at this purity without further

characterization. Chromatography was performed on a CombiFlash Rf 150 Medium Pressure Liquid Chromotography system. ^1H (500 MHz) and ^{13}C (125.7 MHz) NMR spectra were recorded on a Varian Inova spectrometer. ^{31}P (121 MHz) NMR spectra were recorded on a Varian Mercury spectrometer. The chemical shifts were reported in ppm relative to tetramethylsilane (TMS) or residual solvent peaks.

Absorption and Emission Spectroscopy

Steady-state absorption spectra were recorded on a Varian Cary 50 spectrophotometer. Corrected steady-state emission measurements were performed on a Photon Technology International spectrophotometer (QuantaMaster). Absorption and fluorescence experiments were carried out in aerated solution, while phosphorescence samples were deaerated with at least five freeze-pump-thaw cycles. Optically dilute samples with O.D. < 0.1 at the excitation wavelength were used. Fluorescence and phosphorescence quantum yields were determined by relative actinometry, with $\text{Ru}(\text{bpy})_3\text{Cl}_2$ as an actinometer ($\Phi_{\text{FI}} = 0.0379$ in air saturated water).⁷⁰

Phosphorescence lifetimes were obtained with a multichannel scaler/photon counter system with a NanoQuant FluoTime 100 Compact Phosphorescence Lifetime Spectrophotometer. A UV-pulsed diode laser provided the excitation at 375 nm (power < 10 mW). The laser was pulsed by a PDL800-B, which is a pulsed diode laser driver. Optically dilute solutions were freeze-pump-thawed five times. All decays were obtained using single exponential fitting parameters (FluoFit software).

Nanosecond Transient Absorption (TA) Spectroscopy

Measurements were performed on an in-house apparatus that is described in detail elsewhere.⁷⁷ The third harmonic of a Continuum Surelite series Nd:YAG laser ($\lambda = 355$ nm, 10 ns fwhm, $180 \mu\text{J-pulse}^{-1}$) was used as the excitation source. Probe light

was produced by a xenon flash lamp and the transient absorption signal was detected with a gated–intensified CCD mounted on a 0.18 M spectrograph (Princeton PiMax/Acton Pro 180). Solutions had a matching optical density of 0.58 after at least five freeze-pump-thaw cycles. An initial CCD image capture delay of 100 ns following the laser pulse was used to ensure full conversion to the triplet state before observation. An average of 100 images were acquired and the laser energy was 180 $\mu\text{J}/\text{pulse}$, which was established as being sufficiently low to minimize triplet-triplet power dependence.

Computational Details

DFT and TD-DFT calculations were performed in the Gaussian 09, revision C.01,⁷³ suite of programs at the B3LYP level with the 6-31G(d) basis set for C, H, N, the 6-31+G(d) basis set for P, S, and the SDD basis set for Pt. Phosphorous butyl groups and fluorene ethyl groups were replaced by methyl groups to improve computational efficiency. The ground state structures were optimized in the gas phase from idealized starting configurations without symmetry constraints. The optimized structures were confirmed to be minima by the lack of imaginary frequencies. Structures and orbitals were visualized at an isovalue of 0.02 using Chemcraft Version 1.7,⁷⁹ which was also used to generate charge difference density (CDD) plots. CDDs were imaged at an isovalue of 0.0004.

General Procedure for the Hagihara Coupling Reaction for Mixed Platinum Aryl Acetylide Compounds.

A platinum-aryl precursor (**BTF-Pt-Cl** or **DPAF-Pt-Cl**) (0.100 g, 0.11 mmol, 1 eq.) was dissolved in 25 mL of Et_2NH , and the solution was degassed with argon for 25 minutes. CuI (0.005 g) and 1.1 equivalents of the deprotected arylacetylide (**BTFCC-H** or **DPAFCC-H**) were added. The solution was allowed to react overnight at room

temperature, in the dark. The resulting mixture was poured into water and extracted with CH_2Cl_2 . The organic layer was separated, filtered over Na_2SO_4 , the filtrate was reduced to a minimum, and it was loaded on to silica gel. Purification via MPLC using hexanes/dichloromethane afforded the pure products as oils. Microcrystalline products can be obtained by dissolving the compounds in a minimum of acetone and inducing precipitation with MeOH. The mixtures were cooled, decanted, washed with additional MeOH, and dried to afford the four pure mixed ligand platinum products.

***trans*-(PBU₃)₂Pt(BTF)(CCBTF) (BTF-Pt-CCBTF)**

Isolated as yellow microcrystals. Yield: 76%. ¹H NMR (500 MHz, CD₂Cl₂): δ 8.12 (s, 1H), 7.98-8.08 (m, 5H), 7.94 (m, 2H), 7.76 (d, J = 7.5 Hz, 1H), 7.72 (d, J = 7.5 Hz, 1H), 7.64 (d, J = 7.5 Hz, 1H), 7.27-7.55 (m, 9H), 2.11 (m, 8H), 1.79 (m, 12H), 1.58 (m, 12H), 1.41 (sextet, J = 7.5 Hz, 12 H), 0.94 (t, J = 7.5 Hz, 18H), 0.38 (t, J = 7.5 Hz, 6H), 0.36 (t, J = 7.5 Hz, 6H). ¹³C NMR (126 MHz, CD₂Cl₂): δ 169.6, 169.2, 154.94, 154.90, 154.8, 151.3, 151.0, 150.2, 149.6, 147.5, 145.5, 138.4, 137.6, 135.6, 135.5, 135.2, 133.8, 132.2, 131.3, 130.3, 130.2, 127.6, 127.5, 126.8, 126.7, 125.8, 125.5, 125.3, 123.4, 123.2, 122.20, 122.15, 122.09, 122.02, 120.4, 120.1, 119.4, 119.1, 56.8, 56.4, 33.5, 33.3, 26.8, 24.9 (t, $J^{\text{Pt-C}}$ = 6.6 Hz), 23.3 (t, $J^{\text{Pt-C}}$ = 16.8 Hz), 14.2, 9.2, 8.9. ³¹P NMR (121 MHz, CD₂Cl₂) 1.67 ($J^{\text{Pt-P}}$ = 2600 Hz).

***trans*-(PBU₃)₂Pt(DPAF)(CCDPAF) (DPAF-Pt-CCDPAF)**

Isolated as a white powder. Yield: 60%. ¹H NMR (500 MHz, CD₂Cl₂): δ 7.46-7.55 (m, 3H), 7.20-7.33 (m, 13H), 7.09 (m, 10H), 6.93-7.04 (m, 6H), 1.90 (m, 8H), 1.77 (m, 12H), 1.56 (m, 12H), 1.40 (sextet, J = 7.5 Hz, 12 H), 0.92 (t, J = 7.5 Hz, 18H), 0.36 (t, J = 7.5 Hz, 6H), 0.34 (t, J = 7.5 Hz, 6H). ¹³C NMR (126 MHz, CD₂Cl₂): δ 151.8, 150.7, 150.1, 148.9, 148.7, 147.1, 146.0, 139.9, 138.4, 138.0, 137.8, 135.8, 134.0, 133.5,

130.0, 129.7, 129.6, 125.7, 124.8, 124.4, 124.2, 123.7, 122.8, 122.4, 121.0, 120.4, 120.3, 119.4, 119.1, 118.5, 56.4, 56.1, 33.5, 33.2, 26.8, 24.9 (t, $J^{\text{Pt-C}} = 6.6$ Hz), 23.2 (t, $J^{\text{Pt-C}} = 16.6$ Hz), 14.2, 9.1, 8.9. ^{31}P NMR (121 MHz, CD_2Cl_2) 1.66 ($J^{\text{Pt-P}} = 2600$ Hz).

***trans*-(PBU₃)₂Pt(BTF)(CCDPAF) (BTF-Pt-CCDPAF)**

Isolated as dull-yellow powder. Yield: 43%. ^1H NMR (500 MHz, CD_2Cl_2): δ 8.05 (s, 1H), 8.02 (d, $J = 8.0$ Hz, 1H), 7.99 (d, $J = 8.0$ Hz, 1H), 7.93 (d, $J = 8.0$ Hz, 1H), 7.71 (d, $J = 8.0$ Hz, 1H), 7.53 (d, $J = 8.0$ Hz, 1H), 7.46-7.52 (m, 2H), 7.36-7.45 (m, 4H), 7.21-7.27 (m, 6H), 7.10 (m, 5H), 7.00 (m, 3H), 2.10 (m, 4H), 1.90 (m, 4H), 1.78 (m, 12H), 1.57 (m, 12H), 1.40 (sextet, $J = 7.5$ Hz, 12 H), 0.92 (t, $J = 7.5$ Hz, 18H), 0.36 (t, $J = 7.5$ Hz, 6H), 0.35 (t, $J = 7.5$ Hz, 6H). ^{13}C NMR (126 MHz, CD_2Cl_2): δ 169.6, 154.9, 151.8, 150.2, 150.1, 149.6, 148.7, 147.5, 147.1, 138.4, 137.8, 135.5, 135.2, 133.8, 131.3, 130.1, 129.7, 127.5, 126.7, 125.7, 125.3, 124.4, 124.2, 123.2, 122.9, 122.1, 122.0, 120.4, 120.3, 119.4, 119.12, 119.08, 56.41, 56.38, 33.5, 33.2, 26.8, 24.9 (t, $J^{\text{Pt-C}} = 6.7$ Hz), 23.2 (t, $J^{\text{Pt-C}} = 16.8$ Hz), 14.2, 9.1, 8.9. ^{31}P NMR (121 MHz, CD_2Cl_2) 1.59 ($J^{\text{Pt-P}} = 2600$ Hz).

***trans*-(PBU₃)₂Pt(DPAF)(CCBTf) (DPAF-Pt-CCBTf)**

Isolated as light yellow microcrystals. Yield: 80%. ^1H NMR (500 MHz, CD_2Cl_2): δ 8.10 (s, 1H), 8.04 (m, 2H), 7.95 (d, $J = 8.0$ Hz, 1H), 7.76 (d, $J = 8.0$ Hz, 1H), 7.63 (d, $J = 8.5$ Hz, 1H), 7.50 (m, 2H), 7.40 (td, $J = 7.5$ Hz, $J = 1.0$ Hz, 1H), 7.30 (m, 5H), 7.23 (m, 4H), 7.08 (m, 5H), 6.97 (m, 3H), 2.10 (m, 4H), 1.90 (m, 4H), 1.77 (m, 12H), 1.57 (m, 12H), 1.41 (sextet, $J = 7.5$ Hz, 12 H), 0.93 (t, $J = 7.5$ Hz, 18H), 0.37 (t, $J = 7.5$ Hz, 6H), 0.35 (t, $J = 7.5$ Hz, 6H). ^{13}C NMR (126 MHz, CD_2Cl_2): δ 169.2, 154.9, 151.3, 151.0, 150.7, 148.9, 146.1, 145.6, 139.9, 137.9, 137.5, 135.8, 135.6, 133.5, 132.2, 130.3, 129.6, 127.6, 126.8, 125.8, 125.5, 124.8, 123.7, 123.4, 122.5, 122.2, 122.1, 121.0,

120.4, 120.1, 119.4, 118.6, 56.8, 56.1, 33.5, 33.3, 26.75, 24.9 (t, $J^{\text{Pt-C}} = 6.4$ Hz), 23.2 (t, $J^{\text{Pt-C}} = 16.8$ Hz), 14.23, 9.13, 8.86. ^{31}P NMR (121 MHz, CD_2Cl_2) 1.73 ($J^{\text{Pt-P}} = 2600$ Hz).

APPENDIX A TSUNAMI FEMTOSECOND LASER MANUAL

Overview

The Tsunami laser is a titanium doped sapphire (Ti:Saph) laser, with a useable emission from 700 to 1050 nm. It is pumped by a Millennia eV, which emits the 2nd harmonic of a Nd:YAG source in a continuous wave at 532 nm. The pump laser has a maximum power of 10 W, with the standard operating range of 8-9 W. This gives an output laser power from the Ti:Saph of 0.5 to 1.8 W depending on the output wavelength selected. The Ti:Saph repetition rate is 80 MHz, and the pulse width is less than 100 fs. Assuming a 1.5 W average output power, this results in an ~1.9 nJ/pulse energy. If one then assumes a 100 fs pulse width, the power delivered per pulse is 190 kW. Covered in this manual will be general operation of the laser, acquiring a basic emission spectrum from two-photon excitation, determination of a two-photon absorption cross section, and a troubleshooting guide.

Sample concentration may vary between 10^{-4} and 10^{-5} M, depending on the fluorescence quantum yields of the samples. If obtaining a two-photon cross section, reference compounds with similar absorption/emission energies should be selected,⁹⁰ and the exact concentration of all samples and references must be known so that corrections can be made. The basic absorption and emission properties of the sample should be well known prior to attempting to measure a two-photon cross section.

*****Please note that it is incredibly easy to detune the laser to the point where it no longer lases! Be extraordinarily careful when adjusting the colored knobs to optimize the laser power!*****

Laser Start-up

1. Turn on chiller underneath the laser table.
2. Remove all plastic bags from the optics. Additionally, on the fluorimeter, remove the black piece of plastic so the laser may enter the sample chamber.
3. If it is not already there, place the white Teflon block on the Erlenmeyer flask at the laser output. This will eventually act as a beam stop/diffuser.
4. Open the computer. It should already be logged in and at the desktop.
5. Plug the Ocean Optics detector into the side USB port on the laptop.
6. Open the "Spectra Suite" software. After removing the rubber cover from the Ocean Optics detector you should see weak peaks in the visible region from the ambient lighting.
7. Once the chiller has reached 19°C, the laser may be turned on. First look at the back of the small laser (Nd:YAG pump laser). In the top left area, there is a key that needs to be turned 90° clockwise, and a power button that needs to be depressed.
8. Next, on the computer, open the "Spectra Physics" software. It will take a few moments to connect to the instrument.
9. In the middle of the Spectra Physics software, there will be an indicator telling whether the hardware is ready or not. The laser will take 10-20 minutes to warm-up, as depicted by a yellow indicator.
10. Once the laser has warmed-up the indicator will turn green and be ready to be activated. This is shown in Figure A-1.
11. At the bottom of the Spectra Physics software, the power should be set to '8.2 W'. If it is not, change it to this setting.
12. At the top, toggle the 'Emission' switch to turn on the laser. A small window will pop up to confirm that you want to turn the laser on, click 'yes'.
13. The laser will turn on and the power should increase to the power setting selected at the bottom of the software. If the power does not reach the desired setting, or it is not stable, see the troubleshooting section. The software panel with the pump laser at both low power and requested power is also shown in Figure A-1.
14. Toggle the 'Shutter' switch to open the shutter, this will allow the laser to leave the instrument.

15. Turn on the fluorimeter, and on the desktop computer, open the “Instrument Control Panel”. A window will pop up asking to connect to “Generic Fluoromax 3”, click “yes”.

The laser is now ready for operation.

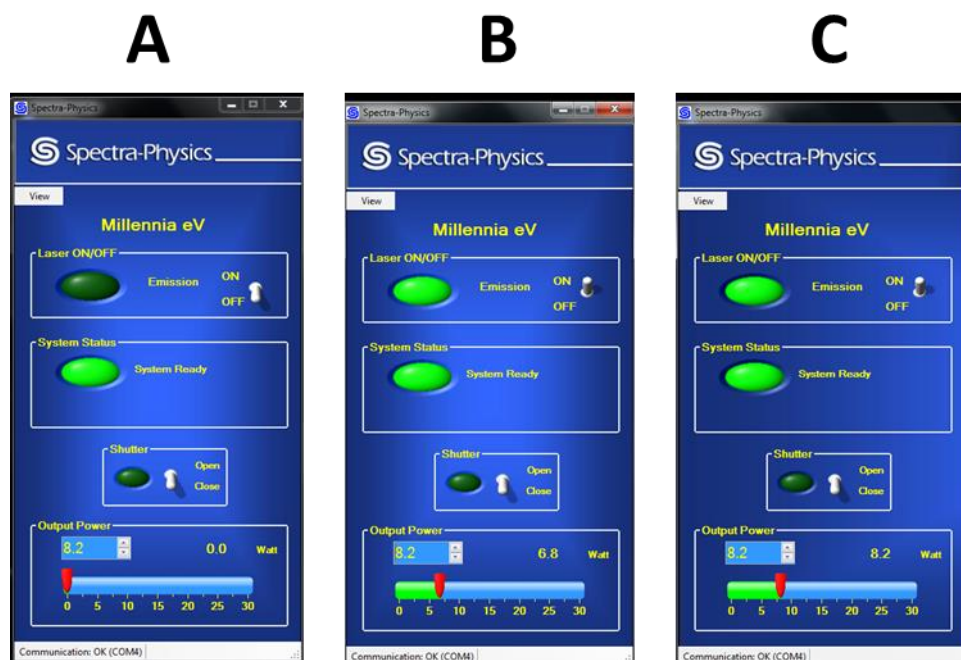


Figure A-1. Spectra-Physics software showing A) the instrument has warmed-up and is ready for to be used. B) Pump laser is operational, but has not come up to the requested power. C) Pump laser is operational, at power, and ready for use.

Laser Wavelength Selection, Mode-Locking, and Output Power Optimization

Wavelength Selection and Mode-Locking

16. On top of the laser there are 2 metal knobs, 2 green knobs, and 2 blue knobs. The two metal knobs are for wavelength adjustment (knob closest to user), and prism adjustment (knob furthest from user). These knobs must be used in tandem to set the output wavelength while keeping the laser mode-locked. The top of the instrument is shown, with knobs labeled, in Figure A-2.
****The instrument is ‘mode-locked’ when the laser output is pulsing. The user will know the instrument is mode-locked by the large bandwidth of the laser output (Full-Width Half-Maximum bandwidth: ~6 nm @ 700 nm output, ~16 nm @ >800 nm output) If the instrument is not mode-locked, the output bandwidth will be very small (~2 nm). This means the output is a ‘continuous wave’, and that the laser is not pulsing. 2PA experiments do not work if the laser is not pulsing. A representative spectra of the output when mode-locked and in continuous wave form is given in Figure A-3****

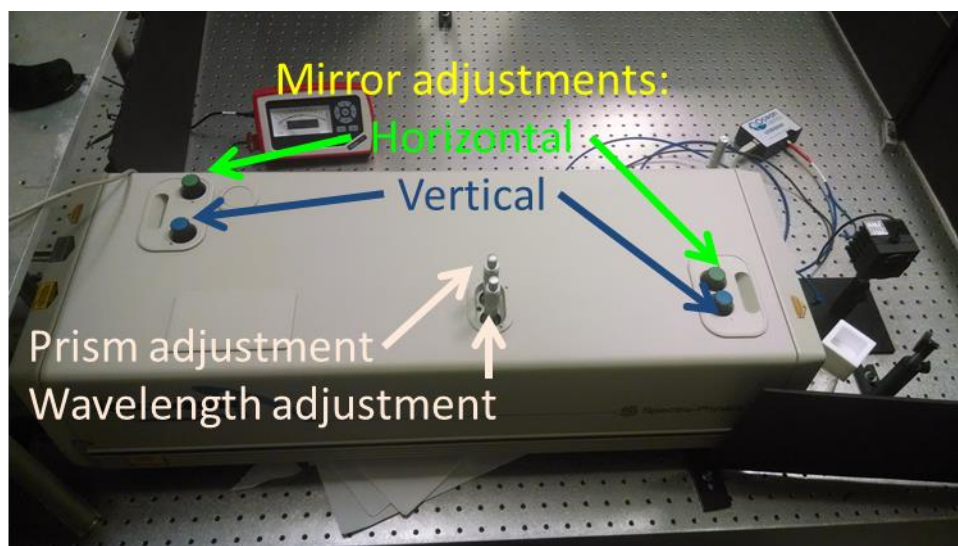


Figure A-2. Top view of the Tsunami laser with each knob labeled.

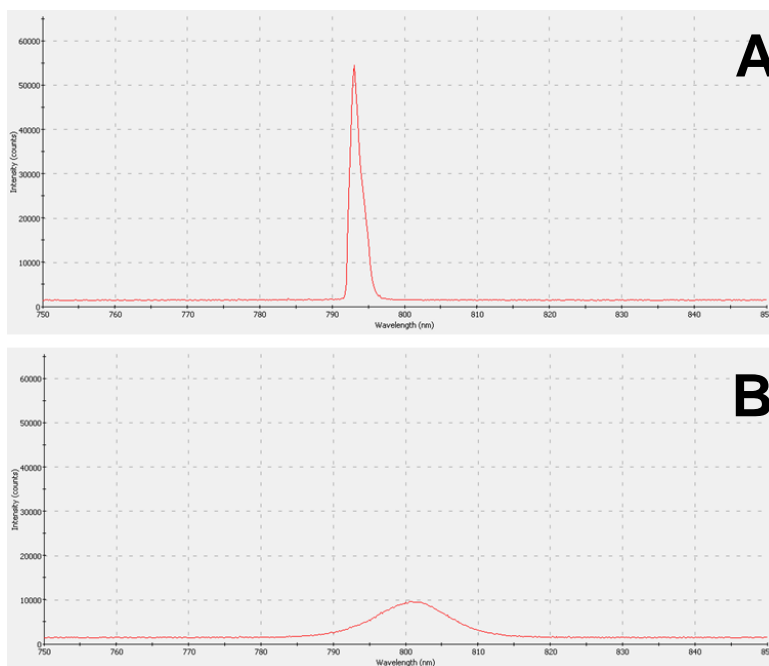


Figure A-3. Shape of the emission band of the Tsunami laser when A) emitting as a continuous wave and B) when pulsing (mode-locked).

17. To change the wavelength, have the Spectra Suite software displayed on the computer and turn the metal knob closest to you in small increments. Clockwise rotation will increase the output wavelength; counterclockwise rotation will decrease the output wavelength.
 **While adjusting the wavelength, it is important to simultaneously adjust the prisms using the other metal knob. When done properly this will keep the instrument mode-locked throughout the entire process of changing wavelength.

Unfortunately, there is no 'hard and fast' rule for prism adjustment, as it is more of an art than a scientific process. With practice this will become easier. A general tip is to try to keep the emission as broad as possible while adjusting the wavelength. If the output bandwidth is narrowing while wavelength adjustment is being made, adjust the prisms to broaden the peak back out.**

Output Power Optimization

18. Once the instrument has been tuned to the proper wavelength, and is mode-locked, move the power meter into the path of the beam after the first mirror. Then remove the white Teflon block that is blocking the beam.
19. Optimum energies at specific wavelengths are given at the end of this document. Depending on the day, you may or may not be able to match the powers given by the technician.
20. To optimize the output power, the four colored knobs on top of the laser will be used. They are **VERY** sensitive! You should never have to take your fingers off of the knob while using it. If twisted even a 1/4 of a revolution TOTAL, lasing can be lost. Use only very, very small adjustments. The green knobs adjust the mirrors horizontally, while the blue knobs adjust vertically. Any knob can be chosen to start, but experience suggests starting with the blue knob closest to the output of the Tsunami (users right). Start by maximizing the power using only that knob.
21. Once the power is maximized using the first knob, move to the other knob of the SAME color, and optimize the power again. Go back and forth with knobs of the same color, one knob at a time, until the power cannot go higher.
22. Repeat this process with the other pair of colored knobs. Ideally, but not always, the power will now match the one reported by the technician.
The mirrors controlled by these knobs should be reoptimized at every new wavelength to ensure maximum output power. If scanning a large region quickly, reoptimize every 50 nm.

Two-Photon Excited Fluorescence (2PEF)

If you are obtaining a two-photon cross section, skip to Step 31. If not continue with Step 23.

23. Before exposing the sample to the laser, make sure that the beam dump is in place in the fluorimeter. This will prevent the laser from being directed into the fluorimeter lamp, which will damage it. Also make sure the black plastic cap has been removed, so the laser may enter the sample chamber without burning through the plastic.
24. Once the beam stop is in place, insert the sample into the fluorimeter.

25. Next, remove all obstructions (power meter/Teflon beam stop) from the path of the beam, so it may pass through the sample. If the sample has 2PA at the current laser wavelength, you should see luminescence from the sample.
26. Before acquiring any data, scan the laser wavelength to see at what input wavelengths your sample has 2PA.
Remember, if you can't see fluorescence, neither can the detector, and there is no point in collecting data at this laser wavelength.
27. Once you know the approximate laser wavelengths that will give 2PA, set the laser to either the highest or lowest wavelength. This will allow you to work from one end to the other.
28. In the software, select your acquisition region, and set the integration time to 0.5 seconds, with a step size of 1.0 nm. Set the lamp wavelength to a value outside of the acquisition region. Be sure to turn off the 'dark offset', as it does not operate properly under these conditions.
29. Give the data a name (use eight characters or less), and then run the acquisition. Repeat this for all samples and blanks before adjusting the laser wavelength.
30. Repeat this for all viable laser wavelengths in 10 nm increments.

Two-Photon Cross Section Measurements

While the data collection steps are the same as described above, some steps must be taken before measuring the two-photon excited fluorescence. First, the samples should be prepared, preferably with an overlap in absorbance at a mutually beneficial wavelength. This wavelength will be the selected excitation wavelength to observe a one-photon emission. The fluorescence observed from the one-photon process determines a parameter called the differential quantum yield (DQY). The DQY is effectively the emission intensity of a sample at a single wavelength (rather than the integration of all emission, hence, 'differential'). This measurement is necessary, as the emission intensity of samples excited with two photons is still based on the fluorescence quantum yield of the sample. A correction is made in the data work-up for the difference in DQY of the sample and the reference.

31. Select an excitation wavelength that is approximately halfway between the absorption maxima of both the sample and the reference. Ideally, the absorption maxima of these compounds will be close to each other. Unfortunately this is not always the case, and you may have to use an excitation wavelength that is not near the maxima. If at all possible, try to make the sample and reference have matching absorptivity values at the excitation wavelength. This ensures the number of photons being absorbed by both compounds are the same. An example of selecting an excitation wavelength from the absorption is shown in Figure A-4. Additionally, this process should be repeated for each new sample.
32. Using the predetermined excitation wavelengths, take a one-photon emission spectrum for all samples and references. Make sure that the beam dump and black card blocking the lamp have been removed. Also replace the black piece of plastic in the side of the fluorimeter and enable the dark offset, as it works properly when the sample chamber is sealed.
33. Once the one-photon emission of all samples and references has been taken, pick an emission wavelength approximately halfway between the emission maxima of both the sample and the reference, preferably where the emission intensities are equivalent. An example of selecting a registration wavelength is also shown in Figure A-4. The ratio of these intensities is the DQY for this sample/reference pair. This DQY is valid ONLY at this one wavelength. Take note of the DQY wavelength. You will need to take emission measurements from the two-photon excited samples at this wavelength.

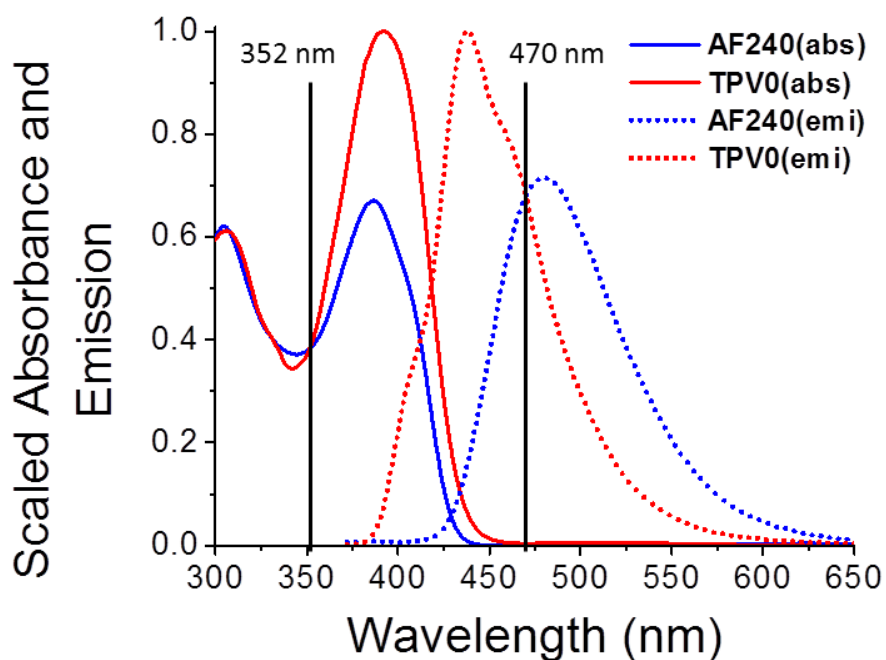


Figure A-4. Absorption (solid colored lines) and emission (dotted lines) of two complexes showing excitation and registration wavelength selections (solid black lines), respectively.

34. Once DQYs have been obtained for each sample/reference pair, replace the beam dump and black card, remove the plastic cap from the side of the sample compartment, and turn off the dark offset in the software.

Return to step 16 to acquire the emission data.

Data Conversion

35. Once all data has been collected, it needs to be converted to a useable file type.
36. Under 'Arithmetic', select 'Do Program', then 'convert.ab' from the left column and 'OK' in the top right. Click 'File Browse', find and select your file, and click okay twice. This converts from the raw instrument data file to a text file.
37. The computer is not connected to the network, so it must be transferred with a flash drive.

Instrument Shut Down

38. Block the laser beam with the Teflon block.
39. In the Spectra Physics software, close the shutter and toggle the laser to off. You should see the power drop to 0 W.
40. On the back of the laser head, push the button and turn the key a $\frac{1}{4}$ turn counterclockwise.
41. After all of the data is converted (as mentioned in the last section) close the Fluoromax software and turn the instrument off. Log the time in the notebook.
42. Five minutes after the laser has been turned off, it is safe to turn off the chiller.

Laser Powers and Bandwidths at Given Wavelengths

Table A-1. Laser powers and bandwidths at given wavelengths.

Wavelength (nm)	Input Pump Power (W)	IR Output (W)	FWHM Bandwidth (nm)
700	8.2	0.7	6
720	8.1	1.1	8
760	8.2	1.75	13
800	8.2	1.6	13
850	8.8	1.5	17
900	8.8	1.1	14
1000	9.0	0.5	14

Data Workup

The final step in a two-photon cross section experiment is to plot the data and run the calculations. If only 2PEF data was collected, simply plot the multiple emission spectra as a function of fluorescence wavelength, with additional curves for each laser wavelength used. The two-photon cross section is calculated using the equation

$$\sigma_{2,s} = \frac{F_{2,s}(\lambda_{reg})c_r\phi_r(\lambda_{reg})}{F_{2,r}(\lambda_{reg})c_s\phi_s(\lambda_{reg})} \sigma_{2,r}, \text{ where } \sigma_2 \text{ is the two-photon cross section, } F_2(\lambda_{reg}) \text{ is the}$$

2PEF intensity at the registration wavelength, c is the concentration, ϕ is the differential quantum yield, and the subscripts 'r' and 's' represent reference and sample, respectively. If the absorption spectra at the selected excitation wavelength were not matched, then a correction factor of $\frac{A_s}{A_r}$ can be multiplied through.

The simplest way to plot these data is to do all manipulations in different worksheets in an Excel workbook. If necessary, due to non-identical absorbance of the sample and reference at the absorption selected excitation wavelength, the first worksheet should contain the absorbance data for both compounds. Take the ratio of the sample absorbance to reference absorbance at the selected excitation wavelength, and make note of this value. If solution and reference absorbance values were matched, the first worksheet should contain the one-photon excited emission data. Take the ratio of reference fluorescence intensity to sample fluorescence intensity, at the registration wavelength, and make note of this value. On the side of one of these initial worksheets, take the ratio of reference solution concentration to sample solution concentration, if they were not identical, and make note of this value.

In the next worksheet, all of the 2PEF data can be added. Make sure to carefully label each data set so there is no confusion as to what value belongs to what data set.

Take the ratio of sample 2PEF intensity to reference 2PEF intensity at the registration wavelength, and repeat this for each laser wavelength. Make note of all of these values. Multiply the 2PEF ratio by the previous values that were noted, as well as the reference two-photon cross section, to give the sample two-photon cross-section. Repeat this for all laser wavelengths, keeping in mind the reference two-photon cross section will change at every wavelength.

Troubleshooting

Pump Laser is not Coming Up to the Set Power

1. In the 'Spectra-Physics' software, click 'View', then 'Communication' to open the communication window.
2. The communication window has a command prompt as well as an input/output section for old commands/returns.
3. This pump laser power problem is caused by un-optimized Second Harmonic Generation (SHG). To query the current SHG setting, type: 'shg?'. Then hit enter. A graphic showing the communication window with the SHG queried and the response from the instrument is shown in Figure A-5.

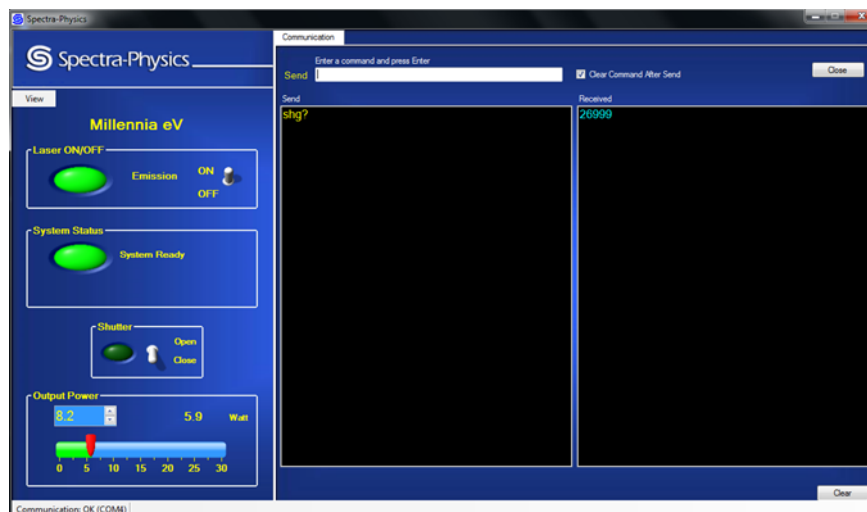


Figure A-5. Spectra-Physics software with the 'Communication' window open with a query sent to the instrument asking for the current value of the 'SHG'.

4. A 5-digit value will be returned, this is the current setting. Typically (>90% of the time), the SHG will need to be adjusted down from the current value. Start in

increments of 25. To adjust the SHG, type: 'shg:XXXXX' where XXXXX is the desired value.

5. After a few seconds, you should notice the energy change. If the energy moves all the way to the desired value and stays stable, you are done and can close the communication window. If the energy increases, but not all the way to the desired value, continue to incrementally adjust the SHG until the desired power is reached. If the energy goes down, adjust the SHG in the other direction as described above.
6. If adjusting in either direction in small increments is not successful, the initial SHG value was probably way off to start. Reduce the value by 1000. This will effectively scan the SHG because the change is not instantaneous. Watch the power meter on the software, and if it spikes at all, the ideal SHG value is somewhere in this range. Work the SHG back towards the initial value to find the ideal value.

Laser Can Not Be Tuned Below 780 nm.

If the laser cannot be tuned to a wavelength below 780 nm, it is typically because the prisms and wavelength cutoff slit are misaligned. This is due to the user turning the wavelength adjustment knob too far, and the laser shooting over the top of the internal slits. To remedy this problem, bring the height of the wavelength selection knob back to a central point. Next, adjust the height of the prism knob to match the height of the wavelength selection knob. Slowly adjust the wavelength back towards 700 nm, while moving the prisms simultaneously, and the 700-780 nm range should now be accessible.

Advanced Troubleshooting

If the system is no longer lasing, the most likely reason is that you have adjusted the knobs for the mirrors too much, and you have detuned the system. If you know exactly which knob you were using when this happened, and did not touch any of the other knobs trying to figure out what you did, then tune only that knob back to its original position. If the system still is not lasing, follow the steps below.

1. Take off the cover of the Tsunami laser, by first releasing the four clasps in each of the corners.
2. Defeat the safety shutter. This will allow the laser to pass into the cavity of the Tsunami. Be careful as the radiation from the pump laser is very intense. Defeating the safety shutter is shown in Figure A-6.

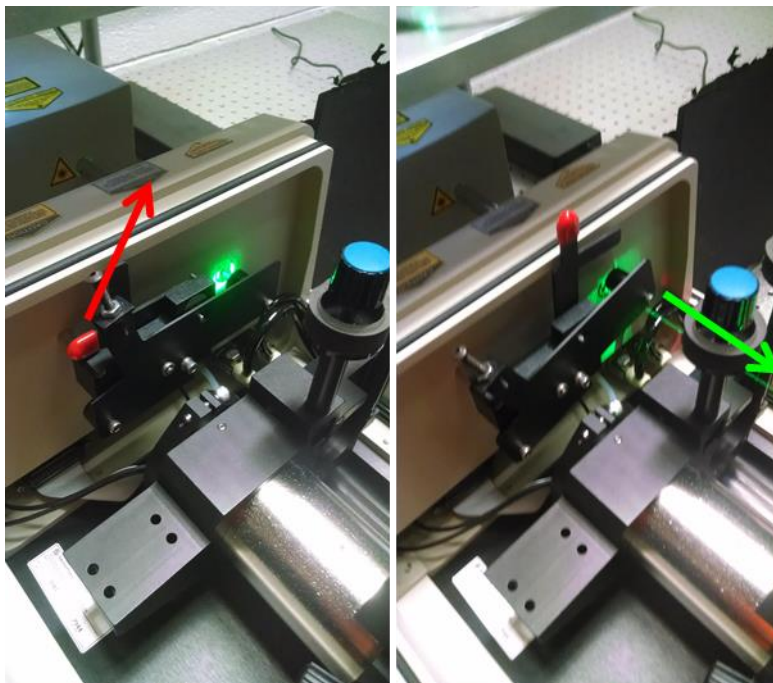


Figure A-6. Defeating the safety shutter on the Tsunami Laser.

3. Because the femtosecond system is not lasing, only a very weak beam will be seen in the cavity of the laser. The IR viewer may be needed, and is helpful regardless, for this process. The first thing to check is that the beam is passing through the wavelength selection slit going forwards (the 'forward' direction will be used when talking about a beam that would be heading out of the instrument).
4. Locate the wavelength selection slit. This will be directly below (attached to) the wavelength selection knob.
5. Ensure the beam is passing through the slit in the forward direction, keeping in mind that a large amount of the laser output is in the near-IR range, and is not visible to the eye. Figure A-7 illustrates the area around the wavelength selection slit while also showing the laser beam passing through.
6. If the beam is missing the slit in the vertical direction, adjust the wavelength selection knob until the beam passes through it. If this does not work, use the blue mirror adjustment knob on the users left (closest to the pump laser).

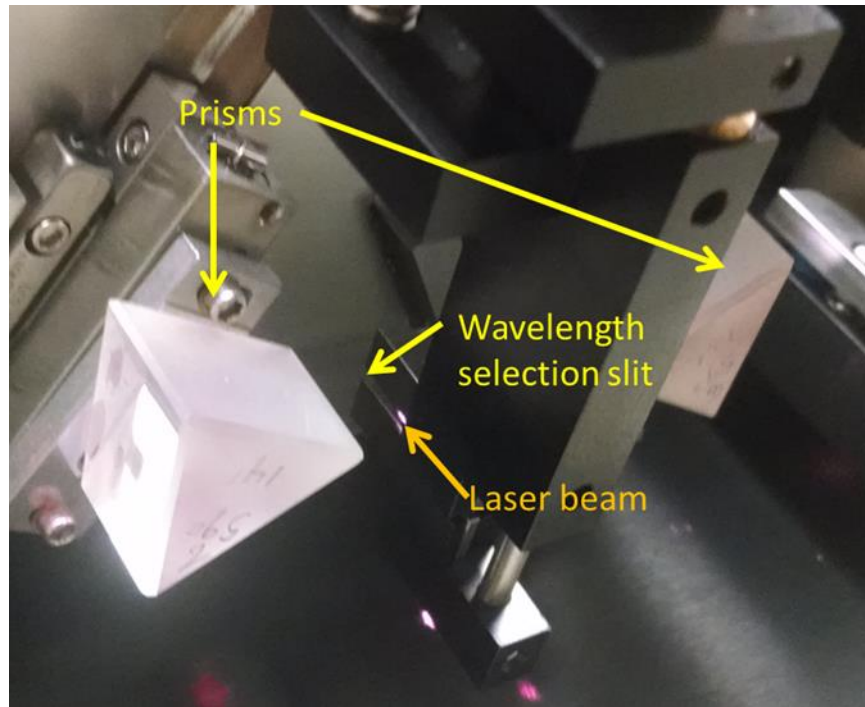


Figure A-7. Area in the region of the wavelength selection slit. The slit itself, the nearest prisms, and the laser beam passing through/being (properly) cutoff by the slit are pointed out.

7. If the beam is missing the slit in the horizontal direction, use the green mirror adjustment knob on the users left (again, the set closest to the pump laser) to bring the beam back into alignment with the slit.
8. Once the beam is passing through the slit in the forward direction, check to see if the retroreflection of the beam is passing through the slit in the reverse direction. This is best done with the IR viewer, especially if the retroreflection is very far off.
9. Do not adjust the wavelength selection knob. If the beam is missing the slit in the horizontal direction, use the green mirror adjustment knob on the users right (closest to the output port) to bring the beam back into alignment with the slit.
10. Once realigned horizontally, use only the blue mirror adjustment knob on the users' right (closest to the output port)
11. Reestablishing lasing takes very precise alignment of the laser (thus why it is so easy to lose lasing). It may take a little bit of very fine tuning to get this to happen. When lasing is reestablished, the beam will become significantly brighter ($>100\times$).
12. Move the power meter into the beam path (outside of the laser cavity), and optimize the power as normal.

APPENDIX B COMPUTATIONAL METHODS

Overview

Computational chemistry is a powerful tool that can enhance knowledge of existing compounds and help try to predict if a target compound will have desirable properties. This appendix will provide first time users with everything they should need to start running their computations from scratch, including but not limited to: a discussion of what job type gives what data, accessing the UF High Performance Computing Center (HPC), using the Gaussian suite of programs, writing input files/reading output files, and visualizing results. This section will discuss only the practical aspects, rather than theory. If the user desires to familiarize themselves with the foundational principles of computational chemistry, *Essentials of Computational Chemistry*⁹¹ does a very good of explaining both fundamental and advanced principles.

There are three main job types that are useful to the Schanze Group, with a few other types that are needed much less frequently. The three main calculation types are: geometry optimization, frequency, and Time Dependent Density Functional Theory (TDDFT). The geometry optimization, as its name implies, takes the atomic coordinates input by the user and finds an energy minimum by systematically altering the coordinates until the force constants on each atom reach a default threshold. The frequency job takes the geometry optimized molecule and computes all vibrational frequencies, effectively giving a simulated IR spectrum. If all frequencies are positive, the molecule is at an energy minimum, and can be used in a subsequent TDDFT job. If not, the molecule will need to have its geometry reoptimized, the method of which will be discussed later. Finally, TDDFT puts the molecule in a simulated electromagnetic

field, and analyzes its response, to simulate a UV-Vis absorption spectrum. A common workflow is shown in Figure B-1.

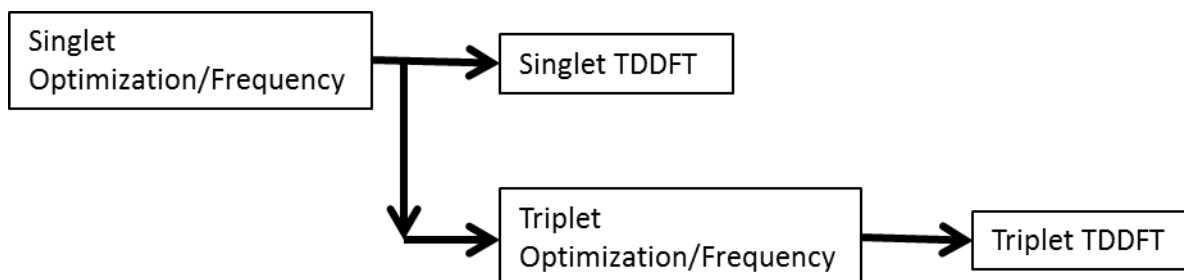


Figure B-1. General workflow of computations.

Less common job types include: stability, population, and volume. Of these, stability is the most common, and is invoked after a failed TDDFT job. During an optimization, the program may have inadvertently used a higher energy wavefunction to describe the molecule rather than the ground state wavefunction. Stability checks this and will reoptimize the molecule with the correct, ground state, wavefunction. The volume job is used to calculate the molecular volume of a system, and is typically used to find a value for the Onsager radius (symbol: a) to be used in a manual calculation of the difference between ground and excited state dipoles. Finally, the population job will print contributions of specific atomic orbitals (AO) to a specified set of molecular orbitals (MO). This allows the user to determine the percent contribution of an atom or moiety to an MO.

Accessing the HPC

In order to start on one's computational endeavor at UF, they must first apply for an account through the HPC and learn how to use UNIX. To open an HPC account, simply visit <http://www.hpc.ufl.edu>, and under the 'Help' tab, select 'Request New Account'. Fill out the form, and usually an account will be created within a couple of

hours. An email will be sent to notify the user of account creation. The HPC is accessed using an SSH shell client at the address 'gator.hpc.ufl.edu'. SSH uses a UNIX interface, and the VI editor word processor. Tutorials to both can be found here: <http://www.ee.surrey.ac.uk/Teaching/Unix/> and here: <http://www.unix-manuals.com/tutorials/vi/vi-in-10-1.html>, respectively. Once connected to the HPC via SSH, the system will start the user in what is termed their 'home folder'. This will be `/home/username` in the HPC file system. No computations should be run in this location. A large amount of storage for each user is allocated at the location `/scratch/lfs/username`, and this is where all jobs should be created and stored. Please see the UF HPC website and their wiki page for additional details on proper use and technical details.

General Considerations

Before diving in to making files and running jobs, some general practices for computational chemistry will be laid out to ensure the user is aware of them. First, the DFT functional and atomic basis set must be consistent throughout the entirety of the workflow. A frequency calculation using the 6-31G(d) basis set on a molecule that had its geometry optimized using 6-311+G(d) (or any other basis set that is not exactly 6-31G(d)) will be invalid. This goes for TDDFT jobs as well. The same principle also applies to the DFT functional that was chosen. For the work of the Schanze Group, the B3LYP functional tends to be superior. The 6-31G(d) basis set can be used for all light atoms ($Z < 10$), the 6-31+G(d) basis set can be used for third-row and lower non-metals, and the SDD basis set for all metals.

Gaussian input files are not submitted directly to the HPC. The HPC uses a batch submission system and a scheduler to determine what jobs should be started to maximize allocation of resources. To achieve this, a submission script is required. This

submission script contains all details about the hardware that the user is requesting for the job. Specific details and an example script will be provided in a later section.

In order to use Gaussian, a confidentiality agreement must be signed. This is because Gaussian is restricted software. The form must be signed in person, is located in NPB 2335, and is available during any office hours of Dr. Deumens. See http://wiki.rc.ufl.edu/doc/Gaussian_License for further details.

Using Gaussian 09 and GaussView 5 via the HPC

The user does not directly interact with the main Gaussian program. All interaction is through the SSH client and the GaussView⁹² program. Gaussian simply accepts the input file, runs the computations, and generates an output file.

Before GaussView can be used, an X Windows Remote display program must be used. Please see <http://wiki.rc.ufl.edu/doc/Gaussview> for details on how to install and configure the software. Once the software is set up, GaussView can be opened. The user should take some time and familiarize themselves with the basic features and tools that can be used to manipulate molecular structures. A reference guide for GaussView can be found here http://www.gaussian.com/g_tech/gv5ref/gv5ref_toc.htm.

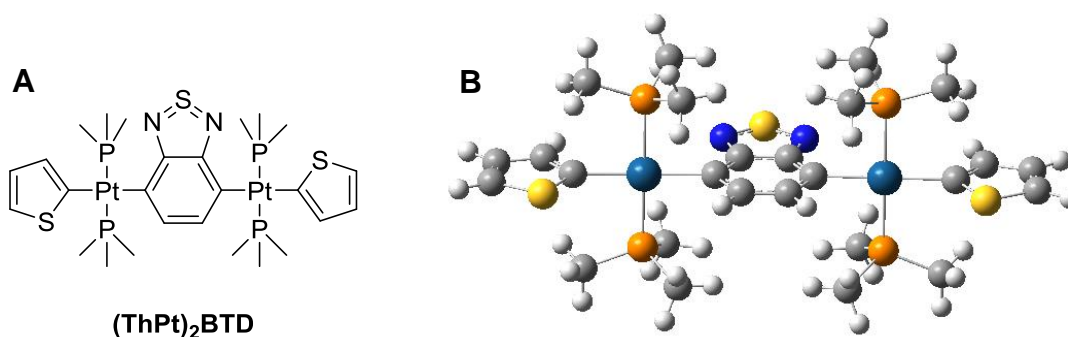


Figure B-2. A) 2-D Chemdraw model of **(ThPt)₂BTD**. B) 3-D model of **(ThPt)₂BTD** built and visualized in GaussView. C: Gray, H: White, N: Blue, P: Orange, S: Yellow, Pt: Cerulean.

Throughout this appendix, the molecule **(ThPt)₂BTD** will be used as an example for all of the common computational methods, and its structure is shown in Figure B-2. Other molecules will be used for less common job types.

Creating Input Files and Submitting Jobs

This section will take the user through saving a created molecule as an input file (.com file type) for all different job types. Examples will be given, and specific keywords will be explicitly discussed. To start creating an input file, click the 'Calculate' tab, and 'Gaussian Calculation Setup', shown in Figure B-3. Figure B-4 shows a blank calculation setup window. The user will be able to specify all commands (keywords) through this window.

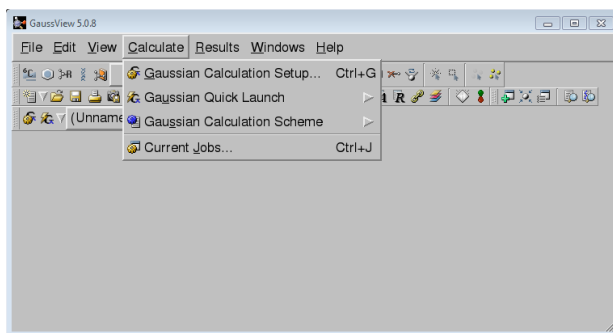


Figure B-3. GaussView main window showing options of the Calculate tab.

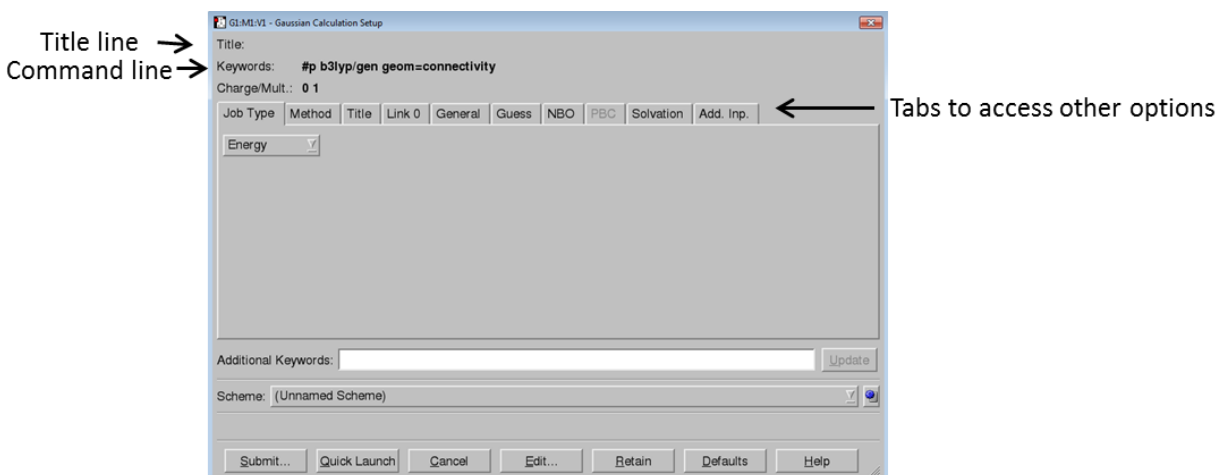


Figure B-4. Blank calculation setup window with notable areas labeled.

Geometry Optimization/Standard Input Parameters

As stated earlier, the geometry optimization, or just optimization, is the first calculation run, and works to find an energy minimum on the potential energy surface of the molecule. However, the optimized geometry found may only be a local energy minimum, rather than the true ground state minimum. This is exemplified by the orientation of the thiophene rings relative to the BTD ring in **(ThPt)₂BTD**. There are three major conformations which can be defined by whether the sulfur atoms in each ring are cis or trans with each other. Thus the three conformations are S-cis, S-cis; S-cis, S-trans; S-trans, S-trans. These three conformations are illustrated in Figure B-5.

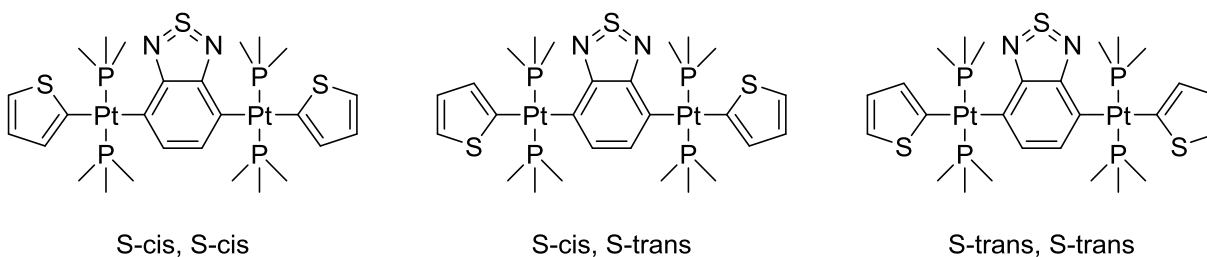


Figure B-5. Major conformations of **(ThPt)₂BTD**.

A single optimization will not be able to look at all three of these conformations because of the relatively high energy barrier to thiophene rotation. Three separate jobs must be created, one for each individual starting geometry. An appended sample input file, with important lines and commands labeled, is shown in Figure B-6.

The input file contains a variety of information, and discussion of these parameters will begin with variables that are seen in multiple job types. The first two lines are commands to allocate the physical resources of processors and RAM. These values must match the values given in the HPC job submission script, which will be shown later. The third line is the name of the checkpoint file. All useful data created by every job is stored in the checkpoint file upon completion of the job. This allows the user

```

%npocshared=8
%mem=8000MB
%chk=thpt2.chk
#p opt freq b3lyp/gen nosymm geom=connectivity int=ultrafine pseudo=read
thpt2 ult freq
0 1
C      0.00000000    0.71317702    1.11491540
C      0.00000000   -0.71317702    1.11491540
C      0.00000000   -1.42029762   -0.09511439
C      0.00000000   -0.68282031   -1.29089849
C      -0.00000000    0.68282031   -1.29089849
C      -0.00000000    1.42029762   -0.09511439
H      0.00000000   -1.22001601   -2.25110057
H      -0.00000000    1.22001601   -2.25110057
Pt      0.00000000   -3.47969424   -0.14496954
Pt      -0.00000000    3.47969424   -0.14496954
N      0.00000000   -1.17199571    2.49164303
N      -0.00000000    1.17199571    2.49164303
S      0.00000000   -0.00000000    3.31340355
.
.
H      4.01563755   -5.19224961   -0.23852666
C      2.94668126    5.18628778   -0.28539781
H      2.62911801    5.56708604   -1.23357832
H      2.55196351    5.80120759    0.49624887
H      4.01563755    5.19224961   -0.23852666

1 2 1.5 6 2.0 12 1.0
2 3 2.0 11 1.0
3 4 1.5 9 1.0
4 5 1.5 7 1.0
5 6 1.5 8 1.0
.
.
.|
77
78 79 1.0 80 1.0 81 1.0
79
80
81

C H N O
6-31G(d)
****
P S O
6-31+G(d)
****
Pt O
SDD
****

Pt O
SDD

```

Number of processors requested

Amount of physical memory requested

Name of checkpoint file

Route section (command line)

Title line

Charge and Multiplicity

Atomic symbol

Cartesian coordinates

Connectivity information

Basis set information

At least two blank lines to signal the end of the script

Figure B-6. Appended input file for the geometry optimization/frequency calculation of (ThPt)₂BTD.

to carry information between jobs so it does not have to be respecified by the user (atomic coordinates) or recalculated by the program (energies, force constants, etc.).

The name of the file can be anything the user desires, as long as the filetype (.chk) is left in place. The user should be careful though, because when the checkpoint file is used in a subsequent job, the file will be overwritten if it has not been copied and given a different name, or if it has not been moved to a different folder. The fourth line is the route section, or command line, and it will be discussed last, as it is the most complex. A blank line must follow the command line to signal termination of the command line to the program. The next line is the title, and it may contain whatever the user desires, as long as there is something there. Another blank line should follow the title line. The next line contains the charge and multiplicity, respectively. Most computed molecules in the Schanze Group are closed shell singlets or triplets, which would be denoted '0 1' or '0 3', respectively. On occasion a radical cation may need to be run, which would be denoted with '1 2'. For reference, the values for radical anion would be '-1 2'. Following the charge and multiplicity, the atom labels and their Cartesian coordinates are given for every atom. The full list is appended to save space in Figure B-5. This list is generated entirely by the program based on the molecule built by the user. After another blank line, connectivity information is written. This is generated by the 'geom=connectivity' keyword, which GaussView automatically activates for geometry optimizations. One more blank line separates the final region of text.

The last area of text specifies basis set information. Simple organic molecules can use a single basis set, which would be specified in the command line; however, molecules with heavier atoms require more specialized basis sets. In order for the

program to recognize commands in this region, the 'gen' basis set and 'pseudo=read' must be specified in the command line. The format of this text first states a string of atomic symbols, followed at the end of the line by a zero (0) and a return. Below the atom string is the basis set, and below that is a series of four (4) asterisks. This is repeated until every atom in the molecule is assigned a basis set. After the last atom or set of atoms are specified, as described above, a blank line is given with the last string of atoms and basis set repeated. Please note that this 'disconnected' basis set specification is only necessary when the molecule contains a metal atom. Finally, at least two blank lines must be given to signal the end of the input script to the program.

Coming back to the command line, all of the keywords specific to individual jobs are specified here. Working from left to right in the file shown in Figure B-6, the pound sign (#) signifies the start of the command line. The command 'p' specifies that the job print extra output information, and it must immediately follow the pound sign (#p) if this is desired. All commands after this point may be in whatever order the user prefers. The next commands shown are 'opt' and 'freq', with 'opt' being the keyword for the geometry optimization and 'freq' being the keyword for the frequency calculation. A convenience of Gaussian 09 is that a molecule may be optimized and have frequencies calculated in a single job. This is neither required nor necessary, but it can be convenient for systems with less than ~150 atoms or ~900 electrons. Specific commands to purely frequency jobs will be discussed in the next section. The next pair of keywords are 'B3LYP/gen', which represent a DFT functional and basis set, respectively. As mentioned earlier, the B3LYP functional tends to be superior to others for platinum acetylide systems. Also mentioned earlier, the 'gen' basis set must be specified if one is to use multiple basis

sets for a single molecule. While 'gen' will usually be used in conjunction with 'pseudo=read', this may not always be the case. If the user does not have any metal atoms, but still wants to use multiple basis sets because of other heavy atoms (for example, in thiophene oligomers), only the 'gen' command is required. The 'pseudo=read' command tells Gaussian that a pseudopotential is to be used for an atom. This atom is specified in the 'disconnected' part of the basis set information. The 'nosymm' command turns off any symmetry constraints that may be placed on the molecule. Typically, molecules subject to symmetry constraints do not optimize to a minimum, and require a second optimization job to reach a minimum. Calculations done on molecules in the triplet state should always specify the 'nosymm' keyword. The last keyword that has not been discussed is 'int=ultrafine', and it corresponds to the number of points used to integrate the electron density of the DFT optimized molecule. This specifies that an integration grid which uses more points than the default grid in order to generate a more precise result. While some computational chemists say that problems can arise from using a finer integration grid, these 'problems' have not manifested in compounds used by the Schanze Group. The 'int=ultrafine' keyword should be specified for all optimizations that the user wishes to publish.

Frequency

Once a geometry optimization has finished, the next thing the user must do is ensure that the optimized geometry is a minimum on the potential energy surface. Again, this can be done in the same job as the optimization, but for large molecules this is not feasible due to time and hardware constraints of the HPC. Before creating an input file for a frequency job, the user should first create a copy of the checkpoint file generated by the geometry optimization. The copied checkpoint file can either have its

name modified, or it can be copied to a new folder. Using new folders is recommended by the author, and will be assumed when discussing subsequent input files, but ultimately this is the users' preference. An example frequency input (shown as if the frequency was run separately from the geometry optimization) file is given in Figure B-7.

```

%nprocshared=8
%mem=8000MB
%chk=thpt2.chk
#p freq b3lyp/gen nosymm guess=read geom=check int=ultrafine pseudo=read

thpt2 freq
0 1
C H N O
6-31G(d)
****
P S O
6-31+G(d)
****
Pt 0
SDD
****

Pt 0
SDD

```

At least two blank lines to signal the end of the script

Figure B-7. Example input file for the frequency calculation of **(ThPt)₂BTD**.

The first thing one should note is that there is no information about atoms, their coordinates, or their connectivity. All of these data are contained within the checkpoint file taken from the geometry optimization. Using the checkpoint file for these data requires three things. First, the name of the checkpoint file in the frequency input file must match the name of the copied checkpoint file generated from the optimization. If the name in the input file is different, the program will not be able to read the file, and the job will fail. Second, the keyword 'guess=read' specifies that an initial guess of the wavefunction is read from the checkpoint file. Third, the keyword 'geom=check' specifies that the molecular geometry is also read from the checkpoint file.

Time Dependent Density Functional Theory (TDDFT)

The final routine job used in the Schanze Group is TDDFT. This job generates vertical electronic transitions for a molecule, as well as the oscillator strength and molecular orbital contributions of the transition. A TDDFT job effectively simulates the UV-Vis absorption spectrum of a molecule. An example input file is shown in Figure B-8.

```
%nprocshared=8
%mem=8000MB
%chk=thpt2.chk
#p b3lyp/gen guess=read geom=check pseudo=read td=(nstates=XX)

thpt2 TDDFT
0 1
C H N O
6-31G(d)
****
P S O
6-31+G(d)
****
Pt 0
SDD
****

Pt 0
SDD
```

Number of processors requested
Amount of physical memory requested
Name of checkpoint file
Route section (command line)
Title line
Charge and Multiplicity
Atomic symbols, Cartesian coordinates and connectivity not required
Basis set information

At least two blank lines to signal the end of the script

Figure B-8. Example input file for the TDDFT calculation of **(ThPt)₂BTD**.

The user will again need to copy the checkpoint file and change its name or copy it to a new folder. The 'guess=read' and 'geom=check' keywords are retained, as these will again be read from the checkpoint file; however, the 'int=ultrafine' keyword is lost, as there is no need for integration in the TDDFT job. The 'freq' keyword is now replaced by 'td=(nstates=XX)', where 'XX' is a number of the users choice. This number tells the program how many vertical transitions to calculate, and it will start with the lowest energy transitions. If only the absorption corresponding to the HOMO-LUMO gap is required, then five (5) is an acceptable number. However, the molecules of the Schanze

Group are typically complex and have more features in their absorption spectra. A value in the range of 15-30 is usually required to see all major electronic transitions at wavelengths longer than 300 nm in these molecules. Be careful though, as the amount of time to run a TDDFT job gets exponentially larger with the number of transitions calculated.

Triplet Computations

General considerations

A major area of study in the Schanze Group is the photophysical properties of molecules in the triplet state. The main purpose of calculating molecules in the triplet state is to simulate the transient absorption (TA) experiment by running TDDFT on a triplet optimized molecule. This process is almost completely analogous to the process for singlet molecules, with one main difference. As alluded to in Figure B-1, the triplet geometry optimization comes after the singlet geometry optimization. This is because, depending on the starting singlet structure input by the user, the triplet may optimize in a completely different way based how it was built. A triplet optimization should start from the optimized singlet structure so that the computational triplet has the best chance to match the structure of the lowest energy experimental triplet.

For this job, it is easiest to have GaussView specify the atomic coordinates and connectivity, rather than trying to use a checkpoint file. The user will open the singlet optimized structure in GaussView and setup a new calculation, but now specifying '0 3' for the charge and multiplicity (no charge/triplet). The subsequent frequency and TDDFT jobs are setup and run exactly the same as before, but again with the '0 3' specification to signal to the program that the molecule is in the triplet state. The triplet TDDFT job should ask for at least 25 states to be calculated, as there are many low

oscillator strength transitions that may not allow higher energy transitions with high oscillator strength to be calculated.

Estimation of phosphorescence energy

For molecules that are not expected to be phosphorescent, Gaussian can be used to approximate this energy. All that is needed are the optimized singlet and optimized triplet. Determination of the phosphorescence energy will be discussed in the Results section.

Stability

On occasion, the wavefunction of an optimized triplet molecule will not be in the ground state. A molecule with this problem will not show any sign of error until the results of the TDDFT job are examined, where an electronic transition of negative energy will be predicted. An output illustrating this problem will be shown in a later section. To remedy this problem, a stability job can be run to find and optimize the lower energy wavefunction for the molecule. An input file for this type of job is shown in Figure B-9. A checkpoint file from any previous job is needed as a starting point, and the keyword 'stable=opt' is required. Upon completion of this job, the user will have to run another frequency calculation to ensure that the new state is an energy minimum, and then run TDDFT again. Only in extremely rare cases will the stability job not fix the error in the wavefunction on the first try.

Population

A Gaussian population analysis gives coefficients for every atomic orbital (AO) in a user specified range of molecular orbitals (MO). This is useful for determining percent contributions of atoms or moieties to the overall MO. This job can be run at any time after a molecule is found to be at an energy minimum, and the appropriate checkpoint

file is again required for proper execution of this job. An example is shown in Figure B-10.

```
%nprocshared=8
%mem=8000MB
%chk=tripfphptphf.chk
#p b3lyp/gen guess=read geom=check pseudo=read stable=opt

bis(4-fluorophenyl)platinum carbene stability

0 3

C H N F O
6-31G(d)
****
Pt 0
SDD
****

Pt 0
SDD
```

Figure B-9. Example input file for a stability job on a platinum aryl compound.

```
%nprocshared=8
%mem=8000MB
%chk=tbtpop.chk
#p b3lyp/gen guess=read geom=check pseudo=read pop=nboread

TBTz NAO orbitals

0 1

C H N O
6-31G(d)
****
P S O
6-31+G(d)
****
Pt 0
SDD
****

Pt 0
SDD

$NBO NAOMO $END
```

Figure B-10. Example input file for generation of Natural Atomic Orbitals.

There are two additions to the 'base' commands for this job. First, the 'pop=nboread' keyword must be specified. This tells the program that the Natural Bond Orbital (NBO) module (NBO version 3.1⁹³) will be used, and that the NBO specific command(s) will be read at the end of the input script. The keyword string to give after the basis set information is '\$NBO NAOMO \$END'. This will print the appropriate data in the output so that it can be read by Multiwfn,^{94, 95} which is a program for MO composition analysis. It should be noted that regardless of the order of 'pseudo=read' and 'pop=nboread' in the command line, the NBO string should always be after the basis set specification. Reversing the order of these two (putting the NBO string before the basis set info) will result in immediate failure of the job.

Volume

If the need arises to calculate an Onsager radius, the volume job will give this value directly. An Onsager radius is one of the variables used in the estimation of the difference in dipole moments between ground and excited state. An example is shown in Figure B-11. The volume job simply requires the 'volume' keyword. Specifying 'volume=tight' gives a more accurate result and is highly recommended.

PBS Script

Once the user has created their input file, they must now properly edit their PBS script to ensure all values here match between the two files. The PBS script is a normal text file, just like all the other files dealt with here, but it should be noted that all commands in this file are case sensitive. The HPC wiki page maintains an up to date version of the PBS script for Gaussian 09 job submission at http://wiki.rc.ufl.edu/doc/Gaussian_PBS. A version that is slightly modified to remove extraneous lines is shown in Figure B-12.

Working from the top down, the first three lines should never need to be changed. The first line specifies that this is a Bourne shell script. It is not important to know what the Bourne shell is. The second line requests that the job is submitted to the

```
%nprocshared=8
%mem=8000MB
%chk=aume.chk
#p b3typ/gen guess=read geom=check int=ultrafine pseudo=read volume=tight

AuMe volume

0 1

C H N O
6-31G(d)
****
P S O
6-31+G(d)
****
Au O
SDD
****

Au O
SDD
```

Figure B-11. Example input file for a volume job of a gold acetylide compound.

```
#PBS -S /bin/bash
#PBS -q default
#PBS -m abe
#PBS -M youremail@ufl.edu
#PBS -N jobname
#PBS -l walltime=72:00:00
#PBS -l nodes=1:ppn=8
#PBS -l pmem=8000mb

module load gaussian
which g09
cd $PBS_O_WORKDIR
g09 < molecule.jobtype.com > molecule.jobtype.out
```

Annotations:

- Script type**: points to `#PBS -S /bin/bash`
- Submission queue**: points to `#PBS -q default`
- Send email upon job abort/begin/end**: points to `#PBS -m abe`
- Email address to send notifications**: points to `#PBS -M youremail@ufl.edu`
- Name of job**: points to `#PBS -N jobname`
- Hardware time requested**: points to `#PBS -l walltime=72:00:00`
- Number of nodes:processors requested**: points to `#PBS -l nodes=1:ppn=8`
- Amount of RAM requested**: points to `#PBS -l pmem=8000mb`
- Program specifications**: points to `module load gaussian` and `which g09`
- Input file name**: points to `molecule.jobtype.com` in the command line
- Output file name**: points to `molecule.jobtype.out` in the command line

Figure B-12. Example PBS script for submitting jobs to the HPC.

default queue. Other queues are available, but not needed for the jobs run by Schanze Group members. The third line requests that an email is sent to the user when the job begins (b), when the job ends (e), or if the job is aborted (a). The fourth line is the email which notifications will be sent to. The fifth line is a job name specified by the user. This name is included in the notification emails, and is very helpful when running multiple jobs at the same time. The sixth line is the amount of real time (as opposed to CPU time) requested by the user. For smaller organometallic optimization/frequency jobs, 72 hours tends to be sufficient. 144 hours is the maximum allowed, and will need to be invoked for large molecules. Any amount of time below 144 hours is permitted, and as the user becomes more comfortable they will be able to more accurately judge the time required for a job. The seventh line is the number of nodes and processors per node requested, respectively. The number of nodes will always be one due to licensing limitations, but the number of processors may range from 1 to 16. Eight (8) processors seem to give the best balance between job time and time spent in the queue for organometallic molecules. While having more processors will allow the job to run faster, it will spend more time in the queue before it starts because it is requesting a larger amount of resources. The final line of #PBS specification is the amount of physical memory (RAM) requested. While there are ways to optimize the amount of RAM per job, so that one is not requesting excess and wasting resources, a safe method is to use 1000MB of RAM per core. It is of utmost importance that the number of processors and amount of RAM requested in the input file and the PBS script is the same in both places. Adverse effects are expected if these values do not match.

The next three lines of commands are for the system and do not need to be changed. 'Module load gaussian' tells the system to load the Gaussian software and make it available to the submitted job. 'Which g09' chooses the appropriate version of Gaussian 09, and it is typically the latest revision (revision D.01. as of this writing). The 'cd \$PBS_O_WORKDIR' command tells the system to "change directory to the place where the job was submitted from". This ensures that all files generated while the job is running are placed in the same folder as the input file.

In the last line, the program to be used, the input file name, and the output file name are listed. The program file name is 'g09'. Again, this is case sensitive, so using 'G09' would immediately return an error. Next, the name of the input file is found between brackets, with a space between the brackets and the file name. The input file name should be intuitive to the user, so that they do not have to open the file to know what type of data is contained. Additionally, input files should always end in '.com'. This is the standard input file type read by Gaussian and GaussView. The output file will ideally have the same name as the input file, but with the '.out' extension. Again, this is to ensure compatibility with the software. The author recommends that a file is named according to the format 'molecule.jobtype.com'. This efficiently gives what molecule and what job is being run.

When the input file and submission script are ready to go, type the command: *qsub submission script file name*. This will submit the job to run, and the HPC will return a job number. While a job is running, the output file can be read. This will let the user track the progress of the job; however, most of the useful data is written only when the job finishes.

Reading and Interpreting Output Files

The output file contains a multitude of data, only a few lines of which is useful to the user. An overview of some non-essential, but good to know, data is shown in Figure B-13. Every output starts with software initialization, copyright and citation information, repetition of the specified input, and molecular structure information. From there, the output moves into data that is specific to individual job types.

```

: ← Initialization and copyright information
:
: ← Suggested citation
Cite this work as:
Gaussian 09, Revision C.01,
M. J. Frisch, G. W. Trucks, H. B. Schlegel, G. E. Scuseria,
:
: ← Citation continues/end of citation
and D. J. Fox, Gaussian, Inc., Wallingford CT, 2010. ←

*****
Gaussian 09: AM64L-G09RevC.01 23-Sep-2011
30-Oct-2013
*****
%nprocshared=8
will use up to 8 processors via shared memory.
%mem=8000MB
%chk=thpt2.chk ← Specified input

-----
#p opt freq b3lyp/gen nosymm geom=connectivity int=ultrafine pseudo=re
ad
-----
1/14=-1,18=20,19=15,26=3,38=1,57=2/1,3;
: ← Software routing info/initial atomic coordinates
:
General basis read from cards: (5D, 7F)
Centers: 1 2 3 4 5 6 14 15 17 19 22 23 25 27 34 38 42 46 50 54
Centers: 58 62 66 70 74 78 7 8 18 20 21 26 28 29 35 36 37 39 40 41
Centers: 43 44 45 47 48 49 51 52 53 55 56 57 59 60 61 63 64 65 67 68
Centers: 69 71 72 73 75 76 77 79 80 81 11 12
6-31G(d)
****
Centers: 30 31 32 33 13 16 24
6-31+G(d) ← Basis set information
****
Centers: 9 10
SDD
****

: ← Steps specific to job type
:
:

```

Figure B-13. Routine information given in every Gaussian output file.

Geometry Optimization

The geometry optimization will continue to iterate geometries until a stationary point has been found. Figure B-14 shows part of the output when a stationary point has been found. Atomic forces and displacements make up the criterion for successful optimization. The output will then list internuclear distances, angles, dihedral angles, and orbital energies. N-pole moments ranging from dipole to hexadecapole, broken down into vectors along Cartesian axes, are then listed. This is shown in Figure B-15.

```

.
.
.
D227      -3.04918    0.00000   -0.00013   -0.00005   -0.00019   -3.04937
D228      -0.93936    0.00000   -0.00013   -0.00003   -0.00015   -0.93951
      Item              value      Threshold  Converged?
Maximum Force           0.000019      0.000450      YES
RMS Force               0.000003      0.000300      YES
Maximum Displacement    0.001703      0.001800      YES
RMS Displacement        0.000367      0.001200      YES
Predicted change in Energy=-1.942921D-08
Optimization completed.
  -- Stationary point found.

-----
!   Optimized Parameters   !
! (Angstroms and Degrees) !
.
.
.

```

Figure B-14. Successful optimization of **(ThPt)₂BTd** to a stationary point.

```

.
.
.
Charge=                0.0000 electrons
Dipole moment (field-independent basis, Debye):
  X=          -0.0002    Y=          -0.0027    Z=          -0.5636
Tot=          0.5636
Quadrupole moment (field-independent basis, Debye-Ang):
  XX=        -268.1906    YY=        -345.9369    ZZ=        -311.9528
  XY=         -0.0352    XZ=          0.0007    YZ=          0.0139
Traceless Quadrupole moment (field-independent basis, Debye-Ang):
  XX=         40.5029    YY=        -37.2435    ZZ=        -3.2594
  XY=         -0.0352    XZ=          0.0007    YZ=          0.0139
Octapole moment (field-independent basis, Debye-Ang**2):
  XXX=        -0.0361    YYY=        -0.1880    ZZZ=        -61.2180
  XYY=        -0.0150
.
.
.

```

Figure B-15. N-pole moments for **(ThPt)₂BTd**.

Finally, a very dense set of data is given summarizing the findings of the job. The tail end of this is shown in Figure B-16. A data point that can be extracted from this information is the total energy of the system. This value is useful in conformational analysis, as a larger negative number represents a more stable system. Additionally, if the triplet geometry of a molecule has been optimized, the difference in energies between the singlet and triplet represent the adiabatic triplet energy.⁴⁵ This energy difference is a good estimation of the triplet energy/phosphorescence. The last few lines consist of a quote, CPU time, and sizes of files generated during the job. The user must be cautious, as the values obtained here are only valid if the molecule is at an energy minimum.

```
.
.
.
.1768008656,0.1327313625\H,2.9122401644,5.889018482,-0.6337251361\H,2.
9799715898,5.6055540339,1.1071058456\H,4.3120292898,5.0180522358,0.066
2226655\\version=AM64L-G09RevC.01\HF=-3925.6671422\RMSD=3.809e-09\RMSF
=4.508e-06\Dipole=-0.0000634,-0.0010654,0.221736\Quadrupole=30.112881
7,-27.6896249,-2.4232568,-0.0262022,0.0005452,0.0103345\PG=C01 [X(C26H
44N2P4Pt2S3)]\\@
Total energy of the system

ONE THORN OF EXPERIENCE IS WORTH A WHOLE WILDERNESS OF
WARNING.... LOWELL - AMONG MY BOOKS
Leave Link 9999 at Thu Oct 31 11:35:27 2013, MaxMem= 1048576000 cpu:      0.6
Job cpu time: 3 days 8 hours 26 minutes 31.4 seconds.
File lengths (Mbytes):  RWf=    317 Int=      0 D2E=      0 Chk=    36 Scr=
1
Normal termination of Gaussian 09 at Thu Oct 31 11:35:27 2013.
.
.
```

Figure B-16. Final lines of the optimization of (ThPt)₂BDT.

Frequency

The frequency output is significantly shorter than that of an optimization. This is because the intermediate steps are only printed as a single line (two if the SSH window is too narrow). An example of this is shown in Figure B-17. A frequency job computes

vectors for every vibrational frequency of the submitted molecule. As some of these vectors converge, there is no need to recompute them, and the time between steps

```
.
.
.
      There are 246 degrees of freedom in the 1st order CPHF. IDOFFX=5.
246 vectors produced by pass 0 Test12= 9.43D-14 1.00D-09 XBig12= 7.25D+02 1
.22D+01.
AX will form 72 AO Fock derivatives at one time.
243 vectors produced by pass 1 Test12= 9.43D-14 1.00D-09 XBig12= 1.86D+02 2
.44D+00.
243 vectors produced by pass 2 Test12= 9.43D-14 1.00D-09 XBig12= 3.42D+00 2
.42D-01.
243 vectors produced by pass 3 Test12= 9.43D-14 1.00D-09 XBig12= 1.17D-02 1
.06D-02.
243 vectors produced by pass 4 Test12= 9.43D-14 1.00D-09 XBig12= 2.51D-05 5
.29D-04.
178 vectors produced by pass 5 Test12= 9.43D-14 1.00D-09 XBig12= 3.26D-08 1
.57D-05.
50 vectors produced by pass 6 Test12= 9.43D-14 1.00D-09 XBig12= 2.88D-11 5
.44D-07.
3 vectors produced by pass 7 Test12= 9.43D-14 1.00D-09 XBig12= 2.36D-14 1
.58D-08.
Inverted reduced A of dimension 1449 with in-core refinement.
.
.
.
```

Figure B-17. Intermediate steps of a frequency job showing the number of vectors yet to converge.

decreases. Eventually, all vectors will converge, and the program will write every frequency, with every unit vector for every atom. If all of the frequencies are positive, then the molecule is at an energy minimum. However, if any negative (imaginary) frequencies are present, the molecule is not at an energy minimum, and it will need to be reoptimized. Fortunately, the negative frequency distorts the molecule in a way that adjusts the geometry closer to the minimum on the current potential energy surface. GaussView has a feature which allows the user to distort the molecule along a frequency mode, and then save the modified geometry for use in a new geometry optimization. Use of this feature will be described in detail in a later section. Examples of **(ThPt)₂BTD** jobs where the molecule is not at an energy minimum, and where it is at an energy minimum, are shown in Figures B-18 and B-19, respectively. Once the user

has confirmed their molecule is at an energy minimum, they can move on to TDDFT, population, or volume jobs.

```

:
:
:
Full mass-weighted force constant matrix:
Low frequencies --- -11.0025  -7.9313  -5.1678  -3.1567  -0.9806   0.0009
Low frequencies ---  0.0010   0.0012   3.0117
***** 2 imaginary frequencies (negative signs) *****
Harmonic frequencies (cm**-1), IR intensities (KM/Mole), Raman scattering
activities (A**4/AMU), depolarization ratios for plane and unpolarized
incident light, reduced masses (AMU), force constants (mDyne/A),
and normal coordinates:

```

		1 A			2 A			3 A		
Frequencies --		-10.8199			-5.1057			2.6970		
Red. masses --		2.9396			2.8654			2.9865		
Frc consts --		0.0002			0.0000			0.0000		
IR Inten --		0.0004			0.0661			0.0186		
Atom	AN	X	Y	Z	X	Y	Z	X	Y	Z
1	6	0.00	0.00	0.00	0.00	0.00	0.00	0.01	0.00	0.00
2	6	0.00	0.00	0.00	0.00	0.00	0.00	0.01	0.00	0.00
3	6	0.01	0.00	0.00	0.00	0.00	0.00	0.01	0.00	0.00

```

:
:
:

```

Figure B-18. Frequency output of (ThPt)₂BDT with negative frequencies, indicating that the geometry is not at an energy minimum.

```

:
:
:
Full mass-weighted force constant matrix:
Low frequencies --- -4.4066  -2.3823  -1.7169  -0.0021  -0.0019  -0.0016
Low frequencies --- 10.0930  12.7324  12.9207
Harmonic frequencies (cm**-1), IR intensities (KM/Mole), Raman scattering
activities (A**4/AMU), depolarization ratios for plane and unpolarized
incident light, reduced masses (AMU), force constants (mDyne/A),
and normal coordinates:

```

		1 A			2 A			3 A		
Frequencies --		10.0929			12.6521			12.8594		
Red. masses --		4.3881			3.0164			3.0570		
Frc consts --		0.0003			0.0003			0.0003		
IR Inten --		0.0003			0.2968			0.2151		
Atom	AN	X	Y	Z	X	Y	Z	X	Y	Z
1	6	0.00	0.00	0.00	-0.01	0.00	0.01	0.01	0.00	0.01
2	6	0.00	0.00	0.00	-0.01	0.00	0.00	0.01	0.00	0.01
3	6	0.00	0.00	0.00	0.00	0.00	0.00	0.01	0.00	0.01

```

:
:
:

```

Figure B-19. Frequency output of (ThPt)₂BDT with no negative frequencies, indicating that the geometry is at an energy minimum.

TDDFT

The TDDFT output contains data involving vertical electronic transitions. A list of excited states is generated, with each state displaying information about the MOs involved in the transition, the CI coefficient(s) corresponding to every pair of ground and excited MOs, the energy of the transition in both electron-Volts and nanometers, and the oscillator strength. These data are illustrated in Figure B-20. Lower energy transitions tend to be straightforward, and typically consist of only one ground state orbital and one excited state orbital. Higher energy transitions typically involve many orbitals.

```

.      MOs involved in transition
.      CI coefficient(s)
.      Transition energy      Oscillator strength
.      Energy in eV      Energy in nm
Excitation energies and oscillator strengths:
Excited State  1:      Singlet-A      2.7716 eV      447.34 nm      f=0.0982      <S**2>=0
.000      179 ->180      0.69840
This state for optimization and/or second-order correction.
Total Energy, E(TD-HF/TD-KS) = -3925.56728282
Copying the excited state density for this state as the 1-particle RhoCI densit
y.
Excited State  2:      Singlet-A      3.1879 eV      388.93 nm      f=0.0001      <S**2>=0
.000      178 ->180      0.70597
.
.
Excited State 16:      Singlet-A      4.3538 eV      284.77 nm      f=0.0680      <S**2>=0
.000      169 ->180      0.61117
      171 ->180      0.15183
      177 ->193      0.10162
      179 ->186      -0.14097
      179 ->193      0.19581
.
.
.

```

Figure B-20. TDDFT output of **(ThPt)₂BTD** showing relevant vertical transitions.

To determine the percent contributions of these ‘complex’ transitions, the CI coefficients are invoked. To obtain the percent contribution of a single transition, square the CI coefficient corresponding to that transition and divide by the sum of the squares

of all CI coefficients for the entire excited state: $\%C_i = \frac{CI_i^2}{\sum_1^n CI_n^2} \times 100\%$, where $\%C_i$ is the percent contribution of the i^{th} term.

Finally, to tell if a transition is relevant, its oscillator strength (f) must be considered. The oscillator strength is directly proportional to the extinction coefficient (ϵ). Thus, a higher value of f corresponds to a stronger transition. For conjugated organic and organometallic molecules, it is rare to see the strongest transition be less than 0.1. However, for complexes with shorter conjugation lengths, such as **(ThPt)₂BTd**, this will happen, and the user must use their best judgement to pick out relevant transitions. For chromophores with very long conjugation lengths, the value of f is overestimated.

Stability

The useful part of a stability output looks similar to that of TDDFT. The program looks at excitation energies, and upon convergence, if an excitation energy of negative energy is present, determines that an instability is present in the wavefunction. This is shown in Figure B-21. Upon detection of an instability, the program will reoptimize the wavefunction, and compute excitation energies again. If these excitations are all positive, then the molecule should now be stable and the job is complete. This is shown in Figure B-22. After the stability job completes successfully, the user should take this checkpoint file and run a frequency job before rerunning TDDFT.

Population

The population output for NAOs is very data intensive, as the program prints all coefficients for all orbitals for all atoms for every MO. Thus it is best for the user to copy the output to a local machine (using an SSH client), and analyze the results using the

```

.
.
.
Excitation Energies [eV] at current iteration:
Root      1 :   -0.246628319485163   Change is   -0.000038689142765
Root      2 :    0.394795901279012   Change is   -0.003494872512238
Root      3 :    0.414476198334860   Change is   -0.000449431985660
Convergence achieved on expansion vectors.
*****
stability analysis using <AA,BB:AA,BB> singles matrix:
*****

Eigenvectors of the stability matrix:

Eigenvector  1:  1.000-A   Eigenvalue=-0.0090634  <S**2>=0.000
  101B ->110B           0.23834
  105B ->110B          -0.16628
  108B ->110B          -0.31701
  109B ->110B           0.88999
SavETr: write IOETrn=  770 NScale= 10 NData=  16 NLR=1 LETrn=      28.
The wavefunction has an internal instability.
.
.
.

```

Figure B-21. Output of a stability job indicating that an instability is present in the wavefunction.

```

.
.
.
Excitation Energies [eV] at current iteration:
Root      1 :    0.285600270765458   Change is   -0.000051163734293
Root      2 :    0.547913183725831   Change is   -0.000209659333575
Root      3 :    0.624808303202553   Change is   -0.000604986909495
Convergence achieved on expansion vectors.
*****
stability analysis using <AA,BB:AA,BB> singles matrix:
*****

Eigenvectors of the stability matrix:

Eigenvector  1:  1.000-A   Eigenvalue= 0.0104956  <S**2>=0.000
  103B ->110B           0.10916
  105B ->110B           0.70026
  106B ->110B           0.41816
  109B ->110B           0.54543
SavETr: write IOETrn=  770 NScale= 10 NData=  16 NLR=1 LETrn=      28.
The wavefunction is stable under the perturbations considered.
.
.
.

```

Figure B-22. Output of a stability job indicating that the wavefunction is now stable.

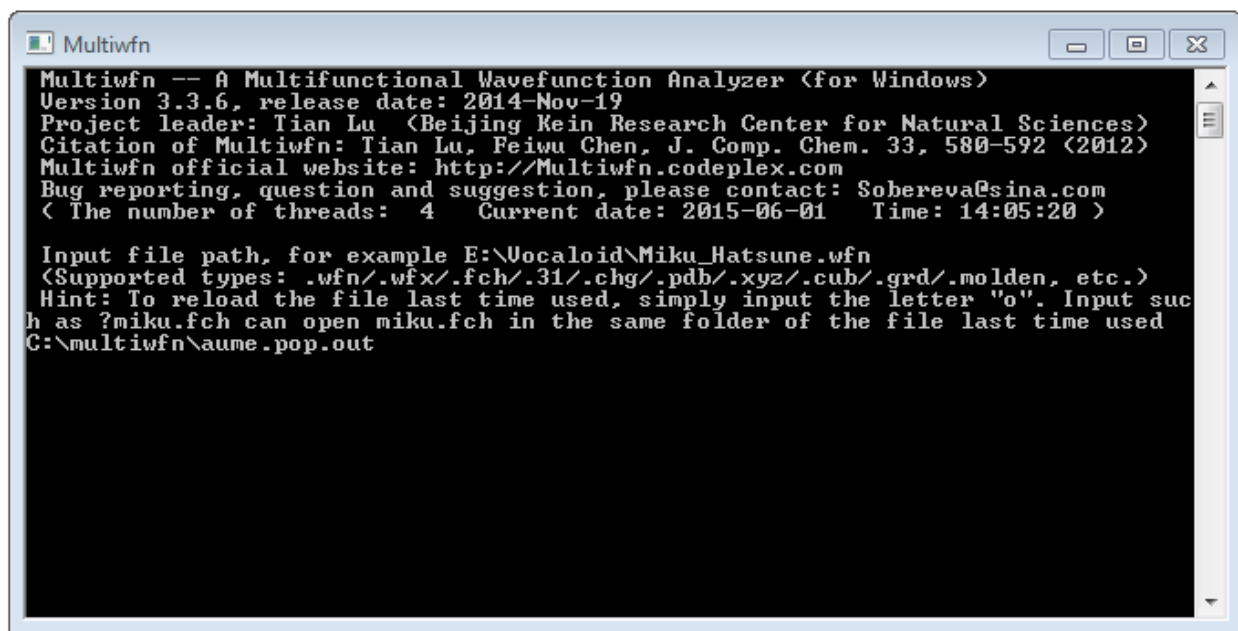
program Multiwfn. Multiwfn is available for free download at the website

<https://multiwfn.codeplex.com/>. A very detailed and very helpful manual is also located

at the same website, but an overview of the specific steps the user must take to obtain

population data is presented here. The program can be installed anywhere on the user's hard drive, but for efficiency, it is helpful to create a separate folder on the first level of the hard drive (ex. C:\multiwfn) to store the transferred Gaussian output files in.

Multiwfn runs in the command prompt, and inputs are purely textual. To get started, open the program, type the input file path (ex. C:\multiwfn\jobname.out), and hit enter. The program startup screen with a sample input file path is shown in Figure B-23.



```
Multiwfn -- A Multifunctional Wavefunction Analyzer (for Windows)
Version 3.3.6, release date: 2014-Nov-19
Project leader: Tian Lu (Beijing Kein Research Center for Natural Sciences)
Citation of Multiwfn: Tian Lu, Feiwu Chen, J. Comp. Chem. 33, 580-592 (2012)
Multiwfn official website: http://Multiwfn.codeplex.com
Bug reporting, question and suggestion, please contact: Sobereva@sina.com
< The number of threads: 4   Current date: 2015-06-01   Time: 14:05:20 >

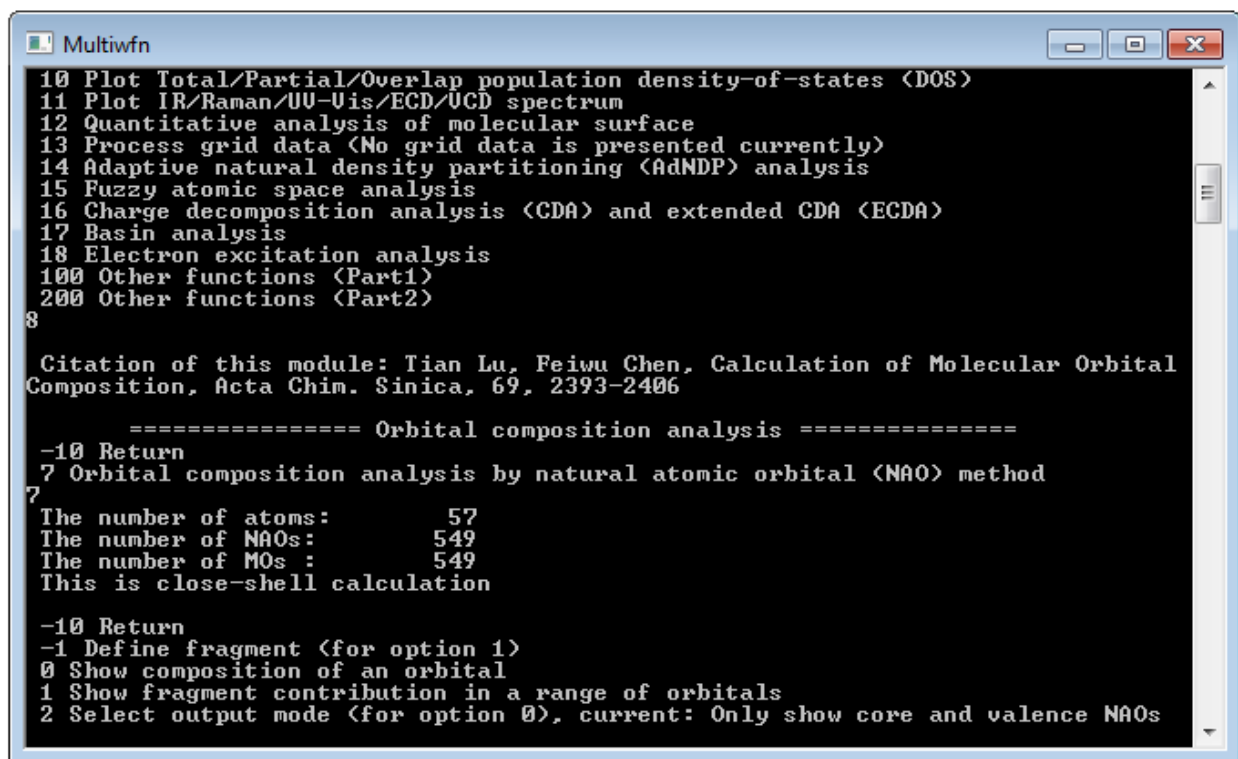
Input file path, for example E:\Vocaloid\Miku_Hatsune.wfn
<Supported types: .wfn/.wfx/.fch/.31/.chg/.pdb/.xyz/.cub/.grd/.molden, etc.>
Hint: To reload the file last time used, simply input the letter "o". Input suc
h as ?miku.fch can open miku.fch in the same folder of the file last time used
C:\multiwfn\name.pop.out
```

Figure B-23. Multiwfn startup screen with input file path typed in the last line of text.

Upon the file loading successfully, the user will be presented with a number of options with varying functionality to examine the molecule. Please note that while the Gaussian job is referred to as 'population', the Multiwfn module to use is called 'orbital composition analysis'. Proceed by typing '8' and hitting 'enter' to select the orbital composition analysis module. Because the Gaussian job specified to use the NAO method, this will be the only option available to the user. Type '7' and hit 'enter' to proceed. A few options are now available to the user. They, along with the previous two

steps, are shown in Figure B-24. Also note that the MOs are numbered rather than named. The equivalent MO number can be deduced from the TDDFT output. Atoms are also numbered. Opening the structure in GaussView and holding the cursor over the desired atom will show the number it has been assigned.

The user has a few paths they can take at this point. If the user only needs information about a single orbital, then they can select option '0', type the orbital



```
Multiwfn
10 Plot Total/Partial/Overlap population density-of-states (DOS)
11 Plot IR/Raman/UV-Vis/ECD/UCD spectrum
12 Quantitative analysis of molecular surface
13 Process grid data (No grid data is presented currently)
14 Adaptive natural density partitioning (AdNDP) analysis
15 Fuzzy atomic space analysis
16 Charge decomposition analysis (CDA) and extended CDA (ECDA)
17 Basin analysis
18 Electron excitation analysis
100 Other functions (Part1)
200 Other functions (Part2)
8

Citation of this module: Tian Lu, Feiwu Chen, Calculation of Molecular Orbital
Composition, Acta Chim. Sinica, 69, 2393-2406

===== Orbital composition analysis =====
-10 Return
7 Orbital composition analysis by natural atomic orbital (NAO) method
7
The number of atoms:      57
The number of NAOs:      549
The number of MOs :      549
This is close-shell calculation

-10 Return
-1 Define fragment (for option 1)
0 Show composition of an orbital
1 Show fragment contribution in a range of orbitals
2 Select output mode (for option 0), current: Only show core and valence NAOs
```

Figure B-24. Multiwfn orbital composition analysis options.

number, and a list of atoms with percentages will be printed. If multiple atoms (ex. a molecule containing multiple metal atoms, or the charge on a donor/acceptor moiety) need to be taken into account, simply add the percentages to get the contributions from the desired group of atoms.

If multiple atoms across multiple MOs need to be analyzed, it is usually faster to first define a fragment before running the analysis. To do this select option '-1', add 'all

NAOs' for the desired atoms (example notation is given directly in the program), then type 'q' to save the fragment and return to the previous menu. Now that a fragment has been defined, select option '1' and input all MO numbers to be analyzed. Hit 'enter' and an output will be printed giving 'core, valence, and Rydberg' contributions (see the Multiwfn manual for the definitions of these), and the total contribution of the defined fragment. This is depicted in Figure B-25.

```

Multiwfn
a 30,31
Done!
q

Fragment is saved, indices of NAOs in current fragment:
332 333 334 335 336 337 338 339 340 341 342 343
344 345 346 347 348 349 350 351 352 353 354 355
356 357 358 359 360 361 362 363 364 365 366 367
368 369 370 371 372 373 374 375 376 377 378 379
380 381 382 383 384 385 386 387 388 389 390 391
392 393 394 395 396 397 398 399 400 401 402 403

-10 Return
-1 Define fragment <for option 1>
0 Show composition of an orbital
1 Show fragment contribution in a range of orbitals
2 Select output mode <for option 0>, current: Only show core and valence NAOs
1
Input orbital range to be outputted e.g. 1,10
Note: Should within 1 to 549
149,150
Orb.#      Core      Valence    Rydberg    Total
149        0.014792%    2.603399%    0.043346%    2.661537%
150        0.005832%    1.396916%    0.026372%    1.429120%

-10 Return
-1 Define fragment <for option 1>
0 Show composition of an orbital
1 Show fragment contribution in a range of orbitals
2 Select output mode <for option 0>, current: Only show core and valence NAOs

```

Figure B-25. Percent contributions of a specified fragment to a pair of specified MOs.

Volume

The last output to be discussed is that of the volume job, shown in Figure B-26. There is not much to this output. If the user scrolls almost all the way to the bottom, a suggested radius is given. This radius can be used in the Onsager equation. Please note that the value is only accurate to two significant figures.

```

.
.
.
Evaluate density.
Using the total density.
Monte-Carlo method of calculating molar volume:
based on 0.001 e/bohr**3 density envelope.
Number of points per bohr**3 = 100 cutoff= 1.00D-04
Using the SCF density.
There are 3601 points. will hold 3601 in memory.
LenV= 1045913254 MDV= 1048576000.
Box volume =46701.280 fraction occupied=0.103
Integrated density= 2.2895613291064188D+02 error=-6.9043867089358116D+01
Molar volume = 4798.521 bohr**3/mol (428.215 cm**3/mol)
Recommended a0 for SCRF calculation = 6.59 angstrom ( 12.46 bohr)
.
.
.

```

Figure B-26. Output of a volume job with the suggested radius boxed.

Visualizing Results

One of the most important aspects of computational chemistry in the Schanze Group is the ability to convey results visually. Specific questions that are best answered visually include: what conformation has the molecule adopted, what do the MOs look like, and where is the charge in an electronic transition starting from/travelling to? All of these questions can be answered graphically using either GaussView or Chemcraft. While GaussView provides the simplest route to visualizing molecular geometries and MOs, its ability to generate charge difference density (CDD) plots (the answer to the final question listed above) is subpar. Thus the author recommends that whenever structure, MO, or CDD graphics are generated for publication, that Chemcraft is used throughout all of the images, for consistency. Chemcraft can be downloaded for free, as a fully functional 150-day trial version, from the website <http://chemcraftprog.com/>. Methods for visualization in both programs will be discussed, as using GaussView is much simpler if the user only needs to see the output without generating publication worthy graphics. GaussView will be discussed first.

GaussView

Before starting in on the discussion of visualization, an addition must be made to a system file in the users HPC account. To do this, have only one instance of SSH open, and go to the home folder. Alternately, one can simply close all instances of SSH and open a new instance, which will start in the home folder. Using the VI editor, open the file `‘.bashrc’`. At the end of the file, two lines need to be added. The first line should read: `# Load modules`. The second line should read: `module load Gaussian/g09-d01`. This will automatically load the Gaussian module to the users SSH shell upon logging in, rather than having to specify it every session.

Molecular geometry

If the user only needs to see the molecular geometry of the molecule, they can simply open the output file in GaussView. If the user desires to see intermediate geometries, select the `‘Read Intermediate Geometries’` box at the bottom of the `‘Open Files’` window. Once opened, the view of the molecule can be manipulated in all of the ways one would expect. GaussView does allow image files to be saved; however, these images are saved to the HPC cluster, rather than to a local machine. Thus, the Snipping Tool, on a Windows machine, or Grab, on a Macintosh, will suffice.

Molecular orbitals

Before MOs can be visualized, a formatted checkpoint (fchk) file must be generated. This file is generated from a normal checkpoint file, and contains all of the same information, but it is able to be read by more than just the Gaussian program. A fchk file may be created from any checkpoint file on hand (ex. the checkpoint file from an optimization, frequency, or TDDFT job), but the author recommends using the checkpoint file from the TDDFT job. This is because in the event that a molecule needs

to be reoptimized many times, due to not being at an energy minimum, many optimization files may be created. Thus it is possible to accidentally format and use the wrong checkpoint file, resulting in invalid data being generated. If a TDDFT checkpoint file is used, the likelihood of this accident is drastically reduced. To format the desired checkpoint file, the user should be in the same folder as the file in an SSH client. Type the command: `formchk jobname.chk jobname.fchk`. The 'formchk' module is loaded directly into the users SSH shell, which allows them to do this directly from the command line.

Once the fchk file has been generated, the user may open it in GaussView. The user must then click on the 'MO Editor' button, which will open a new window. In this window the user will see the structure of the molecule, a list of orbitals with occupancies and energies (in hartrees), along with a series of tabs. This window, with the 'Visualize' tab selected, and the HOMO and LUMO highlighted, are shown in Figure B-27. The user has the ability to change the 'Isovalue' and 'Cube Grid', but these should be left alone. The isovalue controls the size of the generated MOs, and it should remain at 0.02. Changing the cube grid from 'Coarse' will only slow the generation of the MO, with no real gain in resolution.

To select MOs to visualize, leave the 'Type' as 'Highlighted' and click on the desired MOs in the list. By default the HOMO and LUMO are selected. Once all MOs are selected, click 'Update...' and wait for the program to generate and render the orbitals. The window will be inactive during this time. Users should also note the green dotted line between the MOs with negative and positive energy. This line represents the vacuum energy of an electron. Great care should be taken if MOs of higher energy than

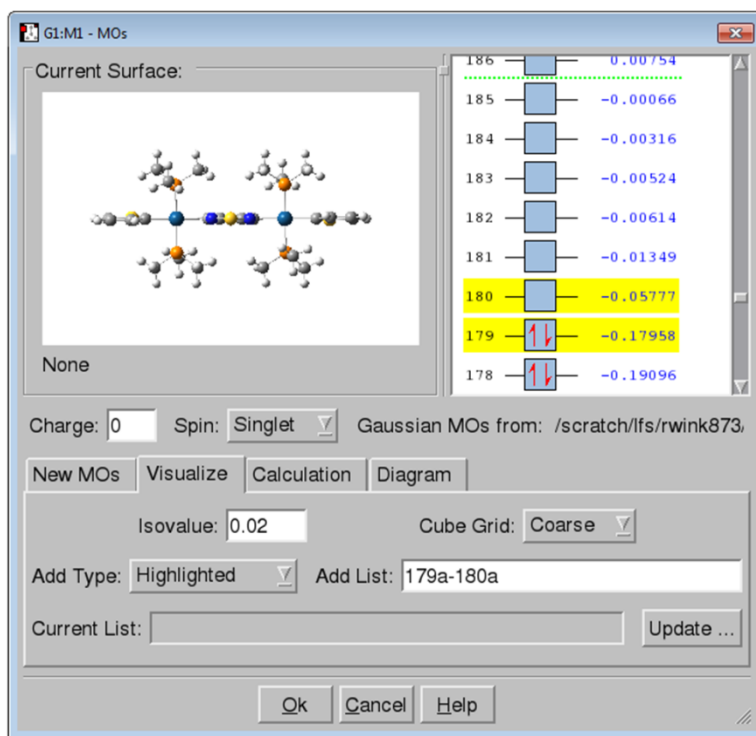


Figure B-27. MO Editor window in GaussView displaying **(ThPt)₂BTD** with the HOMO and LUMO highlighted for MO generation.

this needs to be used, as these orbitals are not always realistic. Once the program finishes rendering the image, the user can click on a box to the right of the energy to select the MO to display. This is shown in Figure B-28, along with the HOMO of **(ThPt)₂BTD**. All MOs that are available for viewing will have this box next to them. If the user desires to view additional MOs, they can highlight the new ones and update the list again. Depending on the size of the molecule, this process takes approximately one to six minutes per MO.

Chemcraft

Generating cube files

In order to use Chemcraft for visualization, two additional steps must be taken. First, MO cube files (extension: .cube) must be generated from the formatted checkpoint file. The cube file contains geometry information as well as the data needed to visualize

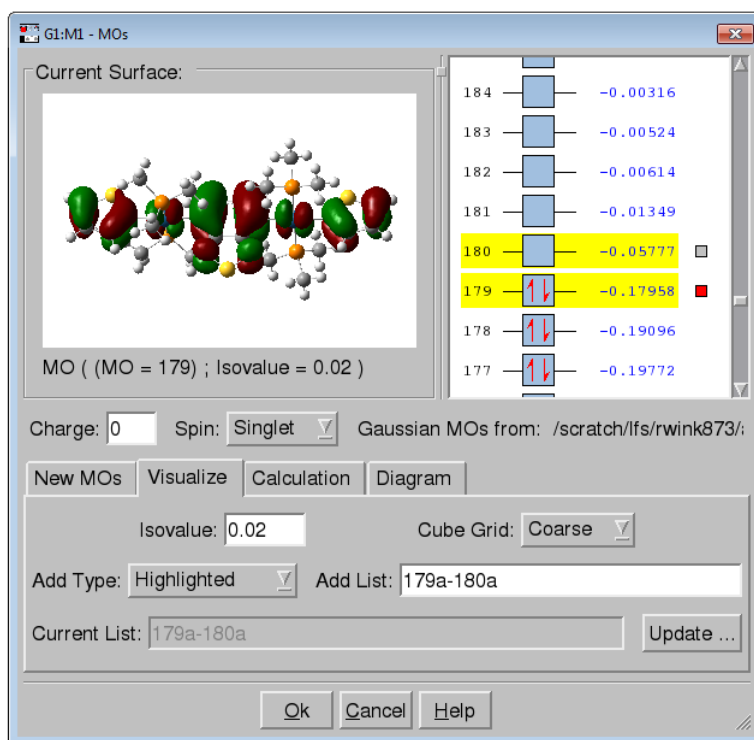


Figure B-28. MO Editor window in GaussView displaying the HOMO of **(ThPt)₂BTD** visualized with an isovalue of 0.02.

MOs. To create a cube file, move to the same folder as the fchk file that will be used in the SSH shell. Type the command: `cubegen 0 mo=XX jobname.fchk XX.cub 80`, where XX is the number of the desired MO. Repeat this process for every orbital needed. Finally, transfer the cube files to a local machine so they may be used by Chemcraft.

Molecular geometry/molecular orbitals

Open Chemcraft and open the cube file of the desired MO. The molecule can be manipulated in space just as in GaussView. Before doing anything else, ensure the program display mode is set to 'Isometry' rather than 'Perspective'. This is found in the row of buttons directly above the displayed molecule and pointed out in Figure B-29. The perspective mode greatly distorts the molecule. Chemcraft also has functionality to change the color scheme and save an image of what it is displaying. To change the color scheme, click on 'Display' and select a style or create your own. The author

recommends the 'GaussView' style with a white background. To save an image, click 'File', scroll over 'Save as' and click 'Save image'. Adjust the image settings as desired, click 'Save', and name the file appropriately so it will be unambiguous as to what the image is of. To display the MO surface, set the 'Contour value' to 0.02 (this is the same as the isovalue), click 'Both-signed', and finally click 'Show isosurface'. These areas are also shown in Figure B-29. Again, the user can manipulate the viewing angle of the molecule before image capture.

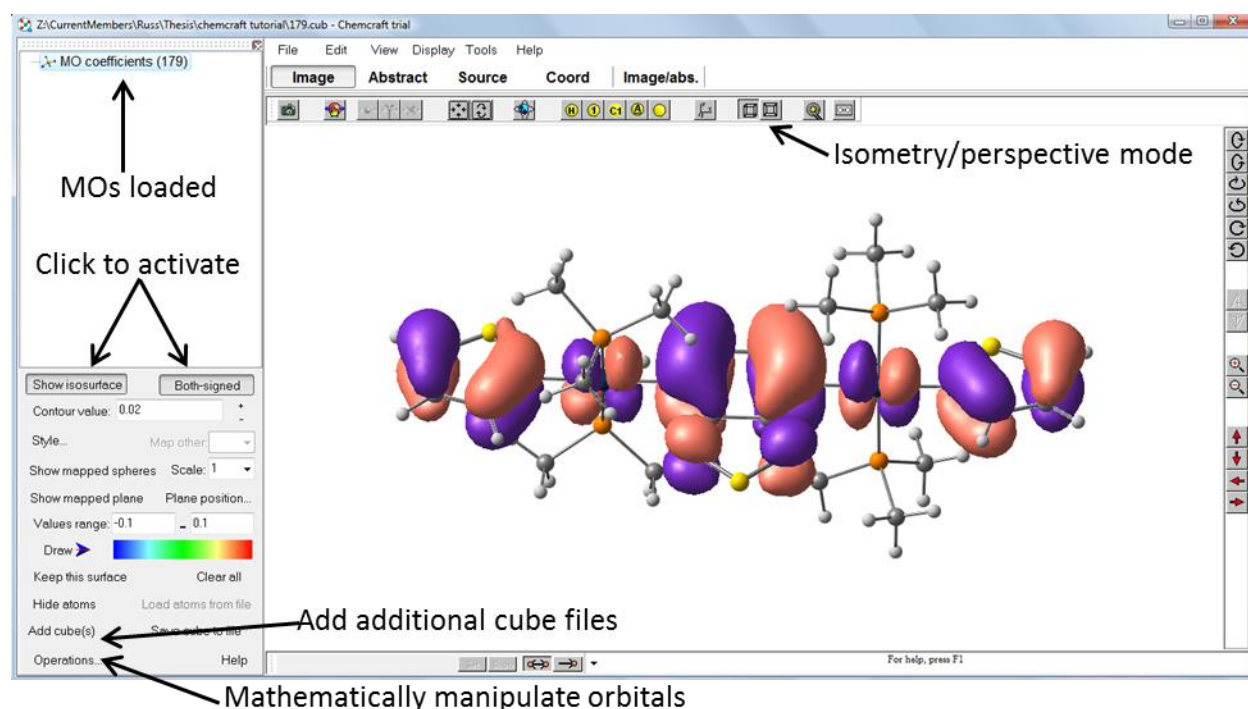


Figure B-29. Chemcraft program displaying the HOMO of **(ThPt)₂BTD** visualized with an isovalue of 0.02. Useful buttons are labeled.

Charge difference density

To start generating a charge difference density (CDD), load all of the needed MOs into the program. The first MO is loaded normally, but each subsequent MO is loaded via the 'Add cube(s)' functionality (see Figure B-29). Before manipulating the cube files, the equation for generating a CDD must be laid out. In its most simple form,

$CDD = \sum ES^2 - \sum GS^2$, where ES = Excited State, and GS = Ground State. Thus the CDD can be as simple as: $LUMO^2 - HOMO^2$. This is the case for the first computed excited state of **(ThPt)₂BTD** (see Figure B-20).

For more complex transitions, the percent contributions need to be figured in. Using the 16th excited state of **(ThPt)₂BTD** as an example (again, see Figure B-20), there are four ground state orbitals and three excited state orbitals, all with different contributions. Please note that only the percent contributions are additive. If the user tries to add the CI coefficients before they are squared and divided by the sum of the squares, the values will come out incorrectly and the generated CDD will be invalid. Once the percent contributions are properly calculated, they are multiplied by the square of the MO: $(MO_i^2)(\%C_i)$. This is repeated for every MO involved in the CDD. Once all MOs have been weighted according to their percent contribution, the excited state MOs can be summed, and the ground state MOs can be subtracted from this sum: $CDD = \sum_i^n (MO_i^2)(\%C_i) - \sum_j^m (MO_j^2)(\%C_j)$. All mathematical orbital manipulations are done from the 'Cubes operation' window. This window, and the operations offered therein, is shown in Figure B-30. It must also be noted that because the MOs themselves have been squared, the isovalue to properly image a CDD must also be squared, resulting in the proper value being 0.0004. Figure B-31 shows the CDD plot of the first computed excited state for **(ThPt)₂BTD** visualized at an isovalue of 0.0004.

Although a CDD resembles a MO, as it should, the fundamental difference comes in how the plot is colored. A CDD shows where electron density is lost (blue coloring) and gained (red color) in an electronic transition. Once the CDD is generated, double check that all orbitals have been manipulated properly, and save the image.

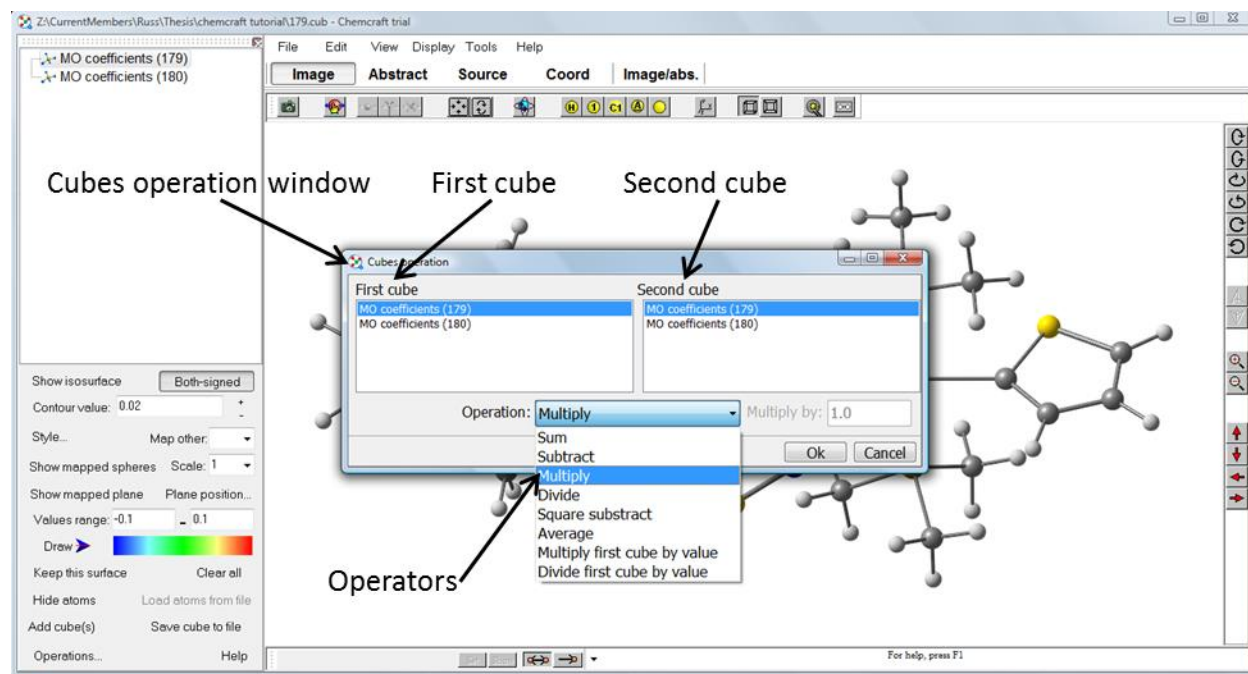


Figure B-30. The 'Cubes layout' window with the operators displayed.

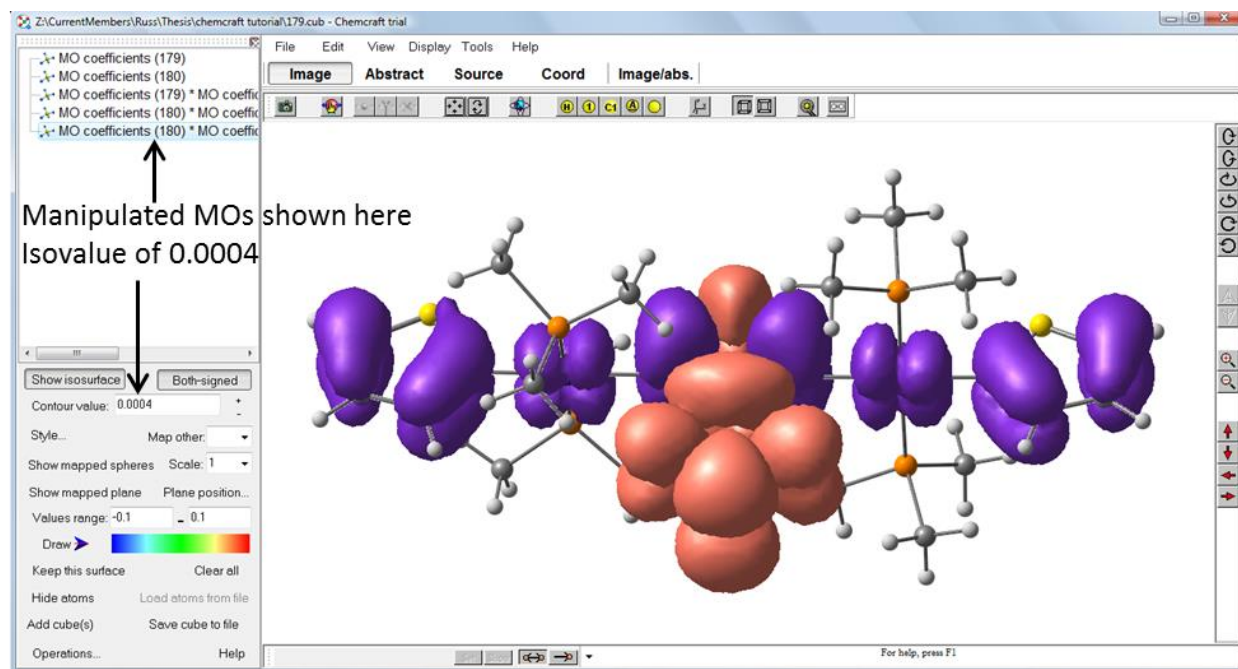


Figure B-31. CDD for the lowest energy computed transition of **(ThPt)₂BTD**. Blue lobes indicate electron density being lost, while red lobes indicate electron density being gained. Image visualized at an isovalue of 0.0004.

Considerations for Triplet Graphics Generation

While all of the above still applies to triplet jobs, the user must keep a few key details in mind when working with triplets. The main concern is in the numbering of the alpha and beta orbitals. Because Gaussian does not pair electrons in a triplet computation, each electron is assigned its own orbital. When the time comes to extract data about these orbitals, the user will find that they are numbered sequentially, alpha then beta, rather than being assigned a symbol, as the Gaussian manual would have one believe. Thus the user must determine the highest numbered alpha orbital, and add it to the desired beta orbital to get the correct MO number to use in the cubegen utility. The author suggests using the MO editor in GaussView to determine the highest numbered alpha orbital. The tab selected by default in the MO editor is the 'Calculation' tab. The user can look at the range given to the right of the 'Occupancy (Alpha)' dropdown list and use the high number there. Additionally, the user has the option of scrolling to the top of the orbital list. An example of this, using the triplet of **(ThPt)₂BTD**, is shown in Figure B-32.

Once the triplet cube files have been generated, they can be loaded into Chemcraft. It is helpful to retain the numbers of the beta MOs used in the cubegen utility, as Chemcraft will use these same numbers. Figure B-33 shows the MOs of the highest energy electron in the alpha and beta manifold loaded in Chemcraft, with the numbering again being sequential.

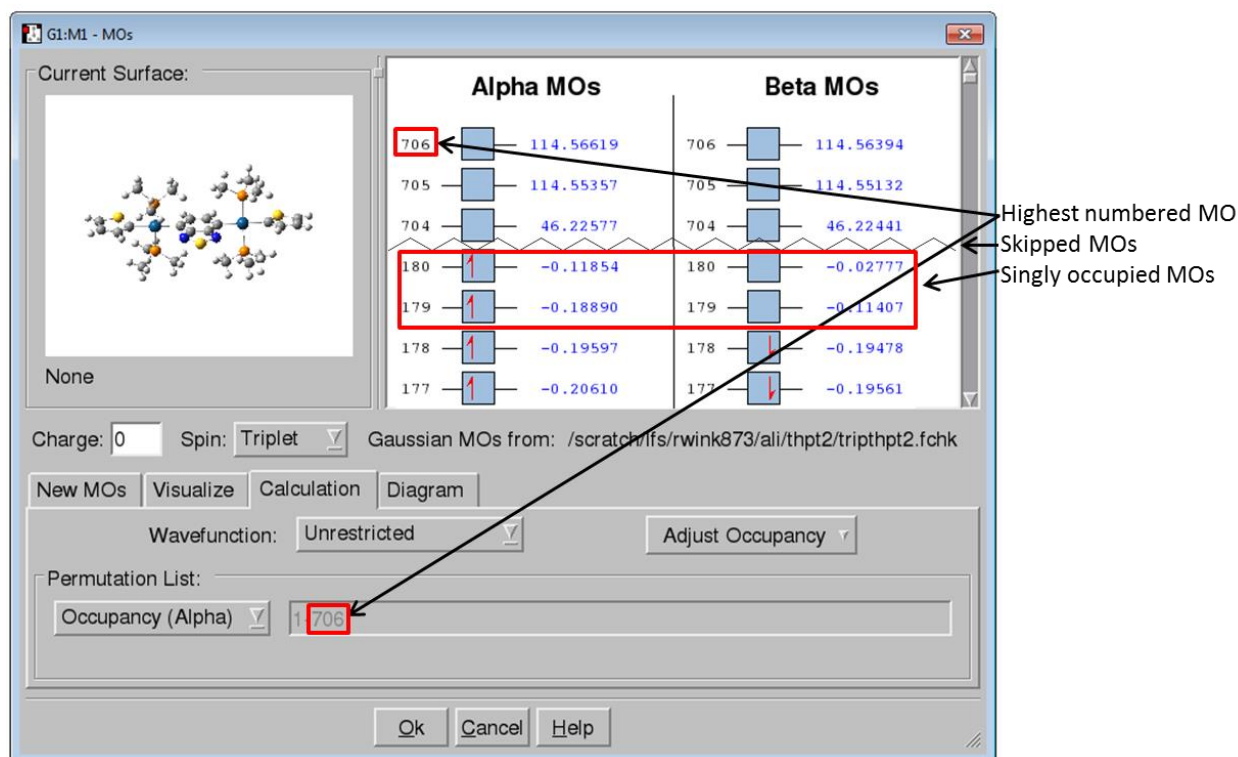


Figure B-32. MO editor window with the highest numbered alpha orbital of $(\text{ThPt})_2\text{BTD}$ pointed out. Singly occupied MOs are also boxed.

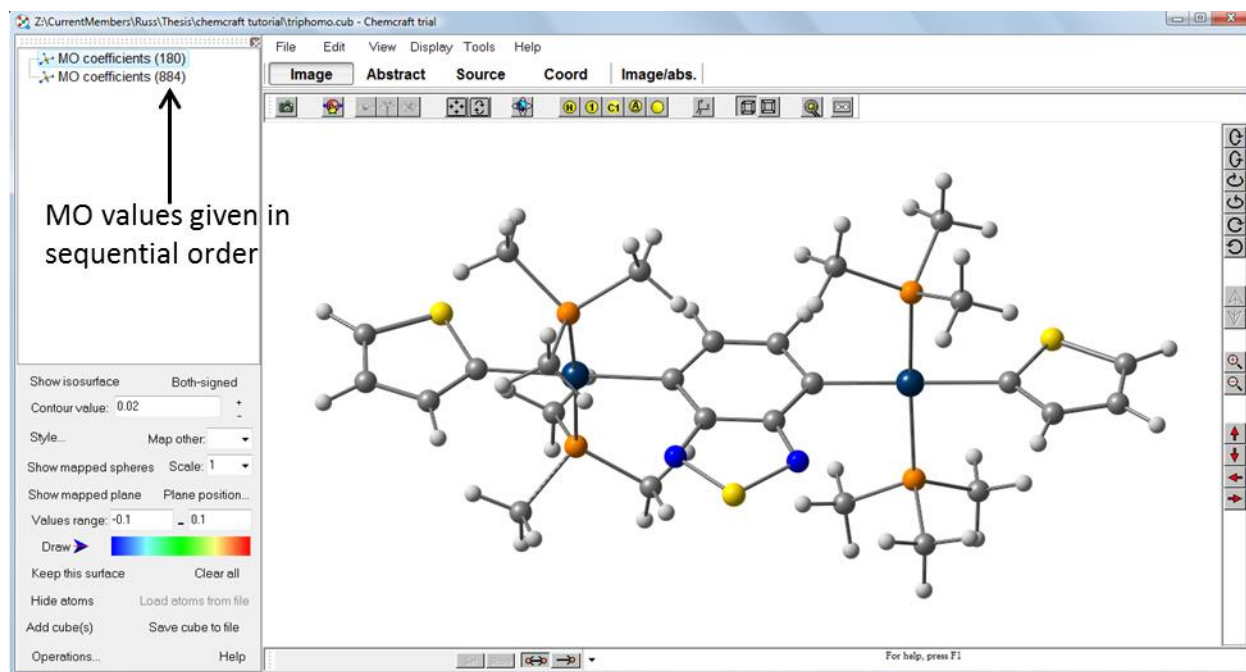


Figure B-33. The triplet of $(\text{ThPt})_2\text{BTD}$ in Chemcraft with the highest energy MO of both the alpha and beta electrons loaded. Note that the numbering in this program is sequential.

APPENDIX C SUPPORTING INFORMATION FOR CHAPTER 2

X-ray Experimental and Data

The asymmetric unit of **1** consists of a half Pt complex (located on an inversion center) and one chloroform solvent molecule in general position. The coordinated Cl ligand and one of the solvent Cl atoms are disordered and each was refined in two parts. In the solvent, the disorder in one Cl atom is accompanied with a smaller disorder in the chloroform C atom but this was not significant enough to be resolved. In the final cycle of refinement, 4584 reflections (of which 4224 are observed with $I > 2\sigma(I)$) were used to refine 225 parameters and the resulting R_1 , wR_2 and S (goodness of fit) were 1.42%, 4.02% and 1.044, respectively.

The asymmetric unit of **2a** consists of a half Pt complex and a dichloromethane solvent molecule. In the final cycle of refinement, 5134 reflections (of which 4881 are observed with $I > 2\sigma(I)$) were used to refine 331 parameters and the resulting R_1 , wR_2 and S (goodness of fit) were 2.50%, 6.29% and 1.085, respectively.

The asymmetric unit of **2b** consists of a half Pt complex and a dichloromethane solvent molecule (located on an inversion center). The C9 cyclohexyl group is disordered and refined in two parts. The methyl group at C31 is also disordered and refined in two parts. Each disordered region's parts were refined with their site occupation factors dependently refined. In the final cycle of refinement, 8708 reflections (of which 6184 are observed with $I > 2\sigma(I)$) were used to refine 422 parameters and the resulting R_1 , wR_2 and S (goodness of fit) were 4.20%, 10.37% and 1.036, respectively.

The asymmetric unit of **2c** consists of a half Pt complex (located on an inversion center) and a dichloromethane solvent molecule. The ethyl group on C21 is disordered

Table C-1. Summary of crystallographic data

	1·CHCl₃	2a·CH₂Cl₂	2b·CH₂Cl₂	2c·CH₂Cl₂
empirical formula	C ₃₂ H ₅₀ Cl ₈ N ₄ Pt	C ₆₃ H ₆₈ Cl ₂ N ₄ Pt	C ₈₄ H ₉₂ Cl ₄ N ₆ PtS ₂	C ₉₄ H ₁₀₄ Cl ₄ N ₆ Pt
fw	969.45	1232.13	1586.65	1654.72
λ [Å]	0.71073	1.54178	0.71073	0.71073
cryst syst	Monoclinic	Monoclinic	Monoclinic	Triclinic
space group	<i>P</i> 2 ₁ / <i>c</i>	<i>P</i> 2 ₁ / <i>c</i>	<i>P</i> 2 ₁ / <i>c</i>	<i>P</i> 1
unit cell dimen				
<i>a</i> [Å]	10.7953(19)	9.0339(4)	8.2552(7)	9.9529(2)
<i>b</i> [Å]	14.724(3)	20.7765(9)	27.997(2)	13.1998(2)
<i>c</i> [Å]	12.701(2)	15.4670(6)	16.4264(14)	15.8601(3)
α [deg]	90	90	90	105.207(1)
β [deg]	97.930	101.326(2)	92.455(2)	93.171(1)
γ [deg]	90	90	90	93.064(1)
<i>V</i> [Å ³]	1999.6(6)	2846.5(2)	3793.1(6)	2002.60(6)
<i>Z</i>	2	2	2	1
ρ_{calcd} [Mg m ⁻³]	1.610	1.438	1.389	1.372
μ [mm ⁻¹]	4.071	6.664	2.094	1.936
<i>F</i> (000)	968	1256	1632	856
crystal size, mm	0.21 x 0.20 x 0.19	0.25 x 0.15 x 0.07	0.24 x 0.10 x 0.07	0.18 x 0.14 x 0.08
θ range [deg]	1.90 to 27.50	5.16 to 68.00	1.45 to 27.50	1.79 to 27.50
index ranges (<i>h,k,l</i>)	-13,14; -15,19; -16,16	-10,10; -24,24; -18,18	-10,8; -35,36; -21,21	-12,12; -17,17; -20,20
no. reflns collected	23816	72981	34768	35226
no. indep reflns	4584 [<i>R</i> (int) = 0.0248]	5134 [<i>R</i> (int) = 0.0291]	8708 [<i>R</i> (int) = 0.0320]	9171 [<i>R</i> (int) = 0.0292]
no. relfns [<i>I</i> > 2 σ (<i>I</i>)]	4224	4881	6184	9118
max. and min. transmn	0.5118 and 0.4862	0.6454 and 0.2888	0.8724 and 0.6378	0.8605 and 0.7219
no. data/restraints/params	4584/0/225	5134/0/331	8708/36/422	9171/0/474
goodness-of-fit on <i>F</i> ²	1.044	1.085	1.036	1.040
final <i>R</i> indices [<i>I</i> > 2 σ (<i>I</i>)]	<i>R</i> ₁ = 0.0142, <i>wR</i> ₂ = 0.0402	<i>R</i> ₁ = 0.0250, <i>wR</i> ₂ = 0.0629	<i>R</i> ₁ = 0.0420, <i>wR</i> ₂ = 0.1037	<i>R</i> ₁ = 0.0253, <i>wR</i> ₂ = 0.0633
<i>R</i> indices (all data)	<i>R</i> ₁ = 0.0158, <i>wR</i> ₂ = 0.0416	<i>R</i> ₁ = 0.0261, <i>wR</i> ₂ = 0.0643	<i>R</i> ₁ = 0.0673, <i>wR</i> ₂ = 0.1111	<i>R</i> ₁ = 0.0256, <i>wR</i> ₂ = 0.0636
largest diff peak/hole [e Å ⁻³]	0.764 and -1.192	1.083 and -0.928	1.607 and -0.764	1.151 and -1.116

^a Data common to all structures: temp of collection, 100(2) K; refinement method: full-matrix least-squares on *F*².

and was refined in two parts. In the final cycle of refinement, 9171 reflections (of which 9118 are observed with $I > 2\sigma(I)$) were used to refine 474 parameters and the resulting R_1 , wR_2 and S (goodness of fit) were 2.53%, 6.33% and 1.040, respectively.

All refinements were carried out by minimizing the wR_2 function using F^2 rather than F values. R_1 is calculated to provide a reference to the conventional R value but its function is not minimized.

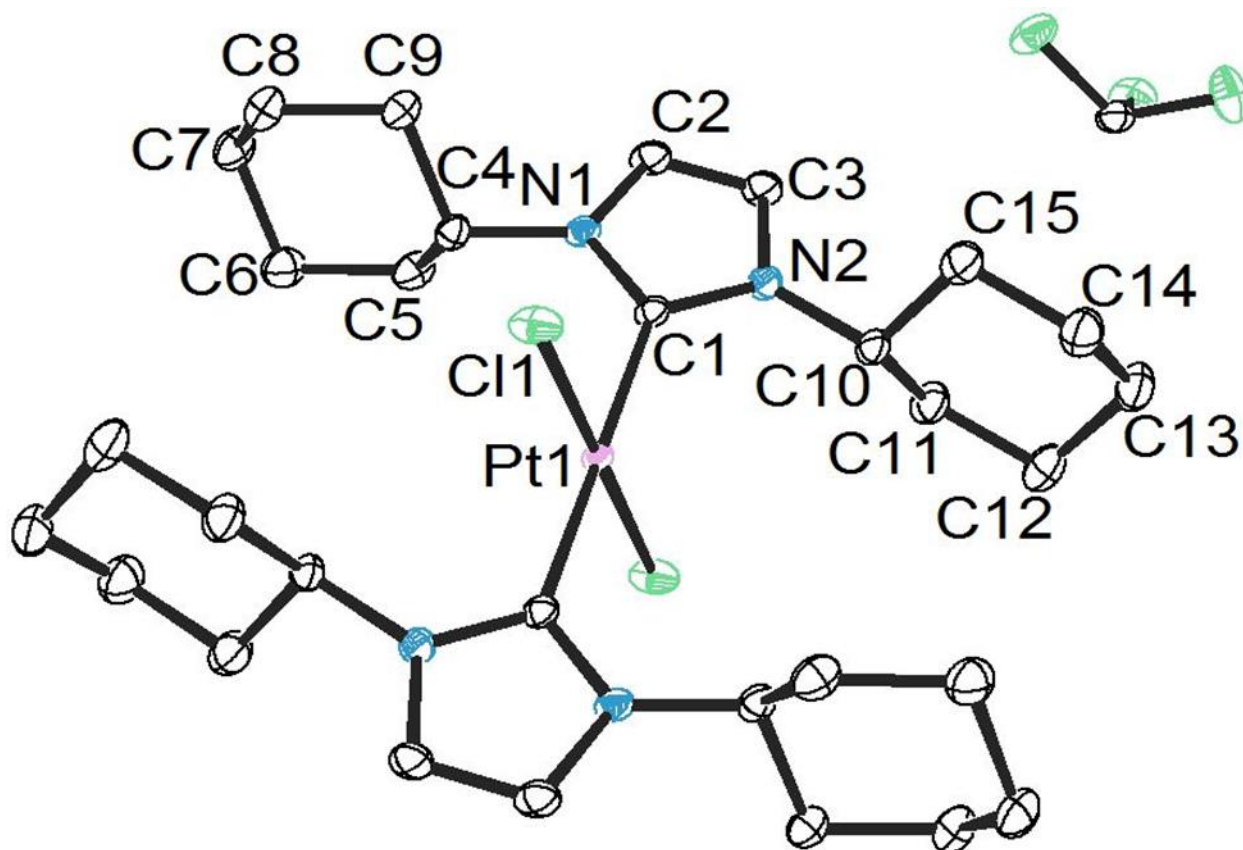


Figure C-1. ORTEP diagram of *trans*-(ICy)₂PtCl₂ (**1**) with the asymmetric unit labeled. Ellipsoids are at the 50% probability level. Hydrogen atoms are omitted for clarity.

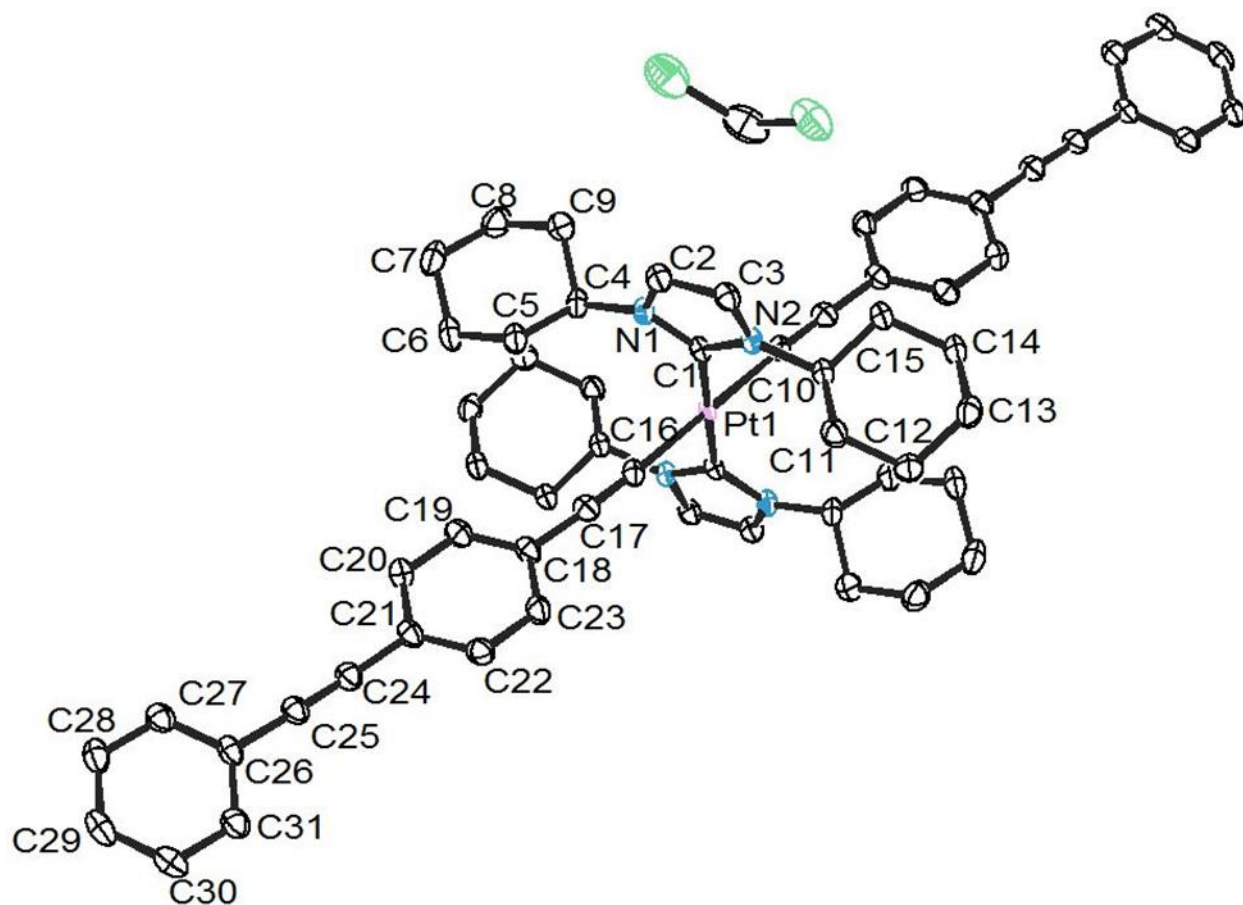


Figure C-2. ORTEP diagram of *trans*-(ICy)₂Pt(PE₂)₂ (**2a**) with the asymmetric unit labeled. Ellipsoids are at the 50% probability level. Hydrogen atoms are omitted for clarity.

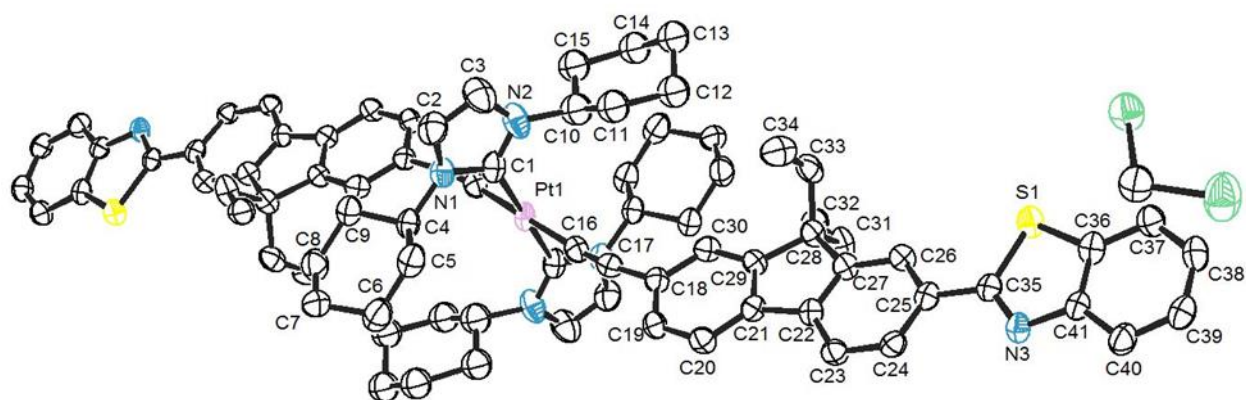


Figure C-3. ORTEP diagram of *trans*-(ICy)₂Pt(BTF)₂ (**2b**) with the asymmetric unit labeled. Ellipsoids are at the 50% probability level. Hydrogen atoms are omitted for clarity.

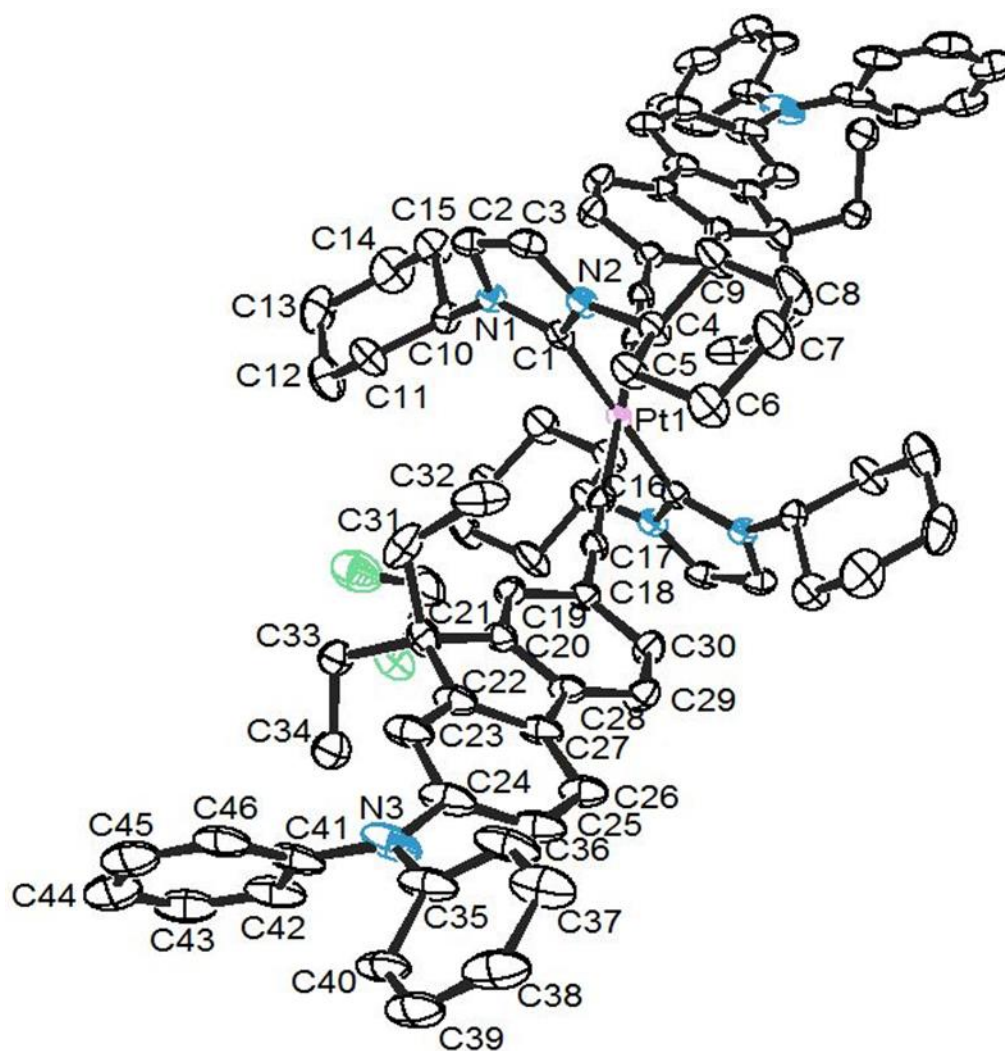


Figure C-4. ORTEP diagram of *trans*-(ICy)₂Pt(DPAF)₂ (**2c**) with the asymmetric unit labeled. Ellipsoids are at the 50% probability level. Hydrogen atoms are omitted for clarity.

NMR Spectra

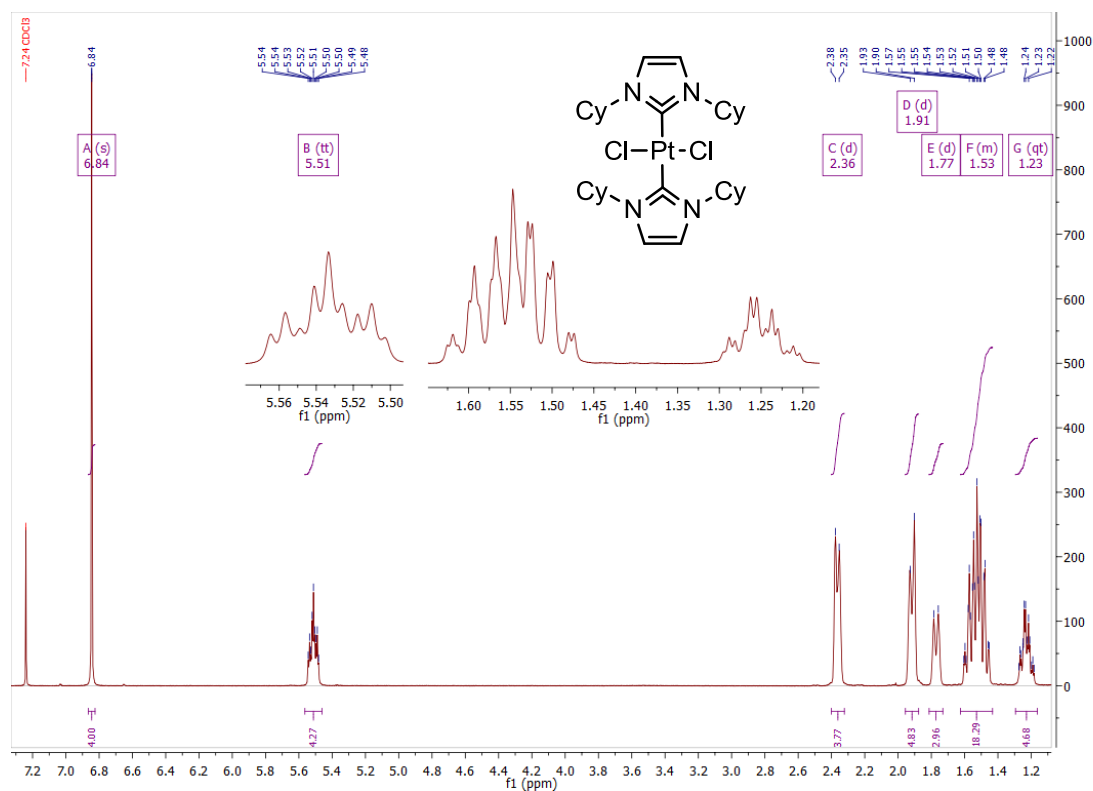


Figure C-5. ¹H NMR (500 MHz, CDCl₃) of 1.

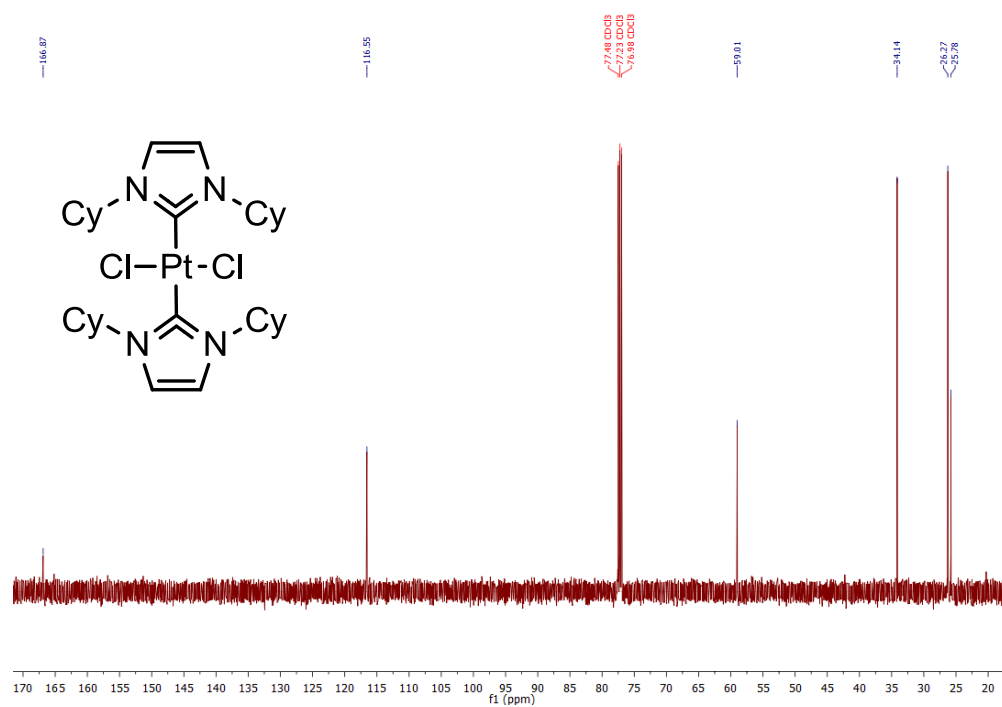


Figure C-6. ¹³C NMR (125.7 MHz, CDCl₃) of 1.

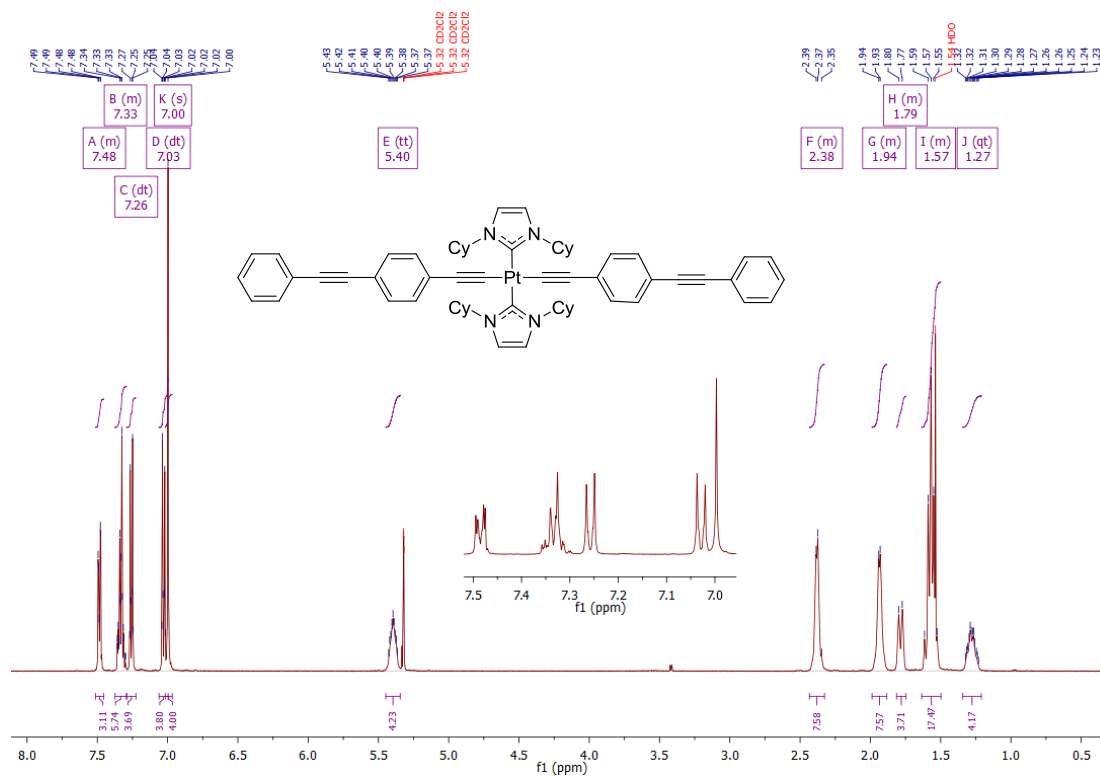


Figure C-7. ¹H NMR (500 MHz, CD₂Cl₂) of **2a**.

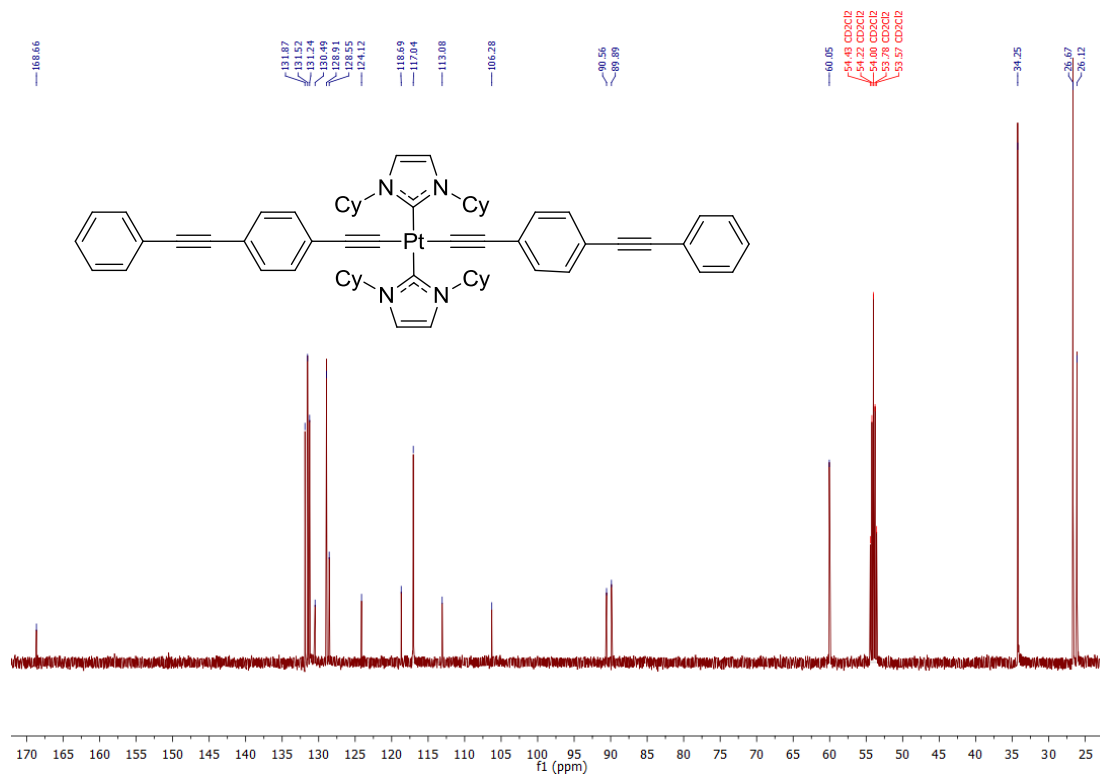


Figure C-8. ¹³C NMR (125.7 MHz, CD₂Cl₂) of **2a**.

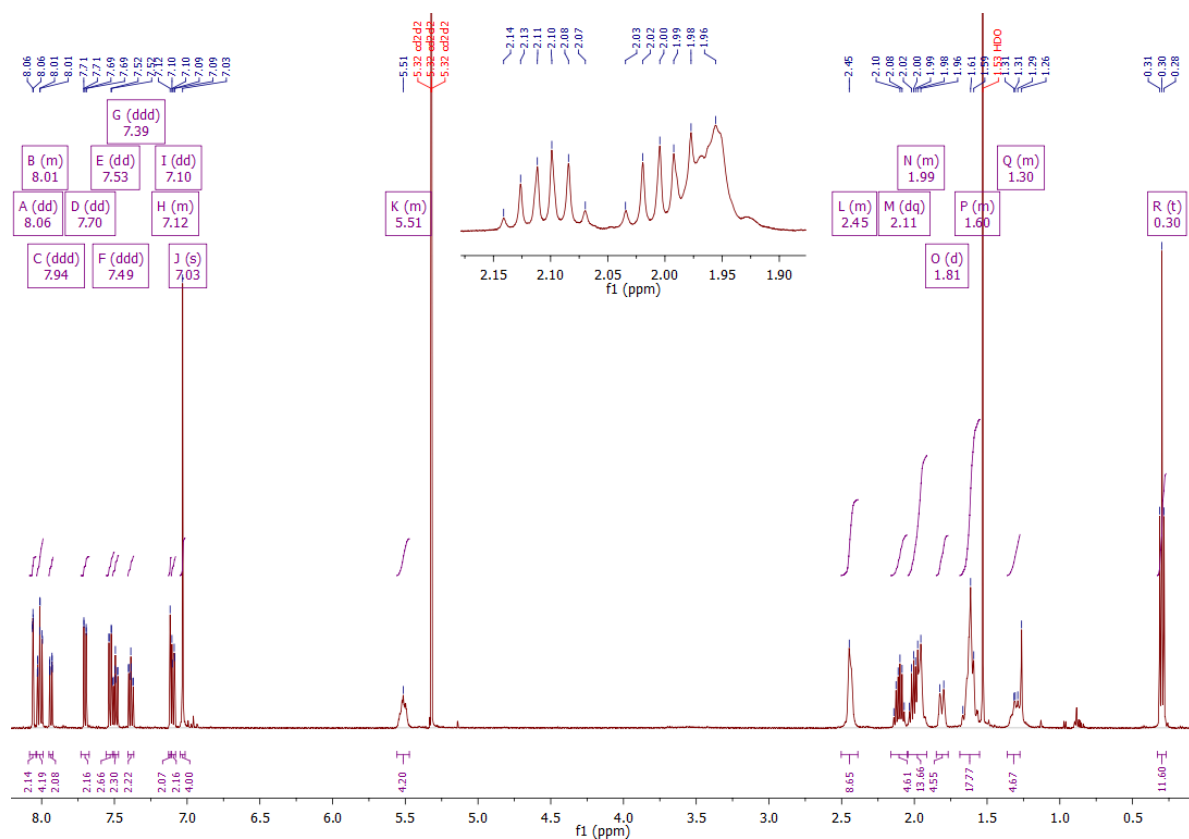


Figure C-9. ^1H NMR (500 MHz, CD_2Cl_2) of **2b**.

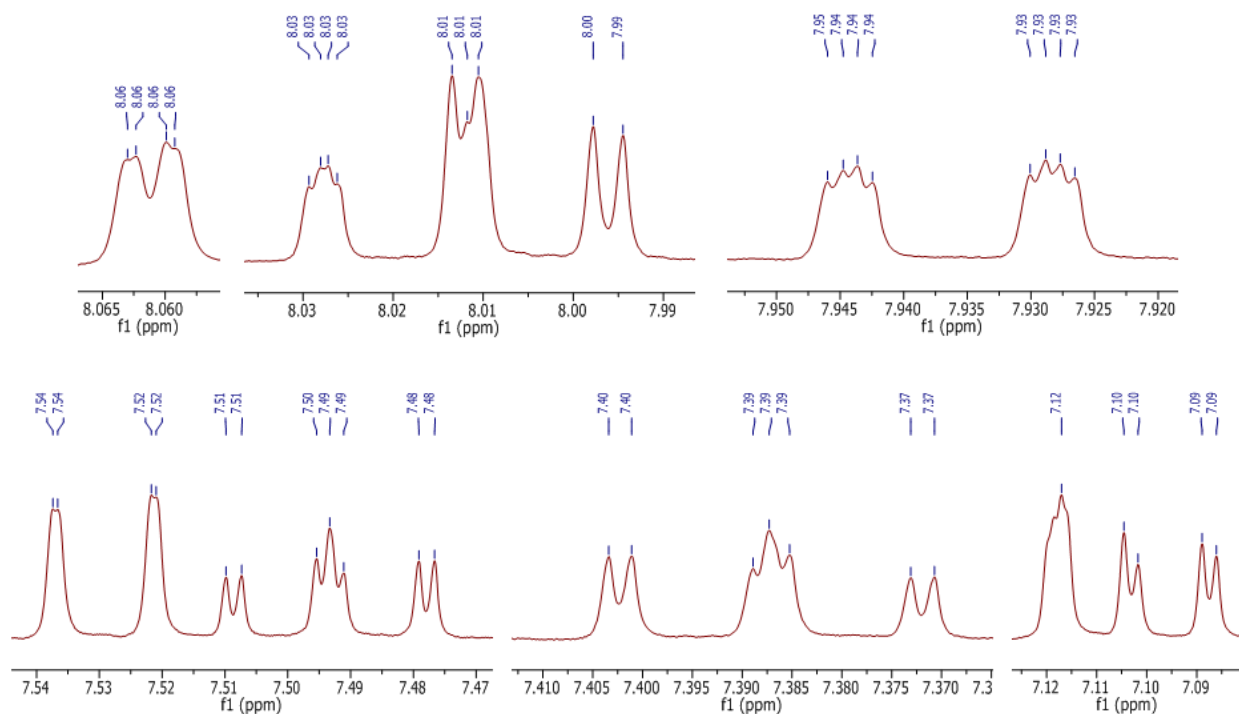


Figure C-10. Insets for selected peaks from the ^1H NMR (500 MHz, CD_2Cl_2) of **2b**.

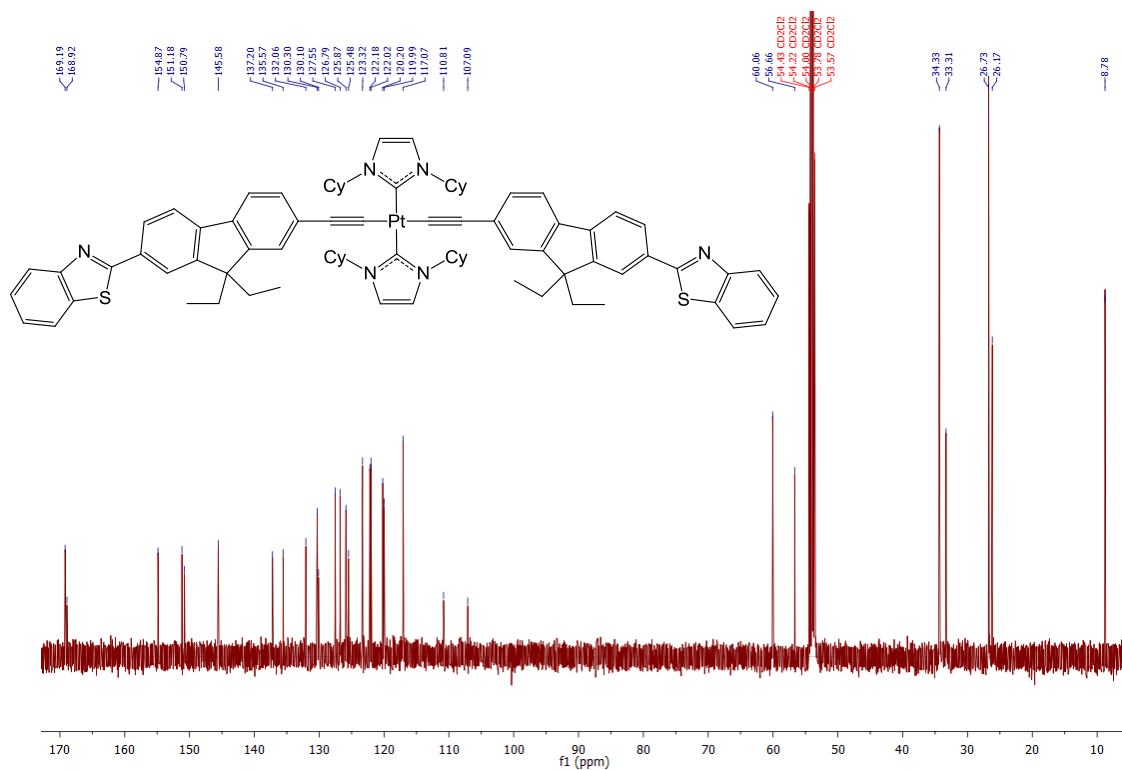


Figure C-11. ^{13}C NMR (125.7 MHz, CD_2Cl_2) of **2b**.

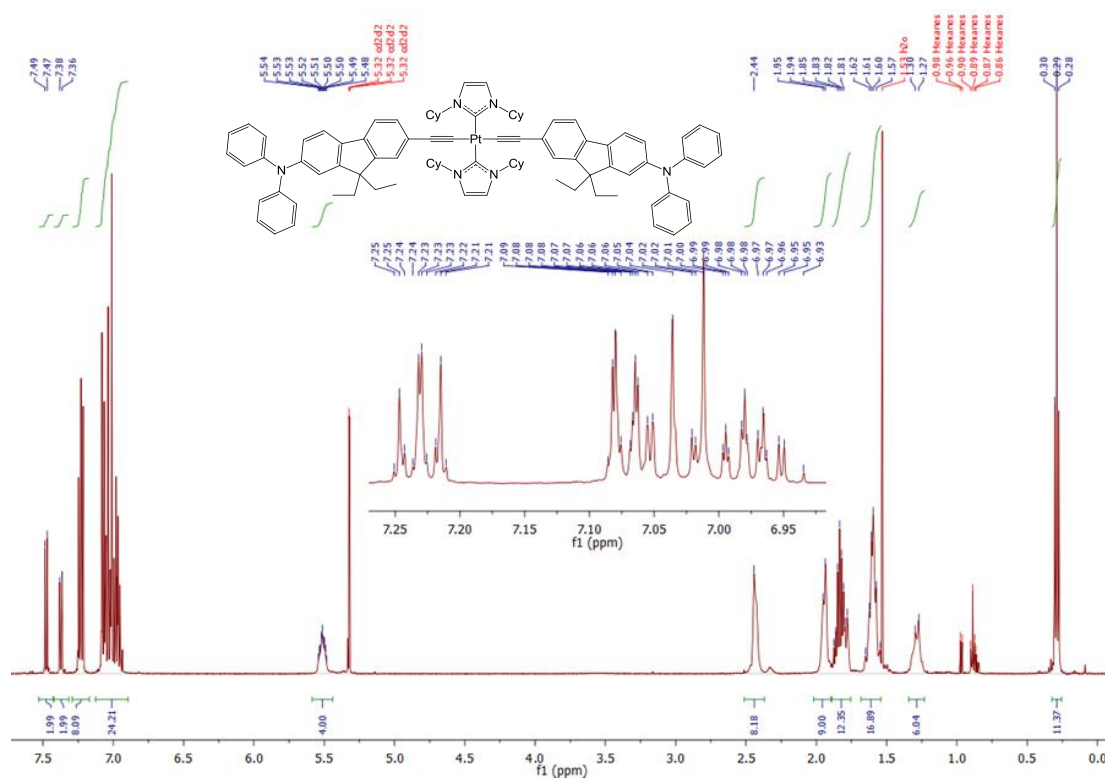


Figure C-12. ^1H NMR (500 MHz, CD_2Cl_2) of **2c**. Residual hexanes are present.

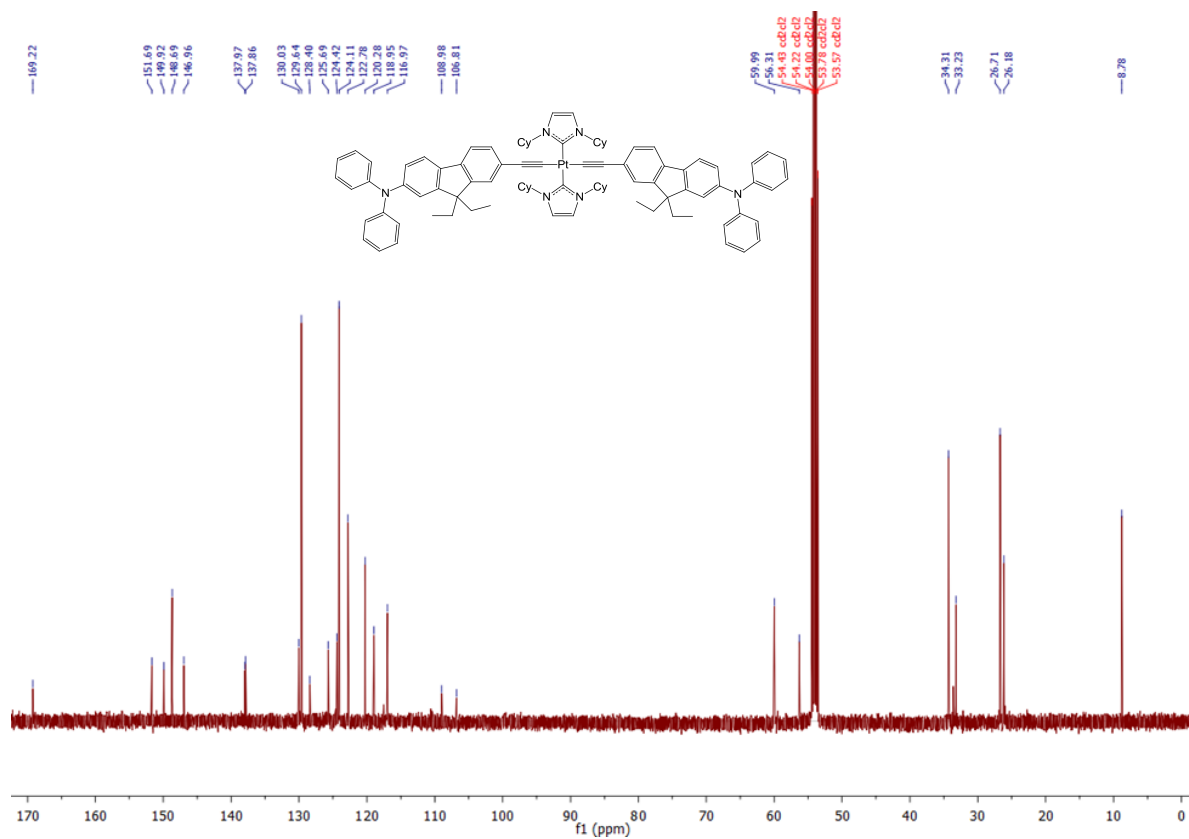


Figure C-13. ¹³C NMR (125.7 MHz, CD₂Cl₂) of **2c**.

IR Spectra

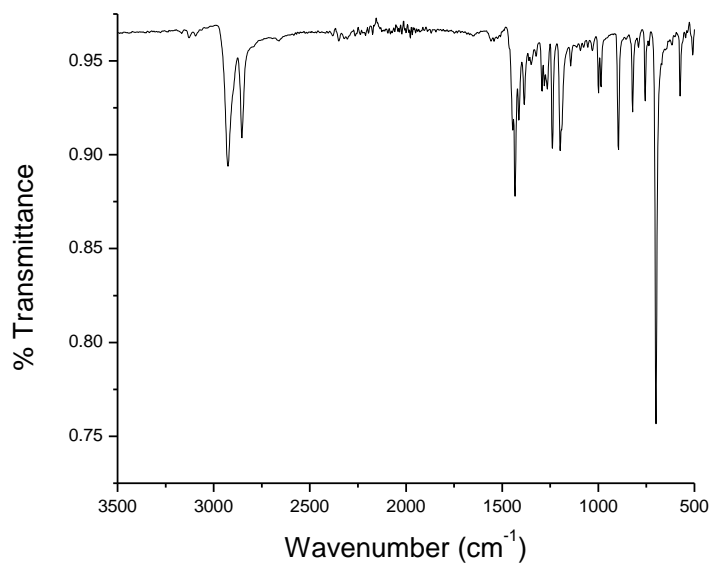


Figure C-14. FTIR spectrum of **1**.

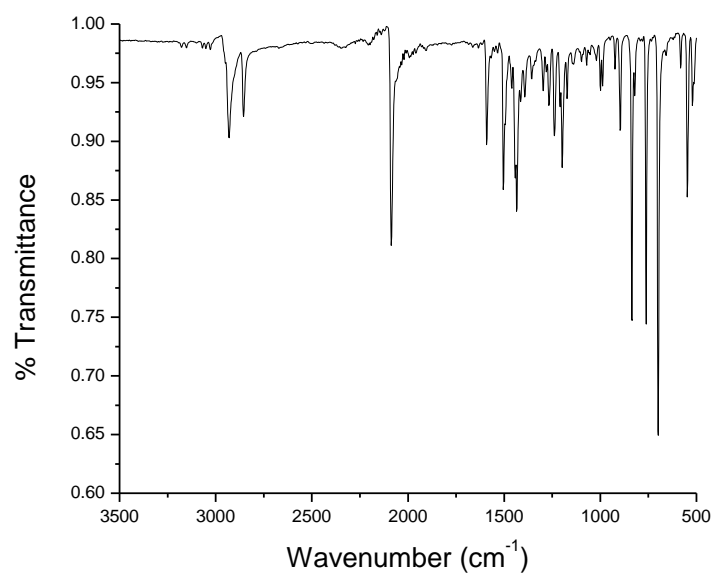


Figure C-15. FTIR spectrum of **2a**.

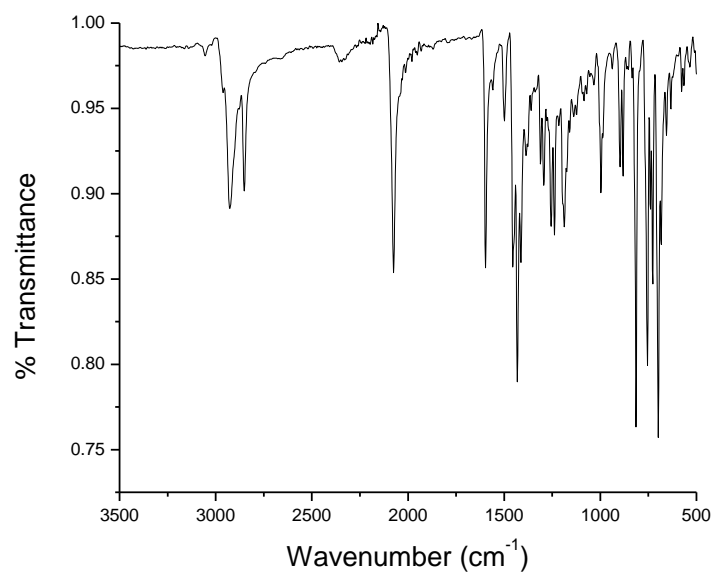


Figure C-16. FTIR spectrum of **2b**.

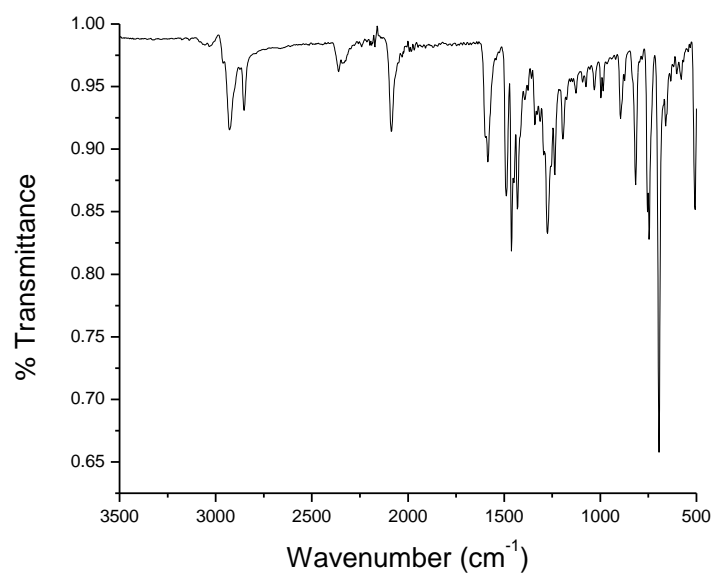


Figure C-17. FTIR spectrum of **2c**.

Emission Lifetime Decays

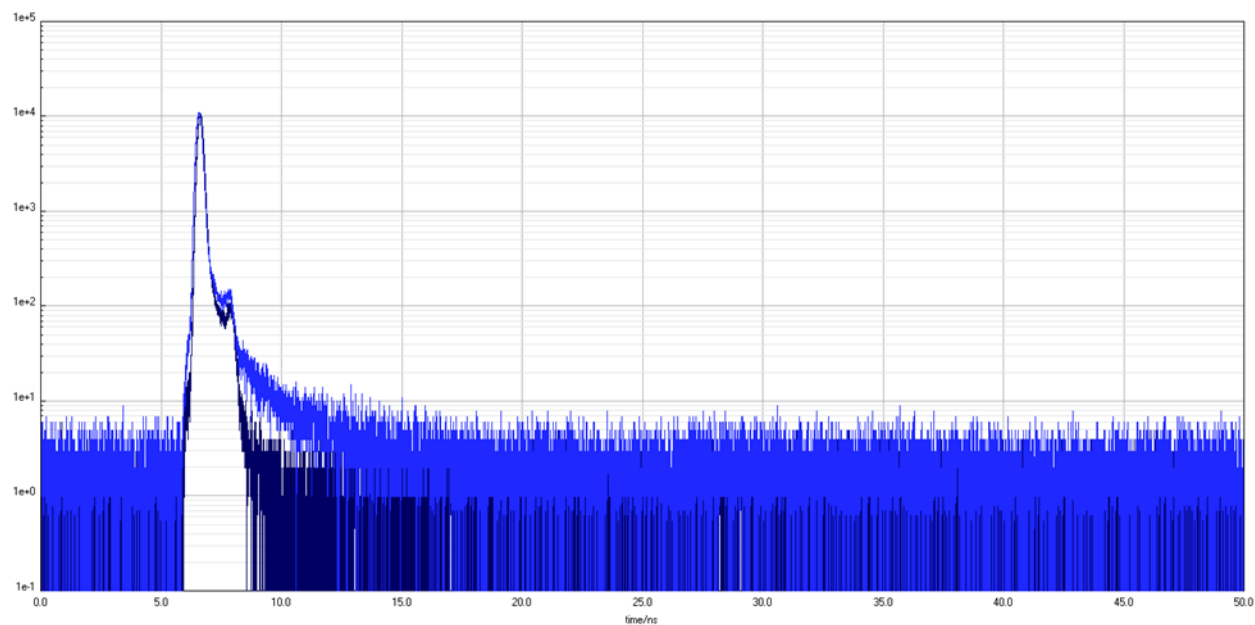


Figure C-18. Fluorescence lifetime decay for **2a** (light blue) with instrument response function (dark blue).

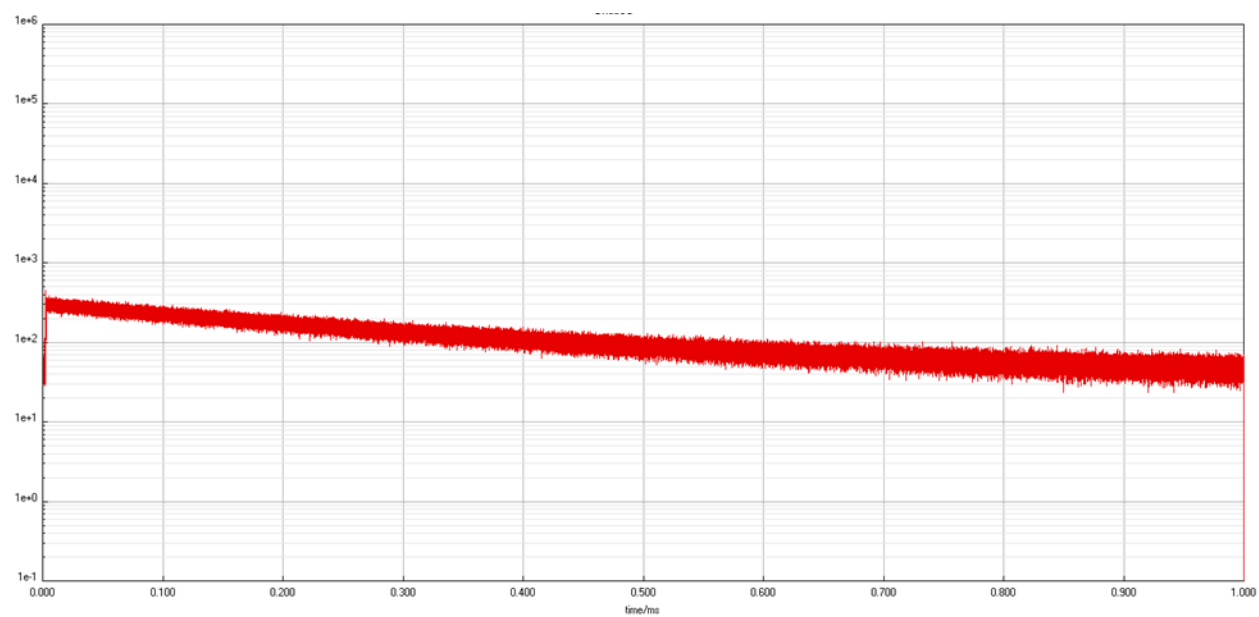


Figure C-19. Phosphorescence lifetime decay for **2a**.

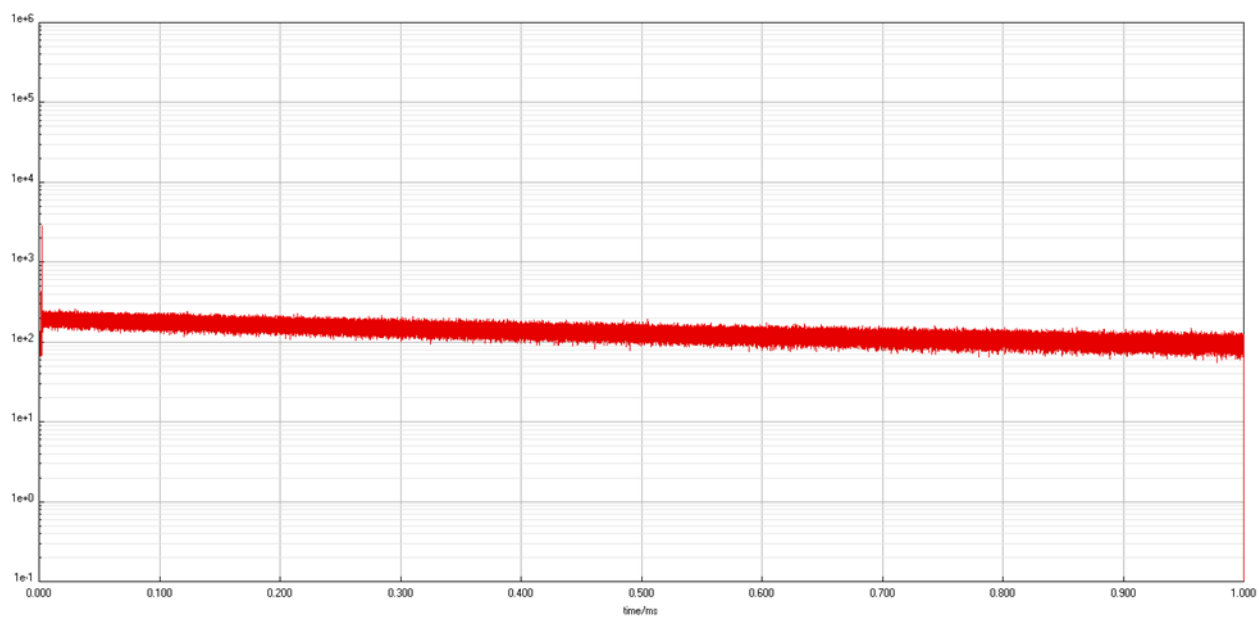


Figure C-20. Phosphorescence lifetime decay for **2b**.

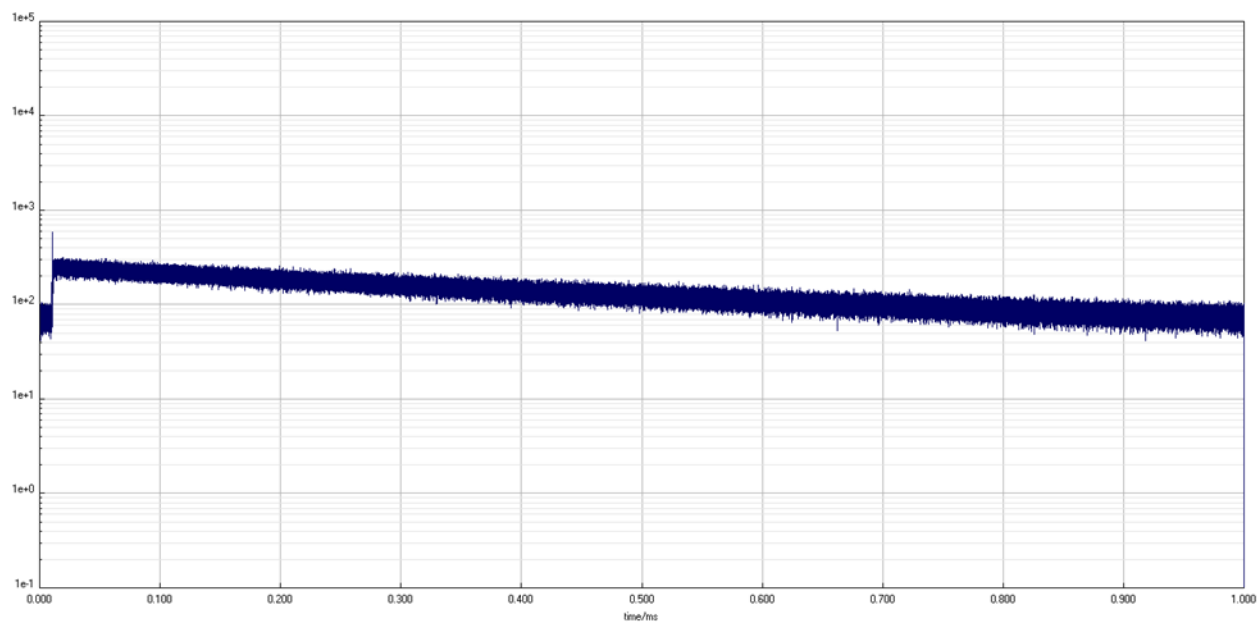


Figure C-21. Phosphorescence lifetime decay for **2c**.

Transient Absorption Decays

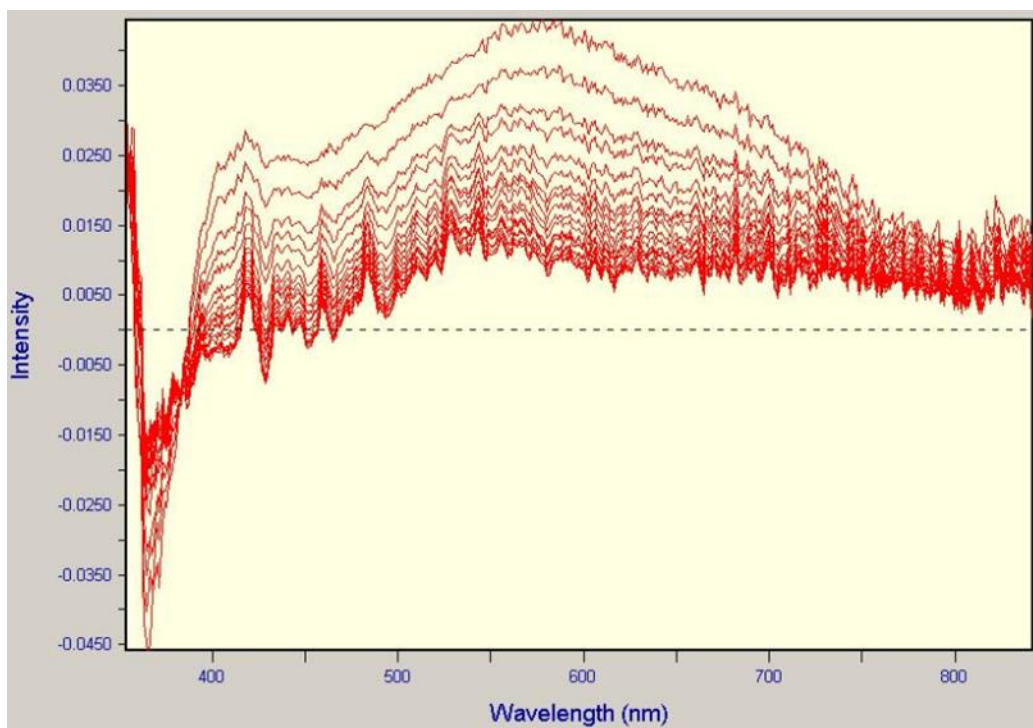


Figure C-22. Transient absorption decay for **2a**. Initial camera delay: 100ns, camera delay increment: 15 μ s, 100 images averaged per trace, Q-switch delay: 380 μ s, 180 μ J per pulse.

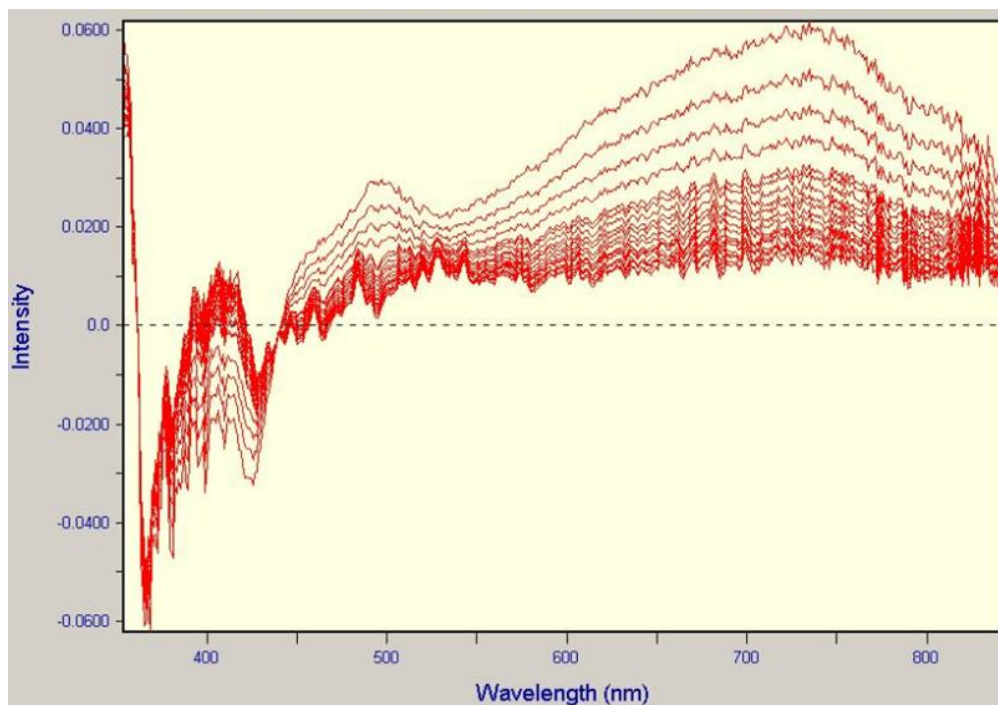


Figure C-23. Transient absorption decay for **2b**. Initial camera delay: 100ns, camera delay increment: 20 μ s, 100 images averaged per trace, Q-switch delay: 382 μ s, 180 μ J per pulse.

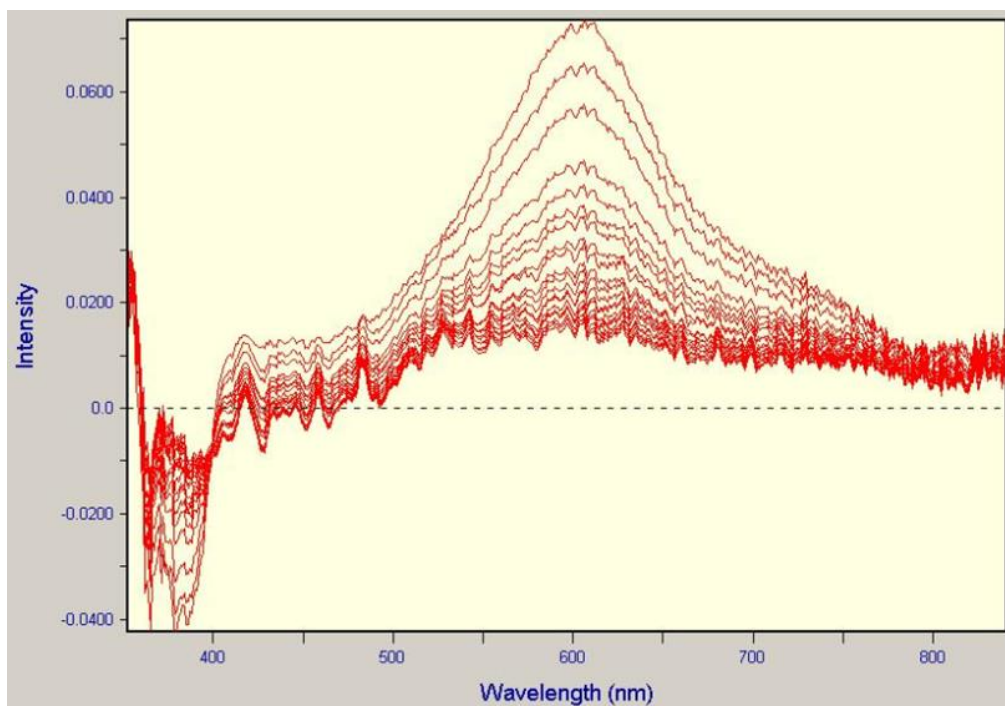


Figure C-24. Transient absorption decay for **2c**. Initial camera delay: 100ns, camera delay increment: 20 μ s, 100 images averaged per trace, Q-switch delay: 379 μ s, 180 μ J per pulse.

Triplet-Triplet Absorption Power Dependence

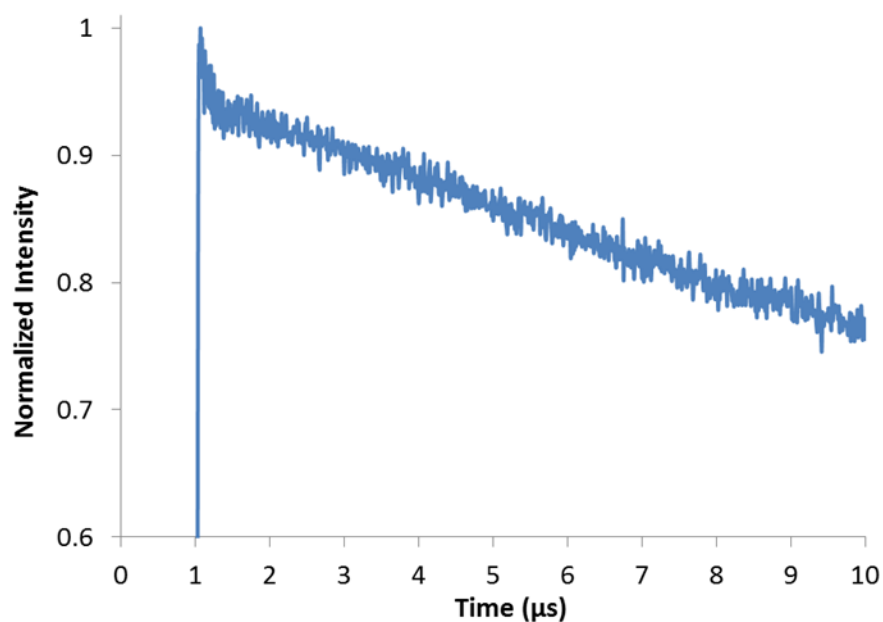


Figure C-25. Transient absorption decay profile for **2a**. Conditions: 200 μJ per pulse, 380 μJ Q-switch delay, 128 scans averaged, decay measured at 584 nm.

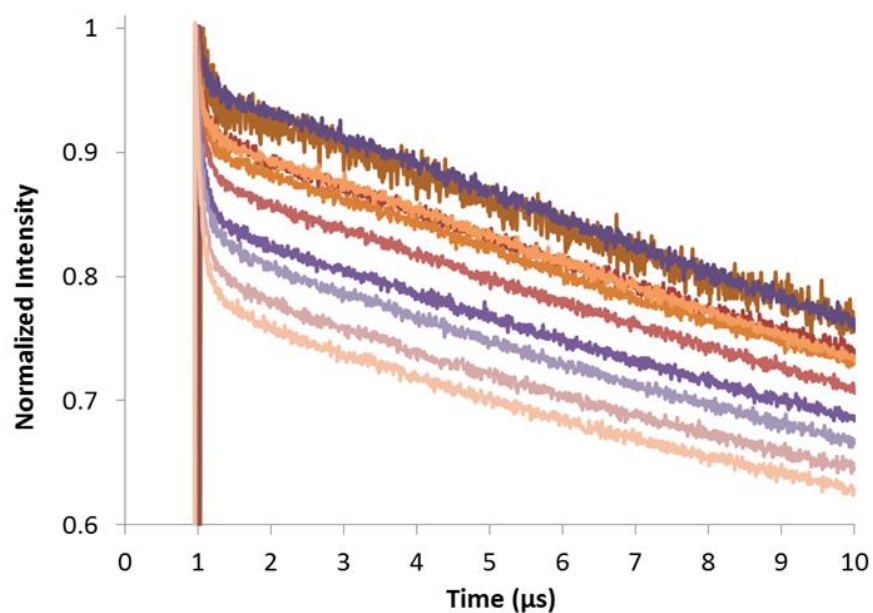


Figure C-26. Transient absorption decay profiles for **2a** at varying laser energies. Conditions: 200 μJ – 18 mJ per pulse, 380-200 μJ Q-switch delay, 128 scans averaged per trace, decays measured at 584 nm.

Computational Studies

DFT and TD-DFT calculations were performed in the Gaussian 09, revision C.01, suite of programs at the B3LYP level with the 6-31G(d) basis set for nonmetals and the SDD basis set for Pt. Carbene cyclohexane groups were replaced by methyl groups to improve computational efficiency. These truncated complexes are denoted as **2a'-c'**. The ground state structures were optimized in the gas phase from idealized starting configurations without symmetry constraints. The optimized structures were confirmed to be minima by the lack of negative modes in a frequency calculation. Structures and orbitals were visualized using Chemcraft Version 1.7, which was also used to generate charge difference density (CDD) plots. Orbitals were visualized at an isosurface value of 0.02, while CDDs were visualized at an isosurface value of 0.0004. Relevant data is shown in Table C-2.

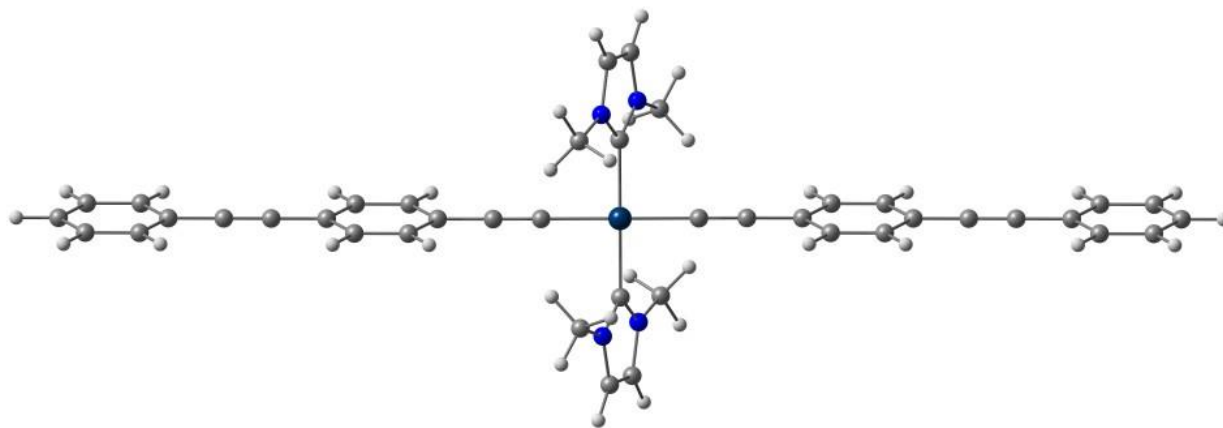


Figure C-27. DFT optimized structure of **2a'**.

Table C-2. Summary of TDDFT computations for vertical excitations of oscillator strength greater than 0.1 for compounds **2a'**-**c'**.

Complex	Wavelength nm	Orbital Transitions (% contribution)		Oscillator Strength <i>f</i>
2a'	373.8	165→168 HOMO-1 → LUMO+1	(2.4%)	2.3830
		166→167 HOMO → LUMO	(97.6%)	
	334.2	165→168 HOMO-1 → LUMO+1	(97.3%)	1.0319
		166→167 HOMO → LUMO	(2.7%)	
2b'	429.3	259→262 HOMO-1 → LUMO+1	(5.3%)	2.2796
		260→261 HOMO → LUMO	(94.7%)	
	381.6	258→261 HOMO-2 → LUMO	(13.7%)	0.7184
		259→262 HOMO-1 → LUMO+1	(81.8%)	
		260→261 HOMO → LUMO	(4.5%)	
	316.4	256→262 HOMO-4 → LUMO+1	(14.7%)	0.7139
		257→261 HOMO-3 → LUMO	(75.6%)	
		260→265 HOMO → LUMO+4	(9.7%)	
2c'	381.5	279→282 HOMO-1 → LUMO+1	(18.3%)	2.6813
		280→281 HOMO → LUMO	(81.7%)	
	344.6	278→281 HOMO-2 → LUMO	(3.6%)	0.1267
		279→282 HOMO-1 → LUMO+1	(77.8%)	
		280→281 HOMO → LUMO	(18.6%)	
	319.53	278→286 HOMO-2 → LUMO+5	(2.3%)	0.1648
		279→286 HOMO-1 → LUMO+5	(24.3%)	
		279→287 HOMO-1 → LUMO+6	(12.9%)	
		280→286 HOMO → LUMO+5	(60.5%)	
	319.50	278→287 HOMO-2 → LUMO+6	(2.2%)	0.1494
		279→286 HOMO-1 → LUMO+5	(13.1%)	
		279→287 HOMO-1 → LUMO+6	(24.4%)	
		280→287 HOMO → LUMO+6	(60.3%)	
	315.3	276→282 HOMO-4 → LUMO+1	(11.1%)	0.2115
		278→281 HOMO-2 → LUMO	(85.7%)	
		279→282 HOMO-1 → LUMO+1	(3.2%)	

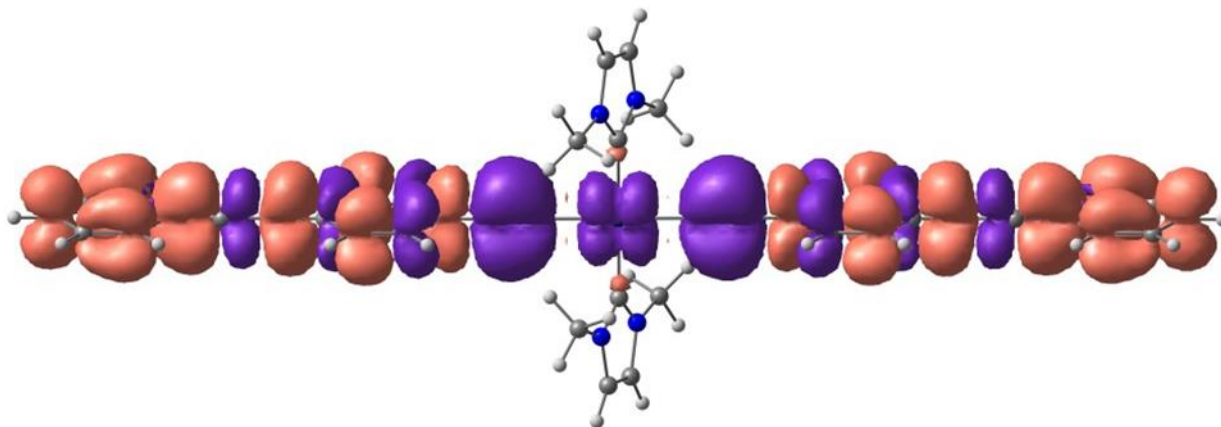


Figure C-28. 373.8 nm CDD of **2a'**. Blue coloring indicates electron density being lost, while red coloring indicates electron density being gained in the electronic transition.

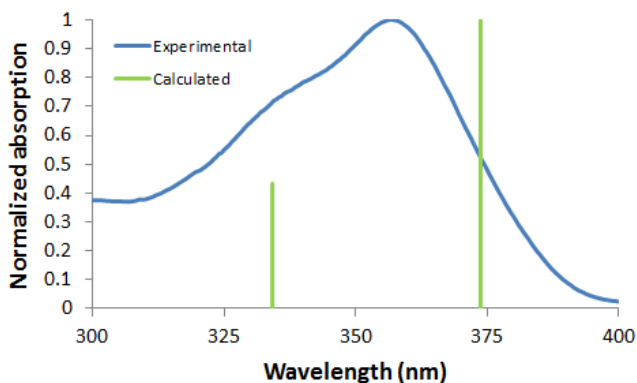


Figure C-29. Normalized overlay of the experimental absorption spectrum of **2a** with the TDDFT computed line spectra of **2a'**. Only vertical excitations with $f > 0.1$ are shown.

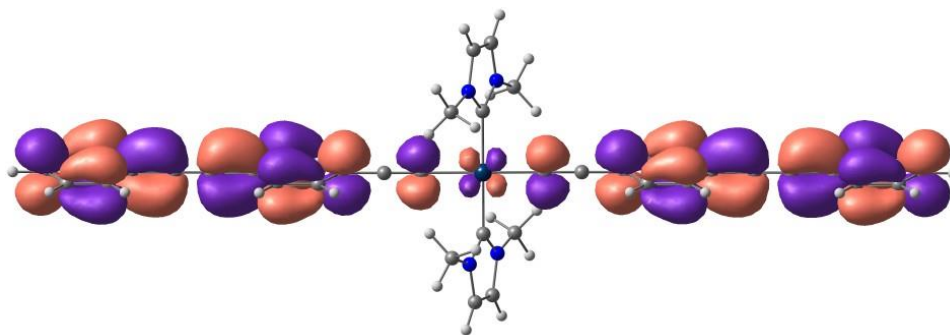


Figure C-30. LUMO+1 (orbital 168) of compound **2a'**.

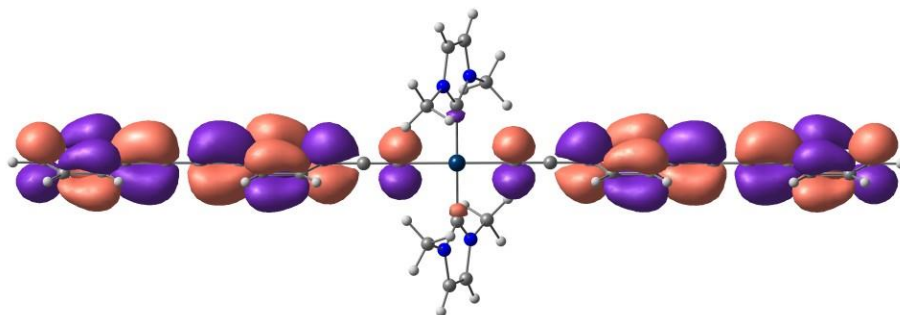


Figure C-31. LUMO (orbital 167) of compound **2a'**.

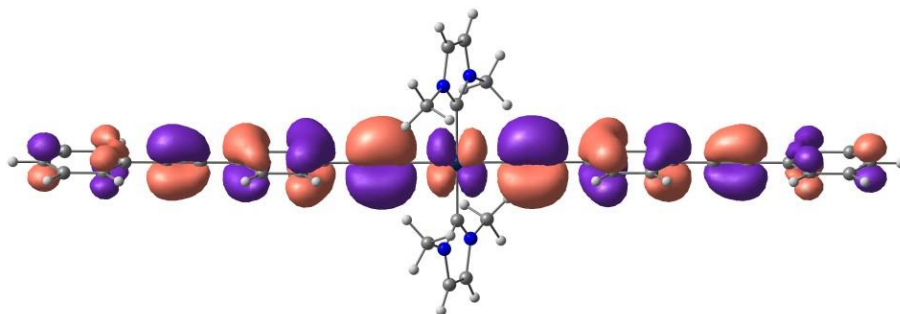


Figure C-32. HOMO (orbital 166) of compound **2a'**.

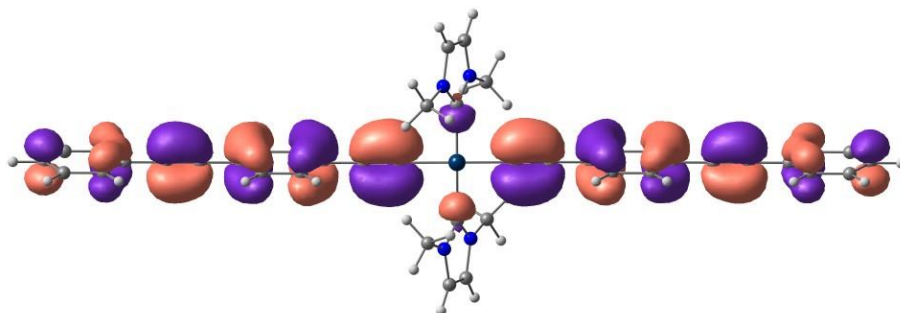


Figure C-33. HOMO-1 (orbital 165) of compound **2a'**.

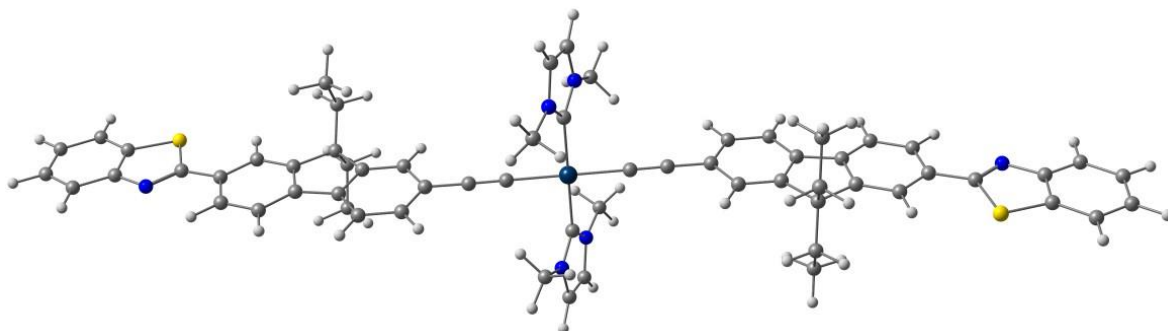


Figure C-34. DFT optimized structure of **2b'**.

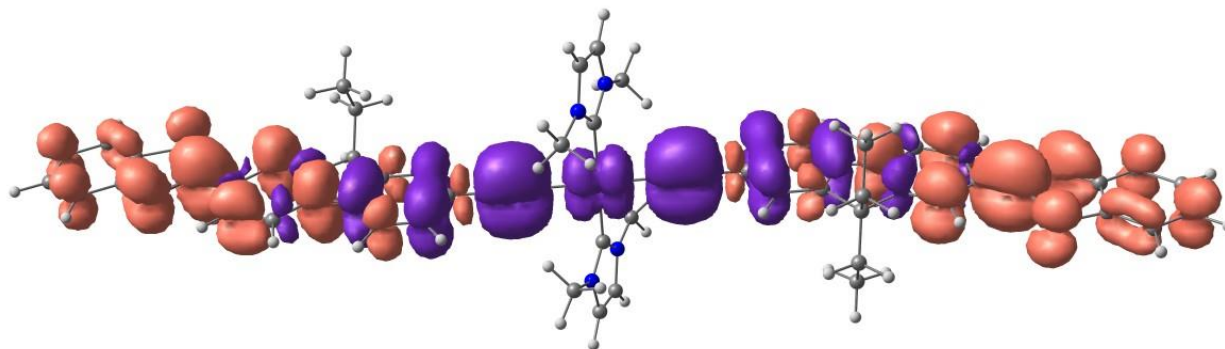


Figure C-35. 429.3 nm CDD of **2b'**. Blue coloring indicates electron density being lost, while red coloring indicates electron density being gained in the electronic transition.

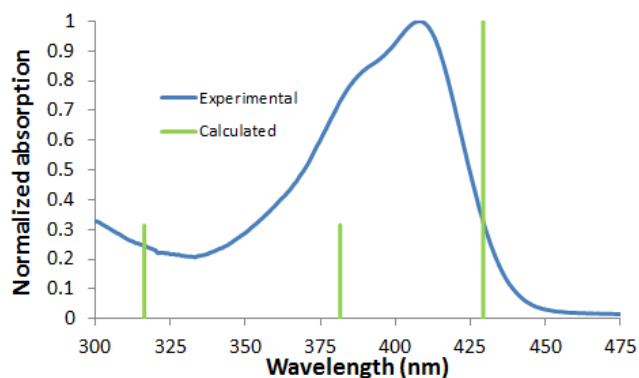


Figure C-36. Normalized overlay of the experimental absorption spectrum of **2a** with the TDDFT computed line spectra of **2b'**. Only vertical excitations with $f > 0.1$ are shown.

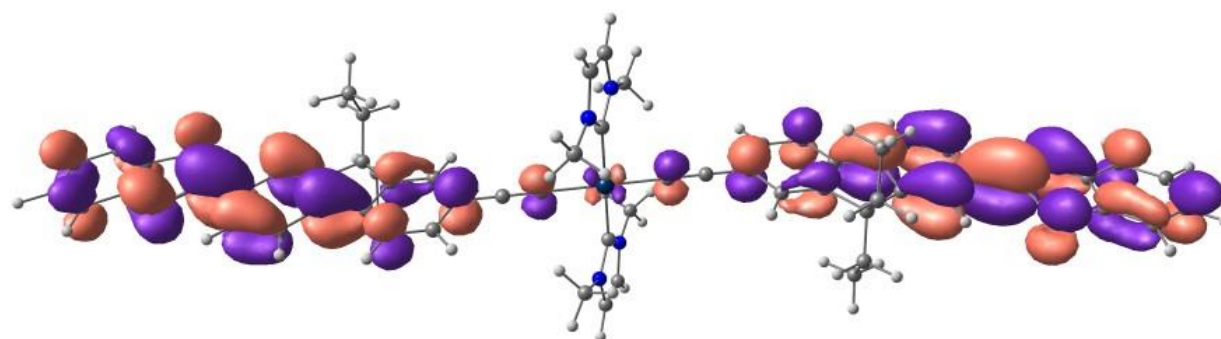


Figure C-37. LUMO+1 (orbital 262) of compound **2b'**.

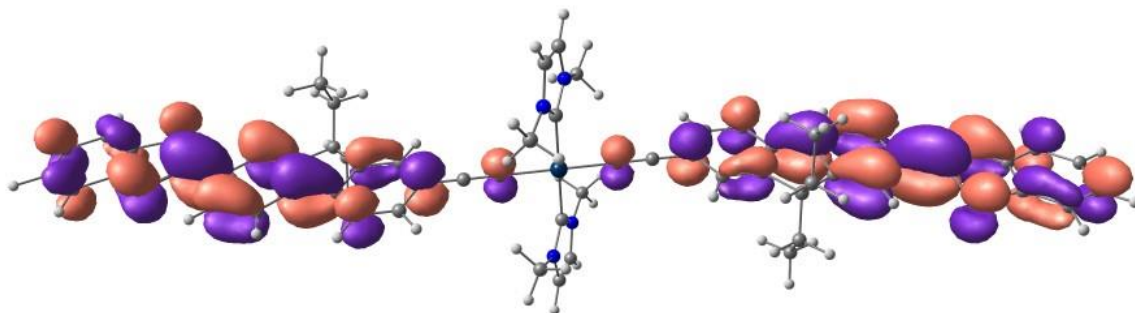


Figure C-38. LUMO (orbital 261) of compound **2b'**.

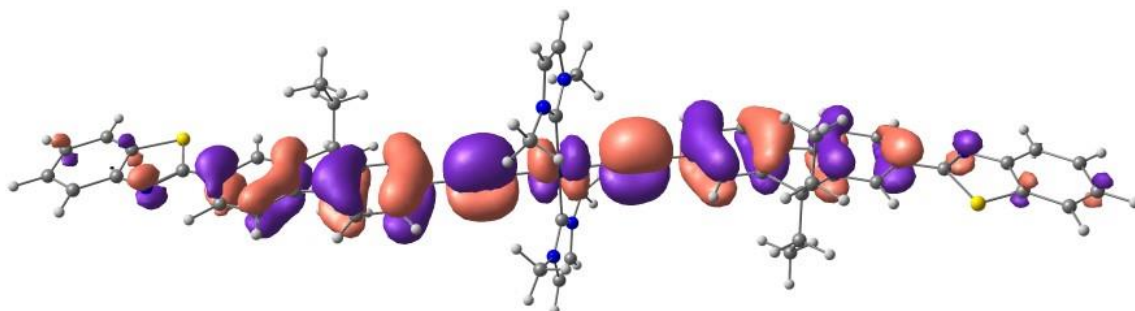


Figure C-39. HOMO (orbital 260) of compound **2b'**.

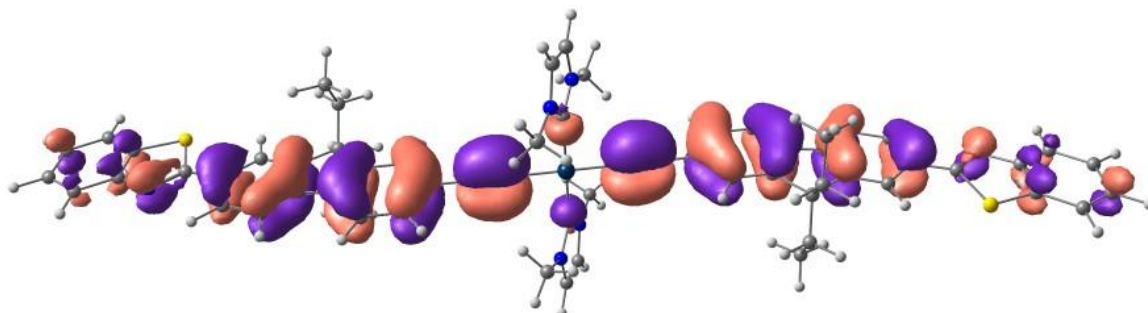


Figure C-40. LUMO+1 (orbital 259) of compound **2b'**.

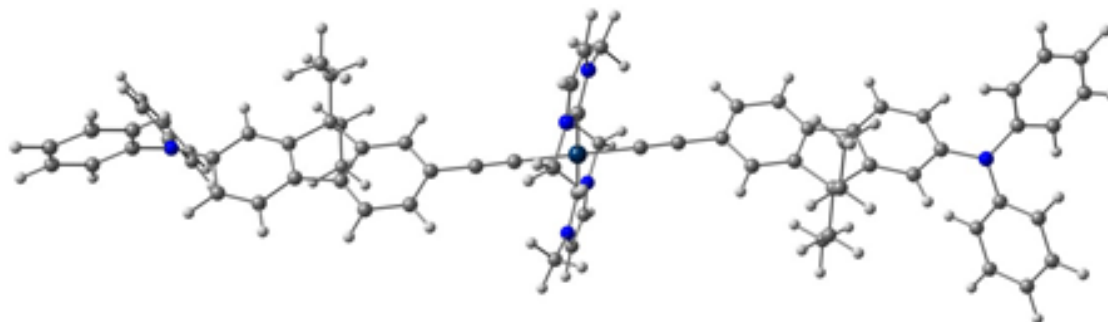


Figure C-41. DFT optimized structure of **2c'**.

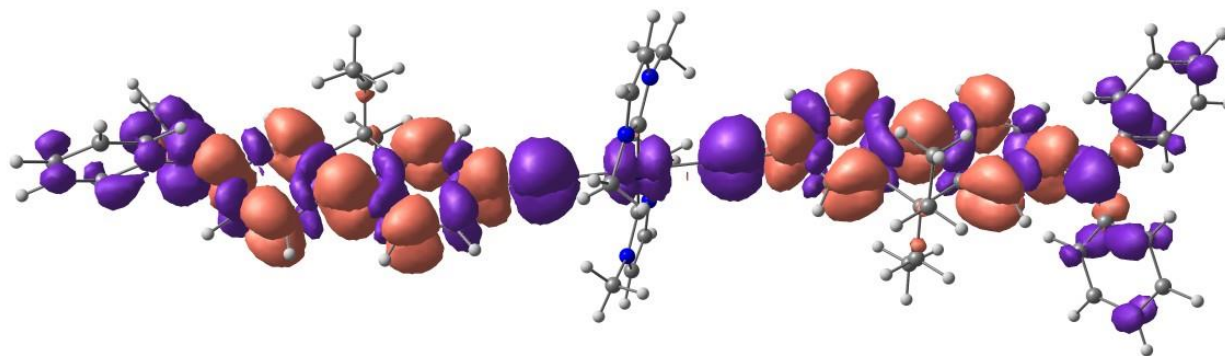


Figure C-42. 381.5 nm CDD of **2c'**. Blue coloring indicates electron density being lost, while red coloring indicates electron density being gained in the electronic transition.

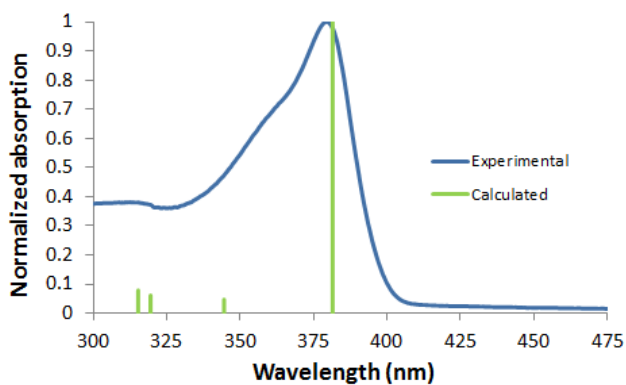


Figure C-43. Normalized overlay of the experimental absorption spectrum of **2c** with the TDDFT computed line spectra of **2c'**. Only vertical excitations with $f > 0.1$ are shown

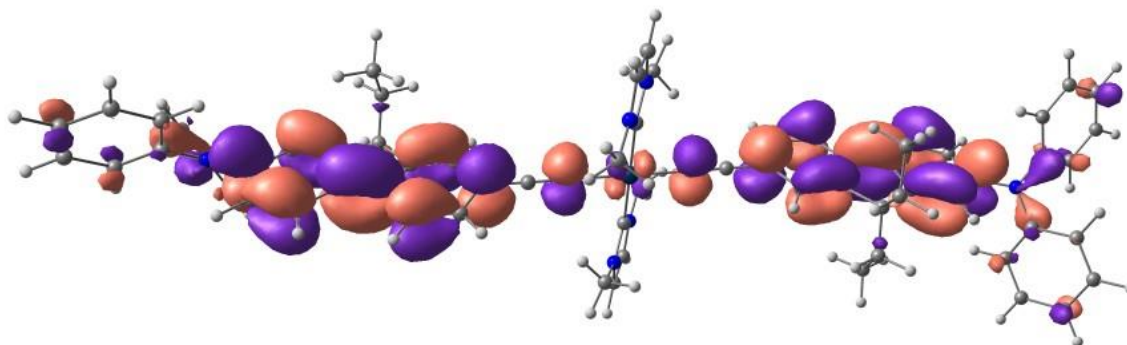


Figure C-44. LUMO+1 (orbital 282) of compound **2c'**.

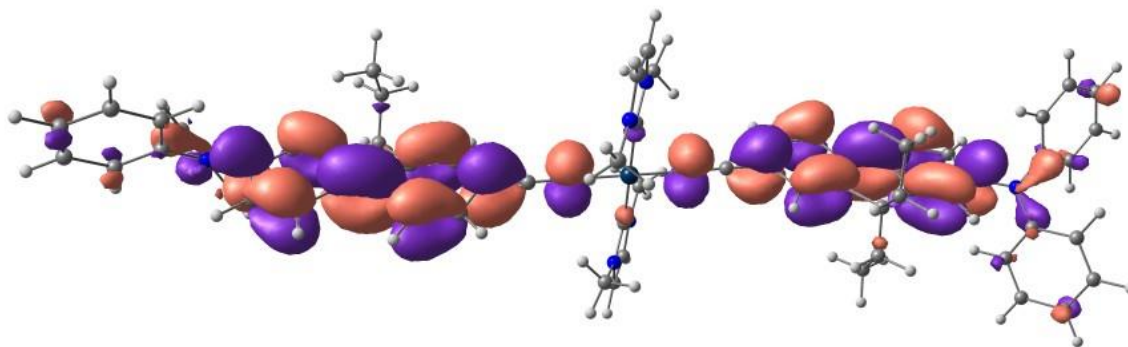


Figure C-45. LUMO (orbital 281) of compound **2c'**.

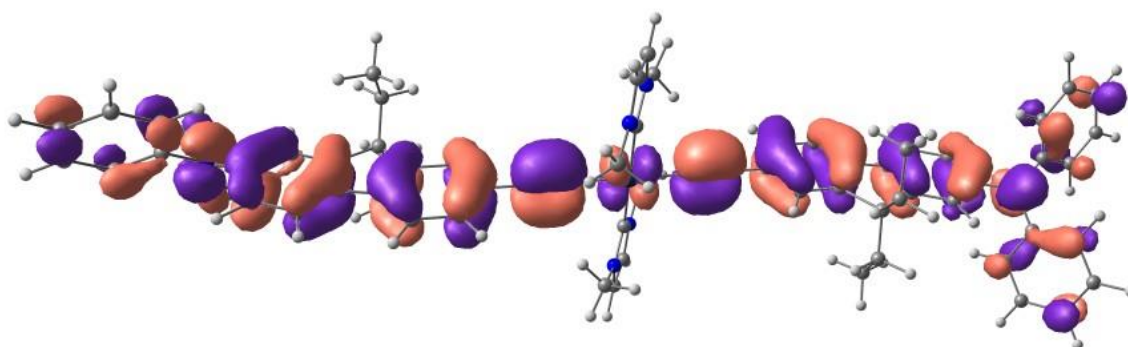


Figure C-46. HOMO (orbital 280) of compound **2c'**.

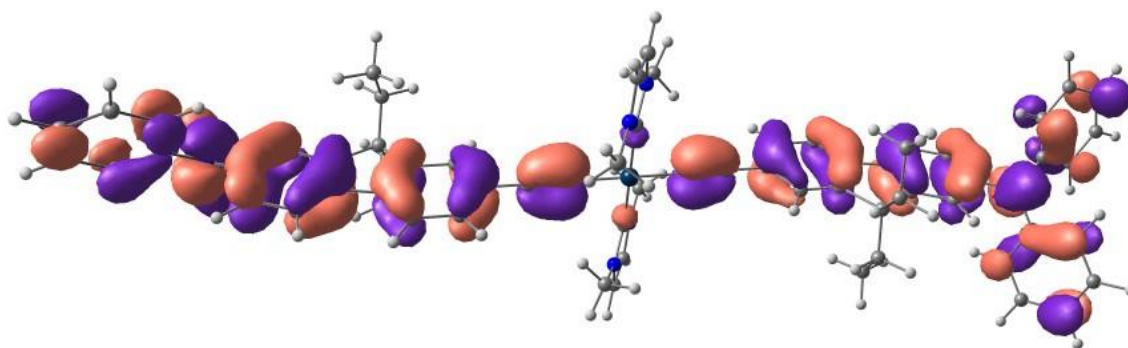


Figure C-47. HOMO-1 (orbital 279) of compound **2c'**.

APPENDIX D
SUPPORTING INFORMATION FOR CHAPTER 3

NMR Spectra

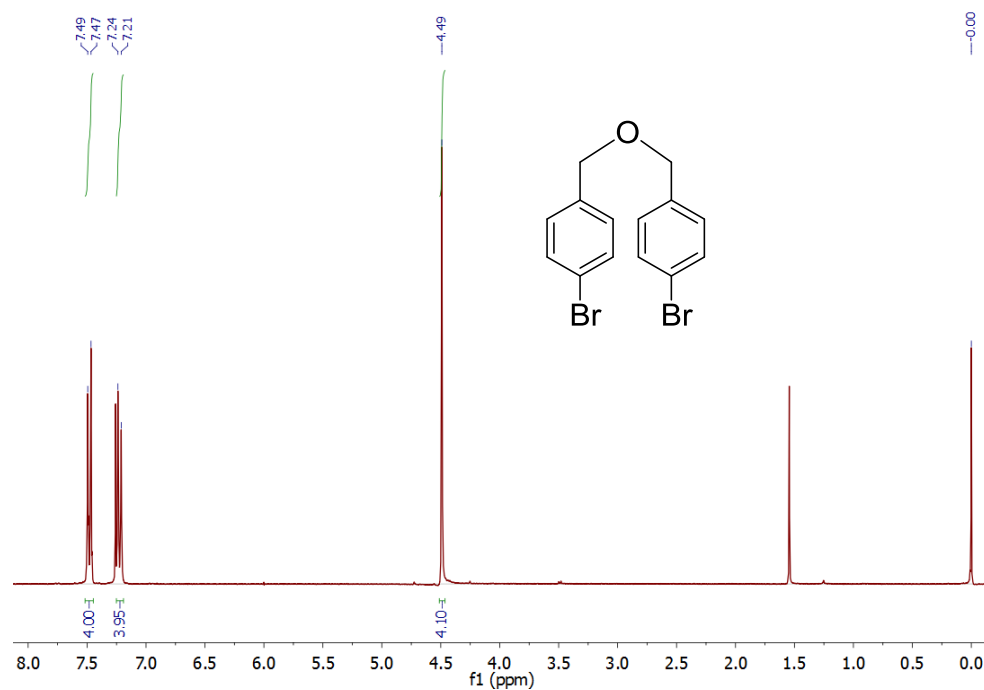


Figure D-1. ¹H NMR (500 MHz, CDCl₃) of **COC-Br**.

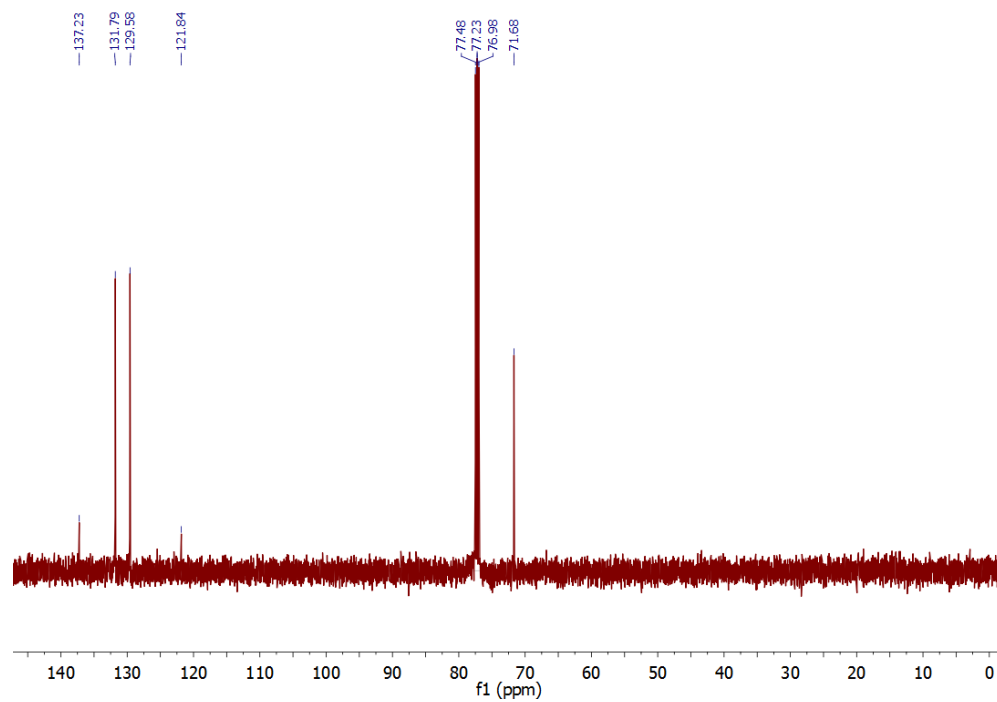


Figure D-2. ¹³C NMR (126 MHz, CDCl₃) of **COC-Br**.

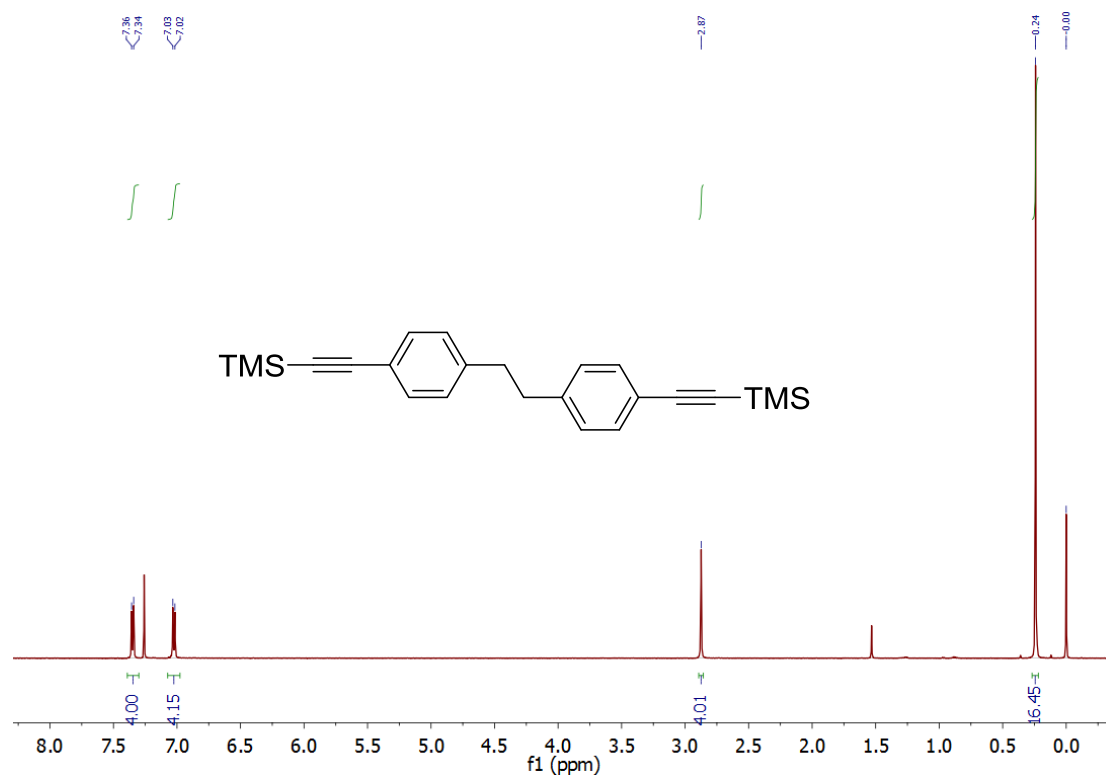


Figure D-3. ¹H NMR (500 MHz, CDCl₃) of **CC-TMS**.

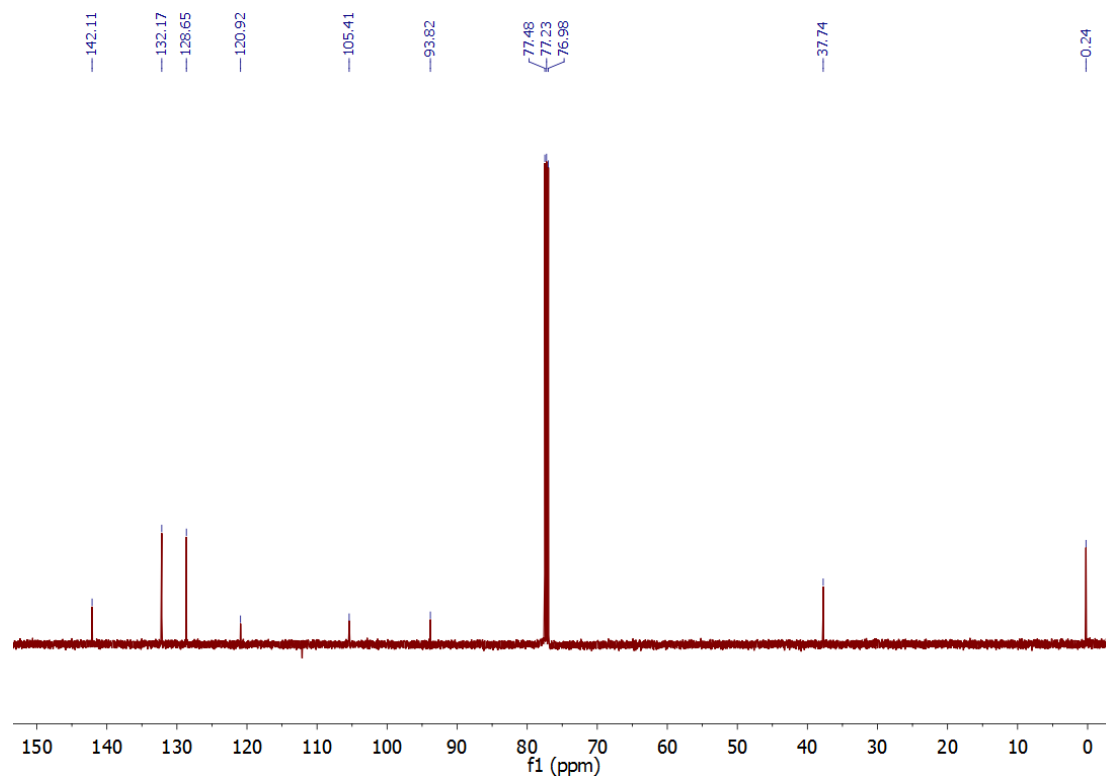


Figure D-4. ¹³C NMR (126 MHz, CDCl₃) of **CC-TMS**.

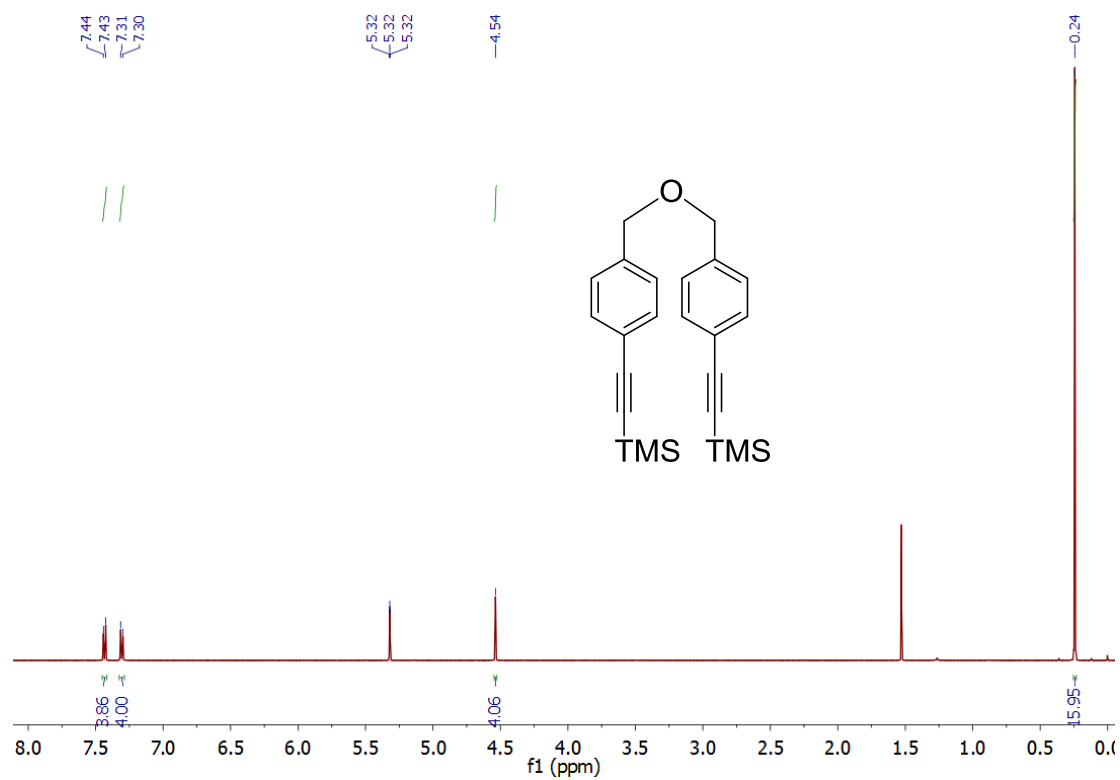


Figure D-5. ¹H NMR (500 MHz, CD₂Cl₂) of **COC-TMS**.

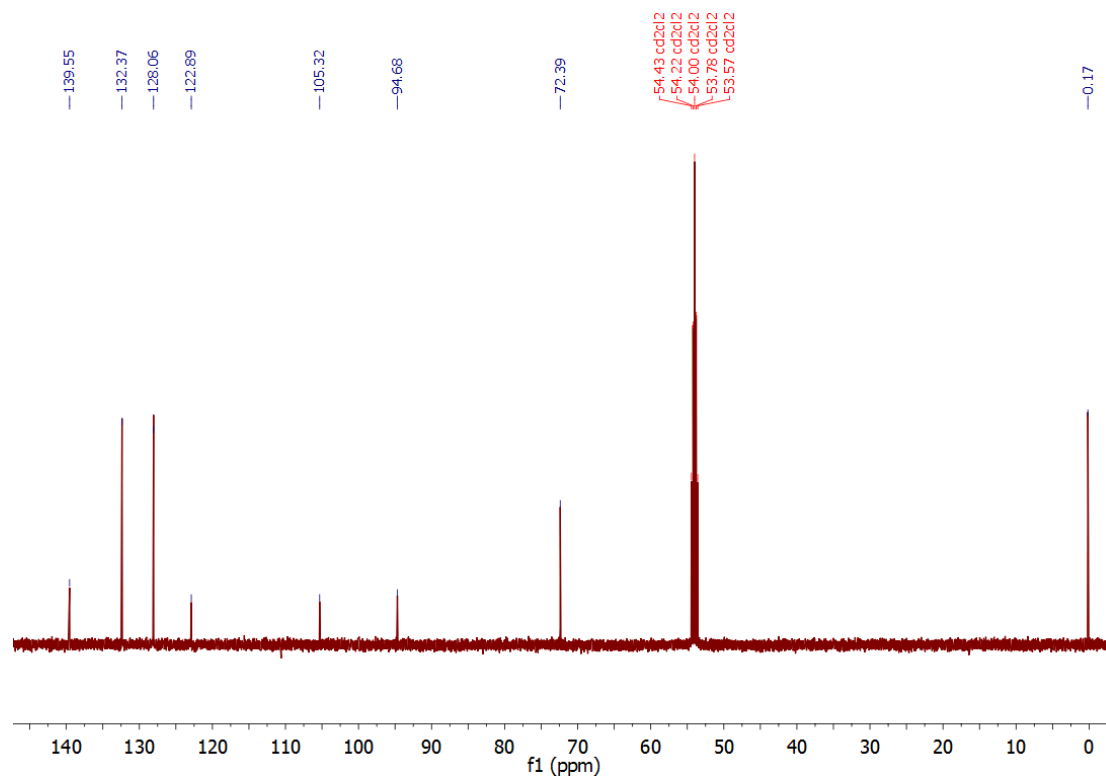


Figure D-6. ¹³C NMR (126 MHz, CD₂Cl₂) of **COC-TMS**.

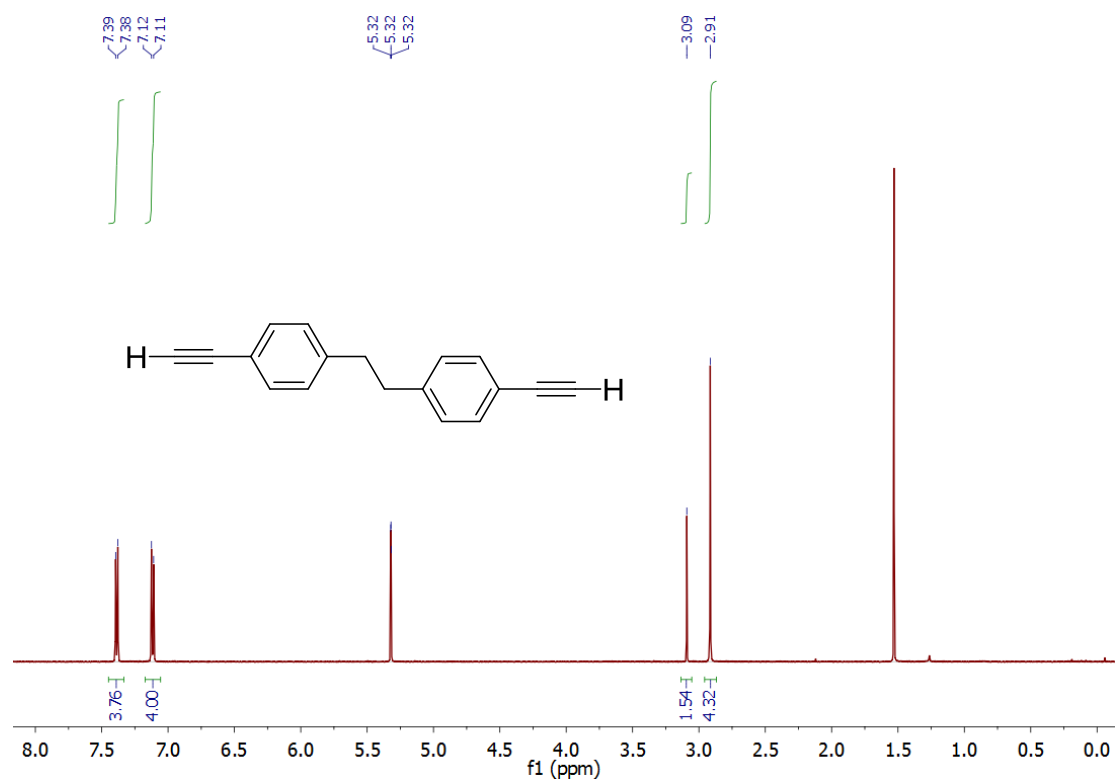


Figure D-7. ¹H NMR (500 MHz, CD₂Cl₂) of **CC-H**.

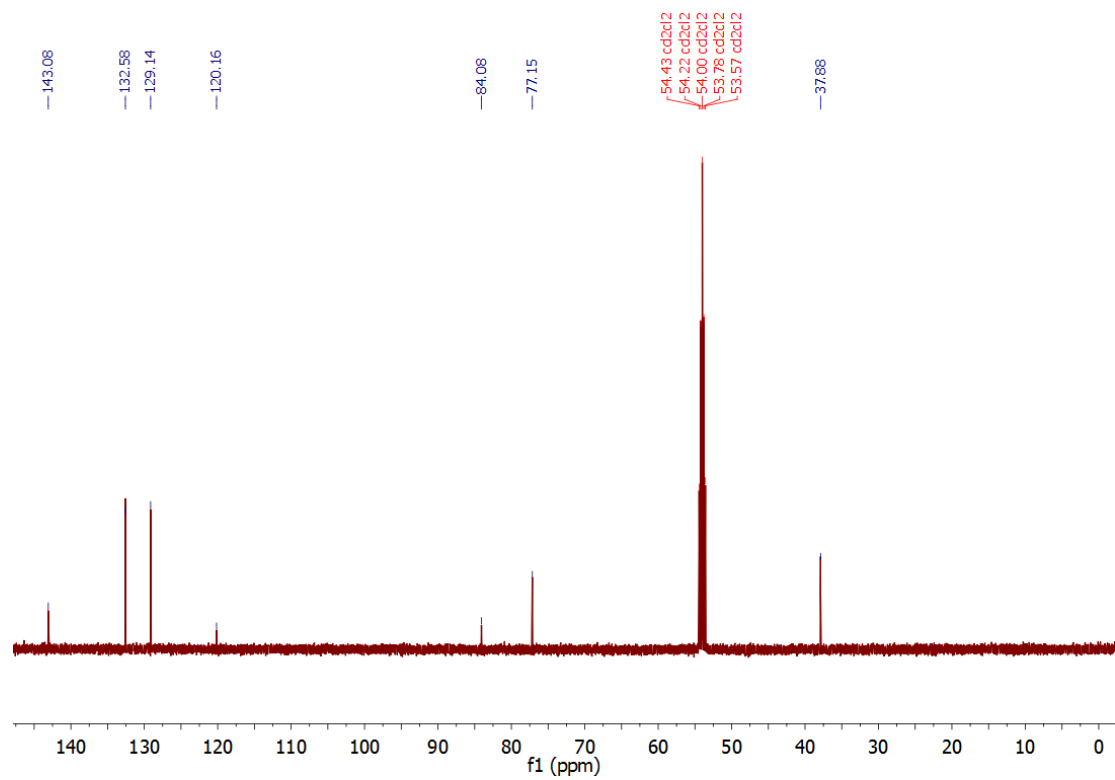


Figure D-8. ¹³C NMR (126 MHz, CD₂Cl₂) of **CC-H**.

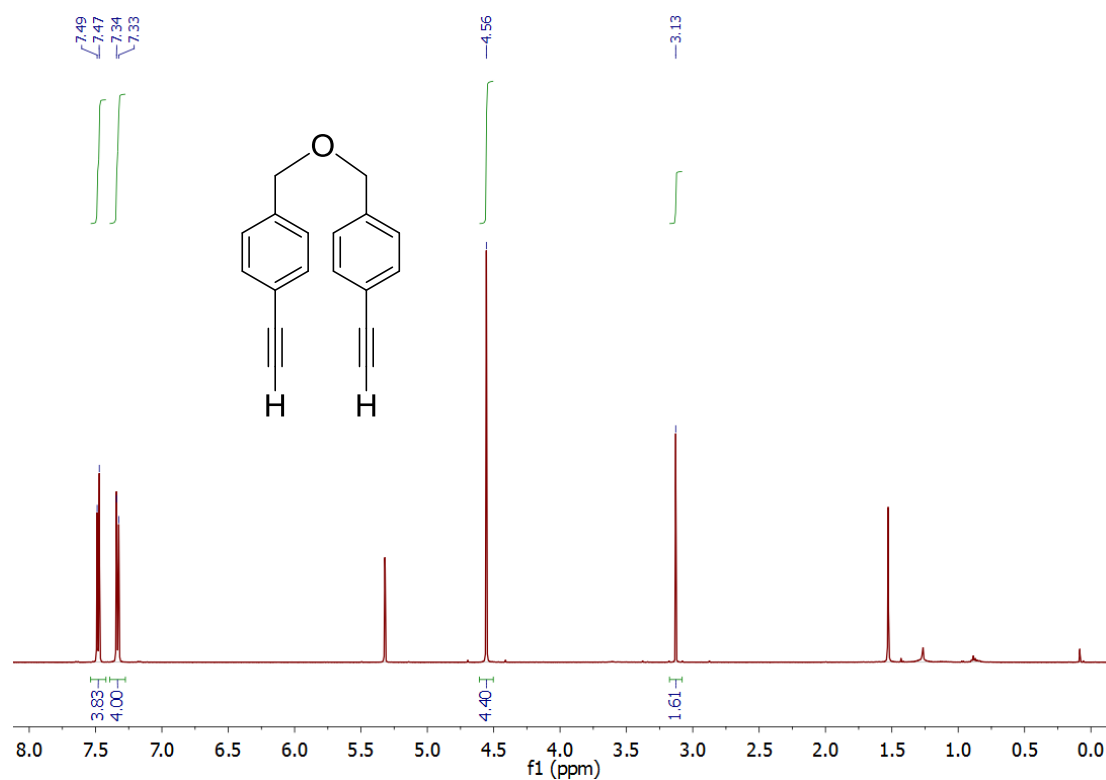


Figure D-9. ¹H NMR (500 MHz, CD₂Cl₂) of **COC-H**.

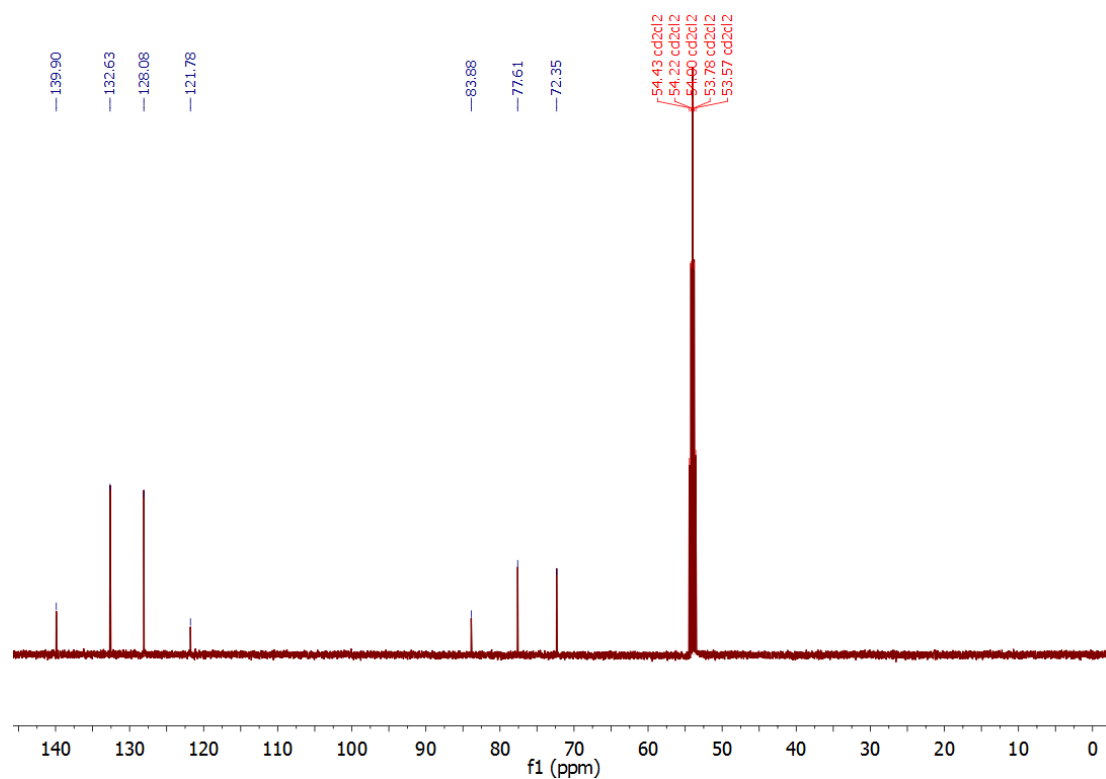


Figure D-10. ¹³C NMR (126 MHz, CD₂Cl₂) of **COC-H**.

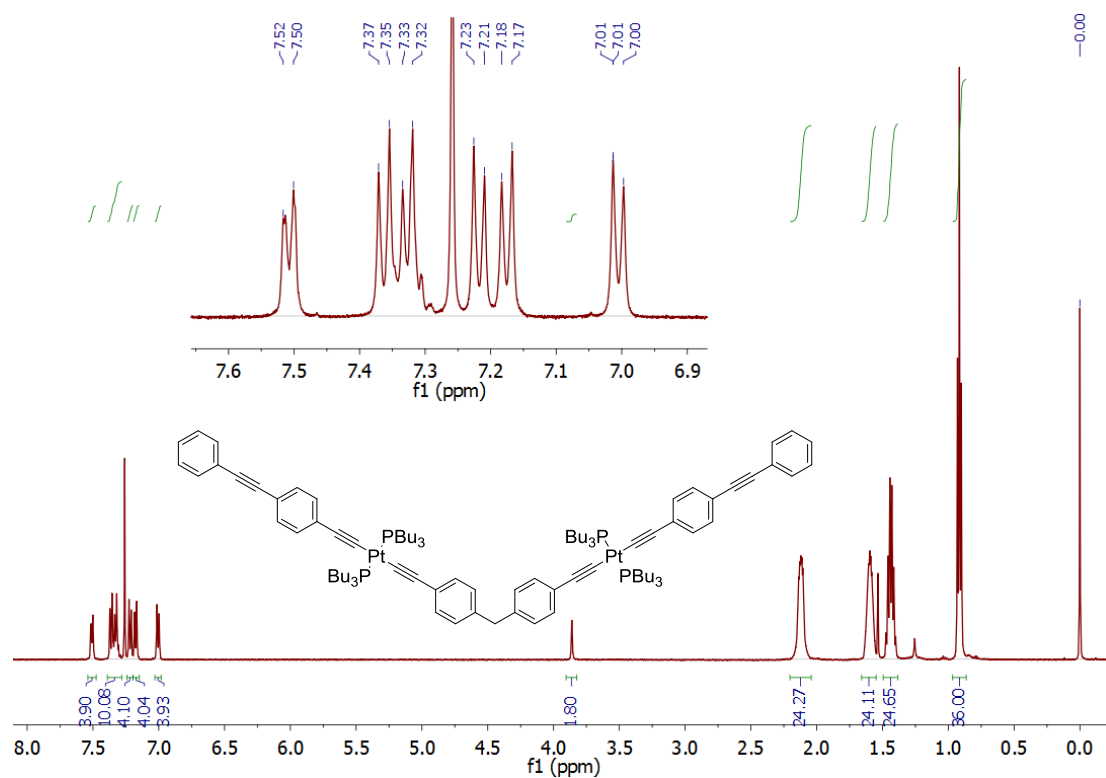


Figure D-11. ¹H NMR (500 MHz, CDCl₃) of **C-PtPE2**.

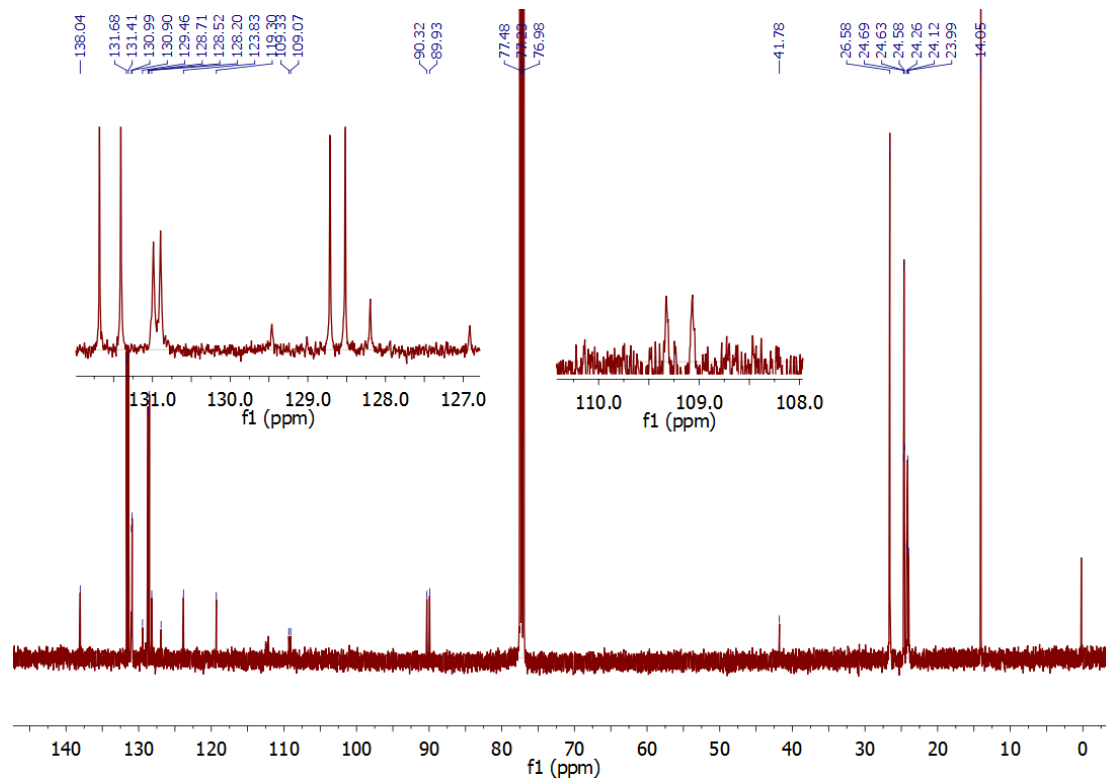


Figure D-12. ¹³C NMR (126 MHz, CDCl₃) of **C-PtPE2**.

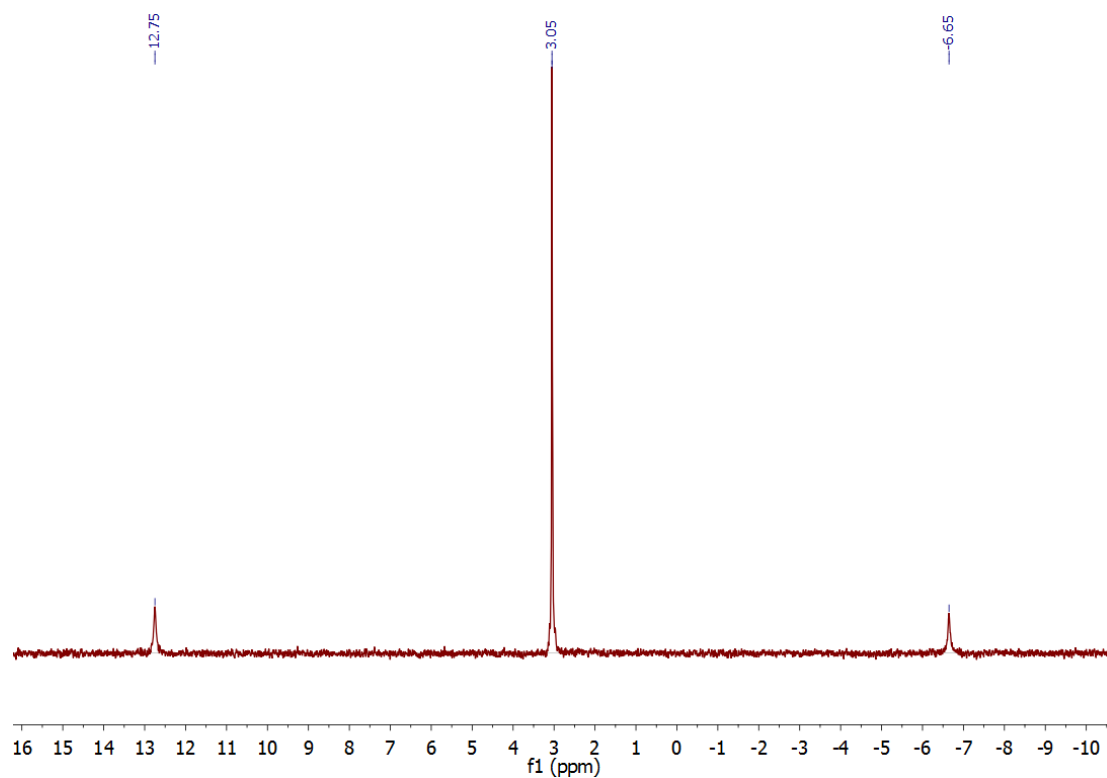


Figure D-13. ^{31}P NMR (121 MHz, CDCl_3) of **C-PtPE2**.

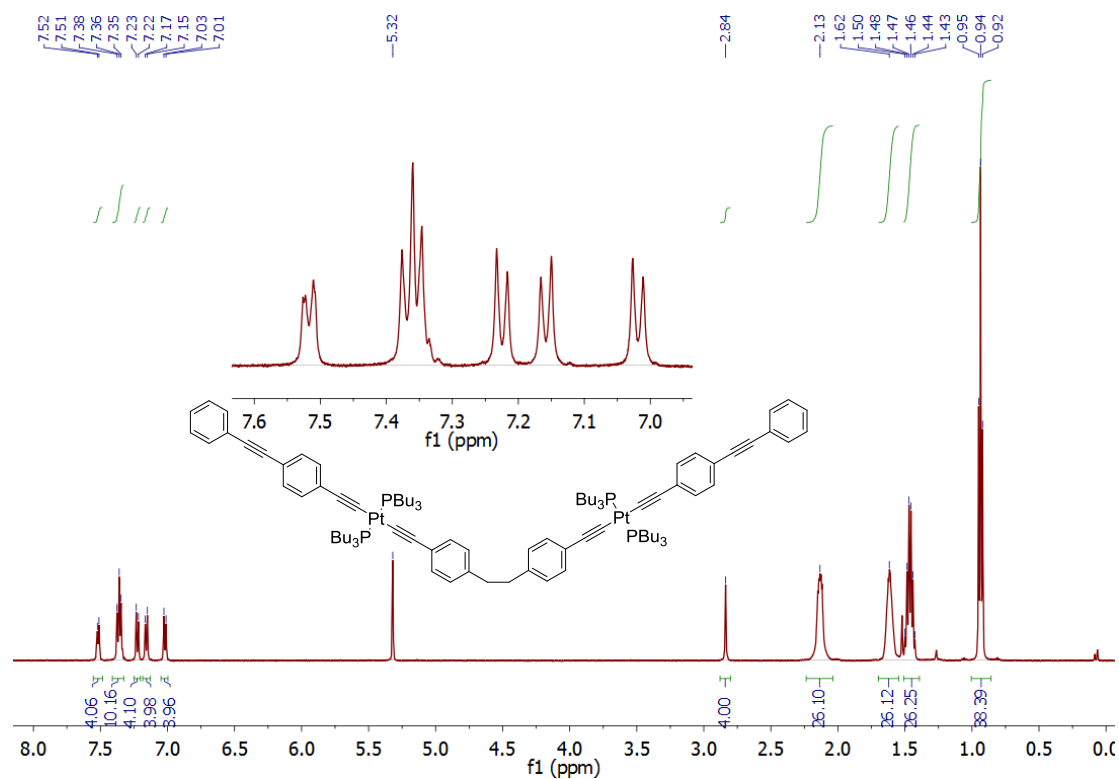


Figure D-14. ^1H NMR (500 MHz, CD_2Cl_2) of **CC-PtPE2**.

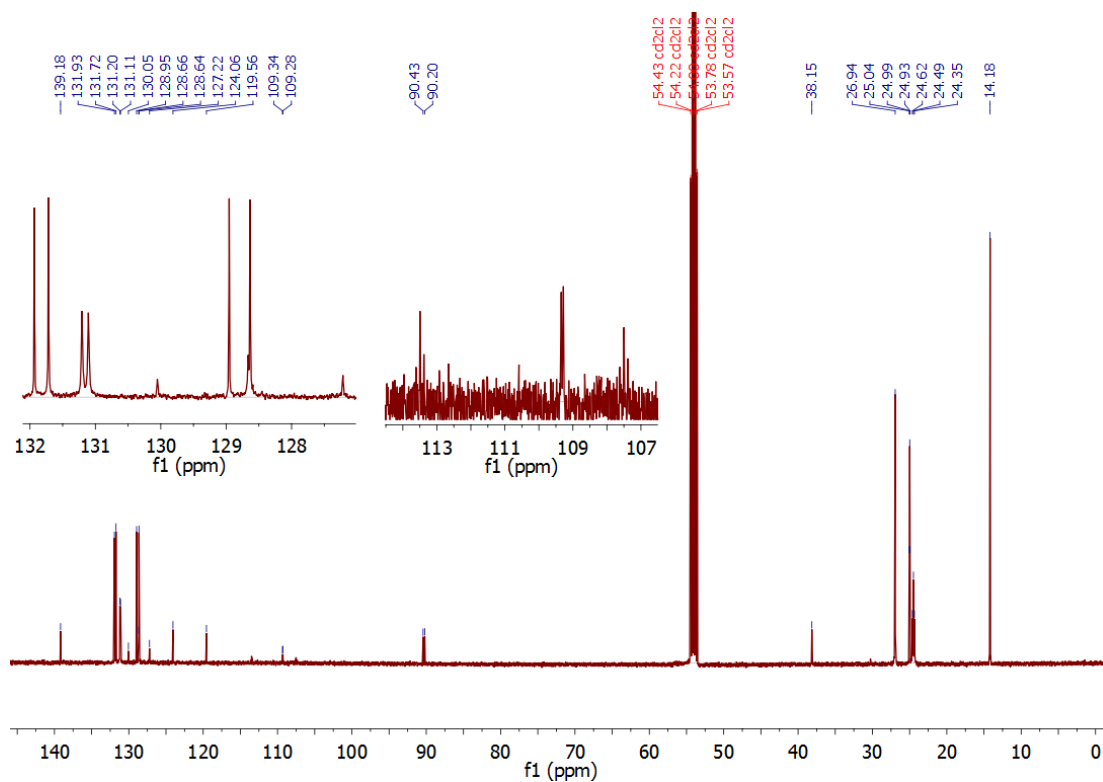


Figure D-15. ¹³C NMR (126 MHz, CD₂Cl₂) of **CC-PtPE2**.

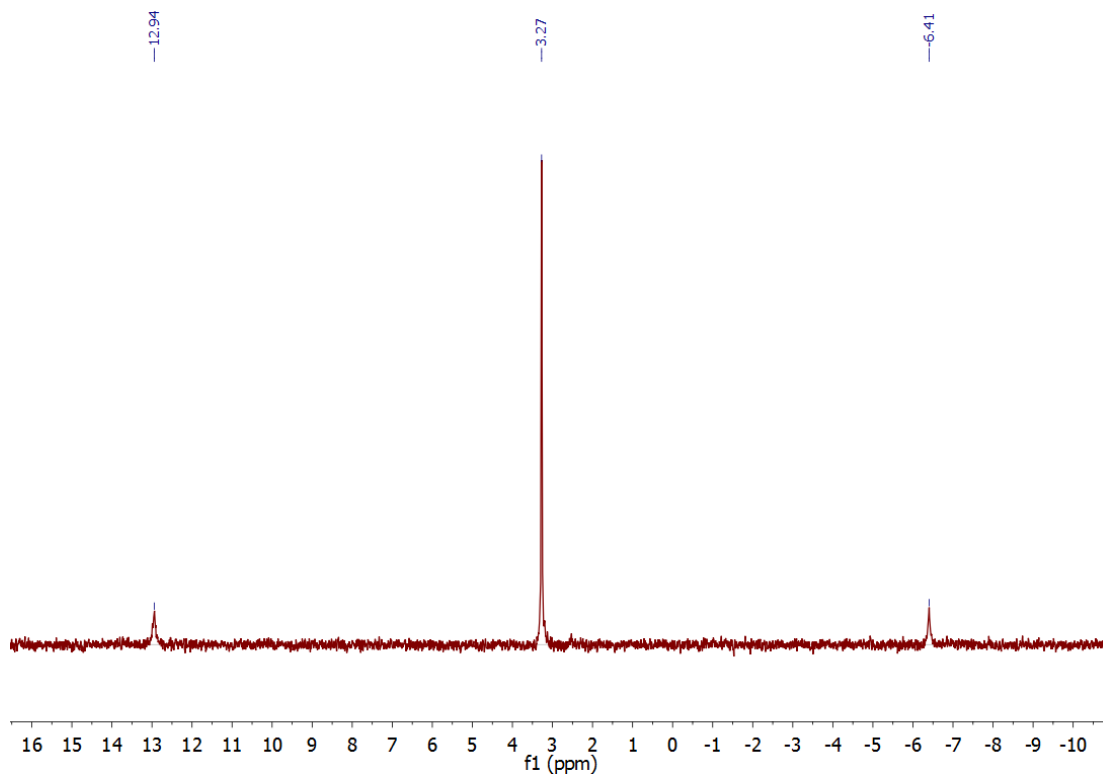


Figure D-16. ³¹P NMR (121 MHz, CD₂Cl₂) of **CC-PtPE2**.

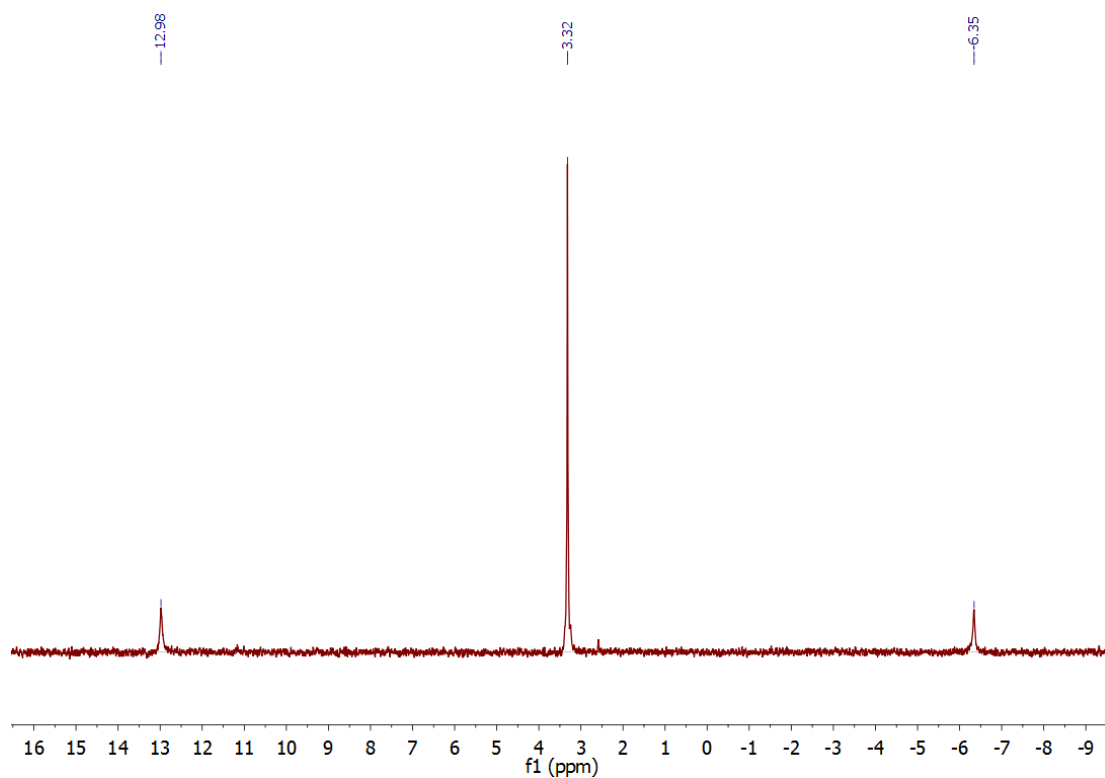


Figure D-19. ^{31}P NMR (121 MHz, CD_2Cl_2) of **COC-PtPE2**.

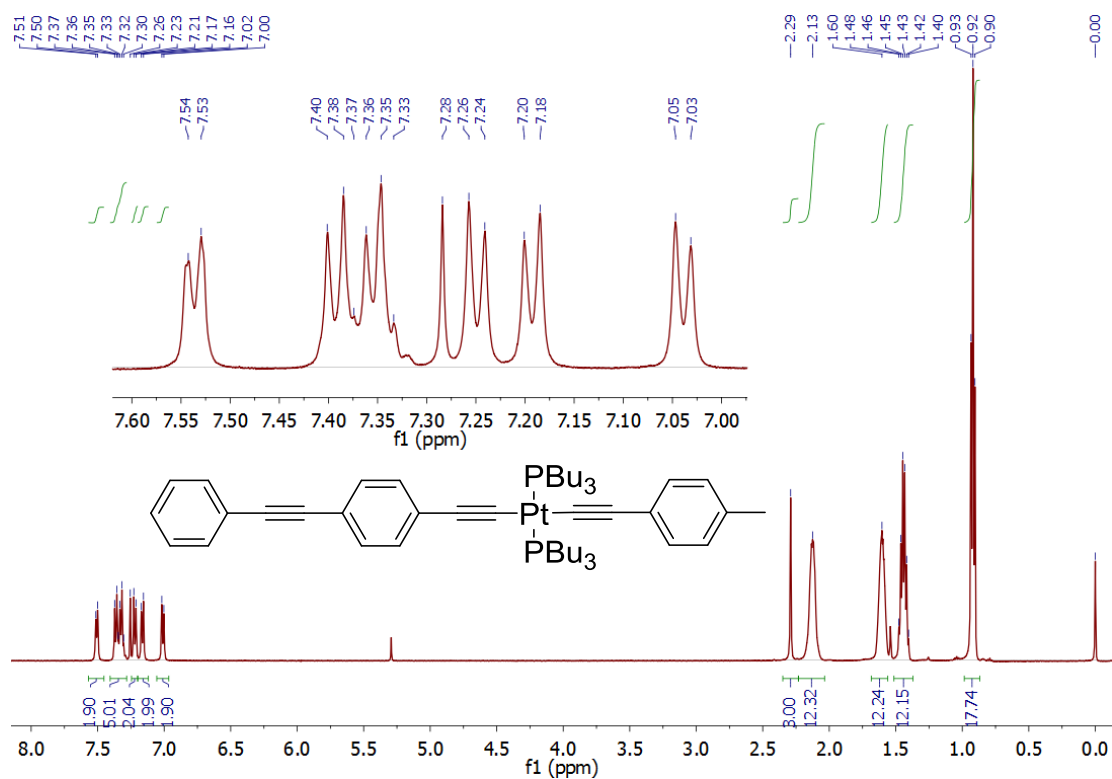


Figure D-20. ^1H NMR (500 MHz, CDCl_3) of **tol-PtPE2**.

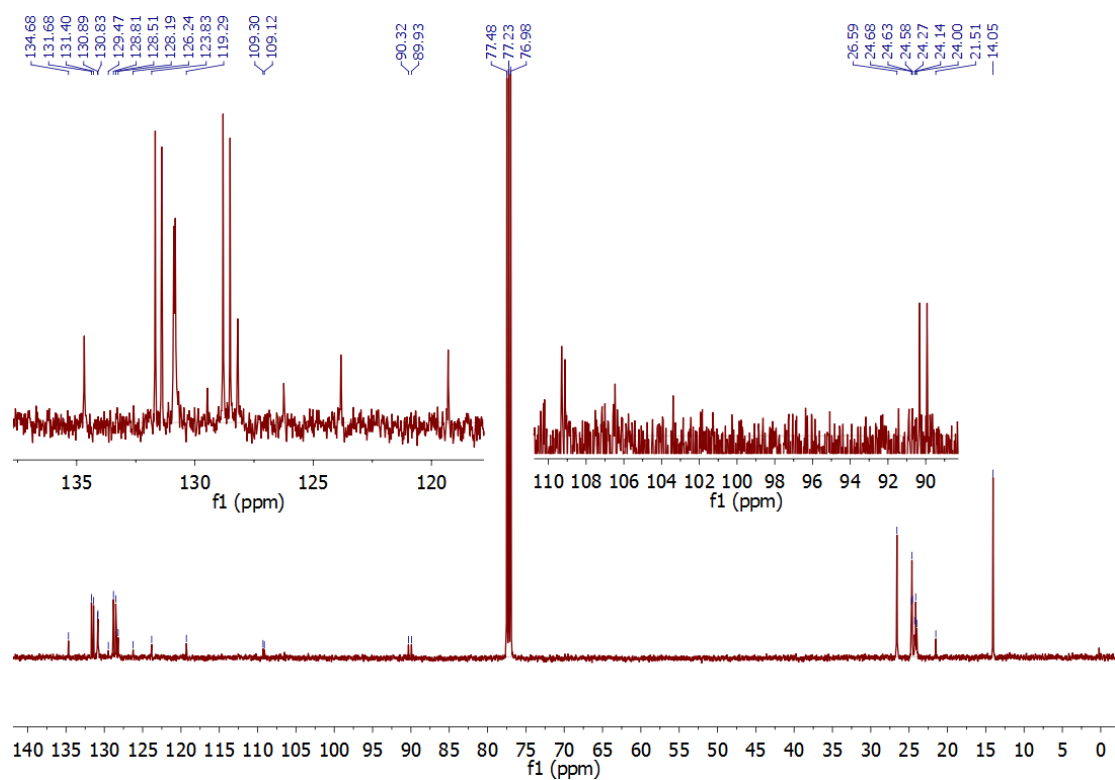


Figure D-21. ¹³C NMR (126 MHz, CDCl₃) of **tol-PtPE2**.

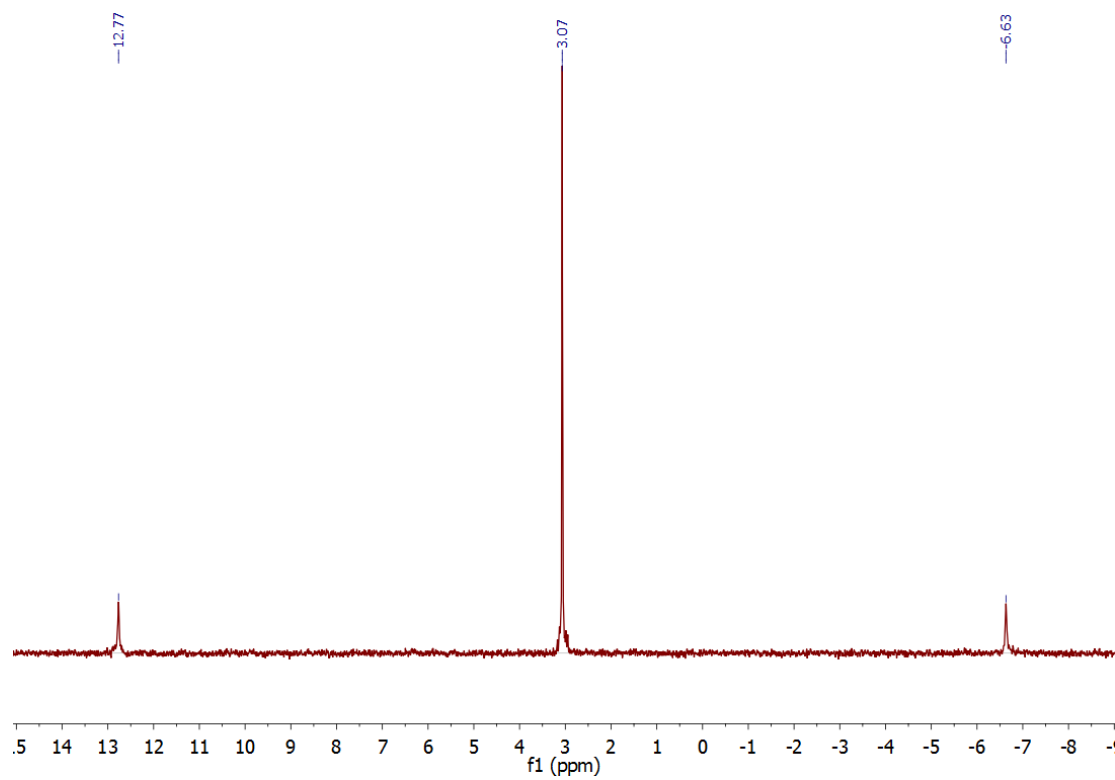


Figure D-22. ³¹P NMR (121 MHz, CDCl₃) of **tol-PtPE2**.

Emission Lifetime Decays

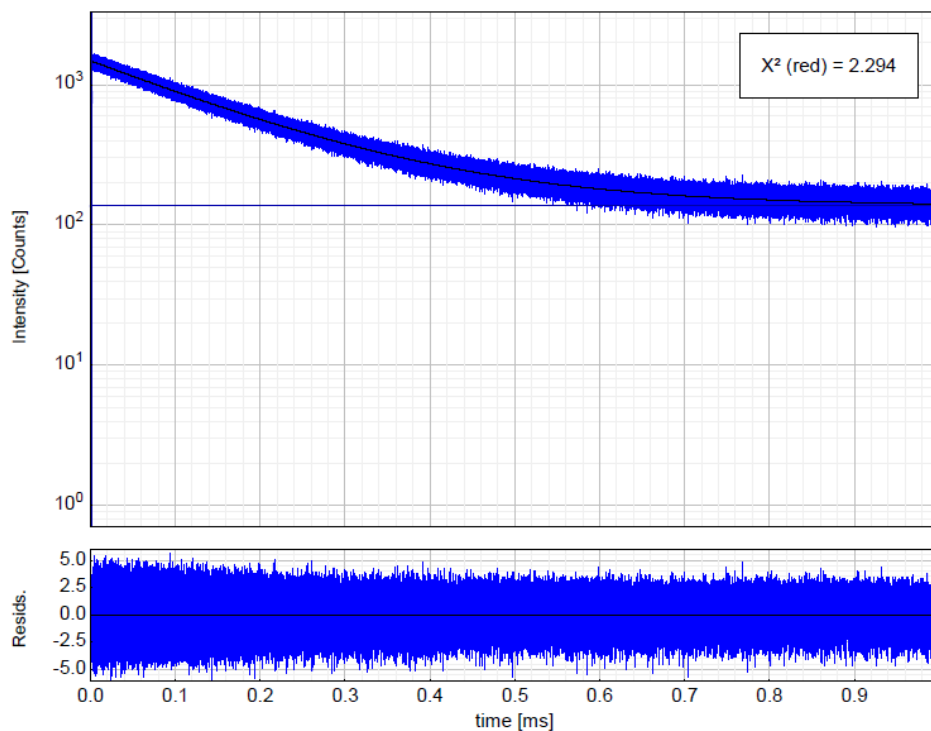


Figure D-23. Phosphorescence lifetime decay for **C-PtPE2**.

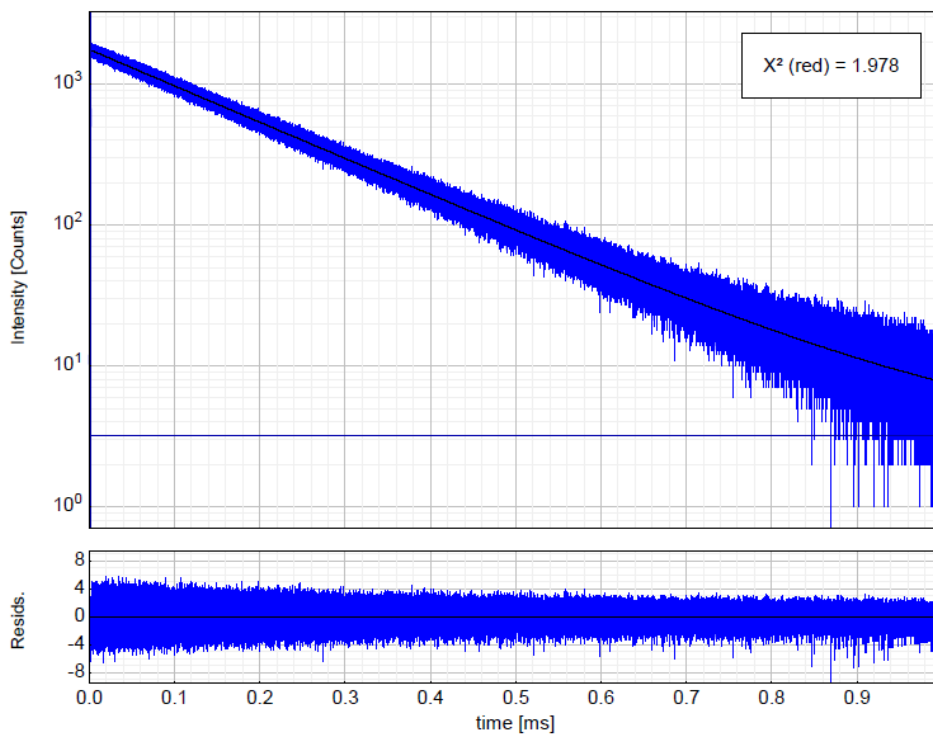


Figure D-24. Phosphorescence lifetime decay for **CC-PtPE2**.

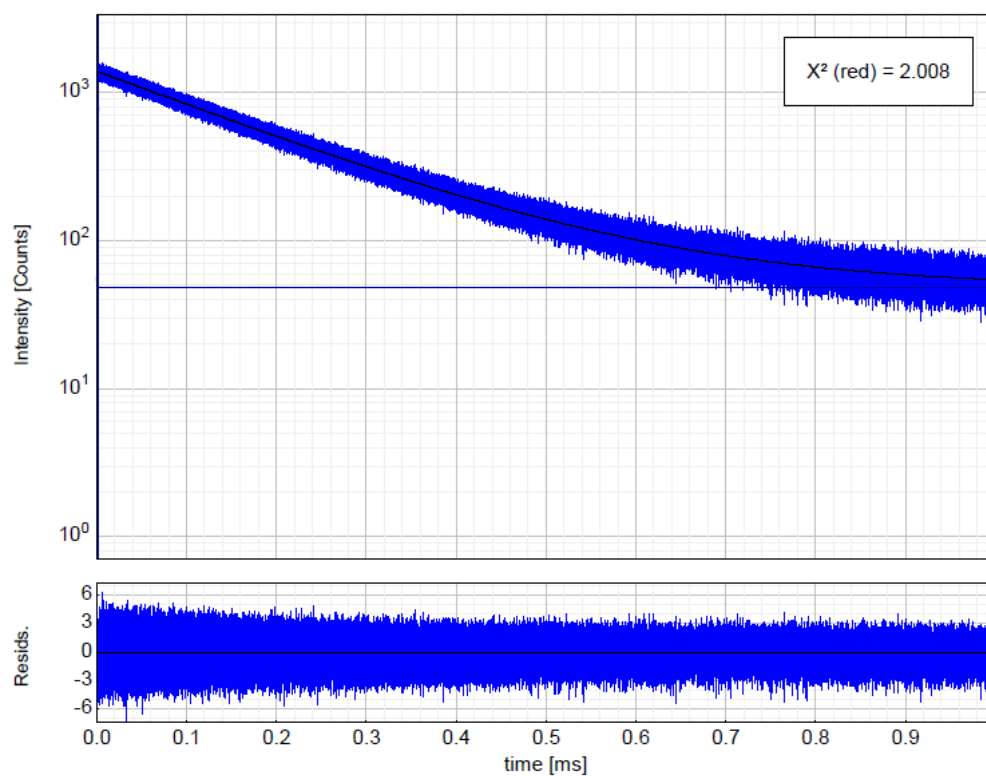


Figure D-25. Phosphorescence lifetime decay for **COC-PtPE2**.

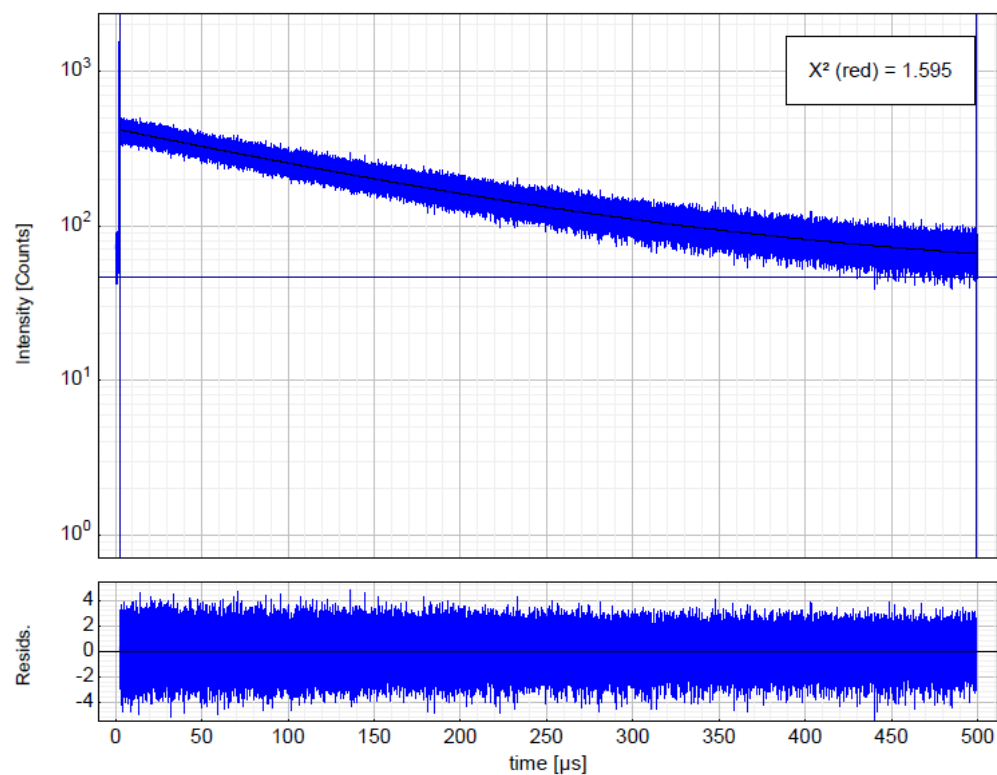


Figure D-26. Phosphorescence lifetime decay for **tol-PtPE2**.

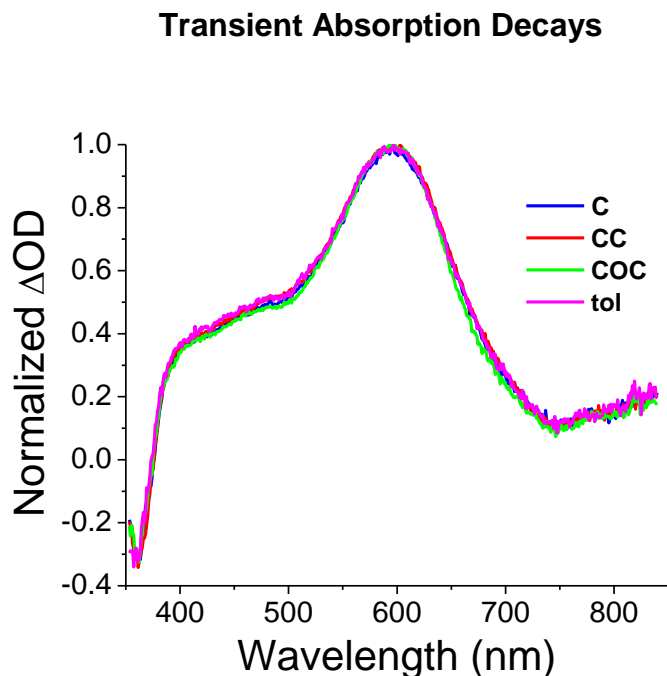


Figure D-27. Normalized transient absorption for **R-PtPE2**. Initial camera delay: 100ns, camera delay increment: 15 μ s, 100 images averaged per trace, 180 μ J per pulse. Solutions had an absorptivity value of 0.58 at 355 nm after five freeze-pump-thaw cycles.

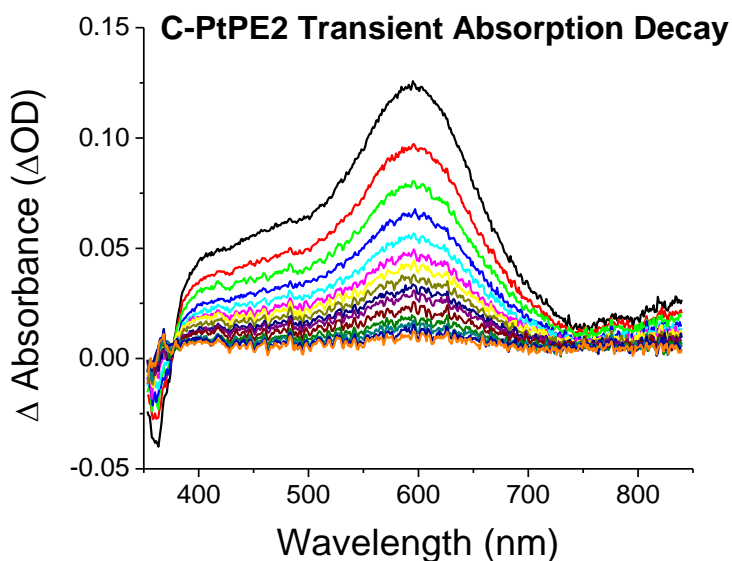


Figure D-28. Transient absorption decay for **C-PtPE2**. Initial camera delay: 100ns, camera delay increment: 15 μ s, 100 images averaged per trace, 180 μ J per pulse. The solution had an absorptivity value of 0.58 at 355 nm after five freeze-pump-thaw cycles.

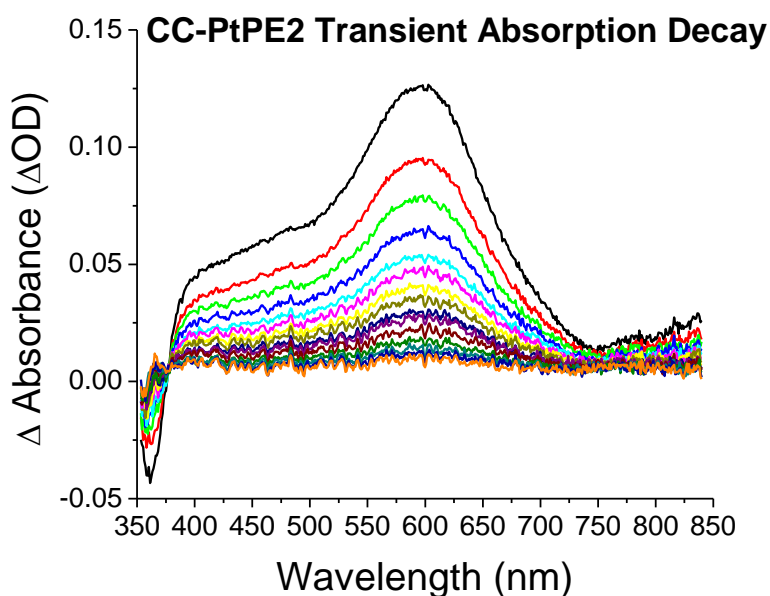


Figure D-29. Transient absorption decay for **CC-PtPE2**. Initial camera delay: 100ns, camera delay increment: 15 μ s, 100 images averaged per trace, 180 μ J per pulse. The solution had an absorptivity value of 0.58 at 355 nm after five freeze-pump-thaw cycles.

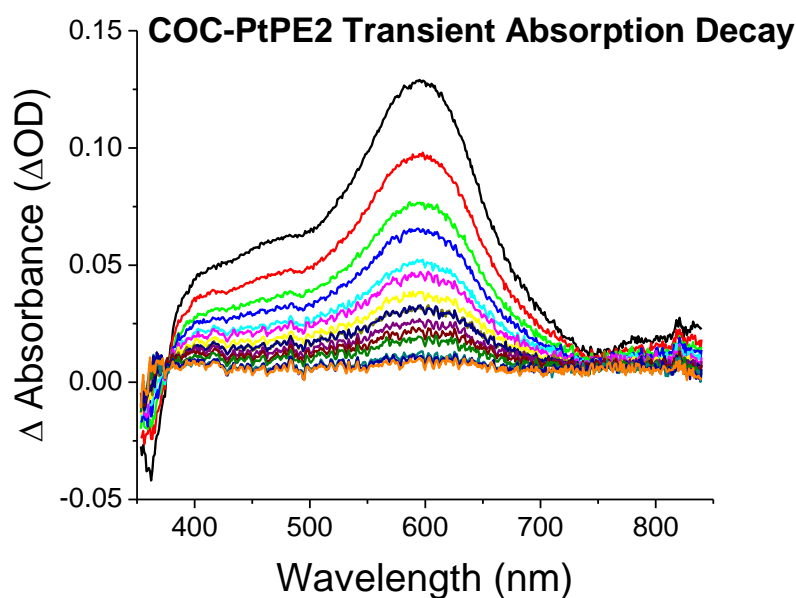


Figure D-30. Transient absorption decay for **COC-PtPE2**. Initial camera delay: 100ns, camera delay increment: 15 μ s, 100 images averaged per trace, 180 μ J per pulse. The solution had an absorptivity value of 0.58 at 355 nm after five freeze-pump-thaw cycles.

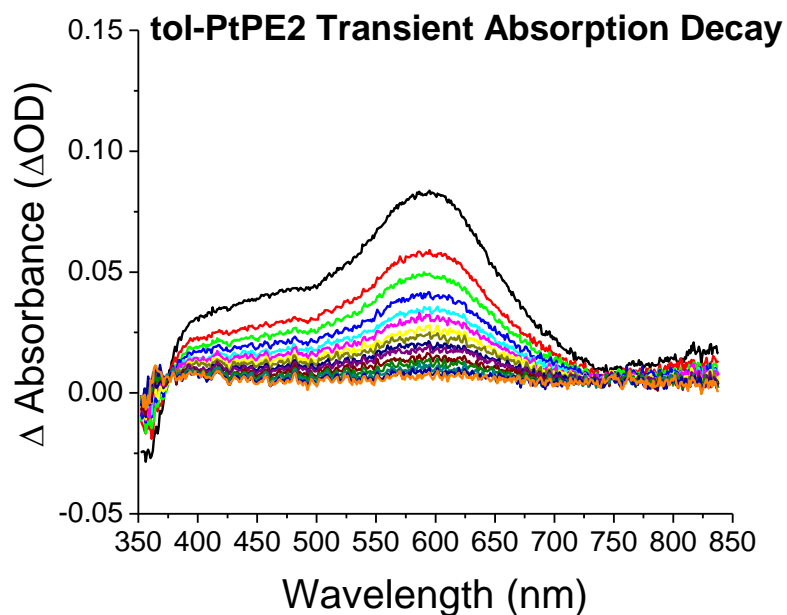


Figure D-31. Transient absorption decay for **tol-PtPE2**. Initial camera delay: 100ns, camera delay increment: 15 μ s, 100 images averaged per trace, 180 μ J per pulse. The solution had an absorptivity value of 0.58 at 355 nm after five freeze-pump-thaw cycles.

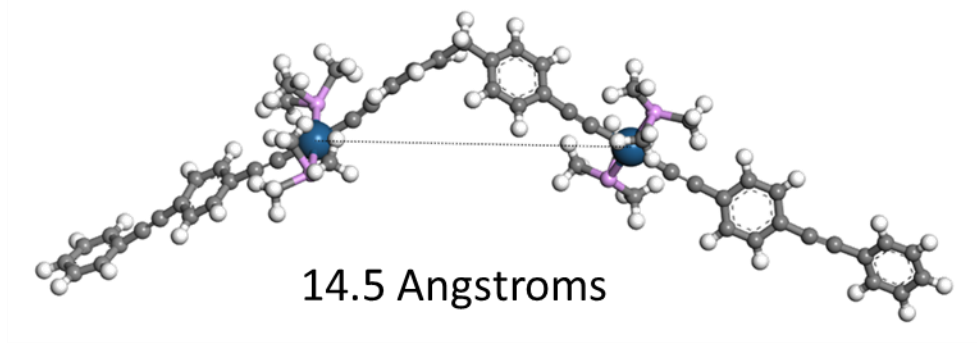


Figure D-32. Representative molecular geometry of **C-PtPE2** during the molecular dynamics simulation process.

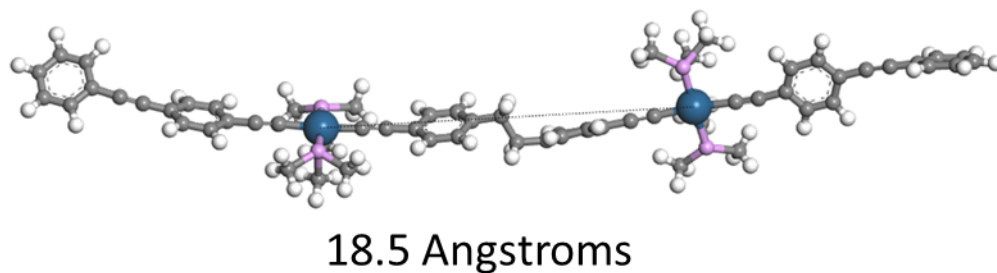


Figure D-33. Representative molecular geometry of **CC-PtPE2** during the molecular dynamics simulation process.

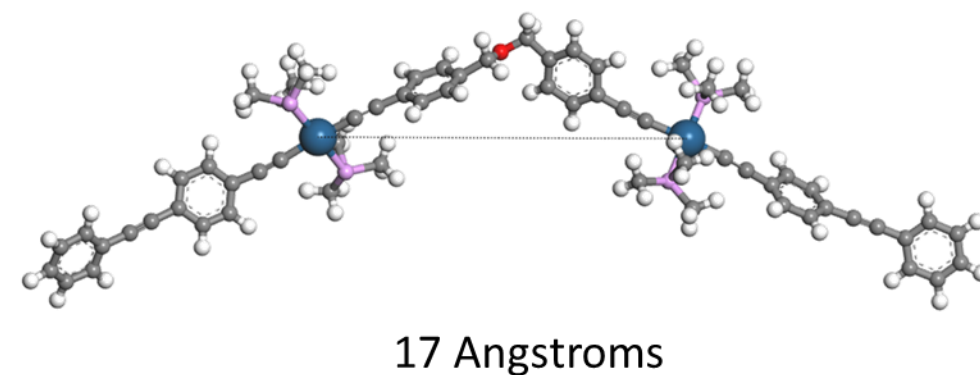


Figure D-34. Representative molecular geometry for the primary distribution of **COC-PtPE2** during the molecular dynamics simulation process.

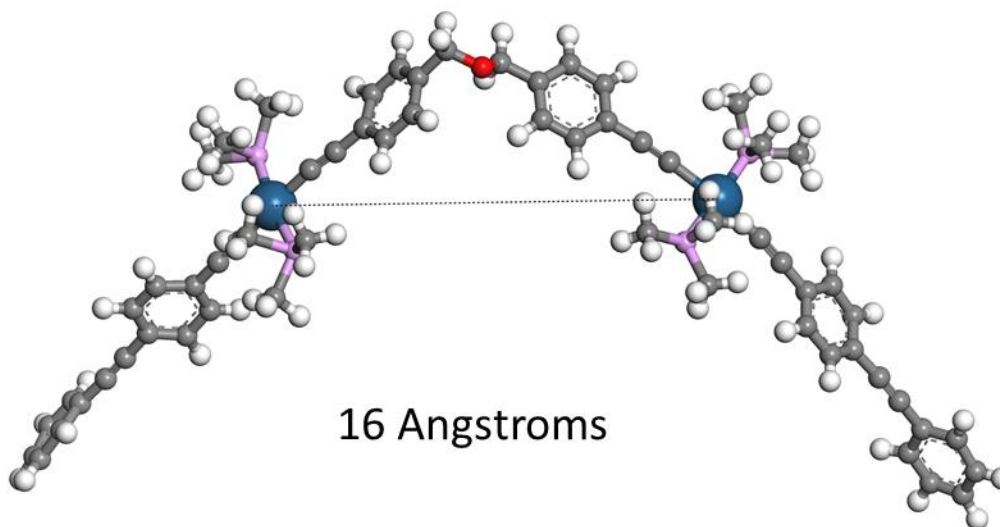


Figure D-35. Representative molecular geometry for the secondary distribution of **COC-PtPE2** during the molecular dynamics simulation process.

NMR Spectra



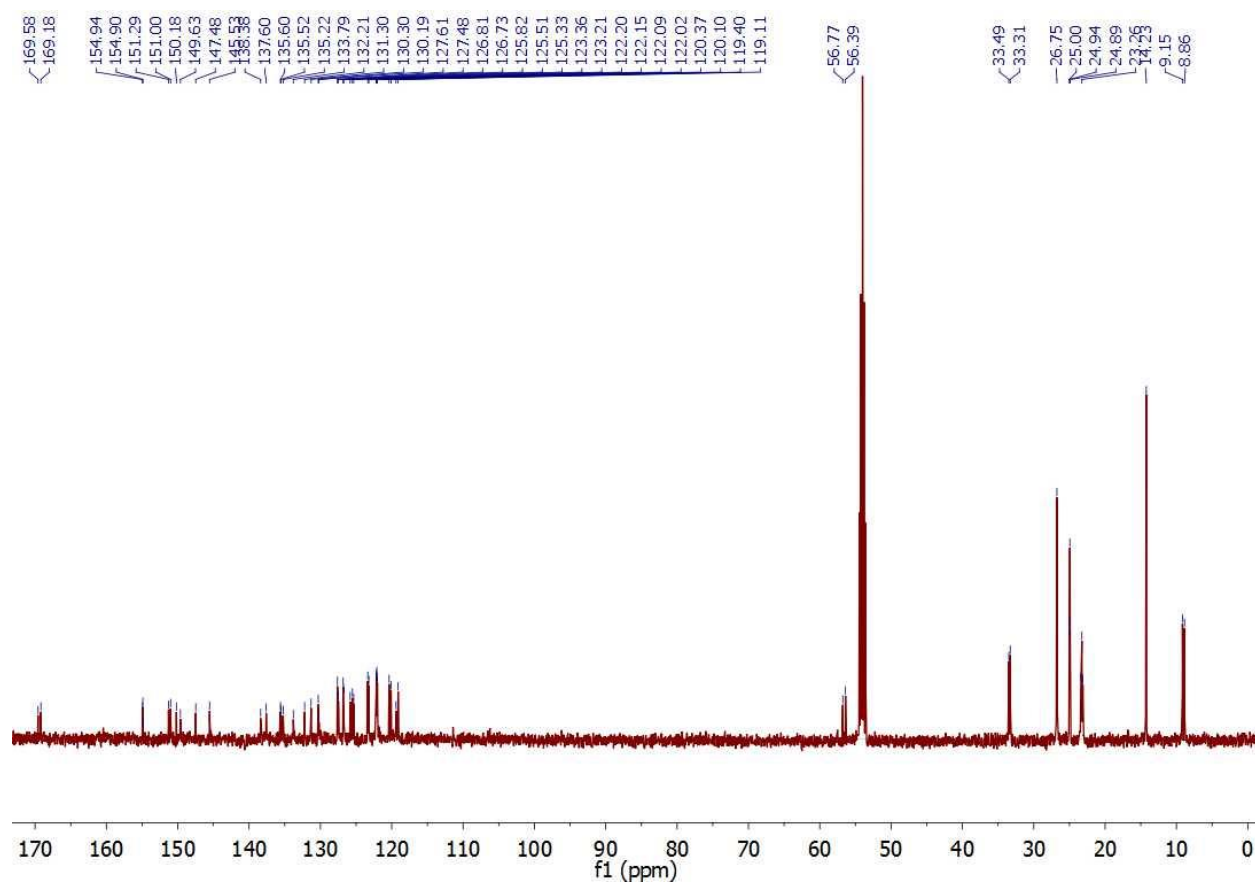


Figure E-3. ^{13}C NMR (126 MHz, CD_2Cl_2) spectra of **BTF-Pt-CCBTF**.

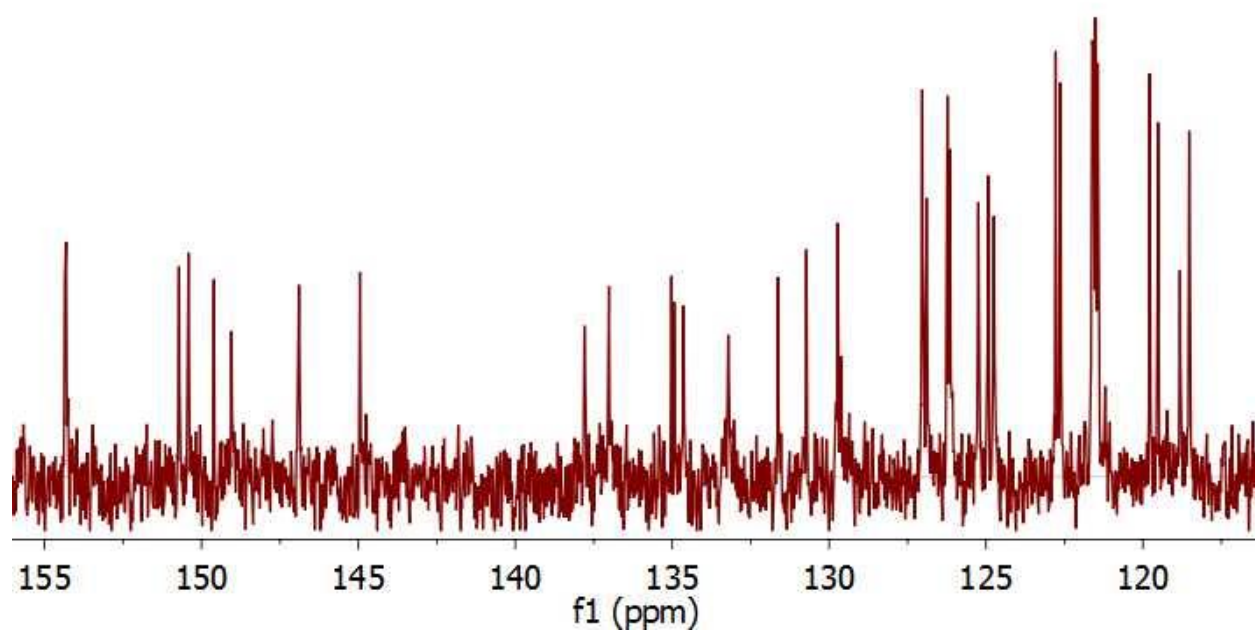


Figure E-4. Aromatic region of the ^{13}C NMR spectra of **BTF-Pt-CCBTF**.

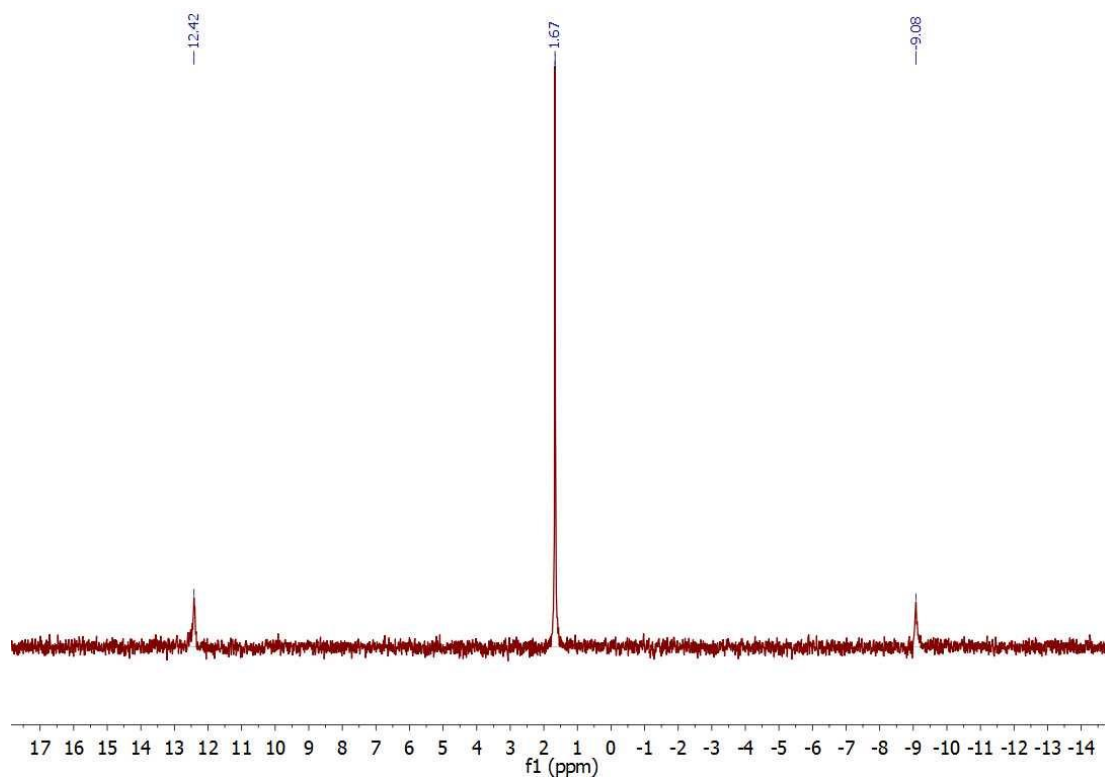


Figure E-5. ^{31}P NMR (121 MHz, CD_2Cl_2) of **BTF-Pt-CCBTF**.

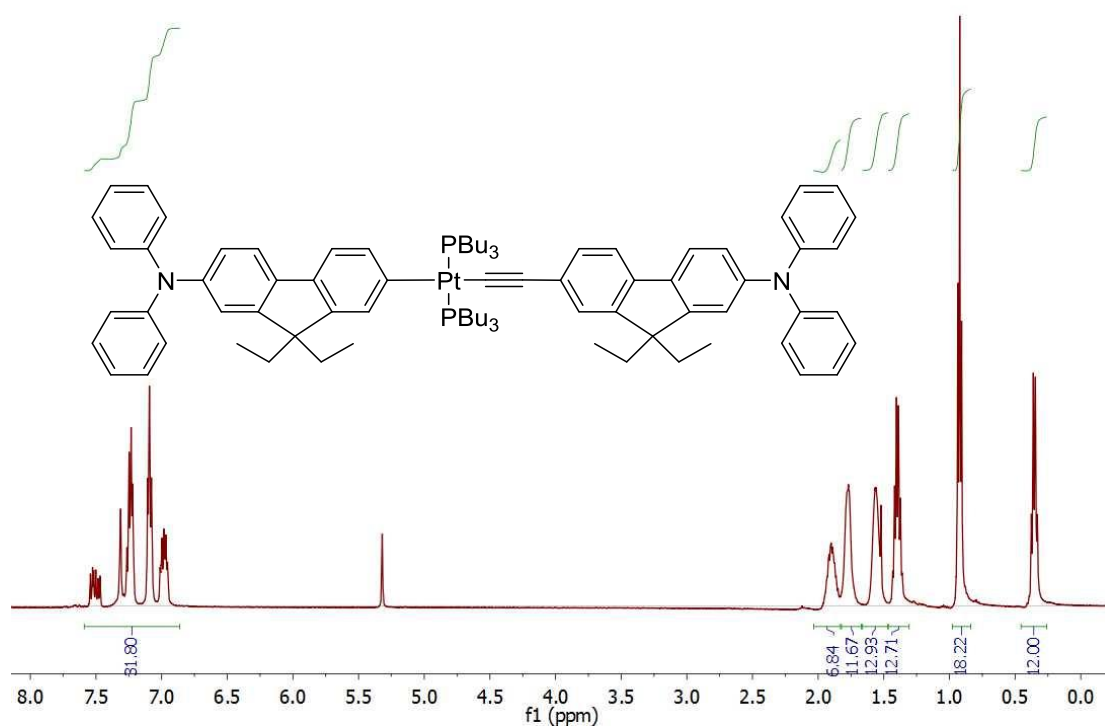


Figure E-6. ^1H NMR (500 MHz, CD_2Cl_2) spectra of **DPAF-Pt-CCDPAF**.

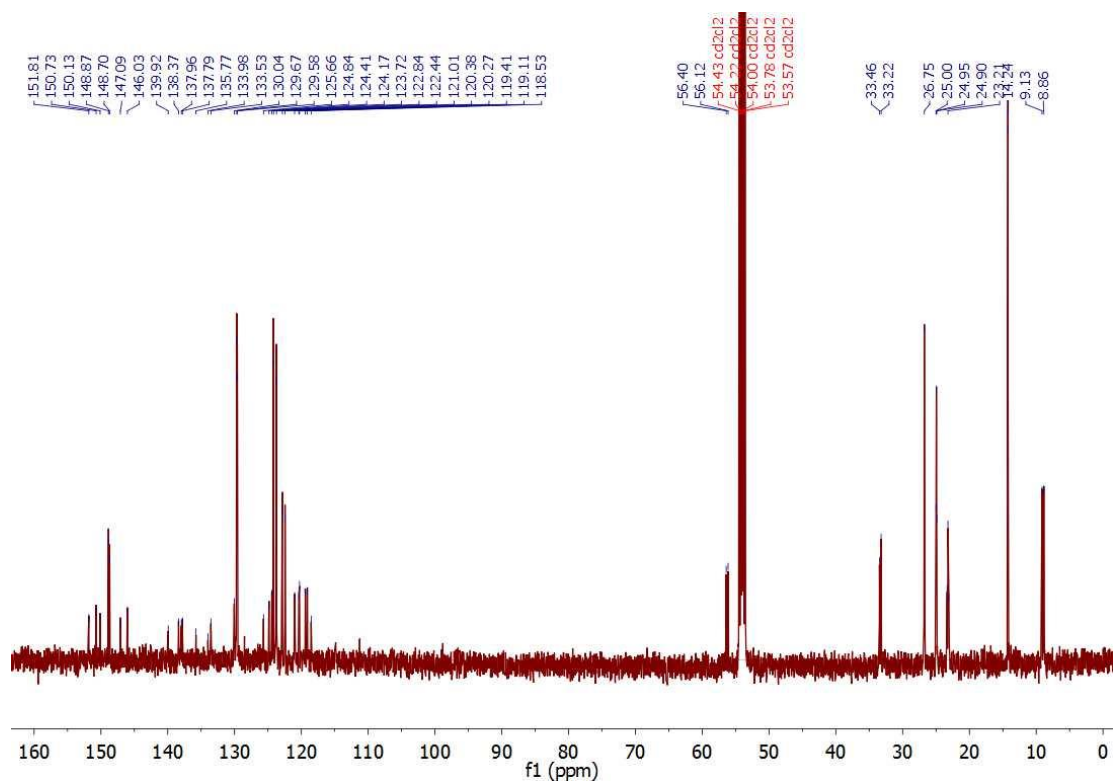


Figure E-7. ^{13}C NMR (126 MHz, CD_2Cl_2) spectra of **DPAF-Pt-CCDPAF**.

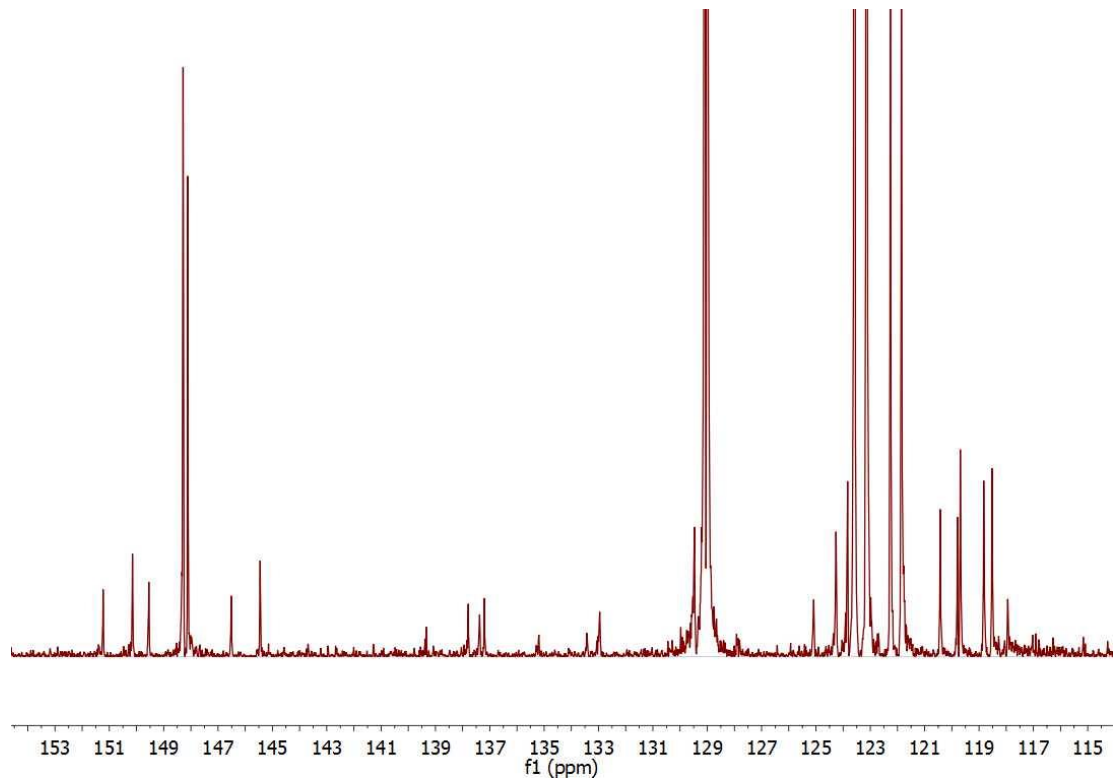


Figure E-8. Aromatic region of the ^{13}C NMR spectra of **DPAF-Pt-CCDPAF**.

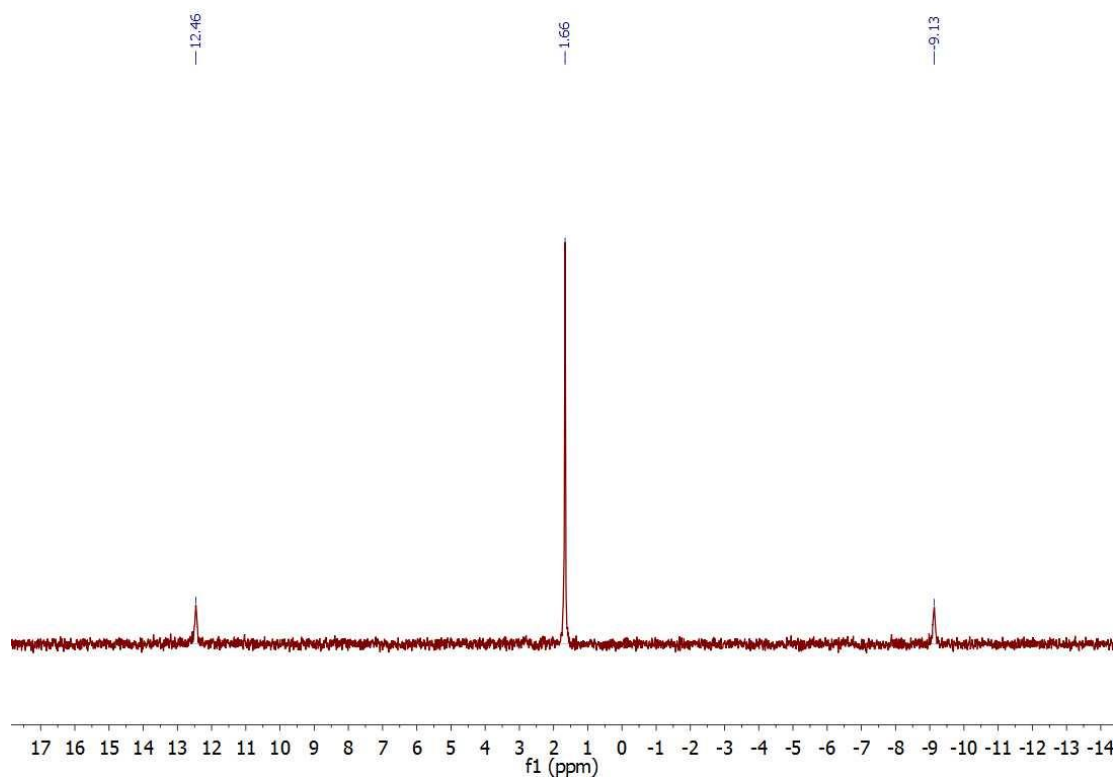


Figure E-9. ^{31}P NMR (121 MHz, CD_2Cl_2) of **DPAF-Pt-CCDPAF**.

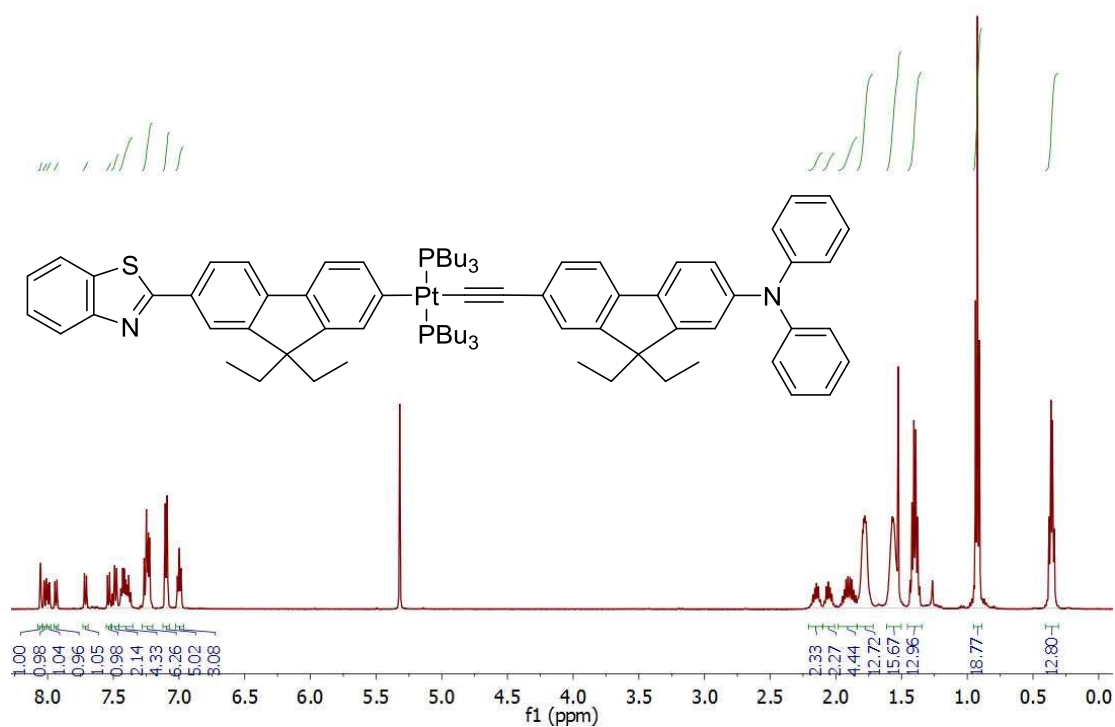


Figure E-10. ^1H NMR (500 MHz, CD_2Cl_2) spectra of **BTF-Pt-CCDPAF**.

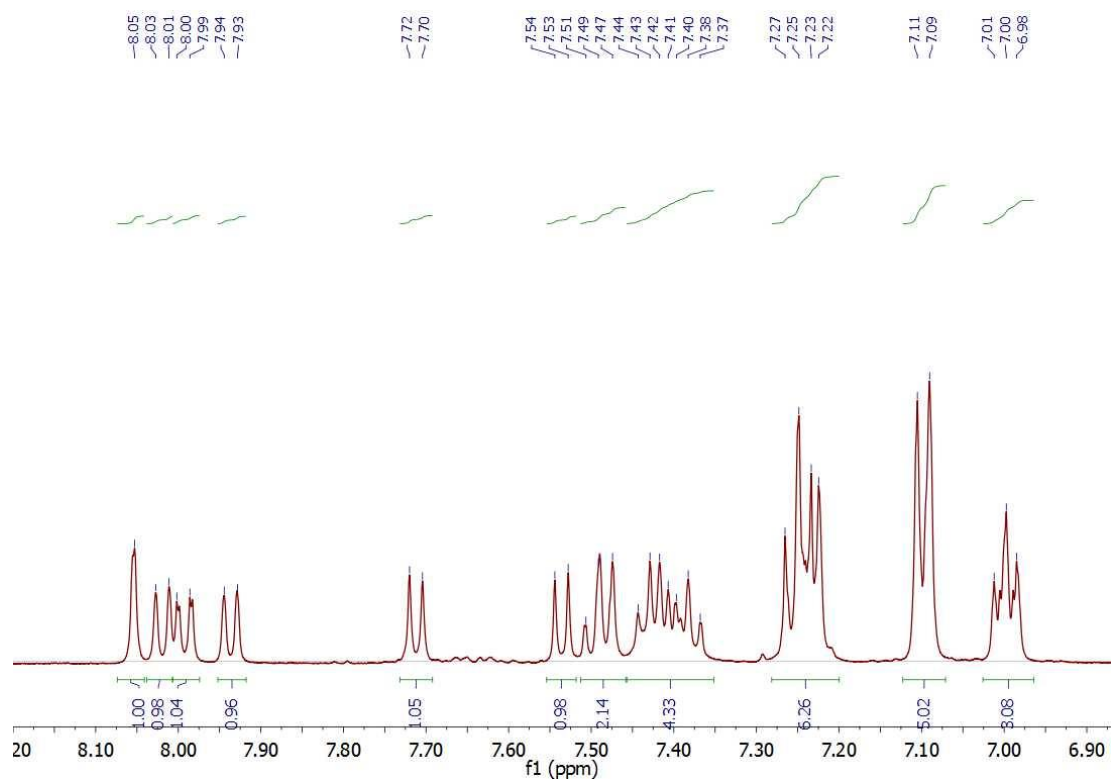


Figure E-11. Aromatic region of the ^1H NMR spectra of **BTF-Pt-CCDPAF**.

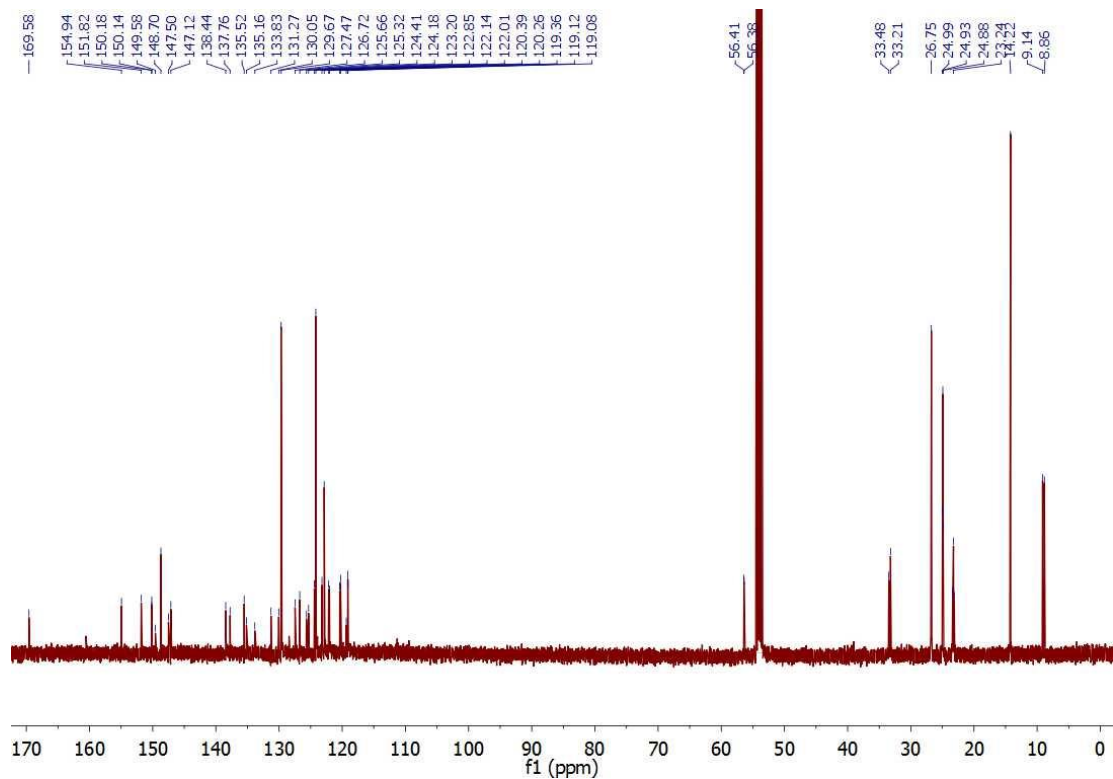


Figure E-12. ^{13}C NMR (126 MHz, CD_2Cl_2) spectra of **BTF-Pt-CCDPAF**.

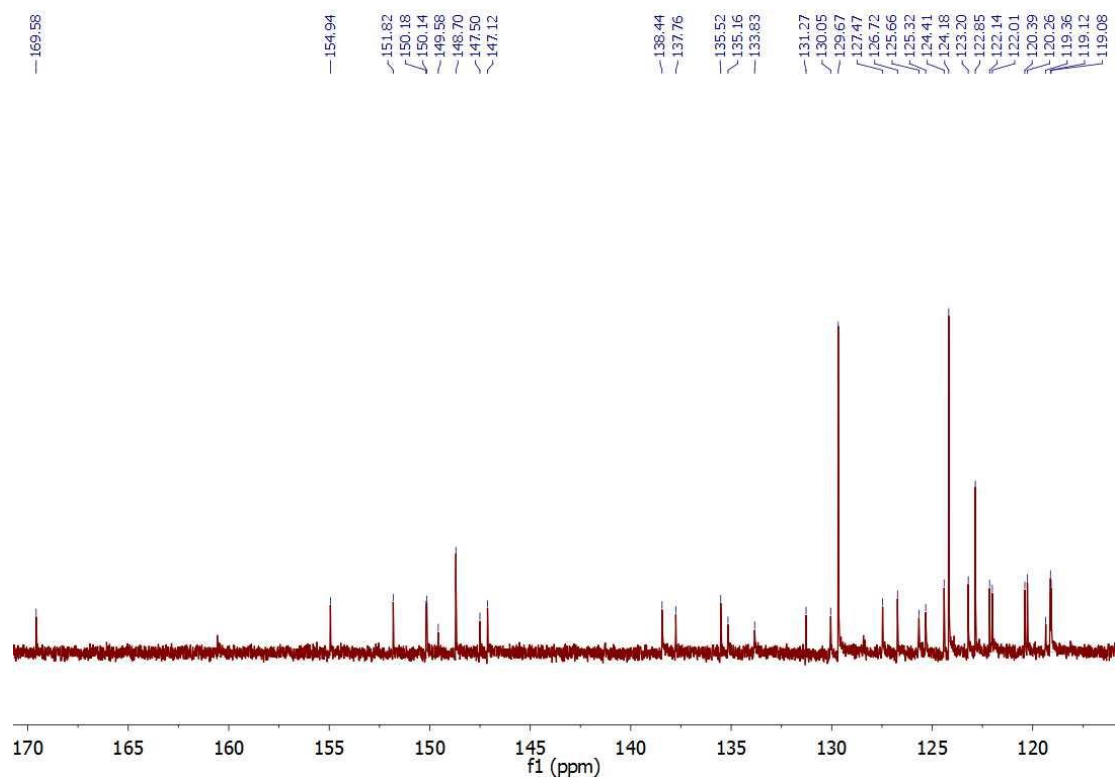


Figure E-13. Aromatic region of the ^{13}C NMR spectra of **BTF-Pt-CCDPAF**.

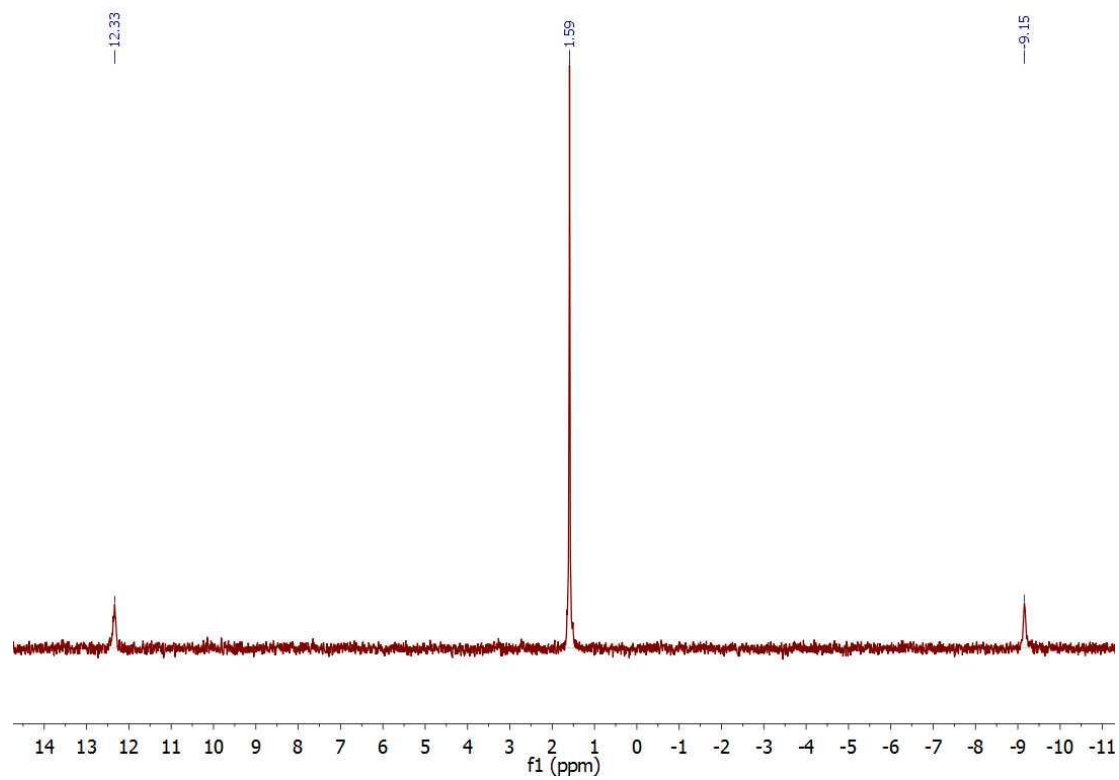


Figure E-14. ^{31}P NMR (121 MHz, CD_2Cl_2) of **BTF-Pt-CCDPAF**.

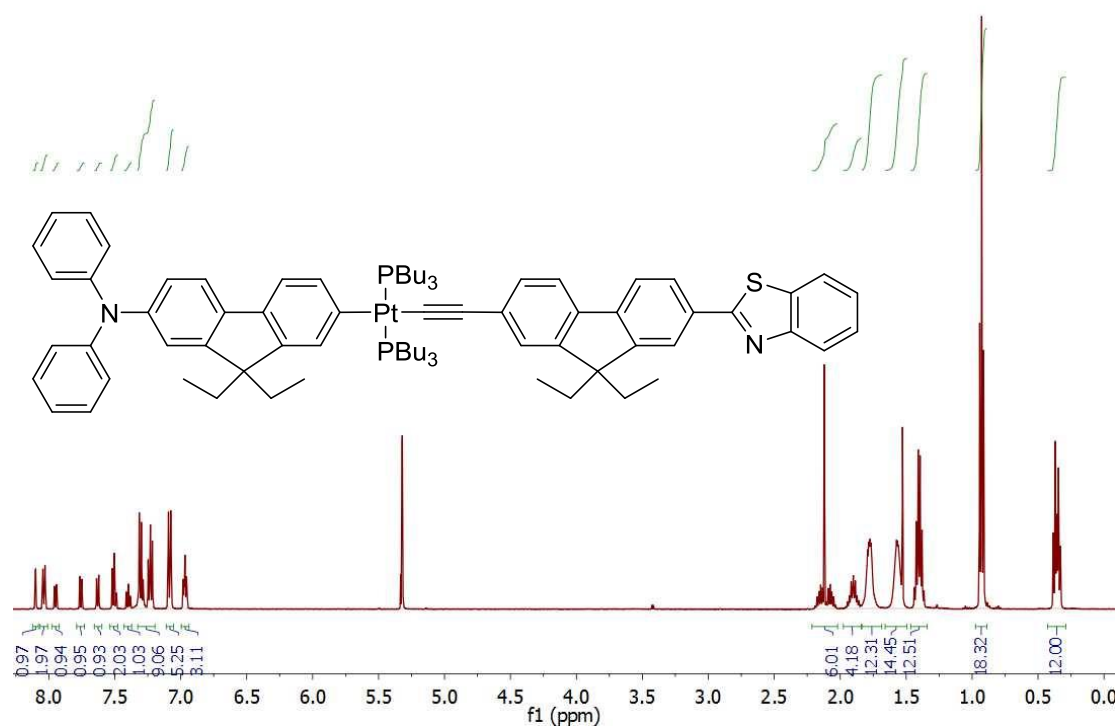


Figure E-15. ^1H NMR (500 MHz, CD_2Cl_2) spectra of **DPAF-Pt-CCBTF**.

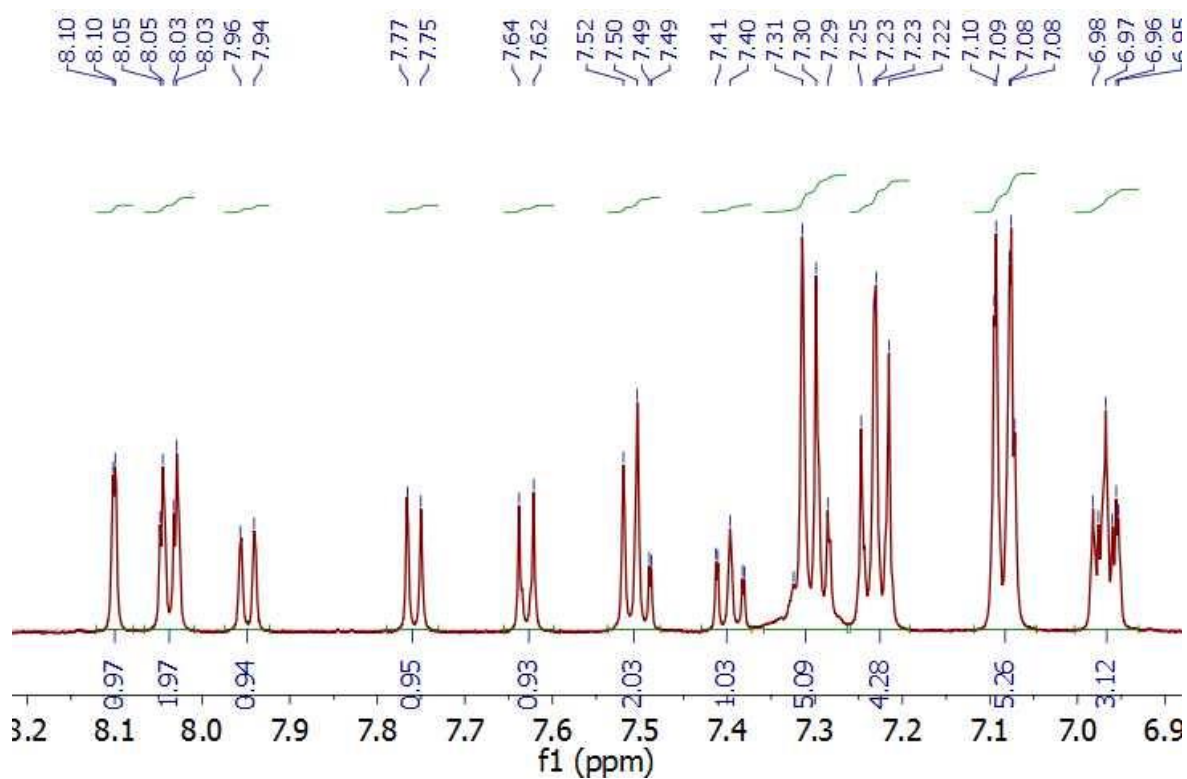


Figure E-16. Aromatic region of the ^1H NMR spectra of **DPAF-Pt-CCBTF**.

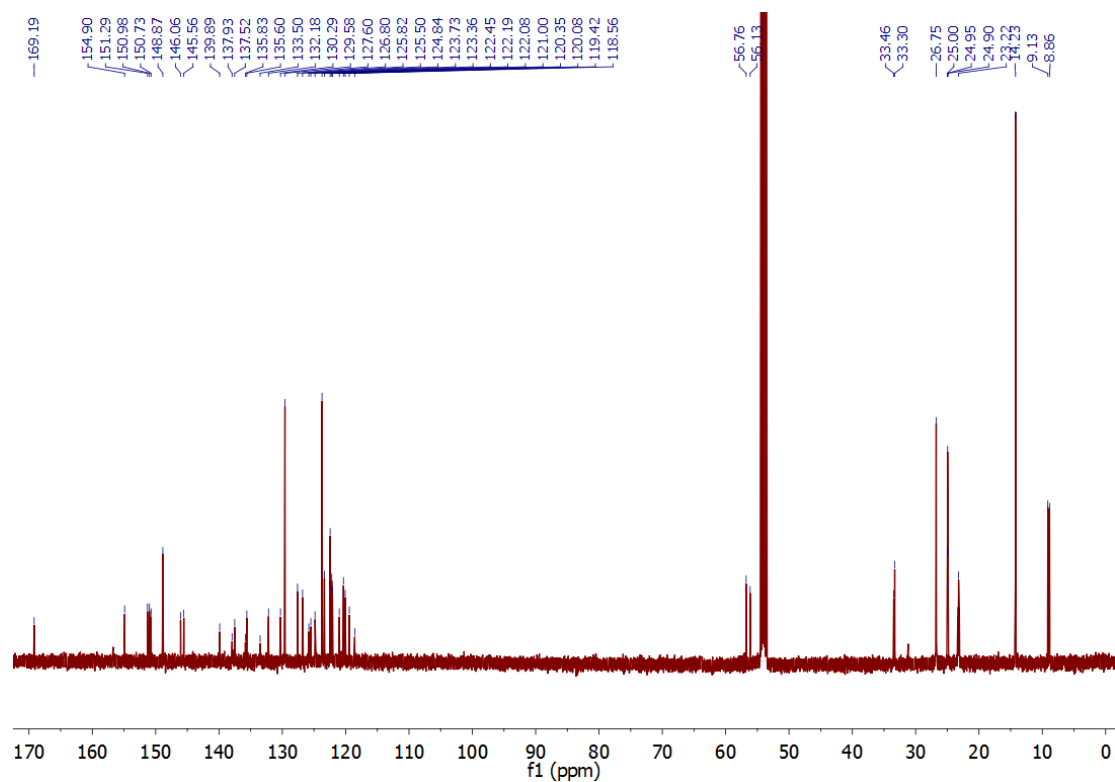


Figure E-17. ^{13}C NMR (126 MHz, CD_2Cl_2) spectra of **DPAF-Pt-CCBTF**.

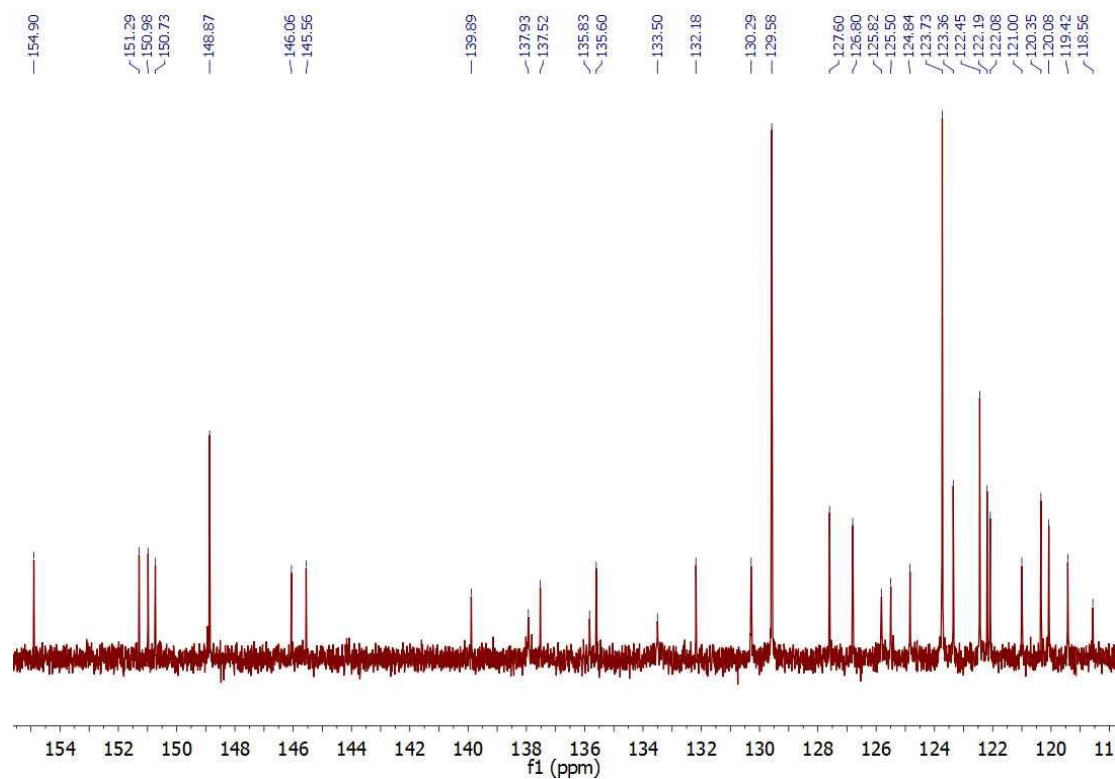


Figure E-18. Aromatic region of the ^{13}C NMR spectra of **DPAF-Pt-CCBTF**.

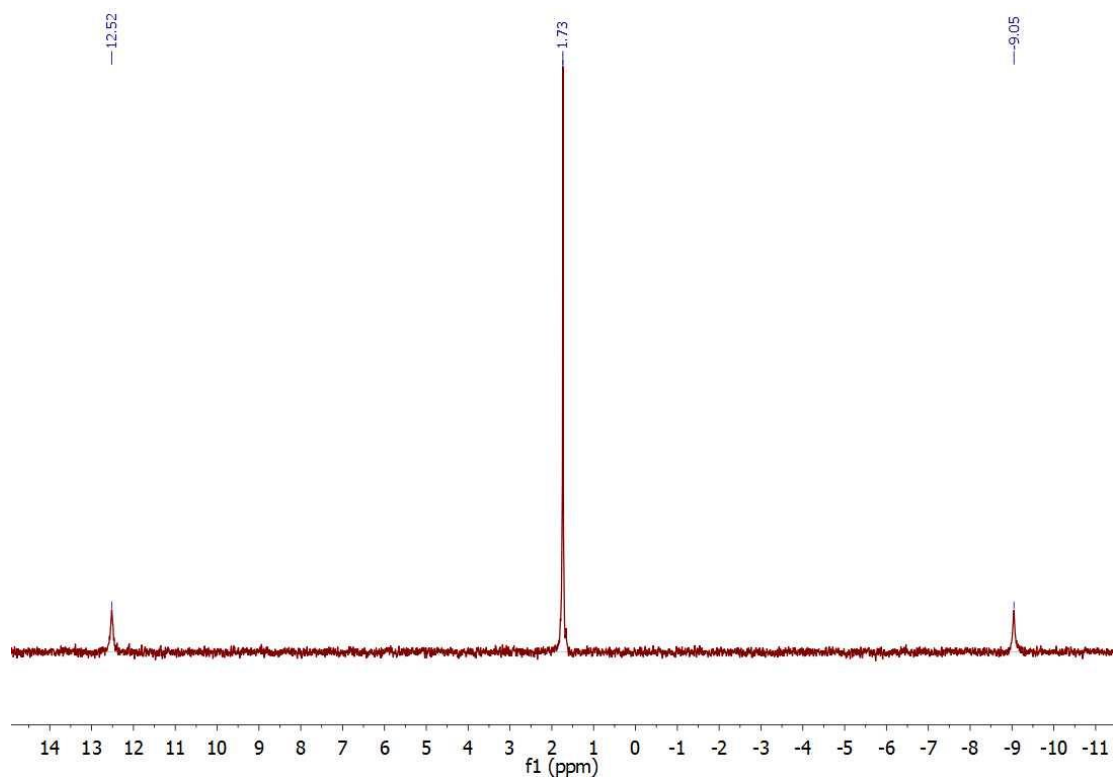


Figure E-19. ^{31}P NMR (121 MHz, CD_2Cl_2) of **DPAF-Pt-CCBTF**.

Emission Lifetime Decays

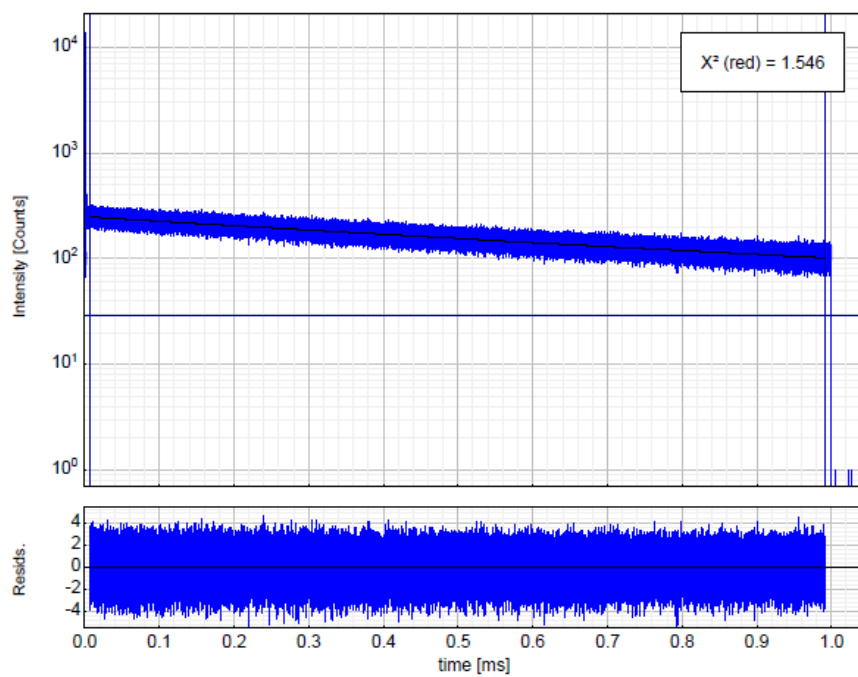


Figure E-20. Phosphorescence lifetime decay for **BTF-Pt-CCBTF**.

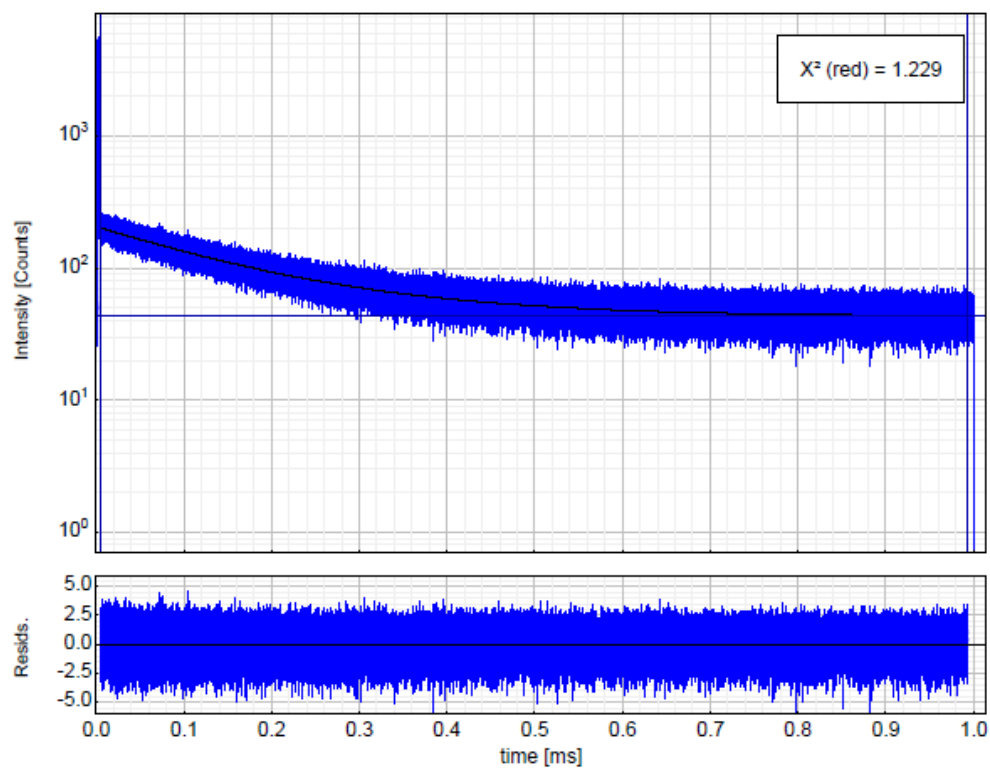


Figure E-21. Phosphorescence lifetime decay for **DPAF-Pt-CCDPAF**.

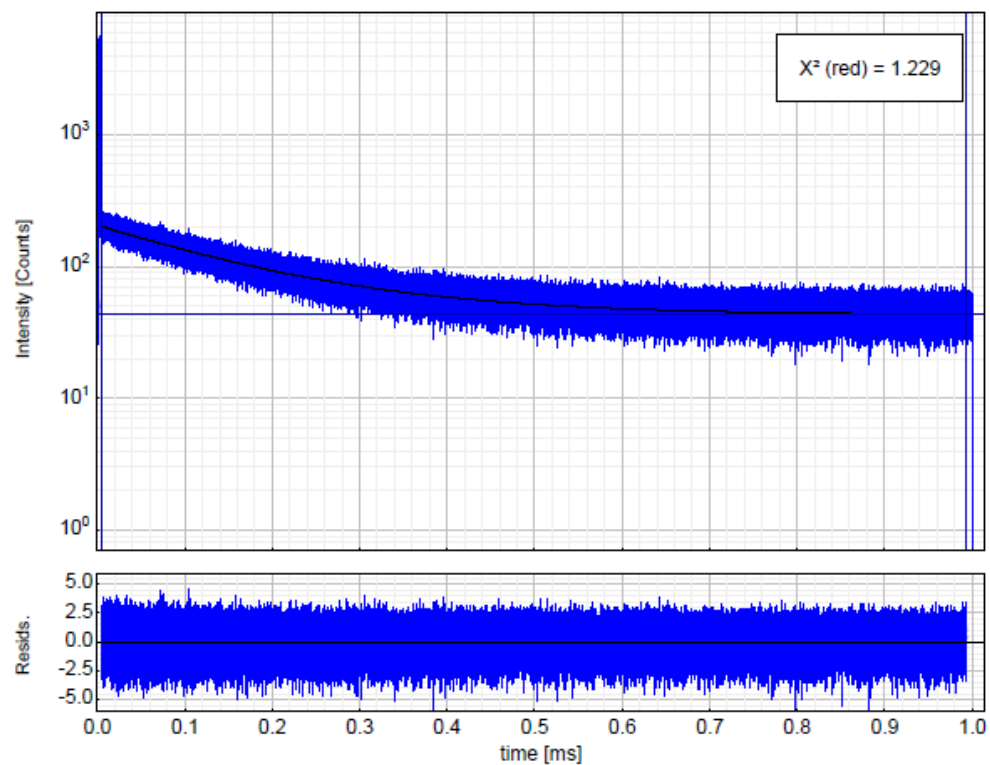


Figure E-22. Phosphorescence lifetime decay for **BTF-Pt-CCDPAF**.

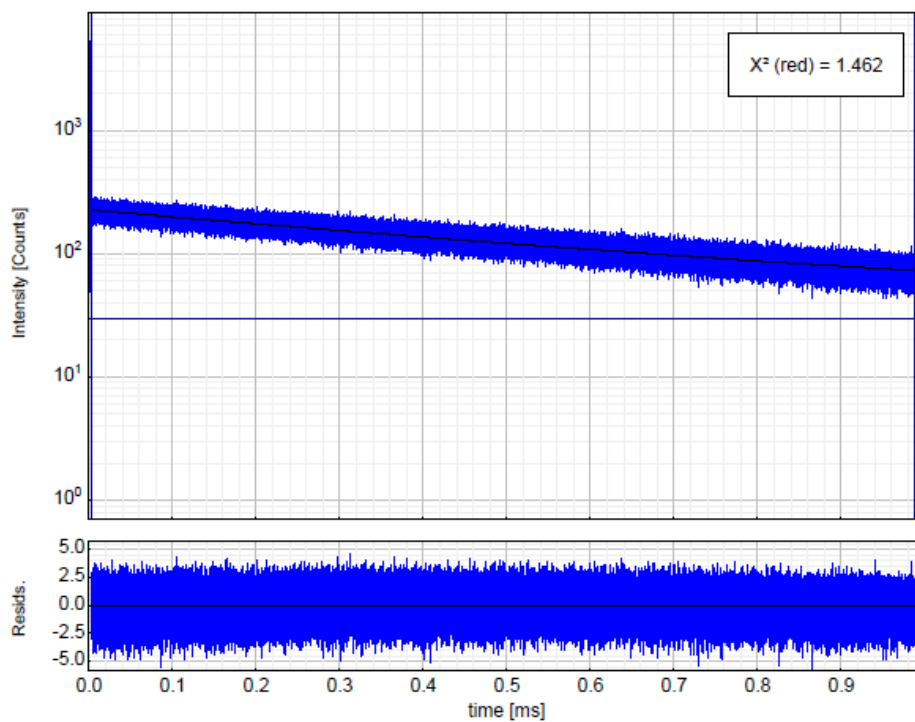


Figure E-23. Phosphorescence lifetime decay for **DPAF-Pt-CCBTF**.

Transient Absorption Decays

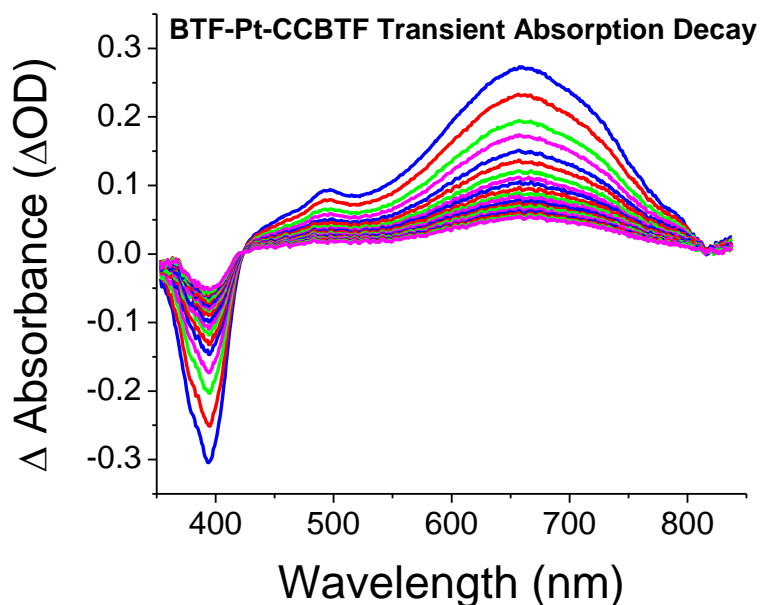


Figure E-24. Transient absorption decay for **BTF-Pt-CCBTF**. Initial camera delay: 100ns, camera delay increment: 10 μ s, 100 images averaged per trace, 180 μ J per pulse.

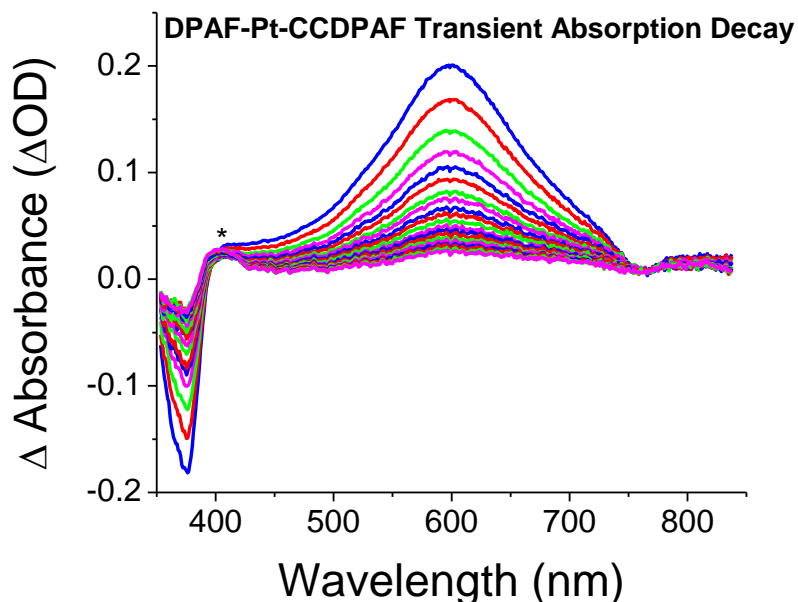


Figure E-25. Transient absorption decay for **DPAF-Pt-CCDPAF**. Initial camera delay: 100ns, camera delay increment: 10 μ s, 100 images averaged per trace, 180 μ J per pulse. The starred feature is absorption from decomposition product generated during the experiment.

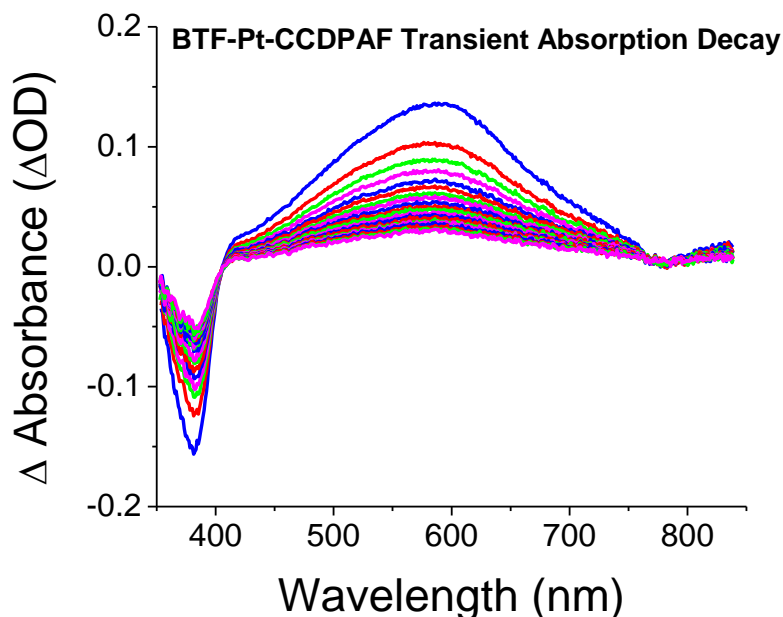


Figure E-26. Transient absorption decay for **BTF-Pt-CCDPAF**. Initial camera delay: 100ns, camera delay increment: 10 μ s, 100 images averaged per trace, 180 μ J per pulse.

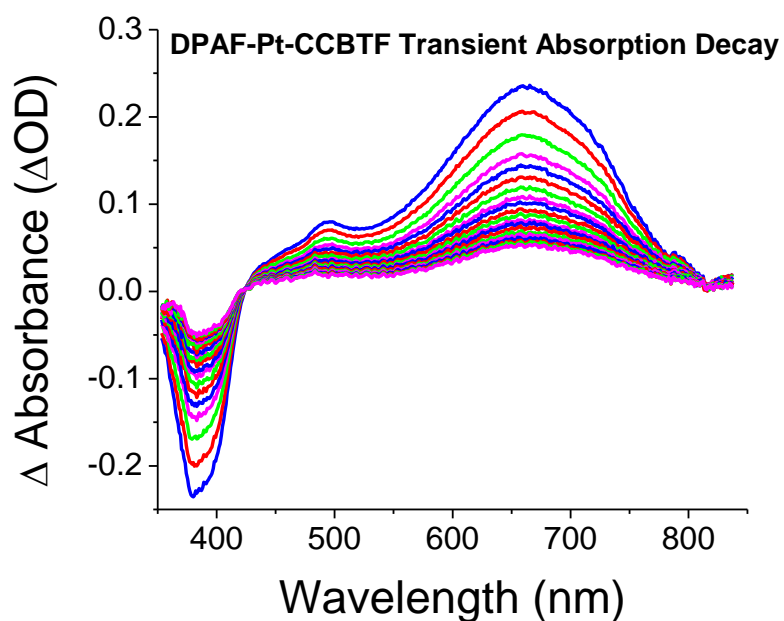


Figure E-27. Transient absorption decay for **DPAF-Pt-CCBTF**. Initial camera delay: 100ns, camera delay increment: 10 μ s, 100 images averaged per trace, 180 μ J per pulse.

Computational Results

Monosubstituted Platinum Model Complexes

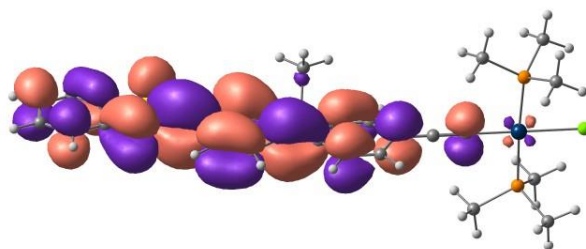


Figure E-28. LUMO of **BTFCC-Pt-Cl'**.

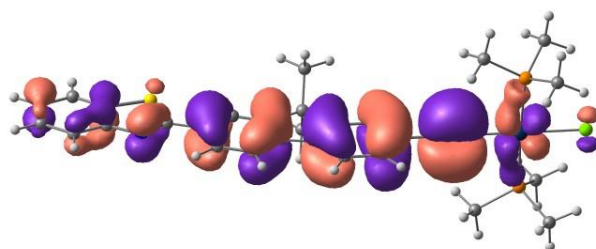


Figure E-29. HOMO of **BTFCC-Pt-Cl'**.

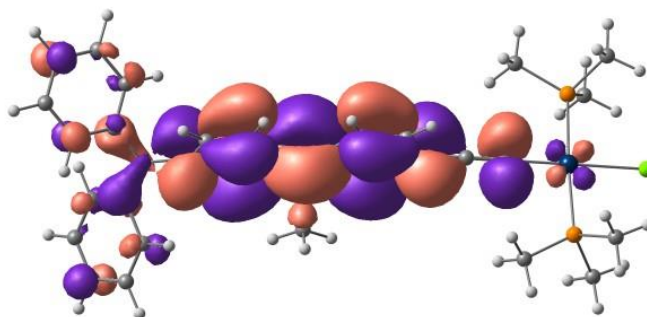


Figure E-30. LUMO of **DPAFCC-Pt-Cl'**.

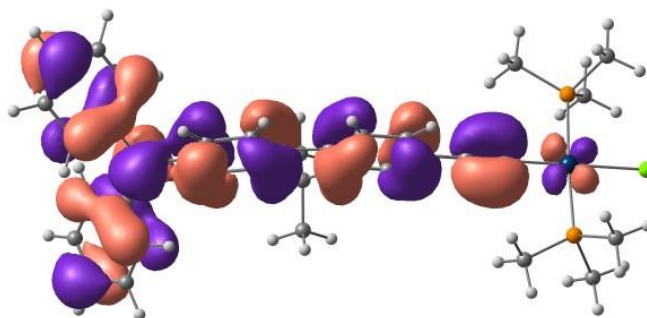


Figure E-31. HOMO of **DPAFCC-Pt-Cl'**.

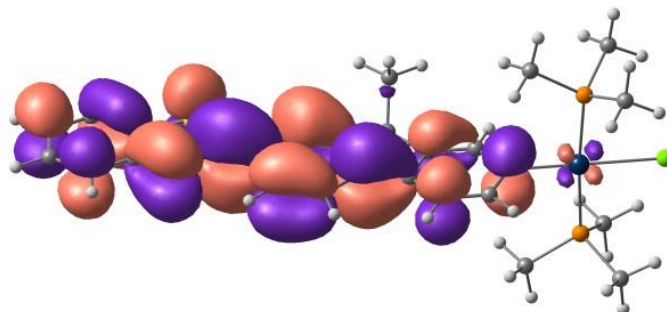


Figure E-32. LUMO of **BTF-Pt-Cl'**.

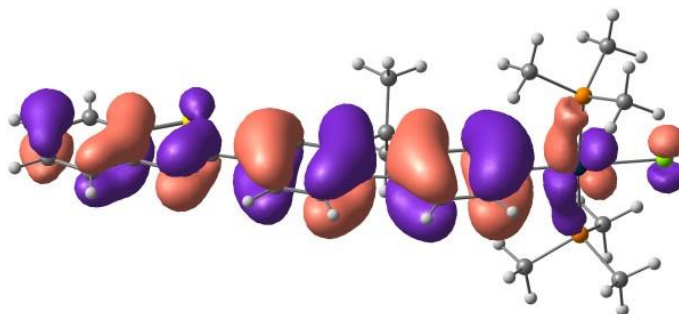


Figure E-33. HOMO of **BTF-Pt-Cl'**.

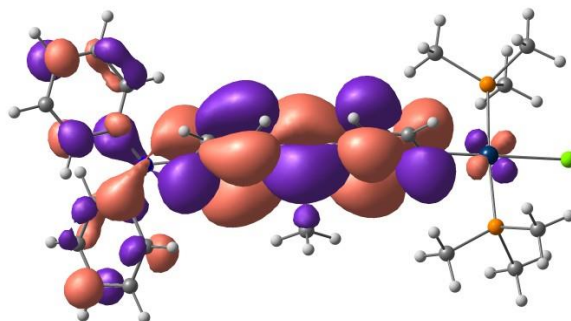


Figure E-34. LUMO of **DPAF-Pt-Cl'**.

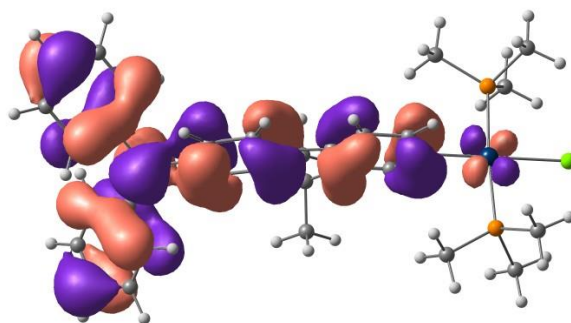


Figure E-35. HOMO of **DPAF-Pt-Cl'**.

Mixed Ligand Platinum Aryl/Acetylide Complexes

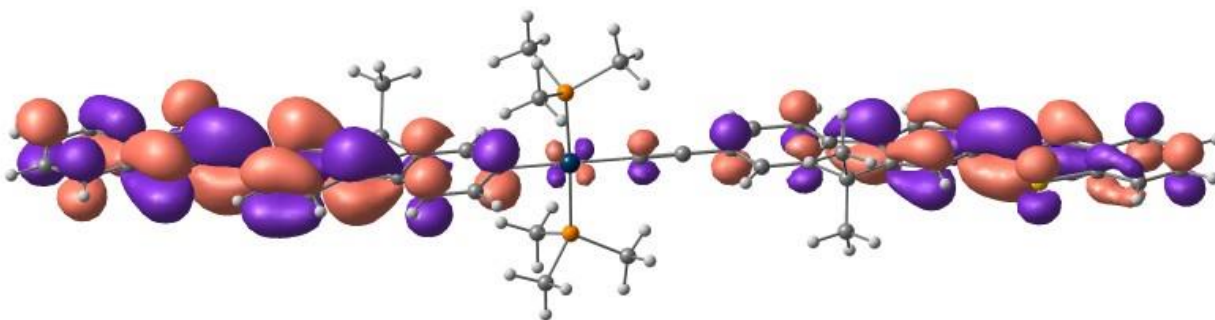


Figure E-36. LUMO+1 of **BTF-Pt-CCBTF**.

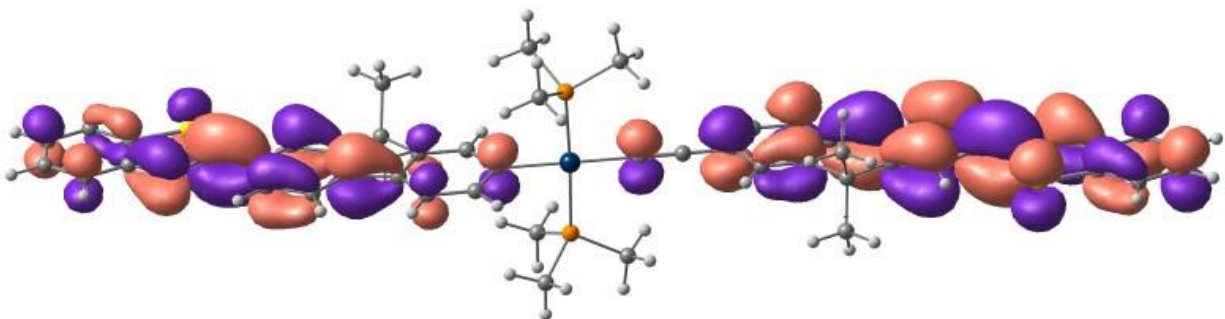


Figure E-37. LUMO of **BTF-Pt-CCBTF**.

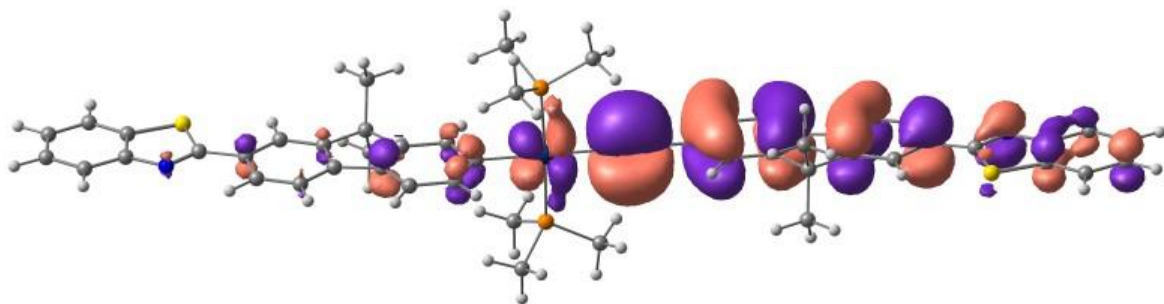


Figure E-38. HOMO of **BTF-Pt-CCBTF**.

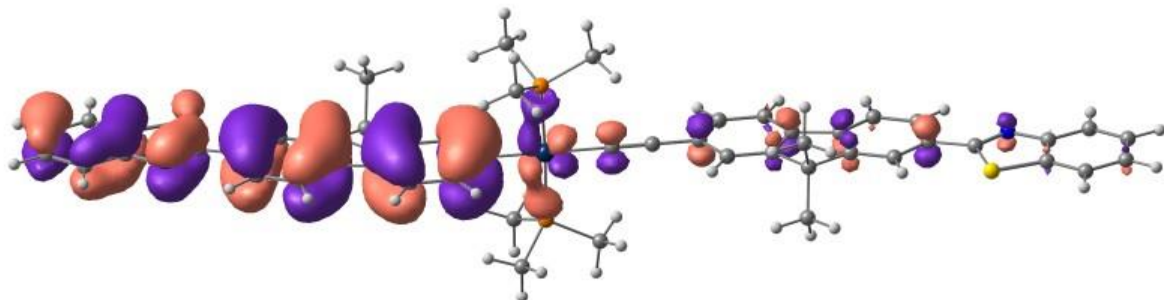


Figure E-39. HOMO-1 of **BTF-Pt-CCBTF**.

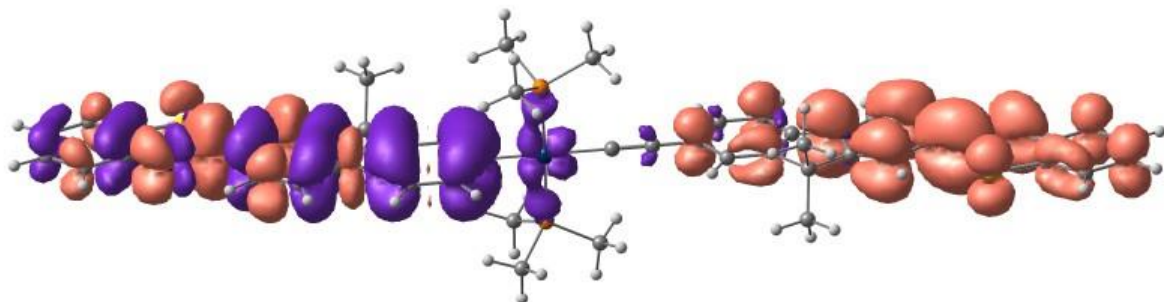


Figure E-40. CDD of the predicted transition at 360 nm for **BTF-Pt-CCBTF**.

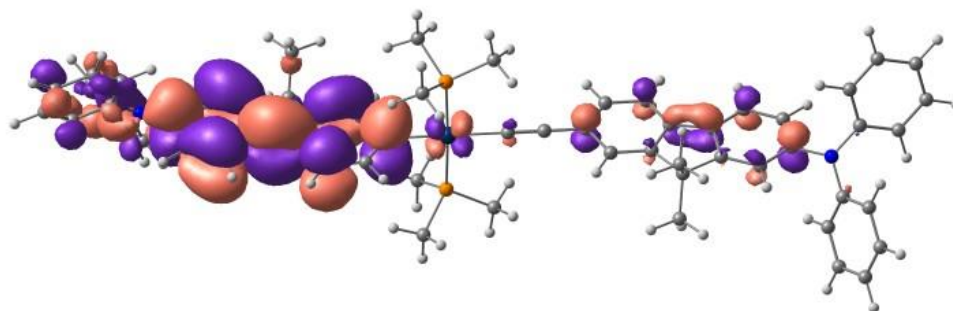


Figure E-41. LUMO+1 of **DPAF-Pt-CCDPAF**.

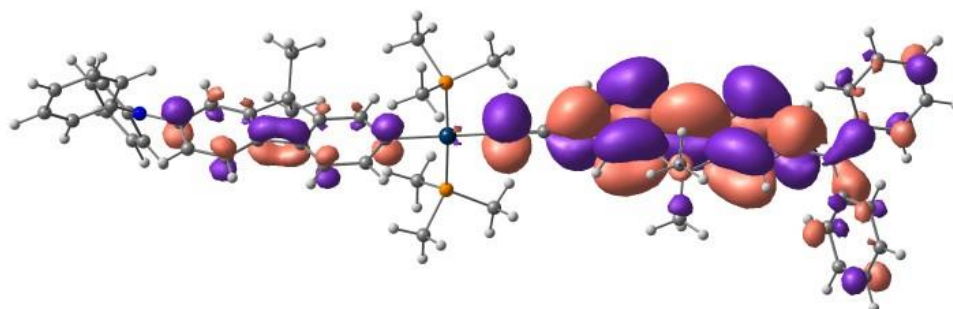


Figure E-42. LUMO of **DPAF-Pt-CCDPAF**.

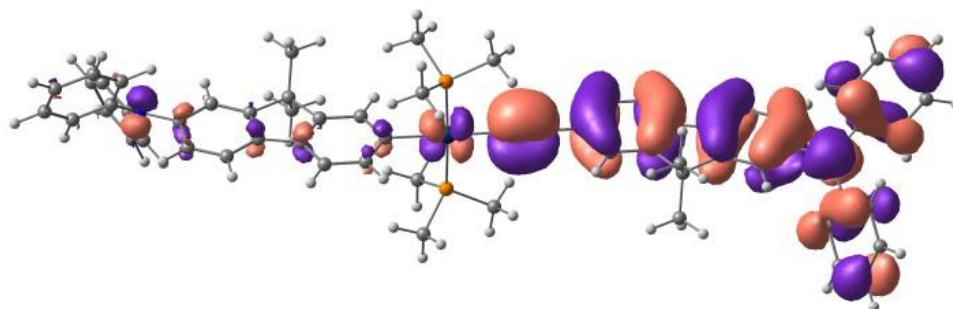


Figure E-43. HOMO of **DPAF-Pt-CCDPAF**.

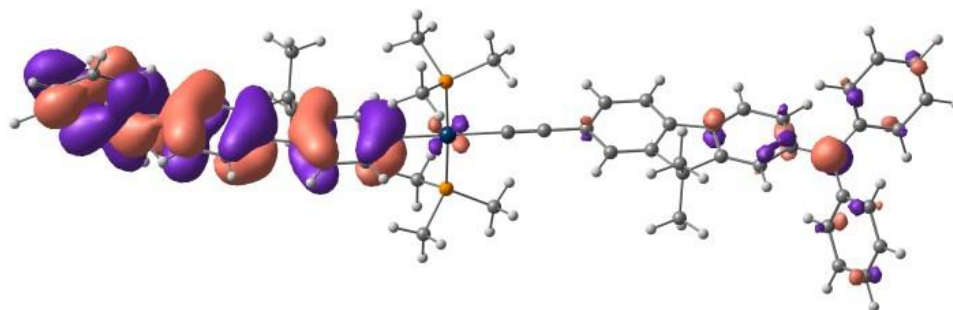


Figure E-44. HOMO-1 of **DPAF-Pt-CCDPAF**.

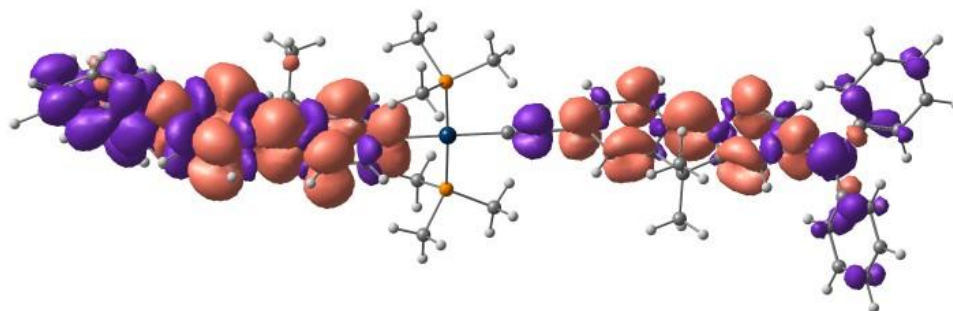


Figure E-45. CDD of the predicted transition at 350 nm for **DPAF-Pt-CCDPAF**.

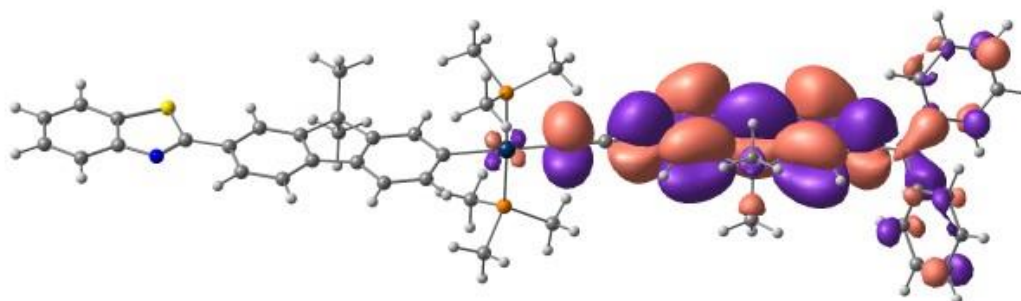


Figure E-46. LUMO+1 of **BTF-Pt-CCDPAF**.

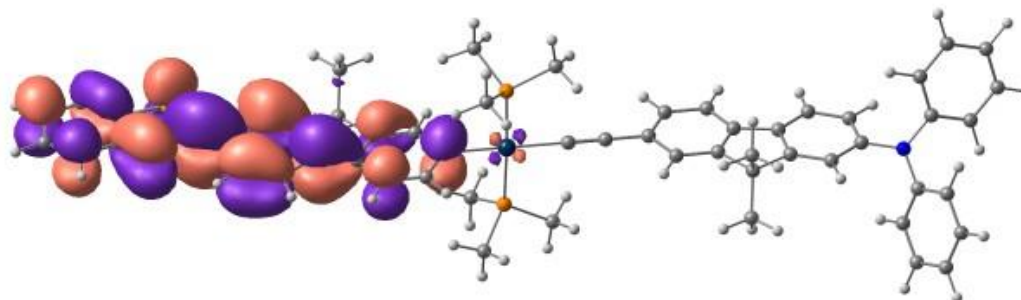


Figure E-47. LUMO of **BTF-Pt-CCDPAF**.

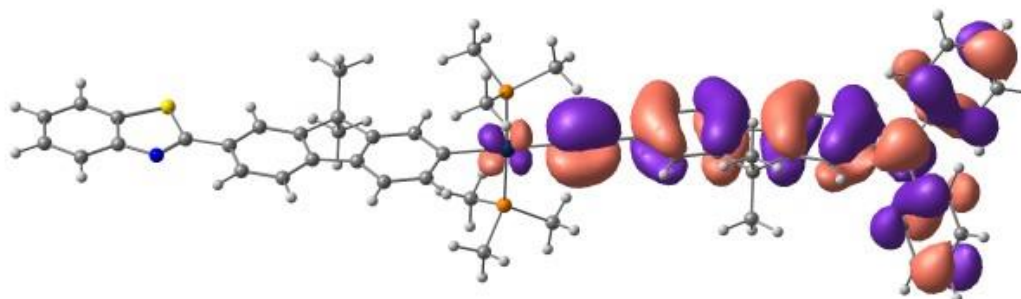


Figure E-48. HOMO of **BTF-Pt-CCDPAF**.

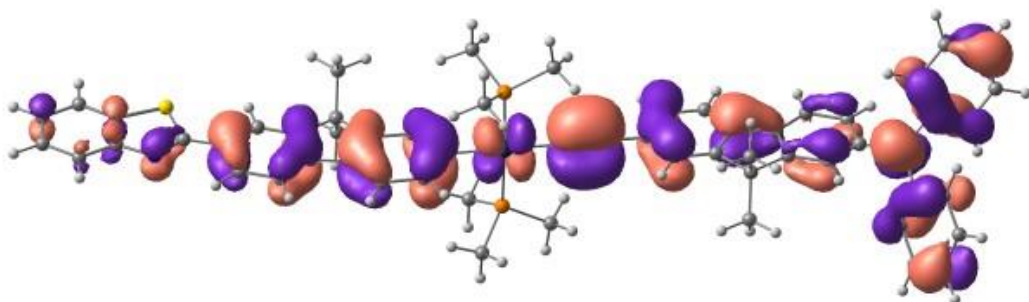


Figure E-49. HOMO-1 of **BTF-Pt-CCDPAF**.

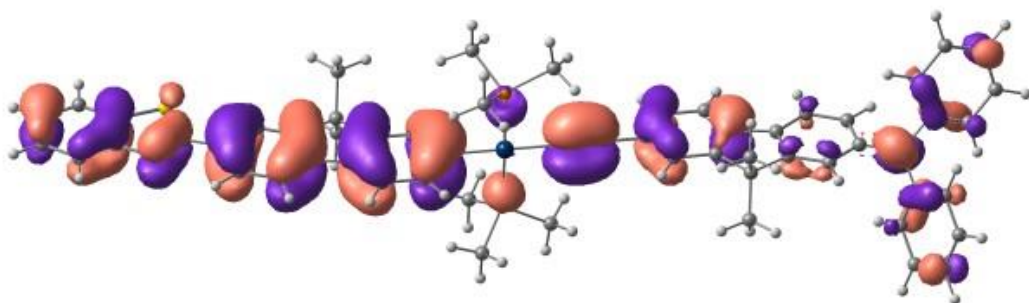


Figure E-50. HOMO-2 of **BTF-Pt-CCDPAF**.

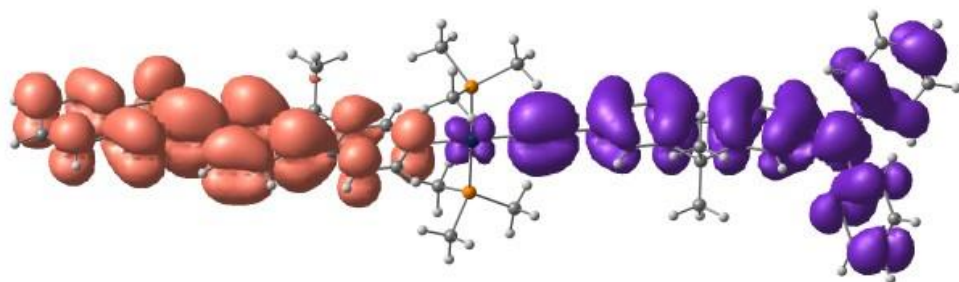


Figure E-51. CDD of the predicted CT transition at 438 nm for **BTF-Pt-CCDPAF**. This transition is not observed in the experimental UV-Vis spectrum.

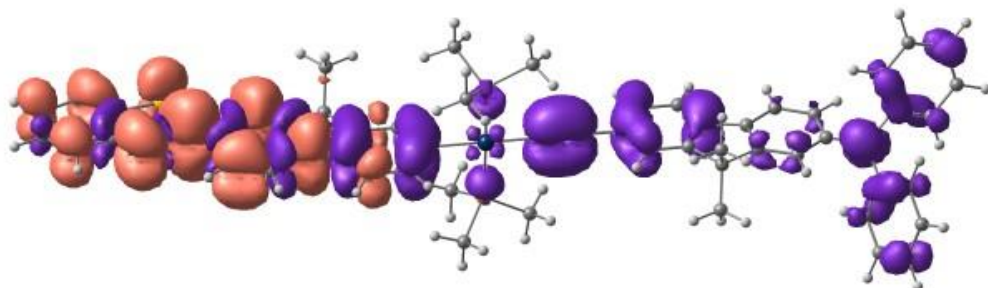


Figure E-52. CDD of the predicted transition at 350 nm for **BTF-Pt-CCDPAF**.

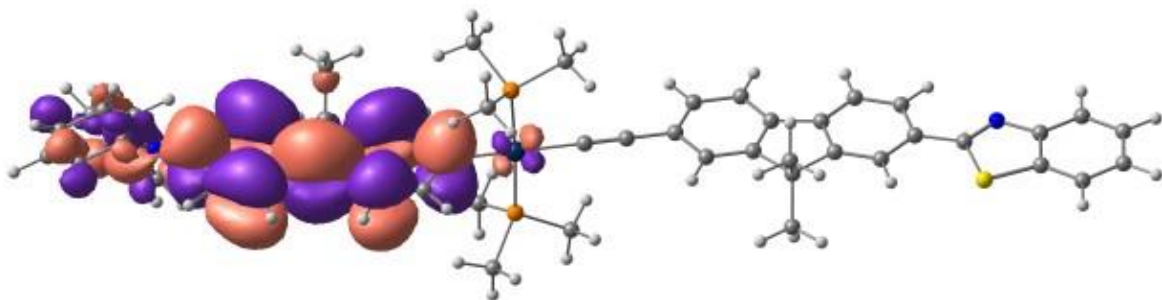


Figure E-53. LUMO+1 of **DPAF-Pt-CCBTF**.

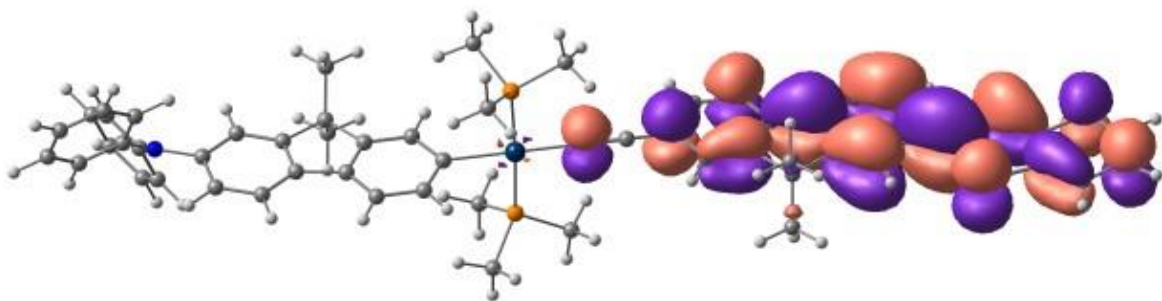


Figure E-54. LUMO of **DPAF-Pt-CCBTF**.

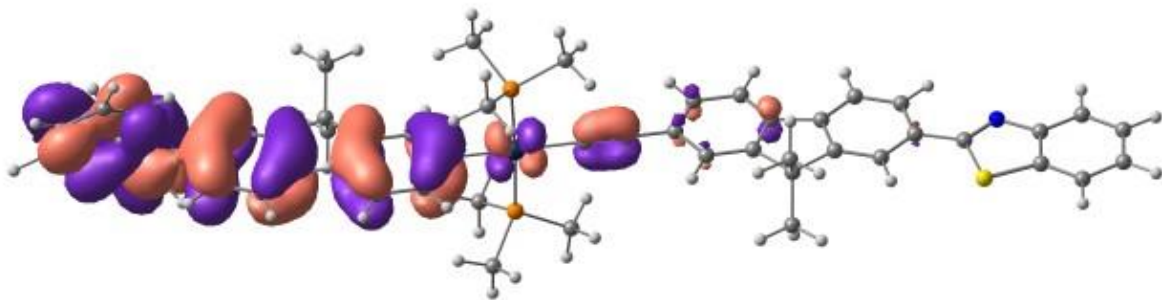


Figure E-55. HOMO of **DPAF-Pt-CCBTF**.

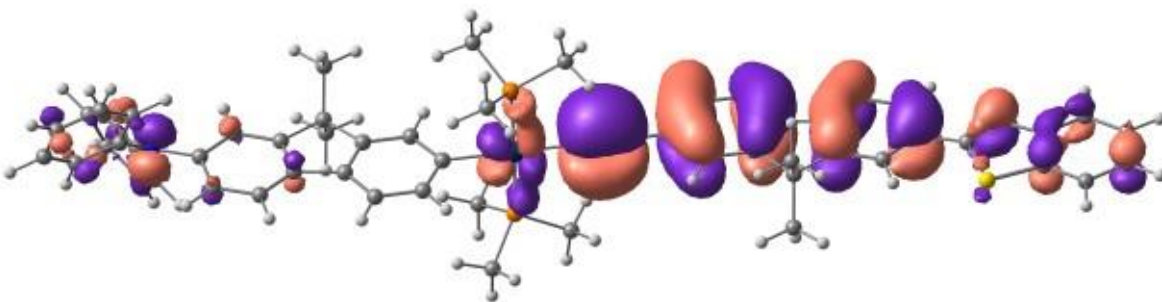


Figure E-56. HOMO of **DPAF-Pt-CCBTF**.

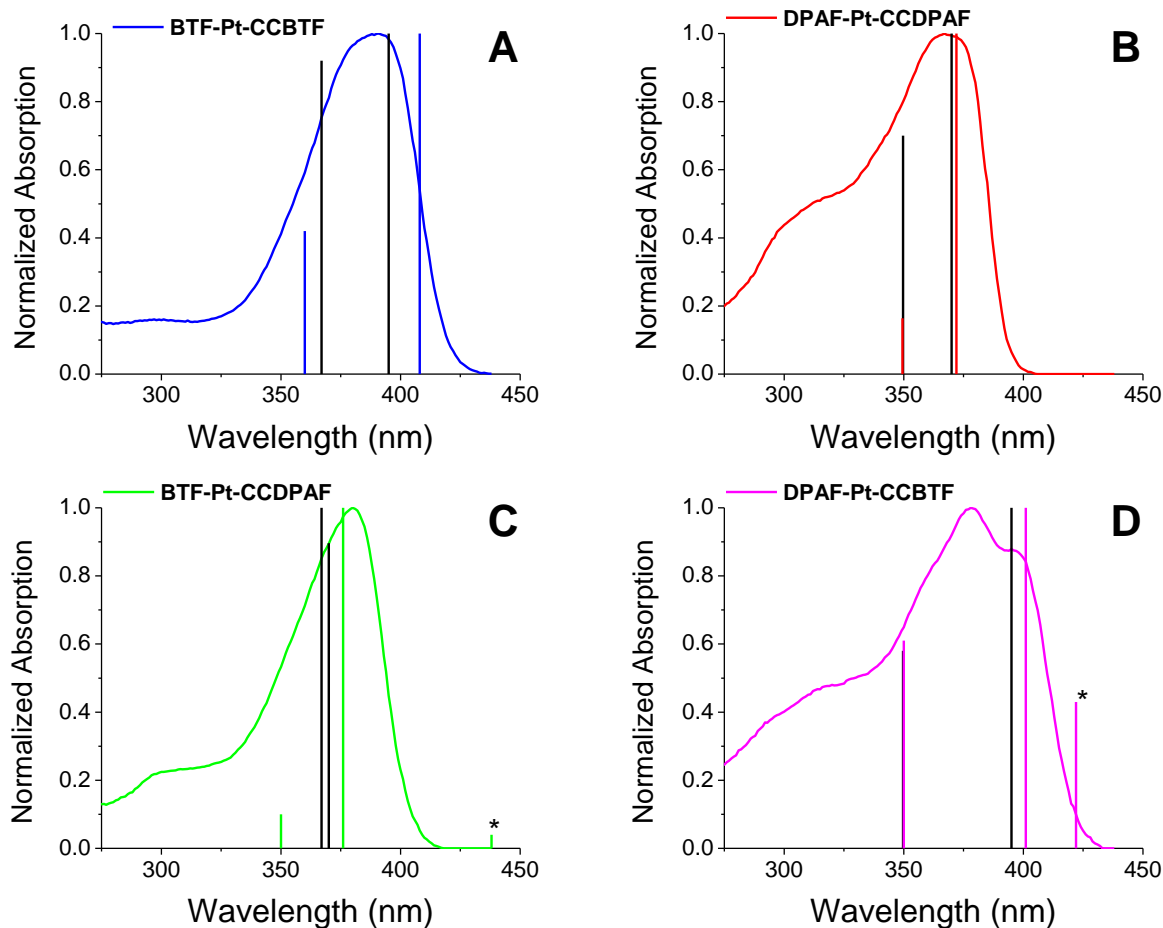


Figure E-57. Normalized UV-Vis absorption spectrum of A) **BTF-Pt-CCBTF**, B) **DPAF-Pt-CCDPAF**, C) **BTF-Pt-CCDPAF**, and D) **DPAF-Pt-CCBTF** with the TDDFT predicted vertical transitions overlaid. Black vertical lines represent predicted transitions from the monosubstituted model complexes, while colored lines represent predicted transitions from the computationally efficient congeners of the parent complex. Vertical transitions are normalized by oscillator strength to the strongest ligand found in each specific complex.

LIST OF REFERENCES

1. J. E. Rogers, T. M. Cooper, P. A. Fleitz, D. J. Glass and D. G. McLean, *J. Phys. Chem. A.*, 2002, **106**, 10108-10115.
2. J. E. Rogers, J. E. Slagle, D. M. Krein, A. R. Burke, B. C. Hall, A. Fratini, D. G. McLean, P. A. Fleitz, T. M. Cooper, M. Drobizhev, N. S. Makarov, A. Rebane, K. Y. Kim, R. Farley and K. S. Schanze, *Inorg. Chem.*, 2007, **46**, 6483-6494.
3. K. Y. Kim, A. H. Shelton, M. Drobizhev, N. Makarov, A. Rebane and K. S. Schanze, *J. Phys. Chem. A.*, 2010, **114**, 7003-7013.
4. E. Glimsdal, M. Carlsson, B. Eliasson, B. Minaev and M. Lindgren, *J. Phys. Chem. A.*, 2007, **111**, 244-250.
5. G. J. Zhou and W. Y. Wong, *Chem. Soc. Rev.*, 2011, **40**, 2541-2566.
6. C. Liao, A. H. Shelton, K. Y. Kim and K. S. Schanze, *ACS Appl. Mater. Interfaces*, 2011, **3**, 3225-3238.
7. G. G. Dubinina, R. S. Price, K. A. Abboud, G. Wicks, P. Wnuk, Y. Stepanenko, M. Drobizhev, A. Rebane and K. S. Schanze, *J. Am. Chem. Soc.*, 2012, **134**, 19346-19349.
8. J. S. Wilson, A. S. Dhoot, A. J. A. B. Seeley, M. S. Khan, A. Kohler and R. H. Friend, *Nature*, 2001, **413**, 828-831.
9. F. Q. Guo, Y. G. Kim, J. R. Reynolds and K. S. Schanze, *Chem. Commun.*, 2006, 1887-1889.
10. W. Y. Wong and C. L. Ho, *Acc. Chem. Res.*, 2010, **43**, 1246-1256.
11. J. Mei, K. Ogawa, Y. G. Kim, N. C. Heston, D. J. Arenas, Z. Nasrollahi, T. D. McCarley, D. B. Tanner, J. R. Reynolds and K. S. Schanze, *ACS Appl. Mater. Interfaces*, 2009, **1**, 150-161.
12. R. Chakrabarty, P. Mukherjee and P. Stang, *Chemical Reviews*, 2011, **111**, 6810-6918.
13. E. M. Badley, J. Chatt, R. L. Richards and G. A. Sim, *J. Chem. Soc. D*, 1969, 1322-1323.
14. S.-W. Lai, M. C.-W. Chan, K.-K. Cheung and C.-M. Che, *Organometallics*, 1999, **18**, 3327-3336.
15. Y. Unger, A. Zeller, S. Ahrens and T. Strassner, *Chem. Commun.*, 2008, 3263-3265.

16. Y. Unger, A. Zeller, M. A. Taige and T. Strassner, *Dalton Trans.*, 2009, 4786-4794.
17. C.-S. Lee, S. Sabiah, J.-C. Wang, W.-S. Hwang and I. J. B. Lin, *Organometallics*, 2010, **29**, 286-289.
18. T. Zou, C.-N. Lok, Y. M. E. Fung and C.-M. Che, *Chem. Commun.*, 2013, **49**, 5423-5425.
19. K. Li, T. Zou, Y. Chen, X. Guan and C.-M. Che, *Chem. Eur. J.*, 2015, **21**, 7441-7453.
20. Y. Wu, S.-X. Wu, H.-B. Li, Y. Geng and Z.-M. Su, *Dalton Trans.*, 2011, **40**, 4480-4488.
21. X. Zhang, A. M. Wright, N. J. DeYonker, T. K. Hollis, N. I. Hammer, C. E. Webster and E. J. Valente, *Organometallics*, 2012, **31**, 1664-1672.
22. M. Tenne, S. Metz, I. Münster, G. Wagenblast and T. Strassner, *Organometallics*, 2013, **32**, 6257-6264.
23. A. Tronnier, S. Metz, G. Wagenblast, I. Muenster and T. Strassner, *Dalton Trans.*, 2014, **43**, 3297-3305.
24. A. Tronnier, A. Poethig, E. Herdtweck and T. Strassner, *Organometallics*, 2014, **33**, 898-908.
25. A. Tronnier, A. Pöthig, S. Metz, G. Wagenblast, I. Münster and T. Strassner, *Inorg. Chem.*, 2014, **53**, 6346-6356.
26. A. Tronnier, U. Heinemeyer, S. Metz, G. Wagenblast, I. Muenster and T. Strassner, *J. Mater. Chem. C*, 2015, **3**, 1680-1693.
27. M. Tenne, S. Metz, G. Wagenblast, I. Munster and T. Strassner, *Dalton Trans.*, 2015, **44**, 8444-8455.
28. K. Li, G. Cheng, C. Ma, X. Guan, W.-M. Kwok, Y. Chen, W. Lu and C.-M. Che, *Chem. Sci.*, 2013, **4**, 2630-2644.
29. T. Fleetham, G. Li, L. Wen and J. Li, *Adv. Mater.*, 2014, **26**, 7116-7121.
30. Y. Z. Zhang, J. A. Garg, C. Michelin, T. Fox, O. Blacque and K. Venkatesan, *Inorg. Chem.*, 2011, **50**, 1220-1228.
31. J. E. Rogers, B. C. Hall, D. C. Hufnagle, J. E. Slagle, A. P. Ault, D. G. McLean, P. A. Fleitz and T. M. Cooper, *J. Chem. Phys.*, 2005, **122**, 214708.
32. Y. Zhang, J. Clavadetscher, M. Bachmann, O. Blacque and K. Venkatesan, *Inorg. Chem.*, 2014, **53**, 756-771.

33. Y. Zhang, O. Blacque and K. Venkatesan, *Chem. Eur. J.*, 2013, **19**, 15689-15701.
34. R. W. Winkel, G. G. Dubinina, K. A. Abboud and K. S. Schanze, *Dalton Trans.*, 2014, **43**, 17712-17720.
35. K. A. Zachariasse, G. Duveneck and W. Kühnle, *Chem. Phys. Lett.*, 1985, **113**, 337-343.
36. H.-J. Galla and E. Sackmann, *BBA - Biomembranes*, 1974, **339**, 103-115.
37. A. E. C. Redpath and M. A. Winnik, *J. Am. Chem. Soc.*, 1982, **104**, 5604-5607.
38. T. Hiraga, T. Uchida, N. Kitamura, H. B. Kim, S. Tazuke and T. Yagi, *J. Am. Chem. Soc.*, 1989, **111**, 7466-7469.
39. T. Abe, T. Itakura, N. Ikeda and K. Shinozaki, *Dalton Trans.*, 2009, **38**, 711-715.
40. S. Okajima, P. C. Subudhi and E. C. Lim, *J. Chem. Phys.*, 1977, **67**, 4611-4615.
41. A. Tsuchida, T. Ikawa, T. Tomie and M. Yamamoto, *J. Phys. Chem.*, 1995, **99**, 8196-8199.
42. K. E. Brown, W. A. Salamant, L. E. Shoer, R. M. Young and M. R. Wasielewski, *J. Phys. Chem. Lett.*, 2014, **5**, 2588-2593.
43. Y. Tamai, H. Ohkita, J. Shimada, H. Benten, S. Ito, S. Yamanaka, K. Hisada, K. Tani, K. Kubono and T. Shinmyozu, *J. Phys. Chem. A.*, 2013, **117**, 7776-7785.
44. J. E. Slagle, T. M. Cooper, D. M. Krein, J. E. Rogers, D. G. McLean and A. M. Urbas, *Chem. Phys. Lett.*, 2007, **447**, 65-68.
45. T. M. Cooper, D. M. Krein, A. R. Burke, D. G. McLean, J. E. Rogers and J. E. Slagle, *J. Phys. Chem. A.*, 2006, **110**, 13370-13378.
46. R. S. Price, G. Dubinina, G. Wicks, M. Drobizhev, A. Rebane and K. S. Schanze, *ACS Appl. Mater. Interfaces*, 2015, **7**, 10795-10805.
47. D. Chateau, F. Chaput, C. Lopes, M. Lindgren, C. Brännlund, J. Öhgren, N. Djourellov, P. Nedelec, C. Desroches, B. Eliasson, T. Kindahl, F. Lerouge, C. Andraud and S. Parola, *ACS Appl. Mater. Interfaces*, 2012, **4**, 2369-2377.
48. R. Vestberg, R. Westlund, A. Eriksson, C. Lopes, M. Carlsson, B. Eliasson, E. Glimsdal, M. Lindgren and E. Malmström, *Macromolecules*, 2006, **39**, 2238-2246.
49. T. R. Cook and P. J. Stang, *Chem. Rev.*, 2015, DOI: 10.1021/cr5005666.
50. W.-D. Müller, G. Schmidtberg and H.-A. Brune, *Chem. Ber.*, 1985, **118**, 4653-4664.

51. S. Shekhar and J. F. Hartwig, *J. Am. Chem. Soc.*, 2004, **126**, 13016-13027.
52. T. A. Perera, M. Masjedi and P. R. Sharp, *Inorg. Chem.*, 2014, **53**, 7608-7621.
53. C. J. Kuehl, S. D. Huang and P. J. Stang, *J. Am. Chem. Soc.*, 2001, **123**, 9634-9641.
54. T. Megyes, H. Jude, T. Grósz, I. Bakó, T. Radnai, G. Tárkányi, G. Pálinkás and P. J. Stang, *J. Am. Chem. Soc.*, 2005, **127**, 10731-10738.
55. A. S. Gundogan, X. Meng, R. W. Winkel and K. S. Schanze, *Dalton Trans.*, 2015, DOI: 10.1039/C5DT00538H.
56. L. Li, C.-L. Ho and W.-Y. Wong, *J. Organomet. Chem.*, 2012, **703**, 43-50.
57. M. Younus, N. J. Long, P. R. Raithby and J. Lewis, *J. Organomet. Chem.*, 1998, **570**, 55-62.
58. H. Zhan, S. Lamare, A. Ng, T. Kenny, H. Guernon, W.-K. Chan, A. B. Djurišić, P. D. Harvey and W.-Y. Wong, *Macromolecules*, 2011, **44**, 5155-5167.
59. K. B. Vincent, M. Parthey, D. S. Yufit, M. Kaupp and P. J. Low, *Polyhedron*, 2015, **86**, 31-42.
60. Z. J. Li, E. Badaeva, D. P. Zhou, J. Bjorgaard, K. D. Glusac, S. Killina and W. F. Sun, *J. Phys. Chem. A*, 2012, **116**, 4878-4889.
61. Y. P. Zhou, M. Zhang, Y. H. Li, Q. R. Guan, F. Wang, Z. J. Lin, C. K. Lam, X. L. Feng and H. Y. Chao, *Inorg. Chem.*, 2012, **51**, 5099-5109.
62. M. H. Nguyen and J. H. K. Yip, *Organometallics*, 2011, **30**, 6383-6392.
63. V. W. W. Yam, R. P. L. Tang, K. M. C. Wong and K. K. Cheung, *Organometallics*, 2001, **20**, 4476-4482.
64. A. Hobbs Shelton, *Synthesis and Photophysical Characterization of π -Conjugated Nonlinear Absorbing Organometallic Platinum Complexes*, Ph.D. Dissertation, University of Florida, Gainesville, FL, 2011.
65. C. P. Newman, R. J. Deeth, G. J. Clarkson and J. P. Rourke, *Organometallics*, 2007, **26**, 6225-6233.
66. C. A. Citadelle, E. Le Nouy, F. Bisaro, A. M. Z. Slawin and C. S. J. Cazin, *Dalton Trans.*, 2010, **39**, 4489-4491.
67. S. Fantasia, A. Pasini and S. P. Nolan, *Dalton Trans.*, 2009, **38**, 8107-8110.
68. M. I. Bruce, J. Davy, B. C. Hall, Y. J. van Galen, B. W. Skelton and A. H. White, *Appl. Organometal. Chem.*, 2002, **16**, 559-568.

69. H. Jacobsen, A. Correa, A. Poater, C. Costabile and L. Cavallo, *Coord. Chem. Rev.*, 2009, **253**, 687-703.
70. A. Harriman, *J. Chem. Soc., Chem. Commun.*, 1977, 777-778.
71. S. L. Murov, I. Carmichael and G. L. Hug, *Handbook of Photochemistry*, Marcel Dekker Inc., New York, 2nd edn., 1993.
72. M. Mardelli and J. Olmsted, *J. Photochem.*, 1977, **7**, 277-285.
73. M. J. Frisch, G. W. Trucks, H. B. Schlegel, G. E. Scuseria, M. A. Robb, J. R. Cheeseman, G. Scalmani, V. Barone, B. Mennucci, G. A. Petersson, H. Nakatsuji, M. Caricato, X. Li, H. P. Hratchian, A. F. Izmaylov, J. Bloino, G. Zheng, J. L. Sonnenberg, M. Hada, M. Ehara, K. Toyota, R. Fukuda, J. Hasegawa, M. Ishida, T. Nakajima, Y. Honda, O. Kitao, H. Nakai, T. Vreven, J. A. J. Montgomery, J. E. Peralta, F. Ogliaro, M. Bearpark, J. J. Heyd, E. Brothers, K. N. Kudin, V. N. Staroverov, R. Kobayashi, J. Normand, K. Raghavachari, A. Rendell, J. C. Burant, S. S. Iyengar, J. Tomasi, M. Cossi, N. Rega, N. J. Millam, M. Klene, J. E. Knox, J. B. Cross, V. Bakken, C. Adamo, J. Jaramillo, R. Gomperts, R. E. Stratmann, O. Yazyev, A. J. Austin, R. Cammi, C. Pomelli, J. W. Ochterski, R. L. Martin, K. Morokuma, V. G. Zakrzewski, G. A. Voth, P. Salvador, J. J. Dannenberg, S. Dapprich, A. D. Daniels, Ö. Farkas, J. B. Foresman, J. V. Ortiz, J. Cioslowski and D. J. Fox, *Gaussian 09, (Revision C.01)*, Gaussian, Inc., Wallingford, CT, 2011.
74. P. de Frémont, N. M. Scott, E. D. Stevens, T. Ramnial, O. C. Lightbody, C. L. B. Macdonald, J. A. C. Clyburne, C. D. Abernethy and S. P. Nolan, *Organometallics*, 2005, **24**, 6301-6309.
75. H. M. J. Wang and I. J. B. Lin, *Organometallics*, 1998, **17**, 972-975.
76. *SHELXTL6*, Bruker-AXS, Madison, WI, 2008.
77. R. T. Farley, *Photophysics of Platinum and Iridium Organometallic Materials: From Molecular Wires to Nonlinear Optics*, Ph.D. Dissertation, University of Florida, Gainesville, FL, 2007.
78. M. Sheikbahae, A. A. Said, T. H. Wei, D. J. Hagan and E. W. Vanstryland, *IEEE J. Quantum Electron.*, 1990, **26**, 760-769.
79. G. A. Andrienko, *Chemcraft*, <http://www.chemcraftprog.com>, 2012.
80. E. Glimsdal, P. Norman and M. Lindgren, *J. Phys. Chem. A.*, 2009, **113**, 11242-11249.
81. T.-C. Cheung, K.-K. Cheung, S.-M. Peng and C.-M. Che, *Journal of the Chemical Society, Dalton Transactions*, 1996, DOI: 10.1039/DT9960001645, 1645-1651.

82. N. B. William B. Austin, William J. Kelleghan, Kreisler S. Y. Lau, *J. Org. Chem.*, 1981, **46**, 2280-2286.
83. G. Bounos, S. Ghosh, A. K. Lee, K. N. Plunkett, K. H. DuBay, J. C. Bolinger, R. Zhang, R. A. Friesner, C. Nuckolls, D. R. Reichman and P. F. Barbara, *J Am Chem Soc*, 2011, **133**, 10155-10160.
84. Y.-T. Wu, T. Labahn, A. Demeter, K. A. Zachariasse and A. de Meijere, *Eur. J. Org. Chem.*, **2004**, 4483-4491.
85. Y. Kikugawa and Y. Ogawa, *Chem. Pharm. Bull.*, 1979, **27**, 2405-2410.
86. G. Joshi and S. Adimurthy, *Synth. Commun.*, 2011, **41**, 720-728.
87. Y. Liu, S. Jiang, K. Glusac, D. H. Powell, D. F. Anderson and K. S. Schanze, *J. Am. Chem. Soc.*, 2002, **124**, 12412-12413.
88. K. Y. Kim, A. Haefele, R. T. Farley and K. S. Schanze, unpublished work.
89. T. M. Cooper, D. M. Krein, A. R. Burke, D. G. McLean, J. E. Rogers, J. E. Slagle and P. A. Fleitz, *J. Phys. Chem. A.*, 2006, **110**, 4369-4375.
90. N. S. Makarov, M. Drobizhev and A. Rebane, *Opt. Express*, 2008, **16**, 4029-4047.
91. C. J. Cramer, *Essentials of Computational Chemistry: Theories and Models*, Wiley, 2nd edn., 2004.
92. R. Dennington, T. Keith and J. Millam, *GaussView*, Semichem Inc., Shawnee Mission, KS, 2009.
93. E. D. Glendening, A. E. Reed, J. E. Carpenter and F. Weinhold, *NBO Version 3.1*.
94. T. Lu and F. Chen, *J. Comp. Chem.*, 2012, **33**, 580-592.
95. T. Lu and F. Chen, *Acta Chim. Sinica*, 2011, **69**, 2393-2406.

BIOGRAPHICAL SKETCH

Russ Winkel was born and raised in Cedarburg, WI. It was during his time at Cedarburg High School that his love of chemistry was discovered and nurtured. Upon graduation, five semesters of chemistry had already been taken. Russ then went on to the University of Wisconsin – Stevens Point in the fall of 2006. He took every course offered by the Chemistry Department and graduated in the spring of 2010 with an ACS Certified Chemistry Degree with Polymer Option and a minor in mathematics.

The fall of 2010 took Russ to the University of Florida, where he started research under the direction of Professor Kirk Schanze. His research entailed the synthesis, photophysical characterization, and computational study of platinum(II) arylacetylide compounds. Russ received his Ph.D. for this work in the summer of 2015.